CRANFIELD UNIVERSITY

CENTRE FOR DEFENCE CHEMISTRY

DEPARTMENT OF ENGINEERING AND APPLIED SCIENCE

PhD THESIS

Academic Year 2010-2011

Christopher S Peel

Laser Induced Breakdown Spectroscopy for Elemental Analysis in Aqueous Media

Supervisor: Dr S Rafi Ahmad

November 2011

Abstract

This thesis is based on extensive experimental work over a three year Ph.D. studentship program sponsored by the AWE on laser induced breakdown spectroscopy (LIBS) for elemental analysis in the water environment. An exhaustive up-to-date literature review has revealed widely different results on the dependence of some of the LIBS parameters on both laser and target parameters. In this research, parametric measurements of the laser-water interaction events were undertaken to validate some quoted values and to attempt to resolve discrepancies within the published results. Analysis of dielectric breakdown in water bulk by focussed laser beam has shown that the threshold laser pulse energy for this was approximately 60% lower in tap water than in distilled water due to impurity content of the former. However, the effect of analyte concentration was found to be much less drastic, giving only a 10% reduction for 2 orders of magnitude of concentration increase of dissolved sodium. Parameters of cavitation bubbles, resulting from the laser induced breakdown process in the water bulk, were measured using two different techniques i.e. probe beam deflection (PBD) and high speed imaging (HSI). Values of bubble diameter before collapse (maximum) and the frequency of the oscillation were found to be different, by 27% for the diameter and by 22% for the frequency, in the results obtained using the two different techniques. The values of the parameters obtained in this study and those found in the literature vary widely and do not show any trend on their dependence with laser pulse energy. It is concluded that large uncertainty in the estimation or control of sampled volume defined by the waist of the laser beam focus render large errors on such measurements. The present work includes parametric measurement of signal-to-noise ratio (S/N) for the detection of signals from analytes dissolved in water for different variable experimental parameters. Optimum values for achieving maximum S/N were obtained. In addition to the spectral and temporal filtering for improving S/N, mechanical filtering techniques were also investigated. This has resulted in the improvement of S/N by more than 25%. The thesis concludes with remarks, based on the analysis of the experimental data, on work for further improvement of sensitivity of the LIBS technique and its wider application as a portable device for *in situ*, real time point monitoring of elemental contaminants in water.

Acknowledgements

This document represents the successful completion of a three year PhD research program within the field of applied laser induced breakdown spectroscopy. The Author wishes to acknowledge the following individuals:

- Dr S Rafi Ahmad for critical review of Progress Reports and Thesis Chapters, emotional support and guidance, continual encouragement and *Promethean* perseverance whilst the Author gradually learned the subtle art of brevity
- Mr Edwin Billiet for patient support in the laser laboratory, an unrivalled knowledge of photonic engineering and demonstrating that humour – of the gallows variety - is the best cure for experimental melancholy
- Professor Peter J Dyer and Dr David Lane for conducting the Author's *viva* as External and Internal Examiners, respectively
- Dr John Bellerby for chairing the Author's Transfer Committee
- Dr Xiao Fang for early support in the laser laboratory
- Professor Ian Horsfall (Bashforth Laboratories) for the kind loan of the high speed imaging equipment
- Parents, Brother and Partner for boundless love and support
- Emma Burke and Lucy Wilkinson for solidarity and friendship
- Heather Nicholson for demonstrating sacrifice and 'grace under pressure' in the pursuit of a more humane future
- Atomic Weapons Establishment (Aldermaston) for financial support

Honour thy father with thy whole heart, and forget not the sorrows of thy mother. Remember that thou wast begotten of them; and how canst thou recompense them the things that they have done for thee?

Ecclesiasticus 7: 27,28

In Loving Memory

of my Father

GEORGE PEEL

19 March 1936 – 30 April 2011

List of Contents

List of Tables

List of Figures

Glossary

c_L	analyte concentration
d_b	cavitation bubble diameter
D	nominal probe beam diameter
D*	de-focussed probe beam diameter
D_L	sensitivity of LIBS system
E_{line}	equivalent energy encapsulated by line emission profile
E_{net}	equivalent energy encapsulated by *Bremsstrahlung* envelope
E_p	laser pulse energy
f	lens focal length
f_p	pulse repetition rate
G_1	(increasing) *Bremsstrahlung* linear gradient
I_p	laser pulse irradiance
I_{th}	dielectric breakdown threshold
L	separation between lens focal point and cavitation bubble centre
m_{bkgnd}	mean intensity of background signal
N	data average number
ppm	parts per million of analyte concentration – equivalent to $\mu g ml^{-1}$
p_∞	pressure in infinite liquid
R_b	cavitation bubble radius
R_b,	cavitation bubble equivalent radius
R_0	maximum cavitation bubble radius
S_{max}	signal maximum
S_{Na}	intensity of sodium emission line (589.00nm)
S_{Pb}	intensity of lead emission line (405.78nm)
S_{pb}	probe beam intensity
S/N	signal: noise ratio
S/N_{blk}	signal: noise ratio acquired from plasma blocking technique
S/N_{mech}	mechanically gated line emission signal: noise ratio
S/N_{temp}	conventionally gated line emission signal: noise ratio

t_b	time between onset of cavitation and probe beam deflection
t_d	delay time
t_g	gate width
t_{Bremss}	duration of *Bremsstrahlung* emission based on defined criterion
t_{FWHM}	full width at half maximum of emission envelope
t_p	pulse duration
t_{peak}	time to achieve peak signal
v_b	measured (apparent) speed of bubble wall expansion
$v_{b'}$	actual (calculated) speed of bubble wall expansion
v_{bcy}	rate of bubble motion due to buoyancy of liquid medium
v_{Ray}	Rayleigh equation reference to bubble wall velocity
V_B	bubble volume
V_0	maximum cavitation bubble volume
z	separation between cavitation bubble centre and probe beam axis
|z|	absolute magnitude of z
z_{max}	critical maximum limit of z
z_{min}	critical minimum limit of z
ΔL	incremental measure of plasma blocking
ΔS	difference between line emission and mean background intensities
ΔS_{pb}	change in probe beam intensity
Δt_1	duration of (increasing) *Bremsstrahlung* linear gradient
ε	bubble eccentricity
Γ	gradient of calibration curve
λ	laser radiation wavelength
ρ_l	bulk density of liquid medium
σ_{bkgnd}	standard deviation of background signal
τ_b	cavitation bubble lifetime
τ_c	cavitation bubble collapse time
τ_{int}	interval between high speed camera images

THIS PAGE INTENTIONALLY BLANK

Chapter One
INTRODUCTION

"During the last few generations mankind has made an extraordinary advance in the natural sciences and their technical application, and has established his control over nature in a way never before imagined. (But) … this subjugation of the forces of nature, which is the fulfilment of a longing that goes back thousands of years, has not made them feel happier."
Sigmund Freud

1.1 Spectroscopic Techniques in an Environmental Context

Laser induced breakdown spectroscopy (LIBS) is an atomic emission spectroscopy (AES) technique in which a focused laser pulse is used for plasma generation. Rapid heating of the target occurs within the focused volume, for the duration of the laser pulse. When irradiance exceeds dielectric breakdown threshold of the target medium molecular dissociation occurs, followed by excitation and ionization of individual atoms. For aqueous media, with laser pulse focused in the liquid bulk, dielectric breakdown is characterized by cavitation and shockwave emission. Radiative emissions from ionized and excited atoms generate discrete lines unique to the emitting species. Emission lines are superimposed on a continuum background emission profile, typically referred to as *Bremsstrahlung* emission. For effective LIBS elemental monitoring, discrete atomic emission lines must be discriminated from the intense continuum background.

Established analytical techniques and methodologies include atomic absorption spectroscopy (AAS), mass spectroscopy (MS), x-ray fluorescence (XRF) and high performance liquid chromatography (HPLC). The ability of these techniques to achieve limits of detection (LoD) in the order of parts per billion (ppb) and lower is well documented. The principal disadvantages of these techniques are their requirement for elaborate sample preparation, significant sample analysis times, considerable expense, and difficulty in achieving portability due to the inherent bulk of their equipment. These disadvantages are in contrast with LIBS, which benefits from having no requirement for elaborate sample preparation, relatively unsophisticated sample presentation, potential for near real time and *in situ* sample

analysis and minimal target ablation. In addition the LIBS technique has the potential for application in hostile (chemically, biologically and radiologically) environments, via the use of optical fibres for laser beam delivery and signal collection. In the interests of balance, it is important to emphasize the not insignificant cost of a *state-of-the-art* LIBS system. A disadvantage of LIBS is the potential for significant interference between unresolved emission lines from the target species, and other species contained within the target substrate. This results in difficulty in emission line discrimination, and relatively poor data precision. In addition, LIBS detection limits are inferior (typically parts per million) compared to conventional laboratory techniques, particularly when utilizing the liquid bulk sample presentation configuration.

AES equipment has four principal sections: *i*. high heat source; *ii*. monochromator or polychromator; *iii*. detection device(s); *iv*. control and display electronics. High temperature is generated in several ways e.g. inductively coupled plasma (ICP) torch, low voltage direct current (d.c.) arc, high voltage alternating current (a.c.) spark, and oxyacetylene flame.

It is noted that qualitative sensitivities for flame-atomic absorption spectroscopy (F-AAS) and flame-atomic emission spectroscopy (F-AES) techniques are dependent on element type, as illustrated in Table 1.1.

Table 1.1: Qualitative Sensitivity of F-AAS and F-AES Techniques[1]

F-AES Superior to F-AAS	F-AES & F-AAS Approximately Equal	F-AES Inferior to F-AAS
Al, Ba, Ca, K, Na, Sr	Cr, Cu, Mn, Sc, Ti	As, Cd, Hg, Pb, Sb, Se

[1]: adapted from Skoog & Leary: p.229

The data in Table 1.1 implies F-AES is typically more sensitive technique for elemental analysis of volatile species i.e. Group I, II & III metals. In contrast, F-AAS technique is typically more sensitive for many traditional D-block metals. These

include species of interest to the current research, *apropos* contamination of the aqueous environment by toxic heavy metals i.e. mercury, lead, cadmium and others.

Reported detection limits for conventional (laboratory based) methodologies and techniques are typically in the parts per billion (ppb) and parts per trillion (ppt) ranges. Detection limits vary depending on the specific technique used and target species. Lighter elements which are more readily vaporized e.g. sodium and calcium, are typically reported at ppt range. By contrast, heavier elements emitting a significantly larger number of emission lines, are typically reported at ppb levels. Reported detection limits for mercury and lead, using conventional AAS and AES techniques, are presented in Tables 1.2a & 1.2b, respectively. Reported detection limits based on the LIBS technique are included for comparative purposes.

Table 1.2a: Limits of Detection for Mercury: Conventional Techniques and LIBS

Method	LoD	Remarks	Reference
CV[1]-AAS	0.2ppt	city lake & deep well water	Duan T *et al* (2006)
ICP-MS	31.5ppb	mercury in blood	McShane WJ *et al* (2008)
ICP-OES[2]	0.93ppb	environmental water samples	Chen D *et al* (2009)
HPLC	0.4ppb	mercury species in river water	Yin Y-G *et al* (2009)
LIBS	7ppm	liquid jet sample presentation	Fang X & Ahmad SR (2007)

[1]: CV → cold vapour [2]: OES → optical emission spectroscopy

Table 1.2b: Limits of Detection for Lead: Conventional Techniques and LIBS

ET-AAS	11ppb	food colourants	Viňas P *et al* (2001)
ICP-MS	0.01ppb	lead in blood	Bonnefoy C *et al* (2002)
ICP-MS	251.2ppb	lead in blood	McShane WJ *et al* (2008)
ICP-OES	0.96ppb	environmental water samples	Chen D *et al* (2009)
SP[1]-LIBS DP[2]-LIBS	18ppm 3ppm	trace elements in oil samples	Yaroshchyk P *et al* (2005)
LIBS	30ppm	bulk liquid sample presentation	Fang X & Ahmad SR (2005)

[1]: SP → single pulse [2]: DP → double pulse

It is clear from Tables 1.2a & 1.2b that limits of detection for the LIBS technique are several orders of magnitude higher than those for conventional methodologies. The main reason for the relatively poor sensitivity of the LIBS technique, using the liquid bulk sample presentation configuration, is the effect of 'quenching'. This is the process involving transfer of energy from the excited and ionized atoms to the molecules within the surrounding environment. Energy is transferred in the form of phonons i.e. non-radiatively, when electrons de-excite within vibration manifolds. The fluid density of the liquid bulk environment is orders of magnitude higher than that for plasma expanding into a gaseous atmosphere. The effect of 'quenching' is therefore significantly greater in the liquid bulk, leading to significant reduction of plasma temperature and lifetime. It is important to note that 'quenching' is a phenomenon common to the expansion of an energy flux into all fluid media i.e. liquid and gaseous/ vapour. This is acknowledged in a quote from a reported study (Shaikh *et al*: 2006) concerning the expansion of mercury plasma into an air atmosphere: "The nature of the ambient gas plays an important role in the *confinement and expansion rate* of plasma" (*italics* mine).

1.2 Historical Development of Laser Induced Breakdown Spectroscopy

Crucial to the development of the laser was it's antecedent, the maser ('microwave amplification through stimulated emission of radiation'). This represented the first practical realization of Einstein's 1917 postulation of stimulated emission, when it was demonstrated at Columbia University in the mid-1950s (Gordon *et al*: 1954, 1955). The utilization of a three level stimulated emission configuration, using a crystalline ruby rod as lasing medium, led to the development of the first optical laser ('light amplification through stimulated emission of radiation'). Invented at Hughes Research Laboratories (Maiman: 1960), the laser was perceived as a revolutionary technological breakthrough for which applications were not immediately apparent. Within a decade of being patented, however, the application of the laser in multiple areas of science, engineering and technology had increased at a significant rate. The laser is one of the more significant discoveries of Western Science in the Twentieth Century.

One of the earliest applications of the laser was in the field of plasma generation. The *næscent* field of laser induced plasma (LIP) has since morphed into the atomic emission LIBS technique. The maturity of any scientific technique may be objectively measured by the volume of peer reviewed published research papers and academic textbooks it has given rise to. According to this criterion LIBS matured during the late 1990s, a decade which witnessed an order of magnitude growth in published research, compared to previous decades. The 1990s also witnessed a broadening of LIBS applications, as well as an increasingly diverse range of theoretical and modeling issues developed by researchers, at a number of prestigious learning Institutes. The proliferation of LIBS research is illustrated in Figure 1.1 (http://www.scopus.com/home.url: search criterion = "laser + induced + breakdown + spectroscopy").

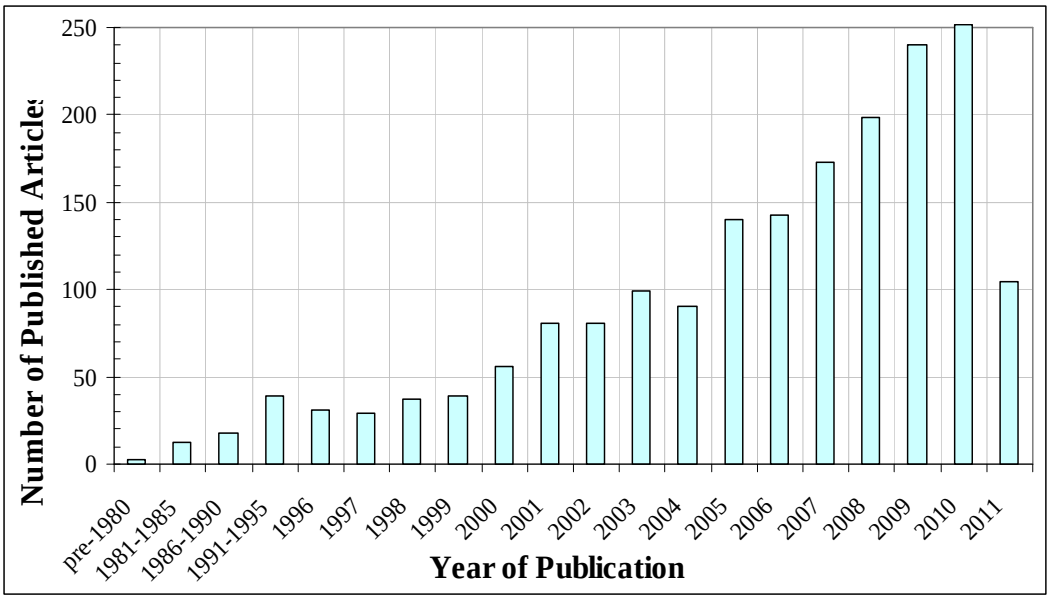

Figure 1.1: Peer Reviewed LIBS Research from pre-1980s to Present

As with other novel scientific techniques, there exists a dialectic between potential *clientele* for the new technique, and the ability of the technique's would-be champions to convince said *clientele* to invest in its development. This concept is elaborated by the following quote: "The laser and maser beautifully demonstrate the interchange of ideas and impetus between industry, government, and university research." (Slusher:

1999). Within this paradigm there exists a complementarity between original experimental research, and innovative theories to adequately describe empirical data. This is a manifestation of the classical 'observation → inference' *rationale* underpinning the physical sciences.

This *rationale* is exemplified by the earliest LIBS research, which generated LIP in steel samples for analysis of Ni and Cr content (Runge *et al*: 1964). This was followed by research *vis a vis* the multi-photon (two- and three- photon) mode of ionization of solid and gaseous target media (Gold & Bebb: 1965; Bebb: 1966, 1967; Gontier & Trahin: 1968; Braerman *et al*: 1969).

Increased confidence in the veracity of the laser induced breakdown (LIB) technique led to greater involvement from the academic research community throughout the 1970s and 1980s. The success of LIBS as a unique AES technique was assured as LIBS applications diversified. Further interest from corporate vested interests led to increased funding for the refinement of the LIBS technique within the research community.

Significant progress was apparent during this period in theoretical and modeling aspects of LIP formation in a range of target media, as well as modeling of the temporal and spatial evolution of expanding laser induced plasma. The commercial success of LIBS is demonstrated by the number of applications based papers published during recent decades, as illustrated in Figure 1.2. It is noteworthy that the context for the current research i.e. environmental (water) contamination, had no presence within the LIBS research *œuvre* until the 1990s, and this *albeit* a limited one.

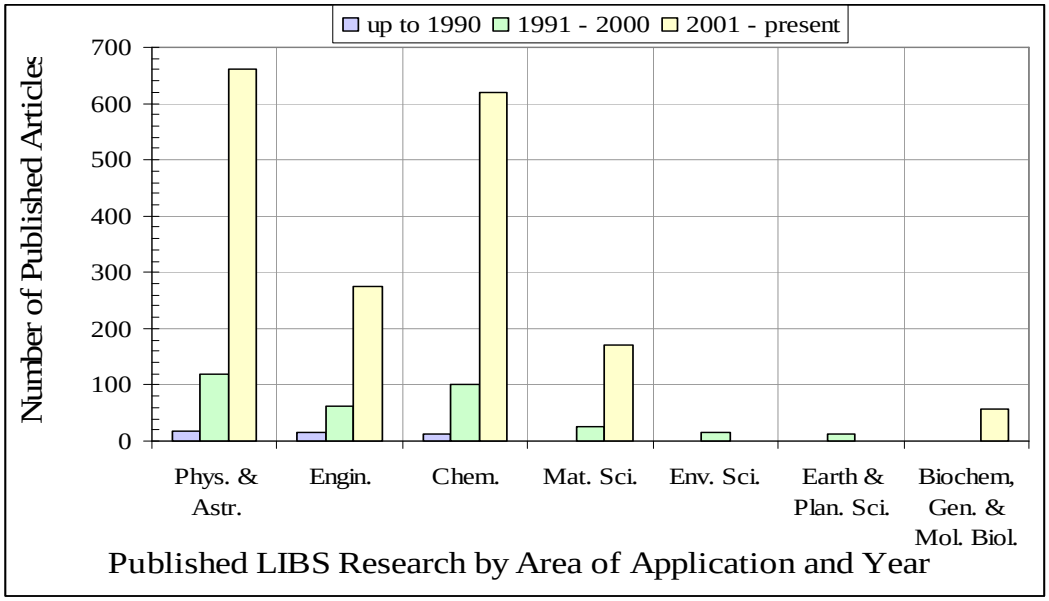

Figure 1.2: LIBS Applications from pre-1990s to Present

Interested parties *vis a vis* LIBS research and applications are hinted at by the principal publication sources. In the earliest days of LIBS research, publication was limited to specific laboratories and organizations of like-minded scientists and engineers. As LIBS grew in popularity as an analytical technique, peer reviewed journals began to dominate the promulgation of LIBS research within the broader scientific community. This trend is illustrated in Figure 1.3.

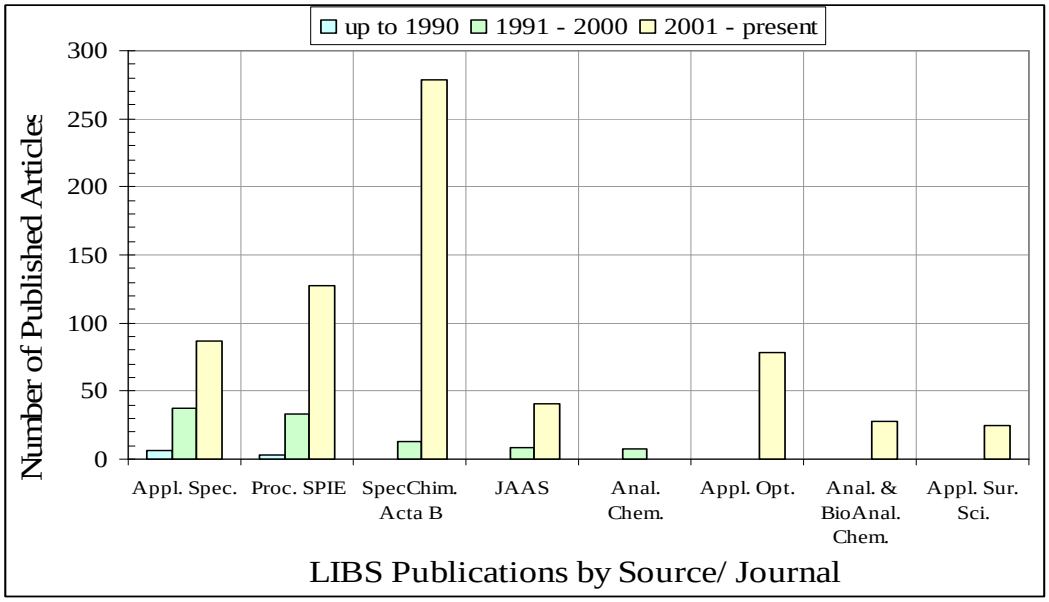

Figure 1.3: Dominance of LIBS Research in the Wider Scientific Community

From an examination of LIBS research it is clear that the majority of studies and applications have involved solid target media. Comparatively little research effort has been devoted to plasma generation in gaseous and nebulized targets, with still less to the study of laser induced plasma generation in liquid media. This discrepancy between target media is illustrated in Figure 1.4, for research published in the journal Spectrochimica Acta B. The significant percentage of theoretical and modeling papers is a trend apparent from the 1990s onward.

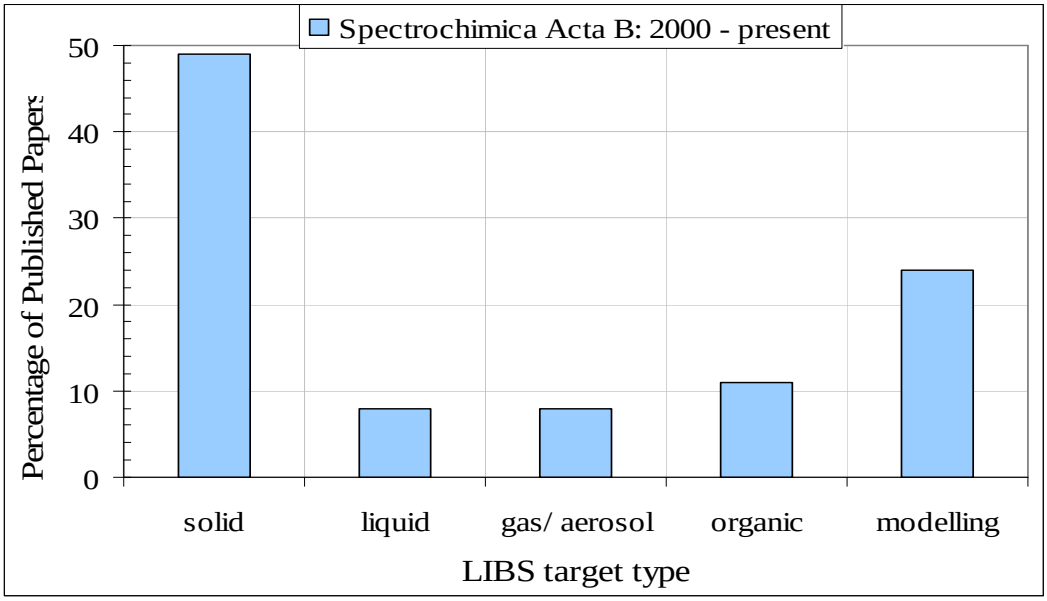

Figure 1.4: Dominance of Solid Target Media for LIBS Applications

The challenge of demonstrating successful LIBS research, for characterization of trace elements in the liquid bulk sample presentation configuration, provides the context for the current research.

1.3 Advantages and Disadvantages of Using Lasers in Atomic Emission Spectroscopy

Lasers are a unique 'light' source, producing an intense, coherent and monochromatic beam of electromagnetic radiation. One of the most common solid state lasers utilizes neodymium: yttrium aluminium garnet (Nd:YAG) as the lasing medium. Efficiency

for this lasing medium is typically in the order of 4%. This figure is derived from the efficiencies for pumping the lasing medium, radiation transfer, absorption into the upper states, beam overlap, as well as extraction of laser energy. Efficacious physical and optical features of the Nd:YAG lasing medium include optical isotropy and high hardness.

The fundamental lasing wavelength for Nd:YAG is 1064nm (1.064μm), in the near infra-red (NIR) window of the electromagnetic spectrum. Photon energy at 1064nm is 1.86×10^{-19}J, equivalent to ~1.17eV. Frequency multiplying allows the fundamental wavelength to be blue-shifted into the VIS and UV regions i.e. 532nm, 355nm and 266nm, with equivalent increases in photon energy.

A high degree of monochromicity and negligible beam divergence allow *state-of-the-art* lasers to deliver irradiance (on focusing of laser pulses) sufficient to induce dielectric breakdown in a diverse range of target media. Monochromicity is a measure of the deviation of the laser spectral profile from the central (nominal) wavelength. The Nd:YAG laser delivers a spectral profile with line-width of 4.5×10^{-4}nm about the fundamental wavelength. This represents the spectral deviation at which intensity falls to a defined fraction of peak intensity. For Gaussian emission profiles, the line width represents that spectra deviation for which intensity falls to $1/e^2$ (17%) of peak intensity. Beam divergence defines the spatial increase in laser beam cross section as a function of beam trajectory. To illustrate this property, a light bulb emits energy omni-directionally i.e. into a solid angle of 4π steradians. By comparison a parabolic searchlight typically has beam divergence of 0.01 radians. A typical gas laser e.g. HeNe probe laser operating in *cw* mode, has beam divergence in the order of mrads, whilst *state-of-the-art* solid state pulsed lasers have beam divergence in the sub-mrad range.

Irradiance (power density) for a pulsed laser is a derived quantity describing the rate of energy delivered per unit area, and is a function of pulse power and laser beam waist. Focal beam waist is a function of laser beam diameter, focal length of the focusing lens, and laser wavelength. Typical beam waist for a pulsed Nd:YAG laser is

in the order of 10μm, providing irradiance in the order of $10^{12}Wcm^{-2}$, for pulse energy and duration in the mJ & ns regimes, respectively. This level of irradiance is sufficient to produce dielectric breakdown in a range of liquid target media, including aqueous solutions containing trace concentrations of contaminants.

One of the principal disadvantages of using lasers in a scientific or engineering context has traditionally been the prohibitive cost of hardware, and support/ maintenance infrastructure. As with any technological breakthrough, and this is particularly true for the laser during the previous three decades, the proliferation of the technology within the research and commercial communities has delivered the advantage of 'economy of scale'. Another traditional problem with the laser in it's earliest form was considerable bulk and weight. As has been the case with other technologies e.g. the ubiquitous personal computer and cellular telephone, miniaturization of components and sub-assemblies have brought forth the realization of portability. Whilst solid state lasers have achieved sufficient size and weight savings to be 'man-portable', the same convenience has not yet been achieved for the typical LIBS system as a whole. Despite the demonstration of prototype LIBS apparatus for operation "in the field" (Harmon *et al*: 2006; Cuñat *et al*: 2008, 2009; Harman *et al*: 2009, Gottfried *et al*: 2009) LIBS remains at the present time an AES technique that is typically confined to the laboratory.

1.4 Dielectric Breakdown in Water

Photolysis is a mechanism of light induced ionization and dissociation. Within the context of plasma generation in the liquid bulk, multi-photon absorption ionizes and dissociates the water molecules, generating photolysis products in the focused laser volume. These products include quasi-free electrons and hydroxyl radicals, which are highly absorbing in the IR & VIS wavebands. This leads to intense heating several orders of magnitude in excess of predictions from classical physics. There is a lack of consistency, both experimentally and in terms of predictions from various models, regarding the dielectric breakdown threshold of water. Estimation of breakdown threshold based on a non-interfering three atom model i.e. two hydrogen and one

oxygen atoms comprising a molecular unit, is significantly different from experimentally measured values. Water is a strongly polar solvent, possessing relative permittivity (ε) of 80.10 at 293K (the organic solvents octane, ethanol and benzene have equivalent values of 1.95, 25.70 & 2.28, respectively). Weak *van der Waals* force causes molecules to form loosely bound clusters. This "clustering" phenomenon suggests the necessity of a physico-chemical description of liquid water at the macro-molecular level. A more sophisticated approach considers liquid water as possessing bulk properties analogous to those of an amorphous solid. This approach considers the valence and conduction bands for electrons within the molecular structure, and estimates the breakdown threshold for ionization based on the energy band gap. Predictions of dielectric breakdown threshold based on the amorphous solid model are more consistent with experimental data. Details of experimentally measured and theoretically predicted breakdown thresholds for water are discussed in Chapter Two.

Investigation of the dissociative and excited states of fragmented water radicals has been an area of active research for at least three decades. Details of the polarized nature of excited hydroxyl radicals has been reported (Becker *et al*: 1981), for water vapour subjected to impact by energetic electrons. The concept of dissociation by incident high speed electrons may be extended to the context of incident energetic photons. The authors reported an excitation minimum of 9.3eV for elevation of dissociated hydroxyl fragments from their ground state vibration manifold to the excited $A^2\Sigma^+$ vibration manifold. A vibration manifold bandgap of 9.3eV implies the dominance of the multi-photon ionization (MPI) mechanism for dielectric breakdown, given photon energy of ~1.17eV for the Nd:YAG fundamental wavelength of 1064nm.

The potential energy manifest in electronic and vibration manifolds of the water molecule has been reported as a function of OH-H bond separation (Stalder & Woloszko: 2007). This relationship is reproduced in Figure 1.5. It is important to note the stability of water in its ground state, represented in Figure 1.5 by the X^1A_1 vibration manifold, up to potential energy of ~5eV. This implies the absorption of at

least four photons at 1064nm, at a temporal flux in excess of equivalent excitation manifold lifetime, for MPI to be an effective mechanism for dielectric breakdown.

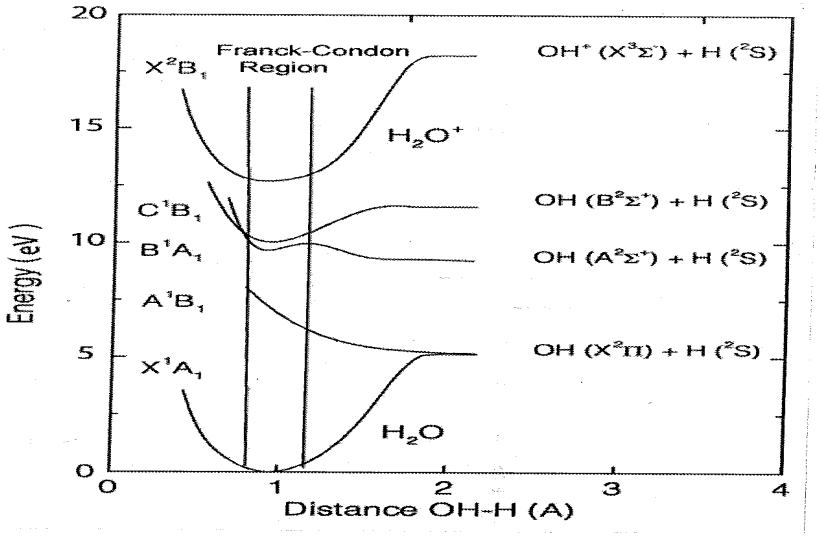

Figure 1.5: Influence of Bond Separation on Potential Manifolds in Water
from Stalder & Woloszko: 2007

Given the inherent complexity of water it is perhaps ironic that a resource taken so much for granted is not only the key to survival of organic life, but also a (deceptively simple) substance whose properties and behaviour are shrouded in nuance. Water is surely the 'ghost in Nature's machine', which is defiantly resisting Renaissance Mans' attempts at exorcism!

The efficiency of absorption of incident laser radiation in water bulk is a function of wavelength. The spectral absorbance of distilled water in the UV-VIS-IR regions, encompassing the Nd:YAG fundamental lasing wavelength of 1064nm, is illustrated in Figure 1.6. Absorption co-efficient for water at 1064nm is ~0.1cm^{-1}. It is only below ~200nm, in the far ultraviolet (UV) region, where water becomes opaque to electromagnetic radiation. For this reason, the utilization of Nd:YAG second, third and fourth harmonics (532nm, 355nm and 266nm) offers limited advantage in terms of improved absorption co-efficient. As will be seen in a later chapter, where ionization mechanisms are discussed, higher photon energies at lower wavelengths prove potentially advantageous for LIB, despite low absorption co-efficient.

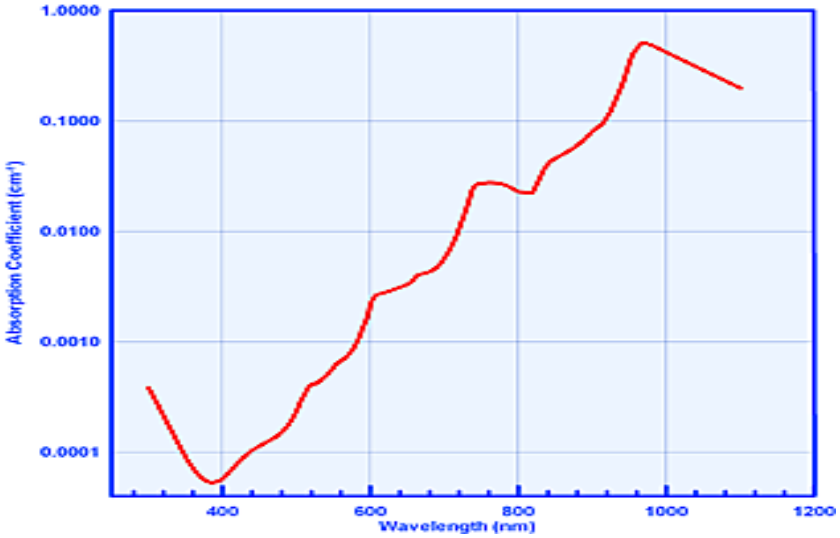

Fig 1.6: Absorption Spectrum for Distilled Water

D & A Instrument Company: http://www.d-a-instruments.com/light_absorption.html: accessed 15 June 2010

The ionized plasma within the focused beam waist strongly absorbs incoming laser radiation (for the duration of the laser pulse) resulting in plasma expansion along the laser trajectory i.e. in the direction of the incident pulse train. Plasma volume and rate of expansion are limited by the 'quenching' effect of water molecules in the immediate vicinity of the plasma, which restricts limits lifetime and plasma temperature. Plasma temperature is a key determinant of the relative population of upper energy levels in excited atomic and ionic species. Theoretical analyses utilize plasma temperature, as well as the critical concept of thermodynamic equilibrium (TE), for accurate prediction of dynamic plasma conditions. The related concept of local thermodynamic equilibrium (LTE) is a complex and troublesome one, which will be reprised in Chapter Three.

Limited plasma lifetime in the liquid bulk limits the population of excited states for dissociated atoms and ions, thus limiting atomic line emission intensity. This has the effect of reducing LIBS sensitivity of trace elements, compared to other liquid sample presentation configurations. In the immediate aftermath of plasma generation, the emission spectrum is dominated by a broadband continuum background, including

contribution from *Bremsstrahlung* emission. It is only slightly pedantic to emphasize that *Bremsstrahlung* is not a category of noise *per se*, *insofar* as it is generated by predictable physical mechanisms. A significant contribution to *Bremsstrahlung* is inelastic scattering of electrons by the radiation field. Another process occurring in the early stage of plasma expansion is collisional ionization of neutral atoms by high speed electrons, which increases plasma free electron density. Electron density is subsequently reduced by the inverse process of "three-body re-combination". In addition to these processes, radiative re-combination between ionic species and free electrons contributes to the *continuum* background. By optimizing the delay time between plasma formation (synchronous, for all intents and purposes, with delivery of the laser pulse) and exposure of detection apparatus to plasma emission, it is possible to take advantage of the finite lifetime of the *Bremsstrahlung* profile, to maximize emission lines signal-to-noise ratio (S/N).

In reality experimental limitations, including electronic "shot" noise, impose an upper limit for emission line (S/N), for a specific experimental set-up. The limited plasma temperature, volume and lifetime for applied LIBS in the liquid bulk typically results in lower S/N for elemental analysis. This leads to poor detection limits compared to other LIBS sample presentation configurations i.e. liquid surface, jet and nebulized spray. Toxic metals of environmental interest e.g. mercury, lead and arsenic, typically occur in sub-trace concentration levels, for which statutory maximum permissible concentrations (MPC) are in the order of parts per billion (ppb).

1.5 Aspects of Environmental Contamination

Heavy metal contamination of the environment is driven by complex natural geo-chemical processes, taking place on and between the Earth's surface and atmosphere. A series of dynamic interactions between atmospheric, terrestrial and marine environments influence local, regional and global contamination trends. The United Nations Economic Commission for Europe (UNECE) has reported significant contamination of the Arctic Region from sources within and beyond the Pan-European region (McGlade: 2007), as a result of marine and atmospheric

transportation phenomena. This raises a secondary concern i.e. the accelerating trend in an increasingly corporate and globalized economy to out-source industrial production to developing New and Third World nations, which typically have less stringent regulations regarding acceptable levels of environmental contamination.

The UNECE represents the interests of 900 million citizens in 53 pan-European countries, in a geo-political zone extending to the Atlantic Ocean in the West, the Mediterranean to the South, the Arctic Ocean to the North, and the Trans-Caucus Region, Russia and the former Soviet Asian States in the East. The three principal challenges defined by the UNECE are air & water pollution, biodiversity loss & river management, and climate change. These challenges are considered within the context of potential environmental pollution from approximately 12000 industrial facilities within the European Union (McGlade: 2007). These issues are cast in sharper focus by the observation that the rate of growth of the EU chemical industry exceeds growth in gross domestic product (GDP). The economic context is illuminated by the observation that the fiscal return on metal recovered from contaminated areas is typically all but worthless.

In order to maintain perspective it is important to appreciate natural, as well as anthropogenic, sources of toxic heavy metal species. As of 2004 there were approximately 2000 lead & zinc smelting facilities globally (Batonneau *et al*: 2004), providing the principal source of airborne particulates from these two metals. Same year estimates for global emission of Hg are in the order of 2000 metric tonnes each from natural and anthropogenic sources (Streetsa *et al*: 2005), plus a similar tonnage via re-cycling of ‘old’ mercury i.e. material previously deposited within the terrestrial system from anthropogenic sources.

Virtually all heavy metals ingested at high concentration are harmful to animals, including humans. Some atomic species (cadmium, lead, arsenic & mercury) are highly toxic and harmful to animal health at trace i.e. ppm and lower, concentrations. Identification and extraction of toxic heavy metals from the environment is problematic due to the trace concentrations that are generally extant. Marine

environments typically contain concentrations in the order of 100 nmol/L (Teresa *et al*: 1997). Ground and waste water typically have concentrations in the order of ppb for lead & arsenic, compared to parts per million (ppm) for (less toxic) zinc, copper & nickel compounds. The issue is, however, more subtle than measured environmental concentration. The 'bio-availability' of a toxic species is the key factor influencing bio-accumulation in the food chain. Bio-availability is driven by the solubility of the inorganic metal salt, as well as the mobility of compounds containing toxic species via water transportation. Through absorption, adsorption and surface precipitation, toxic metal species may become attached to a substrate, thus accentuating the role of solid natural material (soil and sediment) as potential 'sources and sinks' for the transport and accumulation of toxic species.

As well as the principal elements of concern i.e. mercury, lead & arsenic, other metals present a potential hazard to biological organisms, when critical concentrations are exceeded. The semi-conductor industry generates phosphorous, indium, gallium & arsenic, which have traditionally been deposited in landfill sinks (Pécheyran *et al*: 1998) from where they are leached into local and regional water supplies. Silver has potential for toxicity that is complicated by a relative lack of understanding of the mode of action for Ag within ecological systems (Galiová *et al*: 2008). Other metals of concern include copper, chromium & iron, due to the complication of their existence in divalent form, and their vulnerability to being reduced by the action of ultraviolet (UV) radiation to more toxic variants (Glazewski & Morrison: 1996). Common examples include reduction of organo Cr(VI) → inorganic Cr(III), Fe(III) → Fe(II), and Cu(II) → Cu(I). It is not unreasonable to suggest that the majority of metal species are a threat to organic life and animal health, when present within the local environment in excessive concentrations.

The maximum permissible concentration (MPC) for metals in surface and drinking water are generally different. The MPC is steered by the toxicity of any particular metal, and its potential to adversely effect the health of animals and marine life. MPCs imposed by legislation and directives have been standardized for member nations of the EU. Equivalent maximum contaminant levels (MCL) are in place for

the 50 states of the United States of America (US). The United Nations (UN) has independently issued its own guidelines. MPCs and equivalent limits, for toxic metal species of most interest to the current research, are summarized in Table 1.3.

Table 1.3: MPC and Equivalent Limits (ppb) for Selected Toxic Heavy Metals

Element	UN[1] figures drinking water	USA MCL[2] drinking water	EU MPC[3] drinking water	EU MPC[4] surface water
Arsenic, As	10	10	10	50
Cadmium, Cd	3	5	5	5
Chromium, Cr	50	100	50	50
Lead, Pb	10	15	10	50
Mercury, Hg	1	2	1	5
Selenium, Se	10	50	10	10

[1]:UN, World Health Organisation (WHO); 3rd edition, volume 1, 2004
[2] :US Environmental Protection Agency (EPA) 816-F-03-016; June 2003
[3] :Council Directive 98/83/EC; 03-11-1998
[4] :Council Directive 75/440/EEC; 16-06-1975

It is noted that for a particularly toxic elemental contaminant of drinking water (mercury) the guideline for MPCs and equivalent limits are practically the same. However, MCL limits in the US for chromium, lead, selenium & mercury are significantly higher than their equivalent limits in the EU. It is also noted that for some elements (cadmium, chromium & selenium) the MPC is the same within the EU for drinking and surface water. For other toxic metal species (arsenic, lead & mercury) the MPC for surface water is significantly higher (400%) than for drinking water. It is entirely reasonable to anticipate lower MPCs for drinking compared to surface water, given the former is drawn (literally) from the latter.

1.6 Research Objective and Tasks

The objective of the current research is to optimize experimental parameters to maximize LIBS detection sensitivity, for characterization of selected heavy metal species in aqueous media. The successful achievement of this objective is demonstrated within the contents of this Thesis.

The present chapter describes the role of LIBS within the context of AES techniques, advantageous characteristics of lasers for LIBS applications, and the broader geo-chemical and environmental context of the current LIBS research. Chapter Two presents a critical review of published research in the LIBS field, and identifies useful correlation between important trends in reported research and the present work. Chapter Three describes the theoretical concepts underpinning key processes relevant to the current research. These include absorption of electromagnetic radiation within the liquid bulk, dynamics of laser induced cavitation, non-linear processes governing the broadband *Bremsstrahlung* emission profile, and an appreciation of the ubiquitous 'shot noise' component in recorded signals within the context of emission line signal: noise ratio. Chapter Four describes the methodology and experimental apparatus utilized for the current LIBS research. Chapter Five presents a thorough and detailed description of data acquired during the current LIBS experimental research. These data encompass the effect of analyte concentration on dielectric breakdown threshold in the liquid bulk, demonstration of the data averaging technique for reduction of shot noise contribution to emission profile, measurement of maximum bubble radius and total bubble lifetime for laser induced cavitation bubble, optimization of three key LIBS experimental parameters for maximization of S/N for analyte contaminants in aqueous media, and an investigation of two novel techniques for improvement in emission line signal: noise ratio i.e. 'mechanical chopping' and 'plasma blocking'. Chapter Six provides detailed assessment of the previously reported experimental data, within the context of improvements in LIBS sensitivity for detection of analyte in aqueous solution. The potential for the development of a portable LIBS system for *in situ* work 'in the field' is also discussed.

References

Batonneau Y *et al*. Speciation of PM10 Sources of Airborne Nonferrous Metals with the 3km Zone of Lead/ Zinc Smelters. Environmental Science and Technology 38 5281-5289 (2004)

Bebb, HB. Quantitative Theory of the Two-photon Ionization of the Alkali Atoms. Physical Review 149 (1) 25-32 (1966)

Bebb, HB. Theory of Three-photon Ionization of the Alkali Atoms. Physical Review 153 (1) 23-28 (1967)

Becker K *et al*. Polarised Emission from Highly Rotational Excited OH($A^2\Sigma^+$) Radicals Produced by Dissociative Electron-impact Excitation of H_2O. Journal of Physics B: Atomic and Molecular Physics 14 (15) L517-L522 (1981)

Bonnefoy C *et al*. Validation of the Determination of Lead in Whole Blood by ICP-MS. Journal of Analytical Atomic Spectrometry 17 (9) 1161-1165 (2002)

Braerman WF. *et al*. Spectroscopic Studies of a Laser-produced Plasma in Helium. Journal of Applied Physics 40 (6) 2549-2554 (1969)

Chen D *et al*. Chitosan Modified Ordered Mesoporous Silica as Micro-column Packing Materials for On-line Flow Injection - Inductively Coupled Plasma Optical Emission Spectrometry Determination of Trace Heavy Metals in Environmental Water Samples. Talanta 78 (2) 491-497 (2009)

Cuñat J *et al*. Man-portable Laser-induced Breakdown Spectroscopy System for *in situ* Characterization of Karstic Formations. Applied Spectroscopy 62 (11) 1250-1255 (2008)

Cuñat J *et al*. Real time and *in situ* Determination of Lead in Road Sediments using a Man-portable Laser-induced Breakdown Spectroscopy Analyzer. Analytica Chimica Acta 633 (1) 38-42 (2009)

Duan T *et al*. Determination of Hg(II) in Waters by On-line Pre-concentration using Cyanex 923 as a Sorbent - Cold Vapour Atomic Absorption Spectrometry. Spectrochimica Acta - Part B Atomic Spectroscopy 61 (9) 1069-1073 (2006)

Fang X & Ahmad SR. An Optical Technique for *in situ* Monitoring of Trace Elements in Effluent. Environmental technology 26 1271-1276 (2005)

Fang X & Ahmad SR. Saturation Effect at High Laser Pulse Energies in Laser Induced Breakdown Spectroscopy for Elemental Analysis in Water. Laser and Particle Beams 25 1-8 (2007)

Galiová M *et al*. Investigation of Heavy Metal Accumulation in Selected Plant Samples using Laser Induced Breakdown Spectroscopy and Laser Ablation – Inductively Coupled Plasma – Mass Spectrometry. Applied Physics A: Materials Science and Processing 93 (4) 917-922 (2008)

Glazewski R & Morrison GM. Copper(I)/ Copper(II) Reactions in an Urban River. The Science of the Total Environment 189/190 327-333 (1996)
Gold A & Bebb HB. Theory of Multi-photon Ionization. Physical Review Letters 14 (3) 60-63 (1965)
Gontier Y & Trahin M. Multi-photon Ionization of Atomic Hydrogen in the Ground State. Physical Review 172 (1) 83-87 (1968)
Gordon JP *et al*. Molecular Microwave Oscillator and New Hyperfine Structure in the Microwave Spectrum of NH3[7]. Physical Review 95 (1) 282-284 (1954)
Gordon JP *et al*. The Maser - New Type of Microwave Amplifier, Frequency Standard and Spectrometer. Physical Review 99 (4) 1264-1274 (1955)
Gottfried JL *et al*. Progress in LIBS for Landmine Protection. Proceedings of SPIE – The International Society for Optical Engineering 73031F (2009)
Harmon RS *et al*. Man-portable LIBS for Landmine Detection. Proceedings of SPIE – The International Society for Optical Engineering 621701 (2006)
Harmon RS *et al*. LIBS Analysis of Geo-materials: Geochemical Fingerprinting for the Rapid Analysis and Discrimination of Minerals. Applied Geochemistry 24 (6) 1125-1141 (2009)
Maiman TH. Optical and Microwave-optical Experiments in Ruby. Physical Review Letters 4 (11) 564-566 (1960)
McGlade J. Europe's Environment: the Fourth Assessment. European Environmental Agency (2007)
McShane WJ *et al*. A Rugged and Transferable Method for Determining Blood Cadmium, Mercury, and Lead with Inductively Coupled Plasma - Mass Spectrometry. Spectrochimica Acta B – Atomic Spectroscopy 63 (6) 638-644 (2008)
Pécheyran C *et al*. Simultaneous Determination of Volatile Metal (Pb, Hg, Sn, In, Ga) and Non-metals (Se, P, As) in Different Atmospheres by Cryo-focusing and Detection by ICP-MS. Analytical Chemistry 70 2639-2645 (1998)
Runge EF *et al*. Spectrochemical Analysis using a Pulsed Laser Source. Spectrochimica Acta 20 (4) 733-736 (1964)
Shaikh NM *et al*. Optical Emission Studies of the Mercury Plasma Generated by the Fundamental, Second and Third Harmonics of a Nd:YAG Laser. Journal of Physics D: Applied Physics 39 (20) 4377-4385 (2006)

Slusher RE. Laser Technology. Reviews of Modern Physics 71 (2) S471-S479 (1999)
Stalder KR & Woloszko J. Some Physics and Chemistry of Electro-surgical Plasma Discharges. Contributions to Plasma Physics 47 (1-2) 64-71 (2007)
Streetsa DG *et al*. Anthropogenic Mercury Emissions in China. Atmospheric Environment 39 7789-7806 (2005)
Teresa M *et al*. Speciation of Cu, Pb, Cd and Hg in Waters of the Oporto Coast in Portugal, using Pre-concentration a Chelamine Resin Column. Analytica Chimica Acta 353 189-198 (1997)
Viňas P *et al*. Slurry Atomisation for the Determination of Arsenic, Cadmium and Lead in Food Colorants using Electro-thermal Atomic Absorption Spectrometry. Journal of Analytical Atomic Spectrometry 16 (10) 1202-1205 (2001)
Yaroshchyk P *et al*. Quantitative Determination of Wear Metals in Engine Oils using Laser Induced Breakdown Spectroscopy: a Comparison Between Liquid Jets and Static Liquids. Spectrochimica Acta B 60 986-992 (2005)
Yin Y-G *et al*. Direct Chemical Vapour Generation - Flame Atomization as Interface of High Performance Liquid Chromatography - Atomic Fluorescence Spectrometry for Speciation of Mercury without using Post-column Digestion. Journal of Analytical Atomic Spectrometry 24 (11) 1575-1578 (2009)

THIS PAGE INTENTIONALLY BLANK

Chapter Two

REVIEW OF LITERATURE

"There are very many thoughts which have value for him who think them, but only a few of them possess the power of engaging the interest of a reader after they have been written down"
Arthur Schœpenhauer

With the expansion of LIBS-based research during the previous two decades, the contemporary LIBS researcher is faced with an embarrassment of riches in terms of peer reviewed data. The challenge for the current research is to analyze this data to identify and interpret principal LIBS effects, in order to facilitate the realization of current research objectives. Relevant LIBS research was reviewed according to several key processes and LIBS phenomena. These include: *i*. dielectric breakdown thresholds in liquid media; *ii*. saturation of emission signal as a function of LIBS experimental parameters; *iii*. influence of LIBS experimental parameters on line emission signal: noise ratio; *iv*. effect of laser wavelength and pulse duration on LIBS sensitivity; *v*. comparison of alternative sample presentation configurations; and, *vi*. efficacy of double pulse LIBS configuration for improvement in LIBS sensitivity. Conclusions are presented to provide insight into the principal objective of the current research i.e. characterization of trace contaminant species in aqueous solution, using the liquid bulk sample presentation configuration.

2.1 Dielectric Breakdown in the Liquid Medium

Dielectric breakdown in distilled water was considered as the end-point of a series of temporally entrained processes i.e. multi-photon absorption → dissociation and ionization → rapid heating → cavitation effects and acoustic signature. Atomization was considered synonymous with molecular dissociation of water molecules into constituent hydrogen and oxygen atoms. Although not unique in this respect, water molecules possess a relatively high polarity. Molecular polarization induces ‘clustering’ of adjacent molecules, which lends validity to the description of liquid

water as an ‘amorphous solid’ (Kennedy: 1995). The clustering phenomenon justifies modeling the physico-chemical properties of water in macro-molecular terms.

Insight into the behaviour of laser induced plasma (LIP) in aqueous solution was obtained by studying the dielectric breakdown threshold of distilled water. Despite having negligible concentrations of contaminating species, for all intents and purposes, distilled water typically contains low concentrations of dissolved gases, resulting in the presence of vapour pockets. Depending on their scattering cross-section, trapped vapour pockets may have a significant effect on the dielectric breakdown threshold of distilled water.

Published research data differed considerably between theoretical estimates for the dielectric breakdown of water and experimentally measured values. Early work in this field of research was concerned with the application of pulsed lasers to eye surgery (Docchio *et al*: 1986a,b). A comprehensive study, published a decade later, compared theoretical and measured values for dielectric breakdown thresholds in ocular and aqueous media (Kennedy: 1995; Kennedy *et al*: 1995). Similar research has been reported, which compared optical breakdown in aqueous media for fs, ps and ns pulse durations (Vogel *et al*: 1996; Vogel *et al*: 1999).

Experimentally measured dielectric breakdown data (Docchio *et al*: 1986a,b; Saachi: 1991) for normally incident laser pulses, and theoretical estimates for ‘initiation’ and ‘sustaining’ irradiance thresholds (Kennedy *et al*: 1995), are summarized in table 2.1. Experimentally measured breakdown threshold data (I_{exp}) characterized beam waist (ω) according to the 1/e criterion, in terms of distribution of pulse power density. Subsequent theoretical estimates of irradiance thresholds for initiation and sustaining of cascade breakdown (I_{init} and I_{sus}, respectively), were calculated after re-scaling beam waist measurements according to the orthodox Gaussian ($1/e^2$) for pulse irradiance.

Data were obtained utilizing λ = 1064nm and pulse duration = 7ns for plasma generation in distilled water. NB. normal incidence of excitation laser pulse, 1064nm laser wavelength, and pulse duration in the low nanosecond range are laser parameters common to the current research.

Table 2.1: Comparison of Experimental and Theoretical Breakdown Thresholds for Distilled Water

Beam Waist, ω (μm)	I_{exp} (Wcm^{-2} $x10^{10}$)	Reference	I_{init} (Wcm^{-2} $x10^{10}$)	I_{sus} (Wcm^{-2} $x10^{10}$)	Reference
70.71	2.1	Docchio *et al*: 1986a,b	1.78	1.77	Kennedy *et al*: 1995
106.1	1.73	Saachi: 1991	1.36	0.18	Kennedy *et al*: 1995
132.9	1.55	Docchio *et al*: 1986a,b	1.17	0.18	Kennedy *et al*: 1995
325.3	0.685	Docchio *et al*: 1986a,b	0.64	0.19	Kennedy *et al*: 1995
495.0	0.53	Docchio *et al*: 1986a,b	0.49	0.19	Kennedy *et al*: 1995

From the data in Table 2.1 several observations are made:

- theoretical estimates (I_{init}) were consistently lower than experimental values (I_{exp}), for beam waist in the order of 100μm and lower
- theoretical initiation (I_{init}) and experimental (I_{exp}) breakdown thresholds displayed an inverse relationship to beam waist at the laser focus
- theoretical sustain breakdown threshold (I_{sus}) was invariant with beam waist at the laser focus, for dimensions in excess of ~100μm

The relationship between laser beam waist (ω) and dielectric breakdown thresholds (I_{exp}, I_{init} and I_{sus}) is illustrated in Figure 2.1.

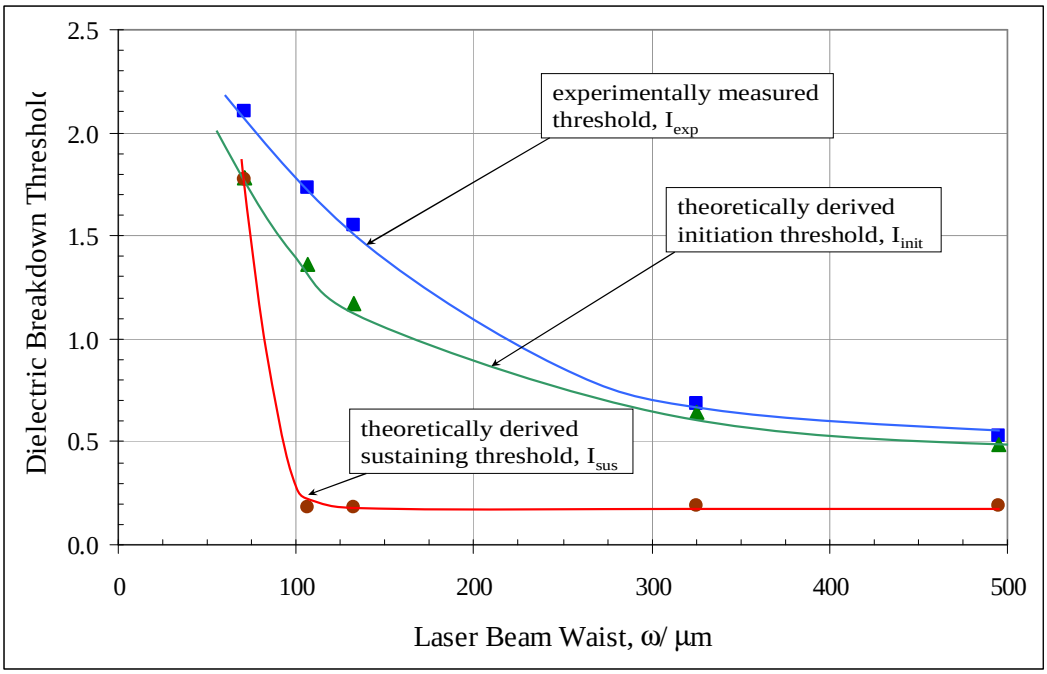

Figure 2.1: Measured and Theoretical Dielectric Breakdown Thresholds as a Function of Laser Beam Waist for Distilled Water

From the data displayed in Figure 2.1 the following observations were made:

- experimentally measured (I_{exp}) and theoretical initiation (I_{init}) thresholds converged for beam waist in excess of ~300μm
- theoretical initiation (I_{init}) and sustaining (I_{sus}) thresholds were approximately equal for lowest beam waist values, corresponding to maximum delivered photon flux
- for beam waist in excess of ~100μm, initiation threshold (I_{init}) was significantly higher that sustaining threshold (I_{sus}), implying higher free electron density in the post breakdown initiation stages of plasma evolution.

At supra-threshold laser irradiance plasma temperature and electron density, and hence emission line intensity, are correlated with the fraction of absorbed laser pulse energy. Reported research (Vogel *et al*: 1999) described a comprehensive energy balance for the interaction of laser energy with a dielectric medium. The authors concluded that conversion to mechanical energy (including an acoustic signature, shockwave propagation and an oscillating cavitation bubble) was the dominant

mechanism. Plasma lifetime depends on the competition between rates of plasma heating and cooling, during and after deposition of laser energy in the target medium. A comprehensive study (Casavola *et al*: 2003) described the three principal processes taking place within the expanding plasma, during deposition of incident laser energy i.e. electron impact ionization, three body re-combination and radiative re-combination.

2.2 Saturation Effects in LIBS Research

Saturation of line emission signals from plasma induced in both barium and copper solutions has been reported (Knopp *et al*: 1996) for analyte concentrations in excess of 5ppm. A linear relationship was reported for concentrations lower than 5ppm. Signal intensity decreased for both species at higher concentrations. These data demonstrated consistently stronger emission signals from Ba(II) at 455.4nm, compared to those from Cu(I) at 324.8 & 327.4nm. The authors also demonstrated consistently higher emission intensities for Group I elements (lithium and sodium), compared to Group II elements (calcium and barium). Emission line intensities from D-block elements (lead and cadmium) were consistently weaker than those of elements from Groups I and II.

A recent report (Koch *et al*: 2004) investigated the concentration of potentially hazardous chromium in the marine environment. The authors reported a non-linear profile for analyte concentrations above ~500ppm, reaching saturation at ~2000ppm, for the chromium triplet centred at 357.9nm. The authors reported a linear relationship between emission line intensity and analyte concentration below ~500ppm.

In addition to saturation of LIBS emission intensity with increasing analyte concentration at fixed laser pulse energy, saturation has also been reported with increasing pulse energy at fixed analyte concentration. A brace of papers (Michel *et al*: 2006, 2007) reported saturation of LIBS signal intensity for Na(I) at 588.99nm with increase in pulse energy. The LIBS signal was reported to increase linearly with

pulse energy up to ~22mJ. At higher pulse energy a non-linear increase in LIBS signal was reported, culminating in signal saturation at laser pulse energy of ~90mJ.

Saturation of LIBS emission signal, as a function of increasing incident photon flux and concentration of emitting species, was recently reported (Fang & Ahmad: 2007a). At specific fixed laser pulse energies (35, 50, 75 and 100mJ), saturation of Na(I) emission line was demonstrated, for corresponding critical analyte concentrations (140, 120, 100 and 65ppm, respectively). Below these critical limits, LIBS signal strength was demonstrated to be linear as a function of analyte concentration, for each of the four pulse energies.

Critical analyte concentrations for the onset of saturation, as reported by the authors, indicated an inverse relationship with excitation pulse energy. Reported critical pulse energy (E_p) and analyte concentration (c_{sat}) limits are summarized in Table 2.2, and displayed in Figure 2.2.

Table 2.2: Laser Pulse Energy and Analyte Concentration for Saturation in Sodium Chloride Solution

E_p/ mJ	c_{sat}/ ppm
35	140
50	120
75	100
100	65

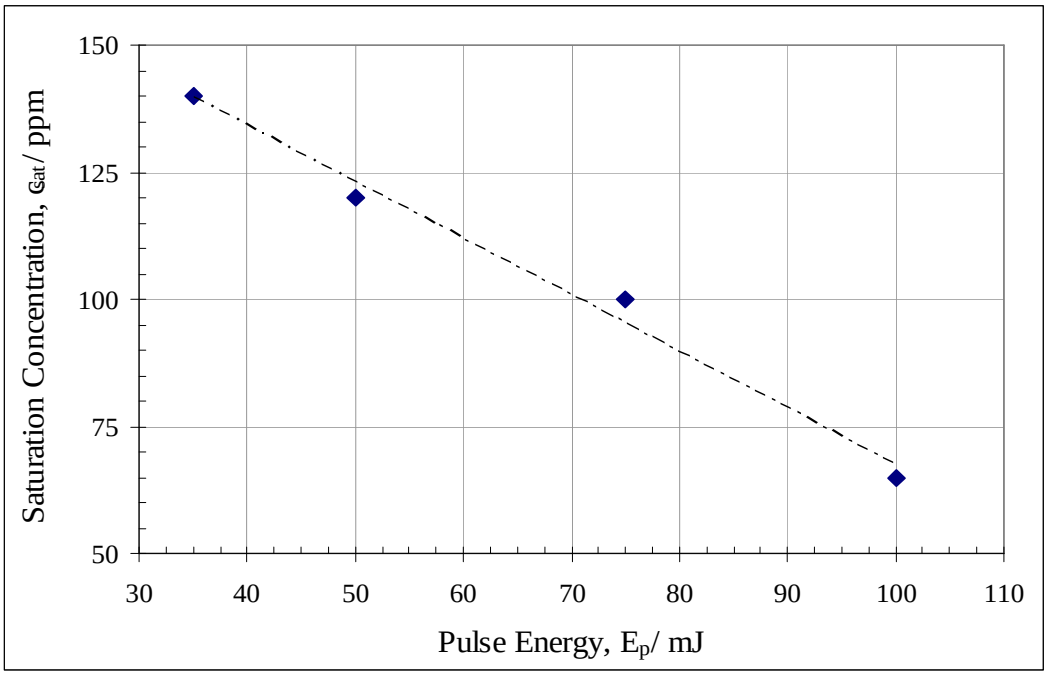

Figure 2.2: Relationship between Critical Pulse Energy and Analyte Concentration for Sodium Chloride Solution

A linear relationship between saturation concentration and pulse energy has been demonstrated by the data displayed in Figure 2.2, for the limited range of pulse energy used.

2.3 Signal-to-Noise Ratio Considerations

Signal-to-noise ratio (S/N) of emission lines has often been utilized as a measure of LIBS sensitivity in reported research. The majority of reported research used similar laser parameters as the current research i.e. laser pulse energy and duration in the low mJ and ns ranges, respectively; and laser wavelength of 1064nm. An early report (Charfi & Harith: 2002) used a surface sample presentation configuration, and a Mg(I) emission line. The authors demonstrated a linear relationship between S/N and delay time (t_d), with S/N reaching a maximum for t_d ~2μs. The same authors reported a positive correlation between S/N and t_d for a Na(I) emission line, with no reported S/N maximum.

A later report (Adamson *et al*: 2007) used a surface sample presentation configuration to generate plasma in water, with negligible concentration of contaminants, and plasma expansion into a nitrogen-rich atmosphere. Dielectric breakdown was reported at laser pulse energies in excess of ~20mJ. Saturation of S/N, as indicated by H_β, H_γ, N(I) and O(I) emission lines, was demonstrated for laser energy ~45mJ. The authors reported the dominance of 'plasma shielding' at laser energy in excess of ~200mJ.

A linear relationship between S/N and laser pulse energy was reported (Fang & Ahmad: 2007a), for Na(I) and Cu(I) emission lines, at fixed concentrations of 10ppm and 300ppm, respectively. Saturation of S/N was demonstrated for pulse energy ~100mJ, for both target species. The principal quantitative difference between the two emitting species (sodium and copper) was the value of maximum S/N, which was approximately double for copper compared to sodium.

2.4 Effect of Laser Wavelength

The importance of laser wavelength for laser induced dielectric breakdown is readily appreciated within the context of multi-photon absorption as a precursor to photolysis of dielectric media. Breakdown is initiated when electrons are elevated across the band gap between vibration manifolds in the liquid medium. The number of photons required is a function of the ratio of band gap energy to photon energy. Photon energy has an inverse relation to laser wavelength, thus illustrating the advantage of shorter wavelengths.

A recent report (Lo & Cheung: 2002) demonstrated the efficacy of using an ArF exiplex laser operating at 193nm (UV), corresponding to an equivalent photon energy of ~6.45eV. Plasma was generated in acidified sodium chloride solution via two photon absorption. The authors also demonstrated linearity of emission line S/N as a function of pump laser energy, up to a limit of ~16mJ.

The advantage of shorter pump laser wavelengths was reported (Ho *et al*: 1997) in an study which compared laser wavelengths of 193nm (exiplex) and 532nm (frequency

doubled Nd:YAG). The authors reported an increase in analyte signal intensity, at fixed laser pulse energy, utilizing methyl violet solution which absorbed preferentially in the UV region. Analyte signal was reported to increase by several orders of magnitude for 532nm & 193nm, respectively.

Another report (Berman & Wolf: 1998) demonstrated the dependence of LIBS sensitivity on laser wavelength. The Nd:YAG fundamental (1064nm) and third harmonic (355nm) wavelengths were used, generating plasma in aqueous nickel solution. Having optimized time delay and gate width, limit of detection was reported to be ~20.7ppm and ~36.4ppm, for 355nm and 1064nm, respectively. This represents an increase in LIBS sensitivity of ~50% for the shorter wavelength. The authors reported a linear relationship between LIBS signal intensity and analyte concentration up to a limit of ~1000ppm.

2.5 Effect of Laser Pulse Duration

The effect of laser pulse duration on plasma properties has been reported (Le Drogoff *et al*: 2004), for laser pulses in the picosecond and femtosecond ranges. Emission intensity, plasma temperature, and free electron density were measured for plasma generated at a solid aluminium target and expanding into air, for pulse durations 270ps, 5ps and 500fs. Atomic line emission intensity and electron density for Mg(I) at 285.21nm were reported to be invariant for these pulse durations. Pulse duration was reported to have a more significant influence on plasma temperature at longer delay times i.e. between 5μs and 35μs. In this range plasma temperature was reported to be weakly dependent on pulse duration e.g. at time delay of 18μs reported plasma temperatures were estimated to be 5750, 5300 & 4600K for pulse durations 270ps, 5ps & 500fs, respectively. Figure 2.3 illustrates the relationship between plasma temperature (T) and pulse duration (t_p). Plasma temperature measurements were reported in an earlier paper (Le Drogoff *et al*: 2001), for laser pulse duration of 100fs, which indicated a similar trend.

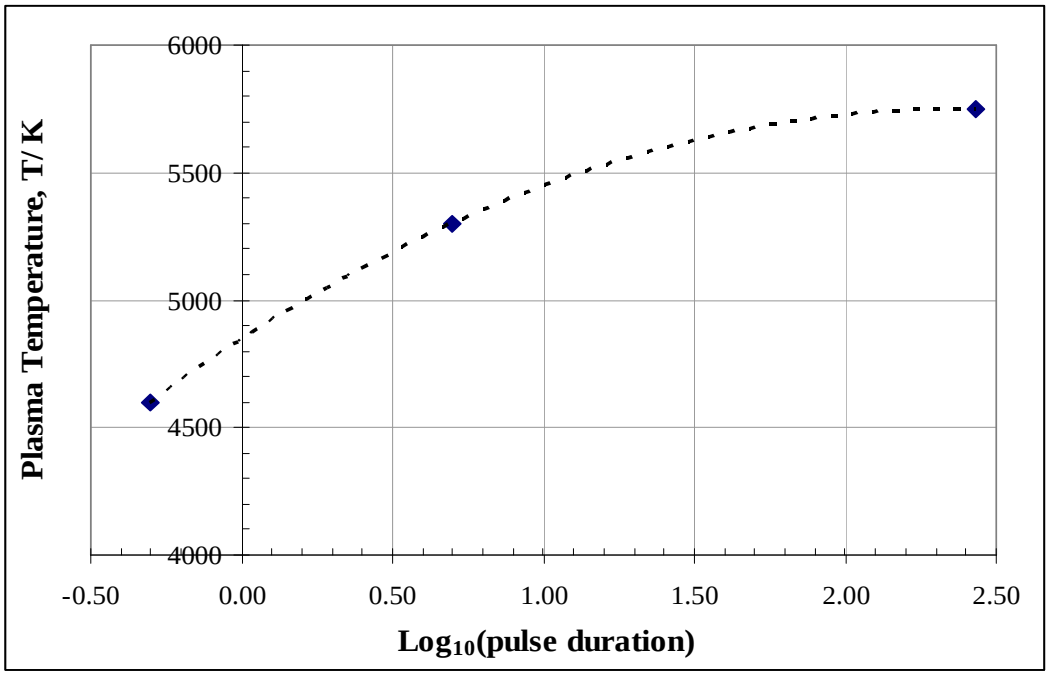

Figure 2.3: Log-Linear Plot of Plasma Temperature and Pulse Duration

The correlation between plasma temperature and pulse duration is weak, based on the limited data displayed in Figure 2.3. An increase in pulse duration by a factor of ~500 (from 500fs to 270ps) is associated with an increase in plasma temperature by ~25% (from 4600K to 5750K).

A recent study (Stavropoulos *et al*: 2004) compared ns and ps laser pulses, with respect to principal parameters of plasma induced at the surface of a solid target. Plasma temperatures were inferred from the classical Boltzmann equation, by measuring the linear gradient of a natural logarithmic plot. Plasma was generated in solid manganese and iron targets, and plasma temperatures measured, using laser pulses of 5ns and 35ps duration. Temperatures were reported to be consistently higher for pulses in the ns range. Similarly, electron density for plasma generated in solid manganese and iron targets was consistently higher for ns pulses compared to ps pulses, over a common range of delay times.

The effect on emission line strengths, for laser pulse durations in the ns and fs regimes, has been reported (De Giacomo *et al*: 2005) for surface plasma generated in a solid titanium target. LIBS elemental analysis indicated an order of magnitude increase in continuum and atomic line emission intensity for Ti(I) at 346.18nm, for pulse duration of 7ns compared to 250fs. The authors also reported consistently higher electron density for 7ns pulse, for delay times in the range 50ns to 950ns. Utilizing the Boltzmann plot method the authors reported consistently higher plasma temperature for 7ns pulses, for delay times in excess of ~250ns.

2.6 Alternative LIBS Sample Presentation Configurations

Conclusions were drawn from data published in a *plethora* of reports which focused on the effect of sample presentation configuration on LIBS sensitivity. One of the principal disadvantages of the surface sample presentation configuration is splashing of the focus optics. The splashing phenomenon is a consequence of conversion of laser energy to mechanical energy, a portion of which is manifest as physical disturbance of the target surface. The problem of splashing was minimized by the use of low laser pulse repetition rates, as reported in two recent papers (Charfi & Harith: 2002; Adamson *et al*: 2007). The authors utilized pulse repetition rates of 0.2Hz & 0.25Hz, respectively.

An early study (Yueh *et al*: 2002) compared the merits of liquid bulk and liquid jet sample presentation configurations, based on the S/N criterion for LIBS system sensitivity. The authors' effort to detect weakly emitting technetium at trace concentrations offered insight into the current research. Using the frequency doubled Nd:YAG laser wavelength of 532nm, operated at a pulse repetition rate of 10Hz, and emitting 5ns pulses in the 100mJ to 320mJ energy range, the authors reported 30% higher S/N for liquid jet compared to liquid bulk. Further, optimum time delay was 35% longer for liquid jet sample presentation configuration, indicative of the relatively strong effect of 'quenching' for plasma generation in the liquid bulk.

The practicalities of developing a portable LIBS system for field work have been described in a recent report (St-Onge *et al*: 2004). Three sample presentation configurations were compared: liquid bulk, static surface, and moving (dynamic) surface. The principal criterion by which the LIBS sensitivities were compared was relative standard deviation (RSD) of background emission intensity. Based on this criterion the liquid bulk sample presentation was rated inferior to the others. The authors concluded that for aqueous sodium chloride, the dynamic surface sample presentation provided superior S/N and measurement accuracy, compared to static surface and liquid bulk configurations.

The extension of comparative sample presentation research to a non-aqueous medium (oil samples) has been reported (Yaroshchyk *et al*: 2005). LIBS sensitivity was compared for static surface and liquid jet sample presentation configurations. The authors' used the fundamental Nd:YAG laser wavelength (1064nm), emitting pulses of 7ns duration at energy of ~70mJ. Sixteen metal species were detected in oil with reported concentrations typically in the ppm range. The detection limit for static surface configuration were typically 2 to 4 times higher than those for liquid jet configuration, implying superior LIBS detection sensitivity in the liquid jet configuration. The reported detection limits for cadmium, a species of interest to the current research, were 22ppm and 10ppm, for static surface and liquid jet configurations, respectively.

A recent report (Boudjemai *et al*: 2008) compared Na(I) emission line intensities for liquid jet and liquid bulk sample presentation configurations. The authors reported linear relationships between emission intensity and pump laser pulse energy, for both sample configurations, up to a limit of ~60mJ. Optimum laser pulse energy was reported to be in the order of 60mJ, for aqueous sodium concentrations between 5ppm and 50ppm. Saturation of emission intensity at ~60mJ was reported for liquid bulk configuration. This was in contrast to the liquid jet configuration, for which no emission intensity peak was reported for the range of pulse energy used.

Significant differences in S/N were reported (Fang & Ahmad: 2007b), between liquid bulk and liquid jet sample presentation configurations, for detection of several metal species. Using the fundamental Nd:YAG laser wavelength (1064nm), with 20mJ pulse energy and ~10 ns pulse duration, improvement in S/N by a factor of 10 for liquid jet configuration was demonstrated, for volatile species (sodium and calcium) at 3ppm analyte concentration. Improvement in S/N by a factor of ~4 was demonstrated for zinc and cadmium, for analyte concentration in the order of hundreds of ppm. The improvement in S/N by a factor of ~10 for the Na(I) emission line, between liquid jet and bulk sample presentation configurations, is of the same order of magnitude as previously reported data from the same authors (Fang & Ahmad: 2007a). The authors' earlier research reported maximum S/N of ~90 and ~17, for liquid jet and bulk sample presentation configurations, respectively. Peak S/N for jet and bulk configurations were measured using laser pulse energies of 100mJ and 20mJ, respectively, for aqueous sodium chloride at fixed concentration of 10ppm.

Based upon this assessment of peer reviewed literature it is concluded that, in terms of LIBS sensitivity, liquid jet sample presentation configuration is superior to liquid surface, with liquid bulk being inferior to both. However, based on practical considerations e.g. relative technical simplicity and potential for portability, it is concluded that the liquid bulk sample presentation configuration is more suitable than the alternatives. LIBS sensitivity for different sample presentation configurations, based on the criterion of detection limit of contaminant species, is summarized in Tables 1 – 4, Appendix II. The data were grouped according to volatility of target species (Groups I, II, III and D-block elements). Table 2.3 presents a comparison of detection limits between alternative sample presentation configurations, for species of most interest to the current research i.e. lead, cadmium, uranium, manganese and chromium.

Table 2.3: Comparison of Detection Limits for Selected Heavy Metals using Alternative Sample Presentation Configurations

Element	Sample Presentation	LoD/ ppm	Reference(s)
Lead, Pb	Bulk	12.5	Knopp (1996)
	Surface	100	Charfi & Harith (2002)
	Jet	40 0.3	Samek (1998) Lo & Cheung (2002)
Manganese, Mn	Jet	10	Samek (1998)
	Nebulized	7.2	Archontaki & Crouch (1988)
Chromium, Cr	Surface	10	Charfi & Harith (2002)
	Jet	100	Samek (1998)
Cadmium, Cd	Bulk	500	Knopp (1996)
Uranium, U	Surface	100	Wachter & Cremers (1987)

From the data presented in Table 2.3 it is apparent that reported detection limits, for elements of most interest to the current research, cover several orders of magnitude. The reasons for this diversity are the significant differences in LIBS experimental parameters sets used by different research groups. Direct comparison between different target species is practicable only when common experimental parameters sets have been used. It is important, however, to take into account the differences in relative intensity of emission lines between species.

2.7 Advantages of Double Pulse Excitation

Double pulse laser induced breakdown spectroscopy (DP-LIBS) uses a secondary laser pulse, lagging behind a primary pulse by a pre-set inter-pulse separation, to generate plasma at increased temperature. The advantages of using DP-LIBS for improving LIBS sensitivity were reviewed.

Historically one of the earliest demonstrations of the use of two high intensity flux sources to generate plasma was reported in the early 1980s (Cremers *et al*: 1984). The authors reported greater sensitivity for detection of a number of volatile metals in

aqueous solution, by utilizing two sparks for plasma generation (repetitive spark pair, RSP), compared to a single spark (repetitive single spark, RSS). The authors used a liquid bulk sample presentation configuration. Experimental parameters included wavelength of 1064nm, pulse duration of 15ns, primary pulse energy is the range 30-76mJ, and fixed secondary pulse energy of 125mJ. Inter-pulse separation was optimized at ~18μs, for detection of O(I) emission line at 777.4nm. The authors reported maximum increase in emission signal intensity of ~50 for RSP compared to RSS plasma generation.

Four principal DP-LIBS configurations have been described (Noll *et al*: 2004) for the study of spatial and temporal evolution of plasma generated from metal targets. A recent report (Rai *et al*: 2003) demonstrated increased LIBS sensitivity for detection of volatile metal species in aqueous solution. The authors used a collinear DP-LIBS configuration i.e. both ionization laser pulses sharing a common trajectory to the target. With liquid jet sample presentation configuration the authors reported typically three times stronger emission line intensity for DP- compared to SP- excitation, for neutral and ionic magnesium emission lines.

A recent paper (Koch *et al*: 2005) reported LIBS signal saturation for the neutral manganese triplet (centred at 403.31nm) for analyte concentration of ~120ppm. The authors also reported a linear relationship between signal intensity and analyte concentration in the range ~40ppm to ~60ppm. Insight was gained into the advantages of DP-LIBS for improvement of LIBS sensitivity by comparing these data with SP-LIBS data previously reported by the same authors (Koch *et al*: 2004), for characterization of aqueous chromium. In this earlier research linearity between LIBS emission signal and analyte concentration was demonstrated between ~25ppm and ~130ppm, with the onset of signal saturation for analyte concentration in excess of ~500ppm. The authors reported LoD for manganese (DP-LIBS) and chromium (SP-LIBS) to be in the order of 80ppb and 40ppm, respectively. Objective commentary regarding improvement in LIBS sensitivity between SP-LIBS and DP-LIBS is inhibited by inconsistencies in experimental parameter sets utilized in this researche.

This is illustrated in Table 2.4, which summarizes experimental parameters for the aforementioned LIBS research (Koch *et al*: 2004, 2005).

Table 2.4: LIBS Experimental Parameters for SP- and DP-LIBS

	SP-LIBS (Koch *et al*: 2004)	DP-LIBS (Koch *et al*: 2005)
Laser Parameters	1064nm, 5ns, 1Hz <1.3GWcm^{-2}	532nm, 6ns, 5Hz 7MWcm^{-2} & 6.2MWcm^{-2}
Exptl. Parameters	20x20x10cm^{-3} cuvette 600mm Ø collection fibre iCCD 756x581 11x11μm^2 pixels Czerny-Turner spectrometer 300 lines mm^{-1} blazed at 300nm t_d optimized *wrt* analyte conc. t_g = 10μs	20x20x10cm^{-3} cuvette 1200mm Ø collection fibre iCCD 1024x1024 13x13μm^2 pixels Czerny-Turner spectrometer 1200 lines mm^{-1} blazed at 500nm t_d 450 & 600μs t_g = 1 to 10μs
Analyte & Emission Line Details	$KCr(SO_4)_2 \cdot 12H_2O$ Cr(I) 357.9, 359.3, 360.5nm 40-2200ppm LoD = 40ppm	$Mn(NO_3)_2 \cdot 4H_2O$ Mn(I) 403.08, 403.31, 403.45nm 0.02-100ppm LoD = 80ppb

The principal parametric difference between the research efforts (Koch *et al*: 2004, 2005) was laser wavelength (1064nm and 532nm, respectively). As previously described, laser radiation at shorter wavelengths is advantageous, due to its efficacy in supporting multi-photon absorption in target species. The principal difference with regard to experimental apparatus was the respective grating specifications. The DP-LIBS set-up utilized a grating with groove density four times higher than the SP-LIBS set-up.

Improvement in LIBS sensitivity by utilization of double pulse laser excitation has been reported (Yaroshchyk *et al*: 2005b), for characterization of metallic elements in samples of crude oil pre-absorbed onto a filter paper substrate. The authors chose a

'crossed beam DP-LIBS configuration' i.e. two laser pulses having mutually oblique trajectories to the target, with plasma formation at the target surface. In common with these authors' companion research (Yaroshchyk *et al*: 2005a) experimental parameters included wavelength of 1064nm, repetition rate of 1Hz and pulse duration of 7ns. Laser pulse energies for double pulse excitation were optimized at 95mJ and 170mJ (primary and secondary pulses) with optimized inter-pulse separation of ~1μs. Limits of detection for double pulse and single pulse excitation, for species of interest to the research current, included: 18ppm & 3ppm for lead, and 7ppm & 4ppm for cadmium. These data represent a typical increase in LIBS sensitivity of ~100%.

The DP-LIBS technique has matured as an effective variation on the LIBS technique, and several reviews have been published. A recent review (Scaffidi *et al*: 2006) was primarily qualitative in its description of alternative DP-LIBS configurations, and speculation as to the *modus operandi* for improvement in DP-LIBS sensitivity. The most incisive comment from the authors was the observation that cavitation generated by the primary excitation pulse reduced 'quenching' of the plasma generated by the secondary pulse. Characterization of laser induced cavitation will be described in considerable detail in a later chapter. Another recent review of DP-LIBS (Babushok *et al*: 2006) provided a comprehensive description of the advantages of DP-LIBS, as well as a detailed consideration of the influence of laser parameters (wavelength, pulse duration, pulse energy, and inter-pulse separation) on DP-LIBS sensitivity for characterization of trace elements. The authors of this review considered the 'orthogonal pre-ablation' DP-LIBS configuration (a primary laser pulse focused at the target surface, followed by a secondary laser pulse focused above the target surface) to be the most efficacious for maximizing DP-LIBS sensitivity. Comparison of detection limits for single pulse and double pulse excitation modes is summarized in Tables 5 & 6, Appendix II. In addition Table 7, Appendix II summarizes experimental parameters and detection limits for LIBS utilizing a solid substrate, onto which liquid samples were pre-absorbed.

2.8 Comments in Conclusion

The majority of reviewed LIBS research is applications based, with laser parameter sets and sample presentation configuration chosen to match a specific research objectives. This critical review allowed two principal insights, both of which proved efficacious with regard to the current research: *i*. the ubiquity of the *state-of-the-art* laboratory Nd:YAG Q-switched laser, emitting pulses in the low ns and mJ pulse duration and energy regimes, with the fundamental wavelength of 1064nm. This parameter set closely matched that used in the current research. The similarity of experimental laser parameters allowed experimental trends from published work to be meaningfully compared to equivalent data acquired during the current research; *ii*. the investigation by a number of authors into detection and characterization of heavy metal species e.g. manganese and chromium in aqueous solution. These species have line emission characteristics typical of D-block elements, a group which includes the elements of most interest to the current research i.e. lead and mercury.

Increase of incident photon flux and concentration of scattering centres (synonymous with laser pulse energy and analyte concentration, respectively), up to and beyond critical limits, resulted in the onset of saturation in LIBS emission intensity. At laser pulse energy and analyte concentration below the saturation limiting value, a linear relationship was typically reported between these parameters and LIBS emission intensity.

The review of the influence of laser wavelength and pulse duration on LIBS sensitivity was somewhat *moot*, given the restriction within the current research of these parameters to 1064nm and ~7ns, respectively. Insight is nevertheless provided into the dominant mechanisms for laser induced breakdown in the liquid bulk. As will be described in the next chapter multi-photon ionization (MPI) and cascade ionization (CI) compete as distinct, but subtly inter-related, modes for dielectric breakdown of optically opaque media.

Similarly the review of the influence on LIBS sensitivity of alternative sample presentation configurations was also *moot*, due to the limitation of the current research to plasma formation in the liquid bulk. Valuable insight was provided, however, into the typical lifetime of expanding plasma in liquid bulk, compared to that for plasma expanding into a gaseous medium. This insight was useful for optimization of LIBS temporal parameters for accumulation of line emission signal. Such optimization is critical for increasing LIBS sensitivity and will be comprehensively demonstrated in a later chapter,.

References

Adamson M *et al*. Laser Induced Breakdown Spectroscopy at a Water / Gas Interface: a Study of bath Gas – Dependent Molecular Species. Spectrochimica Acta B 62 1348-1360 (2007)

Archontaki HA & Crouch SR. Evaluation of an Isolated Droplet Sample Introduction System for Laser – Induced Breakdown Spectroscopy. Applied Spectroscopy 42 741-746 (1988)

Babushok VI *et al*. Double Pulse Laser Ablation and Plasma: Laser Induced Breakdown Spectroscopy Signal Enhancement. Spectrochimica Acta B 61 (9) 999-1014 (2006)

Berman LM & Wolf PJ. Laser-Induced Breakdown Spectroscopy of Liquids: Aqueous Solutions of Nickel and Chlorinated Hydrocarbons. Applied Spectroscopy 52 3 438-443 (1998)

Boudjemai S *et al*. Spectral Sodium Chloride (NaCl) Identification by LIBS Technique in Bulk and Jet Solutions: Some Parametric Aspects. AIP Conference Proceedings (2008)

Casavola A *et al*. Non-Equilibrium Conditions During a Laser Induced Plasma Expansion. Applied Surface Science 208-209 85-89 (2003)

Charfi B & Harith MA. Panoramic Laser-Induced Breakdown Spectrometry of Water. Spectrochimica Acta B 57 1141-1153 (2002)

Cremers DA *et al*. Spectrochemical Analysis of Liquids Using Laser Spark. Applied Spectroscopy 38 (5) 721-729 (1984)

De Giacomo A *et al*. Early Stage Emission Spectroscopy Study of Metallic Aluminium Plasma Induced in Air by Femtosecond and Nanosecond Laser Pulse. Spectrochimica Acta B 60 (7-8) 935-947 (2005)
Docchio F *et al*. Q-switched Nd:YAG Laser Irradiation of the Eye and Related Phenomena: An Experimental Study I. Optical Breakdown Determination for Liquids and Membranes. Laser in the Life Sciences 1 87-103 (1986)
Docchio F *et al*. Experimental Investigation of Optical Breakdown Thresholds in Ocular Media under Single Pulse Irradiation with Different Pulse Durations. Lasers in Ophthalmology 1 83-93 (1986)
Fang X & Ahmad SR. Sample Presentation Considerations in Laser Induced Breakdown Spectroscopy in Aqueous Solution. Applied Spectroscopy 61 (9) 1021-1024 (2007)
Fang X & Ahmad SR. Saturation Effect at High Laser Pulse Energies in Laser Induced Breakdown Spectroscopy for Elemental Analysis in Water. Laser and Particle Beams 25 1-8 (2007)
Ho WF *et al*. Spectrochemical Analysis of Liquids using Laser-induced Plasma Emissions: Effects of Laser Wavelength. Applied Spectroscopy 51 (1) 87-91 (1997)
Kennedy PK. A First-Order Model for Computation of Laser-Induced Breakdown Thresholds in Ocular and Aqueous Media: Part I – Theory. IEEE Journal of Quantum Electronics 31 (12) 2241-2249 (1995)
Kennedy PK *et al*. A First-Order Model for Computation of Laser-Induced Breakdown Thresholds in Ocular and Aqueous Media: Part II – Comparison to Experiment. IEEE Journal of Selected Topics in Quantum Electronics 31 (12) 2250-2257 (1995)
Knopp R *et al*. Laser Induced Breakdown Spectroscopy [LIBS] as an Analytical Tool for the Detection of Metal Ions in Aqueous Solution. Fresnius Journal of Analytical Chemistry 355 16-20 (1996)
Koch S *et al*. Detection of Chromium in Liquids by Laser Induced Breakdown Spectroscopy (LIBS). Applied Physics A 79 (4-6) 1071-1073 (2004)
Koch S *et al*. Detection of Manganese in Solution in Cavitation Bubbles using Laser Induced Breakdown Spectroscopy. Spectrochimica Acta B 60 (7-8) 1230-1235 (2005)

Le Drogoff B *et al*. Temporal Characterization of Femtosecond Laser Pulse Induced Plasma for Spectrochemical Analysis of Aluminium Alloys. Spectrochimica Acta B 56 (6) 987-1002 (2001)
Le Drogoff B *et al*. Influence of the Laser Pulse Duration on Laser-produced Plasma Properties. Plasma Sources Science and Technology 13 (2) 223-230 (2004)
Lo KM & Cheung NH. ArF Laser Induced Plasma Spectroscopy for part-per-billion Analysis of Metal Ions in Aqueous Solutions. Applied Spectroscopy 56 (6) 682-688 (2002)
Michel APM *et al*. Evaluation of Laser Induced Breakdown Spectroscopy (LIBS) as a New *in-situ* Chemical Sensing Technique for the Deep Ocean. Oceans 4098930 (2006)
Michel APM *et al*. Laser Induced Breakdown Spectroscopy for Bulk Aqueous Solutions at Oceanic Pressure: Evaluation of Key Measurement Parameters. Applied Optics 46 (13) 2507-2515 (2007)
Noll R *et al*. Space- and Time-resolved Dynamics of Plasmas Generated by Laser Double Pulses Interacting with Metallic Samples. Journal of Analytical Atomic Spectrometry 19 (4) 419-428 (2004)
Rai VN *et al*. Study of Laser Induced Breakdown Emission from Liquid under Double-Pulse Excitation. Applied Optics 42 (12) 2094-2101 (2003)
Sacchi CA. Laser-induced Electric Breakdown in Water. Journal of the Optical Society of America B 8 337-345 (1991)
Samek O *et al*. Analysis of Liquid Samples using Laser Induced Breakdown Spectroscopy. SPIE Proceedings 3504 (1998)
Scaffidi J *et al*. Emission Enhancement Mechanisms in Dual-pulse LIBS. Analytical Chemistry 78 (1) 24-32 (2006)
St-Onge L *et al*. Rapid Analysis of Liquid Formulations Containing Sodium Chloride using Laser Induced Breakdown Spectroscopy. Journal of Pharmaceutical and Biomedical Analysis 36 (2) 277-284 (2004)
Stavropoulos P *et al*. Calibration Measurements in Laser Induced Breakdown Spectroscopy using Nanosecond and Picosecond Lasers. Spectrochimica Acta B 59 (12) 1885-1892 (2004)

Vogel A *et al*. Plasma Formation in Water by Picosecond and Nanosecond Nd:YAG Laser Pulses- part I: Optical Breakdown at Threshold and Supra-threshold Irradiance. IEEE Journal of Selected Topics in Quantum Electronics 2 (4) 847-860 (1996)
Vogel A *et al*. Energy Balance of Optical Breakdown in Water at Nanosecond to Femtosecond Time Scales. Applied Physics B: Lasers and Optics 68 271-280 (1999)
Wachter JR & Cremers DA. Determination of Uranium in Solution using Laser Induced Breakdown Spectroscopy. Applied Spectroscopy 41 (6) 1042-1048 (1987)
Yaroshchyk P *et al*. Quantitative Determination of Wear Metals in Engine Oils using Laser Induced Breakdown Spectroscopy: a Comparison Between Liquid Jets and Static Liquids. Spectrochimica Acta B 60 986-992 (2005)
Yaroshchyk P *et al*. Quantitative Determination of Wear Metals in Engine Oils using LIBS: the use of Paper Substrates and a Comparison Between Single- and Double-Pulse LIBS. Spectrochimica Acta B 60 1482-1485 (2005)
Yueh F-Y *et al*. Evaluation of the Potential of Laser Induced Breakdown Spectroscopy for Detection of Trace Element in Liquid. Journal of the Air & Waster Management Association volume 52 1307-1315 (2002)

Chapter Three
THEORETICAL CONCEPTS

"It is more important to have beauty in one's equations than to have them fit experiment."
Paul Dirac

In this chapter, fundamental theoretical concepts and related *formulae* relevant to the present research are examined. Key processes are described, as follows: *i*. absorption of laser radiation by the liquid medium; *ii*. formation and growth of laser induced cavitation bubble in the liquid bulk; *iii*. interaction between laser radiation and target medium; *iv*. continuum complexion of *Bremsstrahlung* emission profile; and, *v*. reduction of shot noise contribution to line emission signals.

3.1 Absorption of Laser Radiation in Aqueous Media

Within the context of plasma generation in the liquid bulk, only that fraction of incident laser energy absorbed by the aqueous medium is utilized for dielectric breakdown. Attenuation encompasses two processes which remove energy from the incident laser pulse, during its traversal through the liquid medium i.e. scattering and absorption. Cumulative attenuation as a result of absorption and scattering losses is described by the Beer-Lambert Law, as follows:

$$I(x) = I_0 \exp(-\mu(\lambda) \cdot x) \qquad \ldots \quad \ldots \quad \ldots \quad \ldots \quad [3.1]$$

where,

I_0 = non-reflected intensity in target medium
$I(x)$ = attenuated intensity at distance x from surface
x = path length within liquid medium
$\mu(\lambda)$ = wavelength dependent attenuation coefficient

For the laser wavelength and pulse duration used in the present research, contribution to the overall attenuation from scattering is considered to be negligible. This statement is based upon reported research (Vogel *et al*: 1999), describing empirical assessment of the partition of laser energy focussed in the liquid bulk. The authors reported reflected and scattered components of incident laser radiation to be less than 1%, for

laser pulses of 6ns duration, and energy of 1 & 10mJ. Based on these data, absorption coefficient, $\mu_a(\lambda)$ was synonymous, for all intents and purposes, with attenuation coefficient. For the wavelength used in the current research (1064nm), the absorption coefficient was reported (Vogel *et al*: 1999) to be $0.13cm^{-1}$ for distilled water.

3.2 Theoretical Analysis of Laser Induced Cavitation in the Liquid Bulk

Multi-photon absorption of photons by the liquid medium leads to photolysis i.e. ionization and dissociation of the absorbing medium. Photolysis products, particularly quasi-free electrons and hydroxyl radicals, are strongly absorbing in the IR and visible wavebands. This results in a rapid rise in plasma temperature and pressure in the focussed beam waist, several orders of magnitude greater than predicted by classical theory. Rapid thermal expansion of the focussed laser volume results in three principal mechanical effects. These are: *i*. acoustic signature, *ii*. shockwave propagation; and, *iii*. formation of an oscillating cavitation bubble. Cavitation in liquid was originally described algebraically by (Lord) Rayleigh, following an earlier hypothetical scenario suggested by Besant. Rayleigh's classical *formulæ* have been oft utilized e.g. analysis of laser induced cavitation behaviour in the vicinity of a solid boundary (Gregorčič *et al*: 2007).

Rayleigh's objective was to calculate the energy expended during the collapse of a bubble, due to the pressure differential across the bubble boundary. Rayleigh's *a priori* assumption (following Besant) was a hypothetical liquid of infinite extent, possessing properties of zero compressibility and viscosity. An equation was initially derived which expressed bubble wall velocity (V_B) as a function of bubble radius (R_B), as follows:

$$v_B = [(^2/_3)P_\infty/\rho_l \cdot \{(R_0/R_B)^3 - 1\}]^{0.5} \quad \ldots \quad \ldots \quad [3.2]$$

where,

P_∞ = pressure in infinite liquid ($kg\ m^{-1}\ s^{-2}$)
ρ_l = fluid density (kgm^{-3})
R_0 = maximum bubble radius (m)

Integration of this equation yielded an expression for the bubble collapse time, τ_c, as a function of maximum bubble radius, R_0. Bubble collapse time is the time taken for the bubble radius to change from maximum to minimum i.e. half the bubble oscillation time (τ_b), and is calculated as follows:

$$\tau_c = 0.915R_0 \cdot (\rho_l/P_\infty)^{0.5} = \tau_b/_2 \quad \ldots \quad \ldots \quad [3.3]$$

where,

τ_c = bubble collapse time (s)
τ_b = bubble oscillation time (s)

A differential form of the Rayleigh equation was developed by Plesset, to include bubble radius (R) as well as bubble wall velocity and acceleration. This equation has been oft utilized (Petkovšek & Gregorčič: 2007), and is expressed as follows:

$$R \cdot d^2R/dt^2 + {}^3/_2(dR/dt)^2 = {}^1/\rho_l \cdot \{P(R) - P_\infty\} \quad \ldots \quad [3.4]$$

where,

dR/dt = bubble wall velocity (ms^{-1})
d^2R/dt^2 = bubble wall acceleration (ms^{-2})
$P(R)$ = pressure at bubble surface (kgm^2s^{-2})
ρ_l = fluid density (kgm^{-3})
P_∞ = pressure in infinite liquid ($kg\ m^{-1}\ s^{-2}$)

Rate of bubble expansion reduces asymptotically until maximum radius is achieved. At this stage the pressure differential across the bubble boundary has reduced to zero, and the bubble begins to collapse. When the pressure and temperature within the collapsing bubble are sufficient to generate a further shock wave, subsequent (secondary, tertiary etc.) phases of expansion and collapse occur. Oscillation continues until the energy encapsulated within the bubble is insufficient to generate a further shock wave. During the complete bubble lifetime i.e. indicative of multiple oscillatory periods, energy available to support bubble oscillation is primarily lost due to the thermal gradient across the bubble boundary, as well as energy manifest as shockwave emission.

Further developments of the Rayleigh formula have been reported to account for liquid viscosity and compressibility. An assessment of these equations is beyond the scope of the present study. A comprehensive summary has been reported (A Shima: 1997).

3.3 Interaction between Laser Radiation and Dielectric Target Medium

Molecular ionization in liquid media may be induced via two distinct, but not independent, mechanisms i.e. multi-photon ionization (MPI) and cascade ionization (CI). Cascade ionization requires the presence of 'seed' electrons in the volume defined by the focussed laser beam waist. 'Seed' electrons couple with the laser electromagnetic field, and acquire sufficient kinetic energy to cause ionization of adjacent molecules via direct collision. The subsequent release of an electron pair generates a geometric increase in electron density, forming a cascade of free electrons. If sufficiently high free electron density is generated, dielectric breakdown is induced by further collision with molecules in the immediate vicinity. The pre-collision and post-collision electrons have different energy distributions (ε, ε' and ε'', respectively), the former having a higher mean value than the latter. The inverse process of three-body re-combination establishes a dynamic equilibrium in the expanding plasma phase. This equilibrium has been reported (Casavola *et al*: 2003), as follows:

$$A + e^{-}(\varepsilon) \leftrightarrow A^{+} + e^{-}(\varepsilon') + e^{-}(\varepsilon'') \qquad \ldots \qquad \ldots \qquad [3.5]$$

where,

A = neutral species
A^{+} = ionized species
e^{-} = free (solvated) electron
ε = electron energy distribution pre-collision
ε′, ε″ = electron energy distributions post-collision

The contrast between the two ionization mechanisms is illustrated by consideration of laser induced breakdown in a liquid medium, which satisfies one of two independent conditions: *i*. negligible concentration of potential scattering centres; or, *ii*. scattering

centres of vanishingly low cross-section. At sufficiently high photon flux, target molecules are directly ionized by MPI, providing a reservoir of 'seed' electrons for the onset of cascade ionization. In MPI each electron independently absorbs several photons in order to bridge the energy gap between adjacent vibration manifolds. This process has been reported (Casavola *et al*: 2003), as follows:

$$A + n(h\nu) \rightarrow A^{+} + e^{-}(\varepsilon) \qquad \ldots \quad \ldots \quad \ldots \quad [3.6]$$

where,

A = neutral species
A^{+} = ionized species
$e^{-}(\varepsilon)$ = electron with non-linear energy distribution
$h\nu$ = absorbed photon
n = number of absorbed photons

The number of photons required to induced multi-photon ionization is a function of the ratio between vibration manifold band gap and laser photon energy. The inherent complexity of the physico-chemistry of liquid water, as well as further complications with respect to hydrolysis of photolysis products during the breakdown process, complicates interpretation of experimentally measured band gap energy. Reported values include: *i*. estimate based upon the assumption of two photon absorption of 6.5eV (Longtin & Tien: 1997); *ii*. classical estimate of 5.8eV (De Giacomo *et al*: 2007); and, *iii*. empirically measured value of 8.9eV (Crowell & Bartels: 1996). On exceeding the ionization threshold for a specific target species, free electrons become subsumed within the reservoir of 'quasi-free' electrons.

The most significant difference between the two ionization mechanisms is the time scale on which they operate. MPI operates on a time scale an order of magnitude shorter than CI. This allows the mechanism of MPI to dominate for laser pulses in the sub-ns range e.g. picosecond & femtosecond regimes. In contrast the longer time scale for onset of CI allows the dominance of this ionization mechanism at longer pulse durations i.e. in the nanosecond regime. By this reasoning, cascade ionization was concluded to provide the dominant mechanism for dielectric breakdown in the liquid medium for the present research. A sophisticated mathematical derivation of critical

free electron density thresholds for CI and MPI, as well as the free electron density threshold at which MPI induces the onset of CI, has been reported (Kennedy: 1995). Such a detailed consideration is beyond the scope of the present research.

Irrespective of the ionization mechanism for a specific target, and assuming a state of local thermodynamic equilibrium (LTE) in the expanding plasma phase, calculations of the relative populations of neutral and ionized species have been reported (Capitelli *et al*: 2000) in terms of the Saha-Eggert equation, as follows:

$$n_e \cdot N_{\|}/N_{|} = 2Z_{\|}(T)/Z_{|}(T) \cdot (2\pi m_e kT/h^2)^{1.5} \cdot \exp(-\Delta E/kT) \qquad [3.7]$$

where,

n_e = electron density (cm^{-3})
$N_{\|}$ / $N_{|}$ = population of neutral / singly ionized species (cm^{-3})
$Z_{\|}$ / $Z_{|}$ = partition function of neutral / singly ionized species
m_e = electron mass (kg)
k = Boltzmann constant (JK^{-1})
T = plasma temperature (K)
h = Planck constant (Js)
ΔE = energy gap between levels (J)

For the sake of completeness, it is important to describe a commonly used *rule-of-thumb* for validity of the assumption of LTE i.e. the McWhirter criterion (McWhirter: 1965). This criterion defines the lower limit of electron density for which the validity of LTE may be assumed, as a function of plasma temperature (T) and emission line energy (ΔE). The McWhirter criterion is well established experimentally, and has been reported (Le Drogoff *et al*: 2001, Charfi & Harith: 2002, Ismail *et al*: 2004, Shaikh *et al*: 2006, Adamson *et al*: 2007), as follows:

$$n_e \geq 1.6\text{x}10^{12} \cdot T^{0.5} \cdot (\Delta E)^3 \qquad \ldots \quad \ldots \qquad [3.8]$$

where,

n_e = free electron density (cm^{-3})
T = plasma temperature (K)
ΔE = largest energy transition for which LTE holds (eV)

The subtlety of invoking the McWhirter criterion for testing the validity of LTE is illustrated by the following quote (Cristoforetti *et al*: 2010): "This criterion (McWhirter) will tell us whether LTE conditions *do not exist*, and not whether LTE conditions *exist*" (italics in the original).

3.4 Continuum Complexion of *Bremsstrahlung* Emission Profile

The principal radiative feature in the early stages of plasma expansion is broadband (continuum) *Bremsstrahlung* emission. The dominant process for generation of *Bremsstrahlung* is radiative re-combination, during which an ionic species combines with a free electron, generating a neutral species (typically in an excited state), with complementary photon emission. This process has been reported (Casavola *et al*: 2003), as follows:

$$A^{+} + e^{-}(\varepsilon) \rightarrow A^{*} + h\nu \qquad \ldots \quad \ldots \quad \ldots \quad [3.9]$$

where,

A^{+} = ionized species
A^{*} = excited neutral species
$e^{-}(\varepsilon)$ = non-linear electron energy distribution

The continuum complexion of *Bremsstrahlung* emission may be explained by consideration of the continuum velocity distribution of free electrons, and the heterogeneity of free electron density, in the expanding plasma volume. A Maxwellian velocity distribution is typically reported (Casavola *et al*: 2003) for free electrons, for an expanding plasma assumed to be in a quasi-stationary state (QSS). Such a velocity distribution is described, as follows:

$$f(u, v, w) = n_e \cdot (m_e/2\pi kT_e)^{1.5} \cdot \exp\{-m_e(u^2 + v^2 + w^2)/2kT\} \qquad [3.10]$$

where,

n_e = number of electrons per unit volume (cm^{-3})
m_e = electron rest mass (kg)
u, v, w = Cartesian velocity components
k = Boltzmann constant (JK^{-1})
T_e = electron temperature (K)

The continuous distribution of electron velocity in the three orthogonal Cartesian co-ordinates results in a broadband (blackbody) emission spectrum on interaction with the laser electromagnetic field..

3.5 Reduction of Shot Noise Contribution to Line Emission Signals

Efforts to quantify and reduce noise in experimental work is the proverbial 'albatross about the neck' of the empirical scientist. 'Shot noise' is a ubiquitous presence is emission spectroscopy data collection. Shot noise is an example of 'white noise' insofar as it is not frequency specific for the temperature and system bandwidths used for the present research. A fundamental property of shot noise, S_{shot}, is its relationship to the magnitude of the signal, S, as follows:

$$S_{shot} \propto S^{0.5} \quad \ldots \quad \ldots \quad \ldots \quad \ldots \quad [3.11]$$

The significance of this may be appreciated by consideration of the relative magnitude of the two signal sources of interest i.e. atomic line emission signal, S_λ, and mean background signal, S_{mean}, from which line emission signal: noise ratio (S/N) is calculated. For any specific emission wavelength (λ), S/N is calculated as follows:

$$S/N_\lambda = (S_\lambda - S_{mean}) / \sigma_{bkgnd} \quad \ldots \quad \ldots \quad \ldots \quad [3.12]$$

where,

σ_{bkgnd} = standard deviation of background

The intensity of S_λ is typically an order of magnitude greater than S_{mean}. The contribution of shot noise at the specific emission wavelength is hence significantly greater. For this reason, the application of a data averaging algorithm is required i.e. given the superposition of a statistically significant number (N) of averaged emission spectra, the coincidence of 'peaks' and 'troughs' from these individual spectra will reduce the *rms* shot noise contribution, at any specific emission wavelength, λ.

The inherently random nature of shot noise is described by the Poisson probability distribution, as follows:

$$P(k) = (e^{-\lambda} \cdot \lambda^{k})/k! \quad \ldots \quad .. \quad \ldots \quad [3.13]$$

where,

P(k) = probability of k events
λ = expected number of events in defined interval
k = number of recorded events in same interval

This equality is subject to the *proviso* that the time interval over which data is collected is of sufficient duration such that the Poisson distribution may be demonstrated to be a limiting case of the Binomial distribution. By expressing shot noise in terms of available noise power, over a frequency range representative of the system bandwidth, shot current may be estimated, as follows:

$$I_s = (4k \cdot T \cdot \Delta f/R)^{0.5} \quad \ldots \quad \ldots \quad \ldots \quad \ldots \quad [3.14]$$

where,

I_s = shot current (A)
k = Boltzmann constant (JK^{-1})
T = temperature (K)
Δf = electronic bandwidth (Hz)
R = ohmic impedance (Ω)

The following values are pertinent to the current LIBS research: boxcar integrator bandwidth, Δf = 400MHz; boxcar integrator ohmic impedance, R = 50Ω; T = 298K i.e. room temperature conditions. Based on these values, shot current, $I_s = 3.6 \times 10^{-7}$A (0.36μA). With an impedance matched signal integration and display system, corresponding shot voltage, $V_s \sim 18\mu V$.

References

Adamson M *et al*. Laser Induced Breakdown Spectroscopy at a Water / Gas Interface: a Study of bath Gas – Dependent Molecular Species. Spectrochimica Acta B 62 1348-1360 (2007)

Capitelli M *et al*. Non-equilibrium and Equilibrium Problems in Laser-induced Plasmas. Spectrochimica Acta B – Atomic Spectroscopy 55 (6) 559-574 (2000)

Casavola A *et al*. Non-Equilibrium Conditions During a Laser Induced Plasma Expansion. Applied Surface Science 208-209 85-89 (2003)

Charfi B & Harith MA. Panoramic Laser-Induced Breakdown Spectrometry of Water. Spectrochimica Acta B 57 1141-1153 (2002)

Cristoforetti G *et al*. Local Thermodynamic Equilibrium in Laser Induced Breakdown Spectroscopy: Beyond the McWhirter Criterion. Spectrochimica Acta B 65 (1) 86-95 (2010)

Crowell RA & Bartels DM. Multiphoton Ionization of Liquid Water with 3.0-5.0eV Photons. Journal of Physical Chemistry 100 17940-17949 (1996)

De Giacomo A *et al*. Spectroscopic Investigation of Laser-Water Interaction Beyond the Breakdown Threshold Energy. Spectrochimica Acta B 62 87-93 (2007)

Gregorčič P *et al*. Investigation of a Cavitation Bubble between a Rigid Boundary and a Free Surface. Journal of Applied Physics 102 094904 (2007)

Ismail MA *et al*. LIBS Limit of Detection and Plasma Parameters of Some Elements in Two Different Metallic Matrices. Journal of Analytical Atomic Spectroscopy 19 (4) 489-494 (2004)

Kennedy PK. First Order Model for Computation of Laser Induced Breakdown Thresholds in Ocular and Aqueous Media: Part I – Theory. IEEE Journal of Quantum Electronics 31 (12) 2241-2249 (1995)

Le Drogoff B *et al*. Temporal Characterization of Femtosecond Laser Pulses Induced Plasma for Spectrochemical Analysis of Aluminium Alloys. Spectrochimica Acta B 56 (6) 987-1002 (2001)

Longtin JP & Tien C-L. Efficient Laser Heating of Transparent Liquids using Multiphoton Absorption. International Journal of Heat and Mass Transfer 40 (4) 951-959 (1997)

McWhirter RWP. Plasma Diagnostic Techniques, Chapter 5. Academic Press, New York (1965)

Petkovšek R & Gregorčič P. A Laser Probe Measurement of Cavitation Bubble Dynamics Improved by Shock Wave Detection and Compared to Shadow Photography. Journal of Applied Physics 102 044909 (2007)

Shaikh NM *et al*. Measurement of Electron Density and Temperature of a Laser Induced Zinc Plasma. Journal of Physics D: Applied Physics 39 (7) 1384-1391 (2006)

Shima A. Studies on Bubble Dynamics. Shock Waves 7 33-42 (1997)

Vogel A *et al*. Energy Balance of Optical Breakdown in Water at Nanosecond to Femtosecond Time Scales. Applied Physics B: Lasers and Optics 68 271-280 (1999)

THIS PAGE INTENTIONALLY BLANK

Chapter Four

MATERIALS, APPARATUS AND METHODOLOGIES

"We are no wiser and no less biased than other people. But as a physicist, or a biologist, you are certain to have gone through the experience of making a confident assertion, and then being proved wrong. A philosopher or a sociologist might never have had this wholesome lesson"
Niels Bohr

4.1 Atomic Emission Lines of Target Species

Studies on laser induced cavitation were carried out using triple distilled water, prepared in the Department of Engineering and Applied Science (DEAS) Laser Laboratory. Investigation of variation in dielectric breakdown thresholds was carried out using both distilled water and tap water. The latter samples were collected from the mains supply. Concentrations of dissolved metal species of interest to the current research, as reported by Thames Water, are shown in Table 4.1. Statutory European Union (EU) maximum permissible concentrations (MPC) for drinking water are also included for comparison. The complete Water Quality Report is reproduced in Appendix III.

Table 4.1 Measured Concentration of Elements of Interest Compared to their Statutory Limits

species	As	Cd	Pb	Hg	Se
measured concentration[1]/ ppb	0.52	<0.2	0.62	<0.12	0.82
statutory limit[2]/ ppb	10	5	10	1	10

[1]: Thames Quality Utilities Water Quality Report – 2009 Data (Water Supply Zone S26 : Shrivenham)
[2]: Council Directive 98/83/EC; 03-11-1998

For optimization of principal LIBS experimental parameters (pulse energy, delay time, and data average number) the strong Na(I) emission line at 589.00nm was used. Having completed this preliminary exercise the research was primarily concerned with detection and quantification of two primary elements, lead and mercury, in

aqueous solution. Relative emission line intensities for Pb(I) and Hg(I), normalized with respect to Na(I), are presented in Table 4.2.

Table 4.2 Line Emission Data for Sodium, Lead and Mercury

Element	Neutral Line/ nm	Emission Intensity[1]	Normalized Intensity
Na	589.00	$1.7x10^8$	1.000
Pb	405.78	$2.7x10^6$	0.016
Hg	253.65	$1.7x10^5$	0.001

[1]: taken from Payling and Larkins database v1.5.7

In common with most metals occupying the D-block of the periodic table, lead and mercury have strongest emission lines in the near UV region.

4.2 Methodology and Apparatus

In this research the liquid bulk sample presentation configuration was used. This configuration was preferable compared to other LIBS configurations (surface, nebulized spray and single droplet) because of the relative ease of sample presentation. The utilization of liquid bulk sample presentation configuration is also advantageous for development of a portable LIBS prototype for *in situ* field applications.

4.2.1 Experimental Set-up for LIBS

The schematic in Figure 4.1, and photograph in Figure 4.2, show the layout of LIBS apparatus and various components. The excitation source used was a Q-switched Nd:YAG laser (Litron Nano-L 200-20) operating at the fundamental output wavelength of 1064nm. Pulse duration was fixed at ~7ns, capable of operating at tunable repetition rates up to 50Hz. Pulse energies used were in the range ~15mJ to ~140mJ.

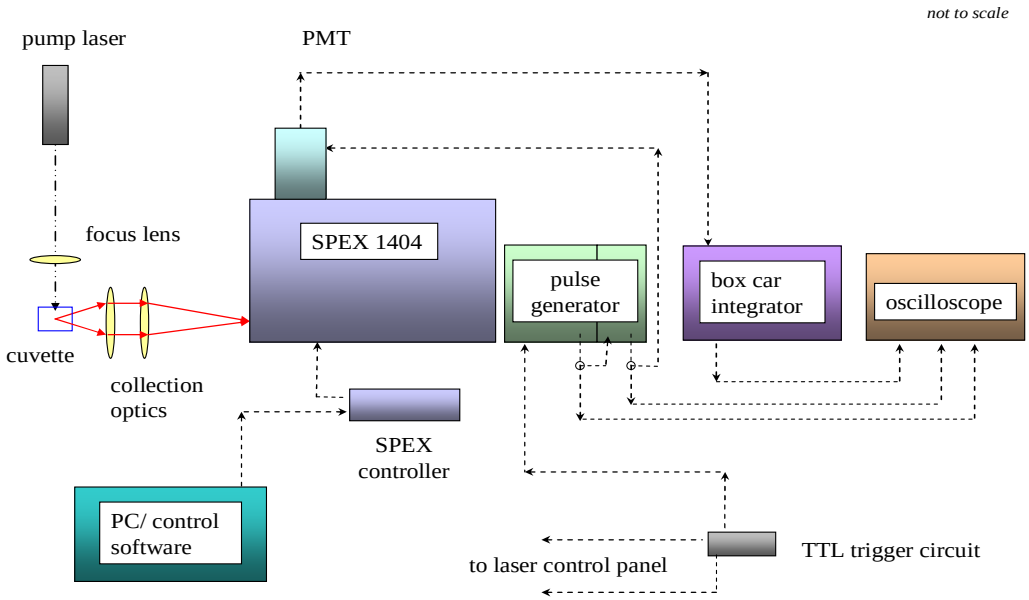

Figure 4.1 Schematic for LIBS Set-up using Liquid Bulk Sample Presentation

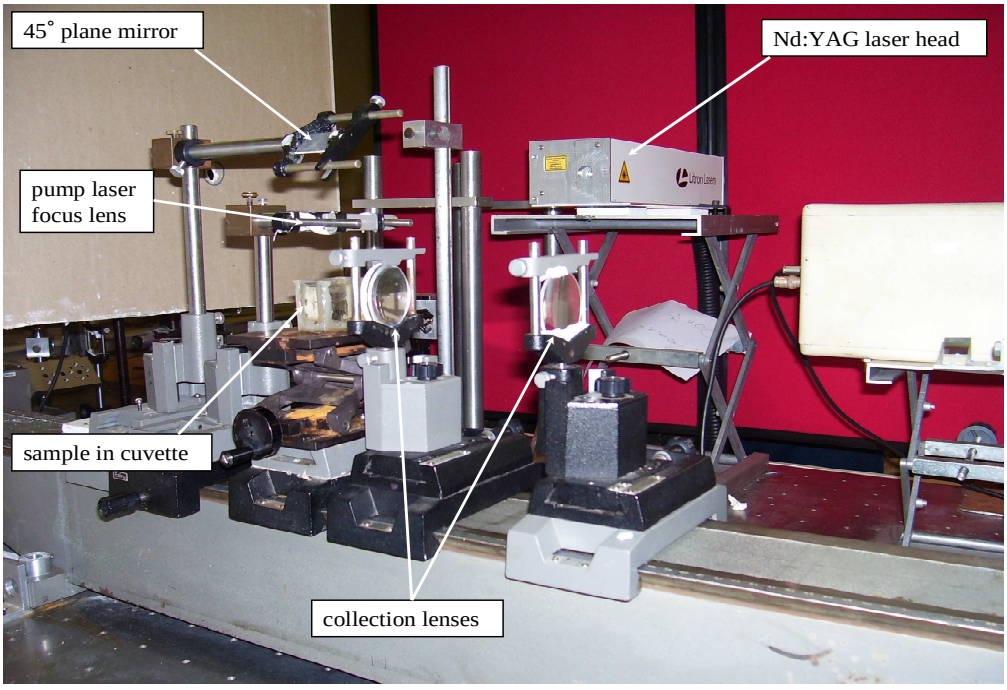

Figure 4.2 Photograph of the Arrangement of LIBS Experimental Apparatus

4.2.2 Experimental Set-up for Spatial Profiling of Pump Laser Pulse

The spatial intensity profile of Nd:YAG laser pulses was recorded using a set-up illustrated in Figure 4.3. The beam diameter at the laser head exit aperture had a nominal diameter of 5mm, with beam divergence in the order of hundreds of μrad. The beam was expanded by a concave lens, and reflected from a suitably positioned section of plane glass. The expanded beam cross section matched the area of the CCD array at the front of the digitizing video camera. Recording and analysis was carried out using proprietary software, loaded onto a dedicated laptop. Owing to the high sensitivity of the camera, two neutral density (ND) filters (reducing transmission by a factor of 10^7) were positioned in front of the detecting surface.

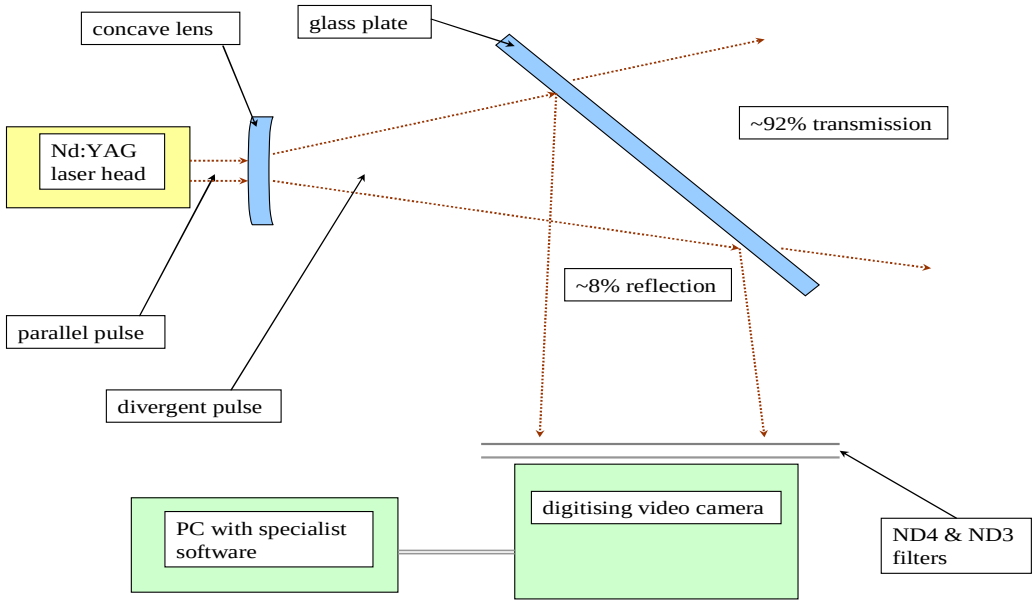

Figure 4.3: Schematic for Measurement of Nd:YAG Pulse Intensity Profile

A digitized representation of the Nd:YAG beam intensity profile is illustrated in Figure 4.4. The measurement criterion was averaged power density per pixel on the detecting surface.

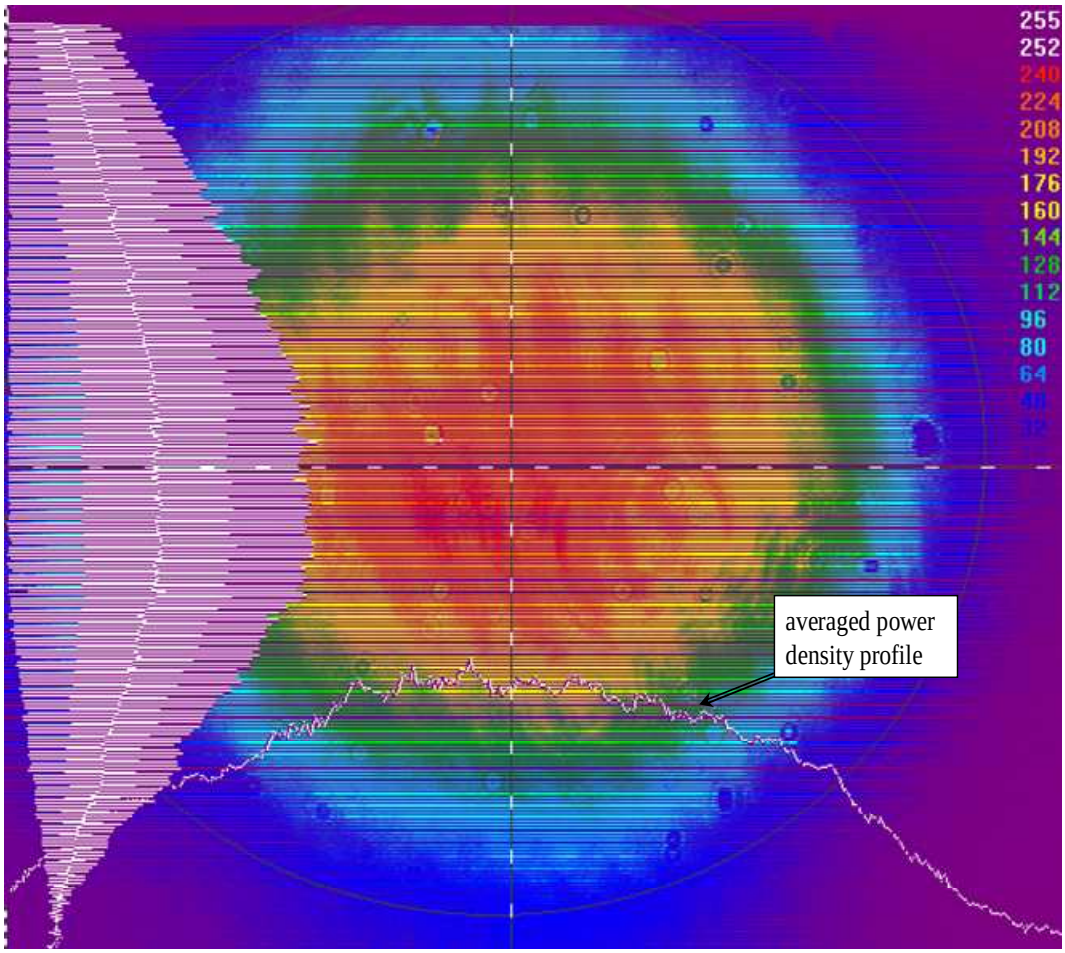

Figure 4.4: Digitized Intensity Profile for Nd:YAG Laser Pulse

Visual inspection of the digitized intensity profile in Figure 4.4 lead to two conclusions: *i*. the Nd:YAG intensity profile was non-Gaussian; *ii*. the Nd:YAG intensity profile demonstrated a high degree of symmetry.

4.2.3 Beam Collimation, Focusing and Radiation Detection

Laser pulses were directed into the liquid bulk (contained within a quartz cuvette) vertically, as shown schematically in Figure 4.5, using a plane mirror fixed at 45° to the horizontal.

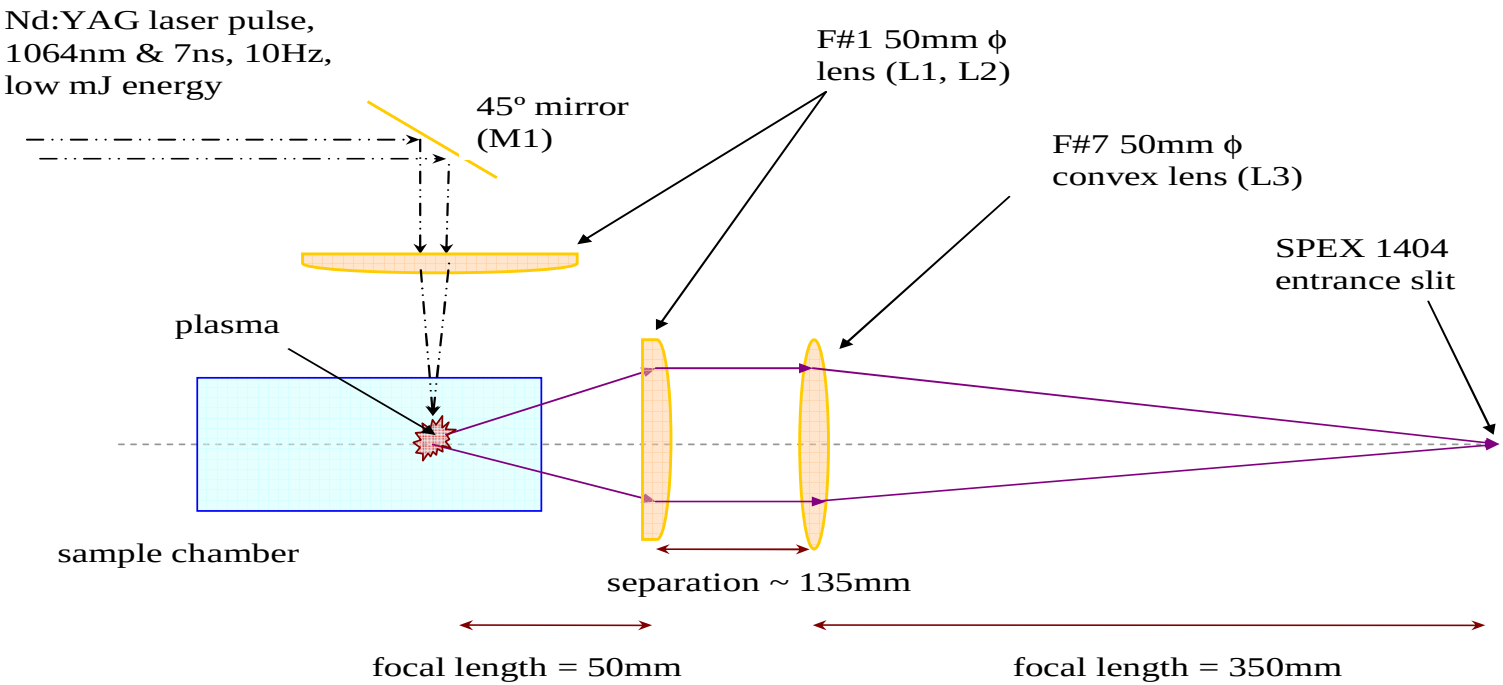

Figure 4.5 Schematic for Delivery of Focused Laser Pulse to Target Medium and Subsequent Collection of Radiative Emissions

Laser pulses were focused by a 50mmϕ convex quartz lens (L1) with focal length of 50mm. The focal point of the lens was ~25mm below the liquid *meniscus*. The capacity of the quartz cuvette was 20x50x50mm^3. The plasma was formed approximately half way between the centre of the cuvette and the cuvette wall adjacent to the collection optics. Radiation emitted from the laser-induced plasma was collected by a nominally F#1 convex lens (L2) with focal length of 50mm. The diameter of the collection lens, and its proximity to the plasma emission source, governed the proportion of emitted radiation captured by the optics. The solid angle, Γ_{pl}, subtended by a circular lens with focal length, f, and diameter, ϕ, is calculated as follows:

$$\Gamma_{pl} = \pi/4 \times (\phi/f)^2 = \pi/4 \times (F\#)^{-2} \qquad \ldots \qquad [4.1]$$

For the F#1 collection lens (L2) used in the current research the solid angle subtended was calculated to be ~π/4, representing a signal collection efficiency of <7% assuming a spherically uniform radiative emission profile. A F#7 convex lens (L3) with focal length of 350mm focused the collimated plasma radiation onto the monochromator entrance slit. This lens arrangement was optically matched to the monochromator, which had focal length of 850mm and primary mirror diameter of 120mm.

Another crucial aspect of collection optics was their transmission properties. *Bremsstrahlung* is characterized by a broadband emission profile, with a spectral distribution synonymous with that of a classical blackbody (assuming validity of the assumption of LTE in the expanding plasma). A challenging task for the current LIBS research was to detect and identify, from within the *Bremsstrahlung* profile, discrete atomic emission lines in the near UV region. This requirement governed the choice of quartz glass lenses which have relatively high transmission in the UV region.

For the current LIBS research the monochromator grating specification was matched to the atomic emission wavelength of interest. For detection of Na(I) emission line at 589.00nm a visible dispersion grating, blazed at 500nm, was used. For detection of Hg(I) emission line at 253.65nm a UV grating, blazed at 250nm, was used. Manufacturers transmission characteristics for both gratings are re-produced in Appendix IV. For the current LIBS research a photo-multiplier tube (PMT) was used for detection of plasma emission. The PMT module set-up, in relation to the monochromator entrance slit, is shown in the photograph in Figure 4.6.

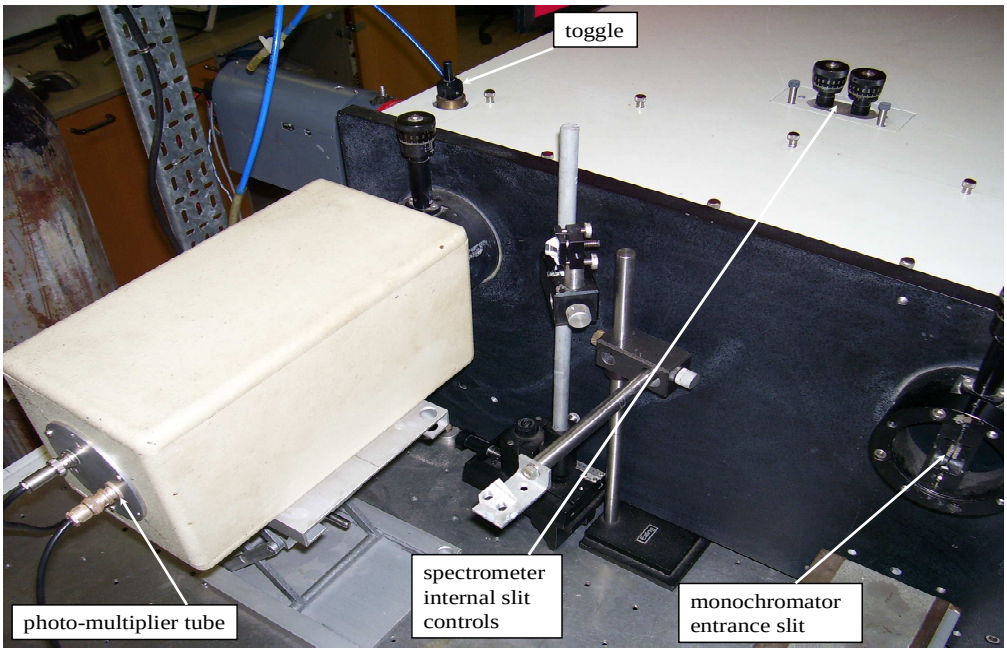

Figure 4.6 Photograph Showing Photo-Multiplier Tube and Monochromator Entrance Slit

For the PMT based system the detected optical signals were accumulated by a box-car integrator (BCI - HP5411D), before being displayed and recorded by a digitizing oscilloscope (Agilent DSO5054A). Key performance parameters for the PMT, BCI and oscilloscope used in the research are presented in Appendix I.

4.3 Characterization of Laser Induced Cavitation

Two independent techniques were used for the characterization of the laser induced cavitation bubble: *i*. probe beam deflection, and, *ii*. high speed imaging. The probe beam deflection (PBD) technique is indirect, *insofar* as the behaviour of the oscillating bubble boundary is inferred, via interpretation of deflected probe beam signal profiles. In the current research a HeNe probe laser (Uniphase 1125P), operating in continuous wave (cw) mode and emitting at 633nm at 6mW, was used. In the high speed imaging (HIS) technique the dynamics of the oscillating bubble were observed directly.

4.3.1 Experimental Set-up for Profiling of Probe Laser Beam

The intensity profile of the probe beam was measured by expanding the beam with a short focal length concave lens onto a semi-transparent screen, and using a photodiode to measure the intensity at incremental points across the maximum beam diameter. This arrangement is illustrated schematically in Figure 4.7.

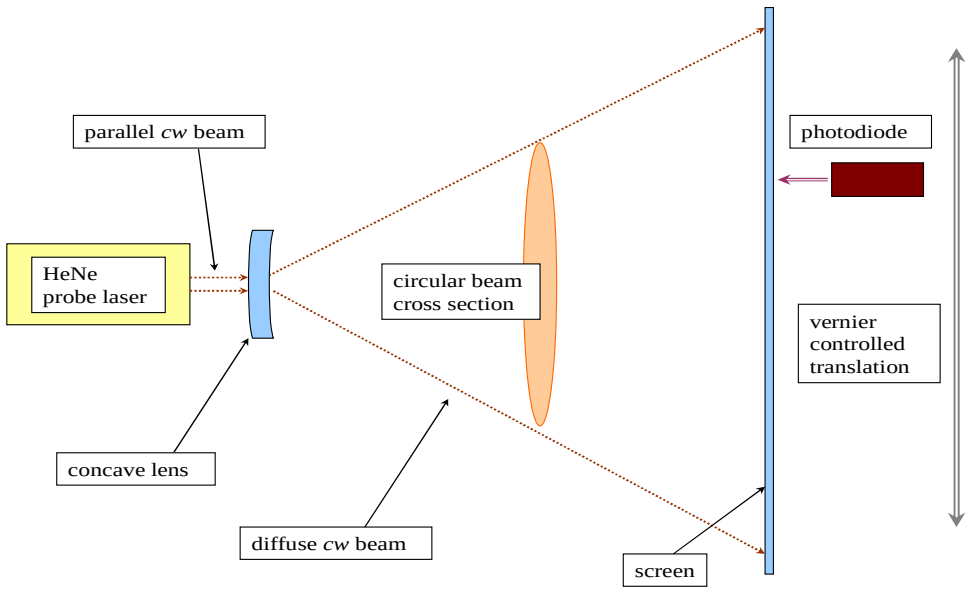

Figure 4.7 Schematic for Measurement of Probe Beam Intensity Profile

Precision of photodiode positioning was maintained by fixing the photodiode to a travelling microscope. A single rotation of the knurled adjustment screw, on an attached vernier scale, translated the photodiode by ~1.16mm across the expanded probe beam image. The increment of photodiode translation for measurement of expanded probe beam intensity was fixed at ~0.58mm i.e. half a complete rotation. Given a linear expansion factor of ~15, between nominal and expanded probe beam dimensions, the equivalent resolution was ~40μm, given nominal probe beam diameter of ~2mm. The measured intensity profile is shown in Figure 4.8.

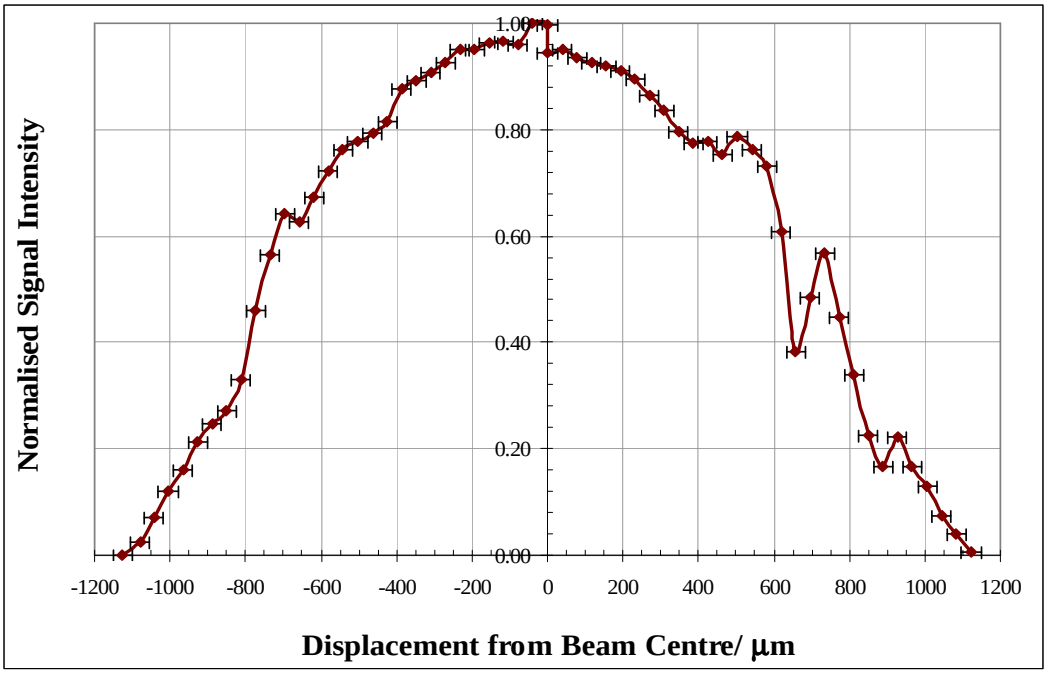

Figure 4.8 Measured Probe Beam Intensity Profile

The probe beam intensity profile was symmetrical, for all intents and purposes. Anomalous data were likely due to inconsistencies in probe laser intensity output.

4.3.2 Probe Beam Deflection Technique

Two configurations of the PBD technique, denoted (I) and (II), were used. Both configurations shared a common experimental set-up, as shown in Figure 4.9.

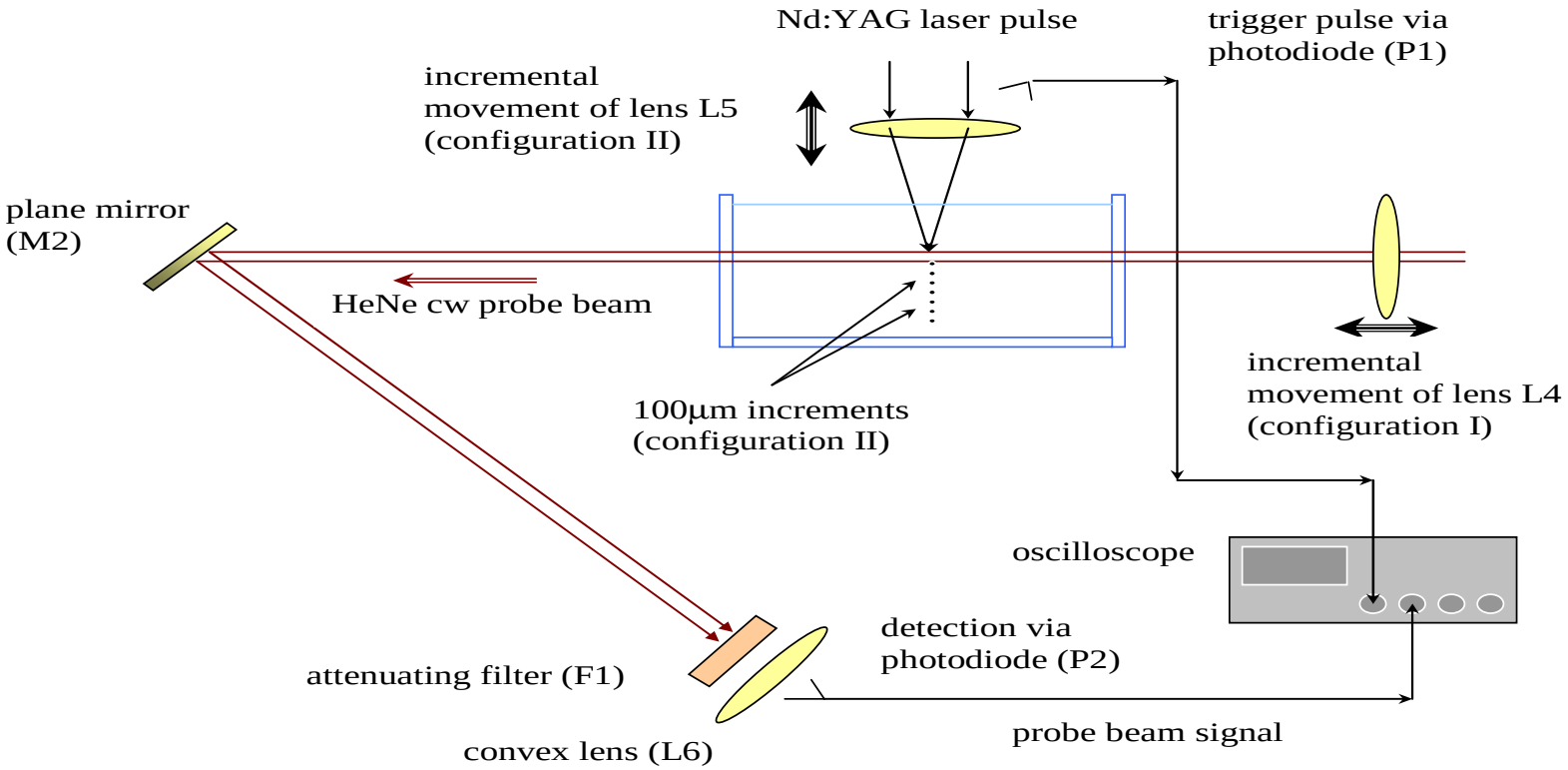

Figure 4.9 Schematic for Probe Beam Deflection Technique: Configurations I & II

The trajectory of the probe beam, in relation to the main components of the PBD apparatus, is shown in the photographs in Figures 4.10 and 4.11.

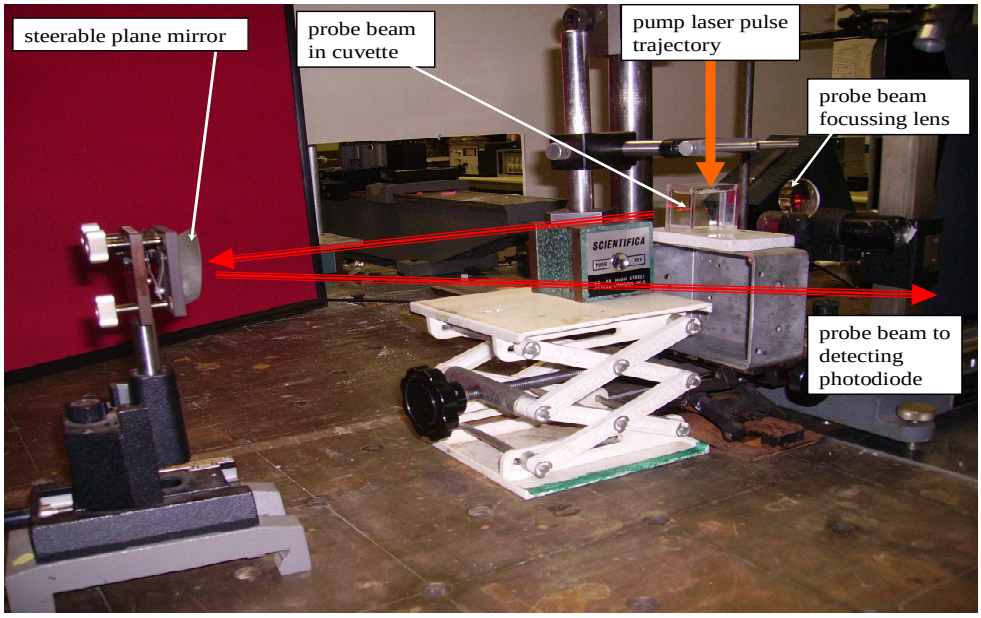

Figure 4.10 Photograph Showing Sample Cuvette and Probe Beam Trajectory

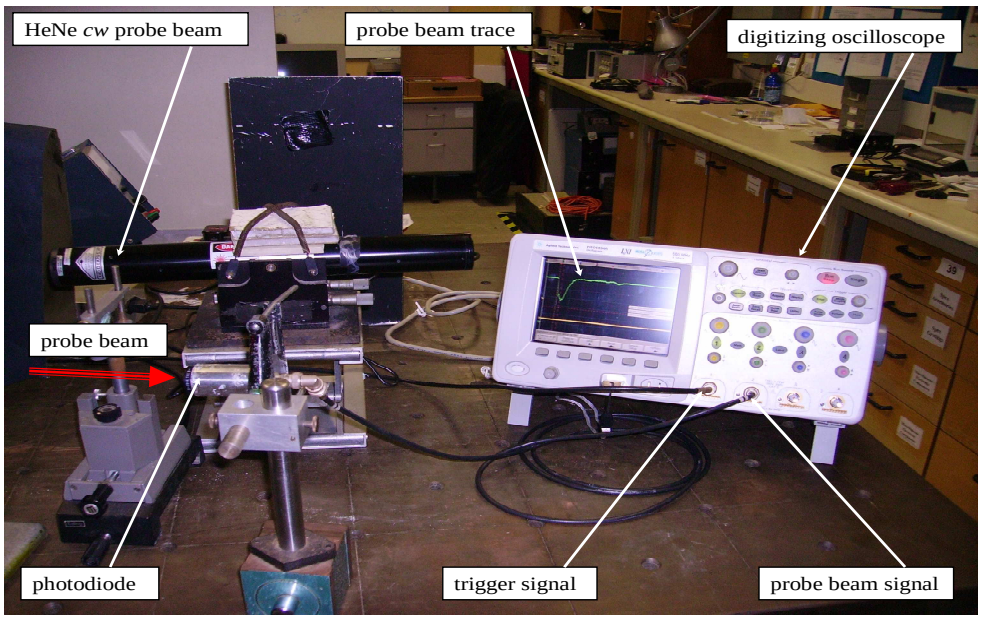

Figure 4.11 Photograph Showing Typical Probe Beam Signal Profile

For the PBD configuration (I), the focus of the pump laser pulse was fixed to coincide with the centre of the probe laser beam. The probe beam is initially focused by a convex lens (L4) into the pump laser focal volume. By incrementing the horizontal position of this lens, parallel to the probe beam axis, the unfocussed diameter of the probe beam in the plane of the focused pump laser pulse was increased. At a critical displacement of this lens, the defocused probe beam diameter exceeded the maximum diameter of the primary cavitation bubble. The relative decrease in transmitted probe beam signal intensity allowed inferences to be made regarding spatial and temporal evolution of the primary cavitation bubble.

In the alternative configuration (II) of the PBD technique, the trajectory of the probe beam was fixed in the horizontal plane of the optical bench, orthogonal to the (vertical) direction of the Nd:YAG pump laser pulse. The pulse laser pulse was focused by a convex lens (L5) fixed in the horizontal plane. The separation between the pump laser focus and the fixed probe beam was altered incrementally via a vernier screw thread, with resolution of 10μm. The pump laser focus position was varied incrementally above and below the probe beam axis, for comparison of the effect of bubble expansion on the probe beam signal. For each separation between pump laser focus and probe beam axis, the expanding bubble wall crossed the probe beam after a finite time delay. In the interval between the occlusion of the probe beam by the expanding bubble, and the bubble wall re-crossing the probe beam on bubble collapse, the probe beam was subject to a transmitting medium with refractive index significantly different from that of the unaffected distilled water. The change in refractive index induced deflection in the probe beam trajectory, which allowed inferences to be made regarding spatial and temporal bubble dynamics.

For both configurations of the PBD technique the probe beam signal was detected by photodiode (P2 - Centronic BPX65 series). Temporal variation in probe beam signal intensity was displayed on a digitizing oscilloscope (Agilent DSO 5054A). To avoid

saturation of the photodiode by the transmitted probe beam, an attenuating filter (F1) was introduced into the probe beam path. A convex lens (L6) was used to focus the probe beam signal onto the photodiode (P2).

The oscilloscope was triggered synchronously with the emission of pump laser pulse via a second photodiode (P1 - Centronic BPX65 series), which detected laser light reflected from the upper surface of the focusing convex lens (L5). This allowed temporally accurate measurements to be made of changes in probe beam intensity, and allowed inferences regarding the dynamics of the expanding and contracting bubble wall. A typical PBD trace is shown in Figure 4.12.

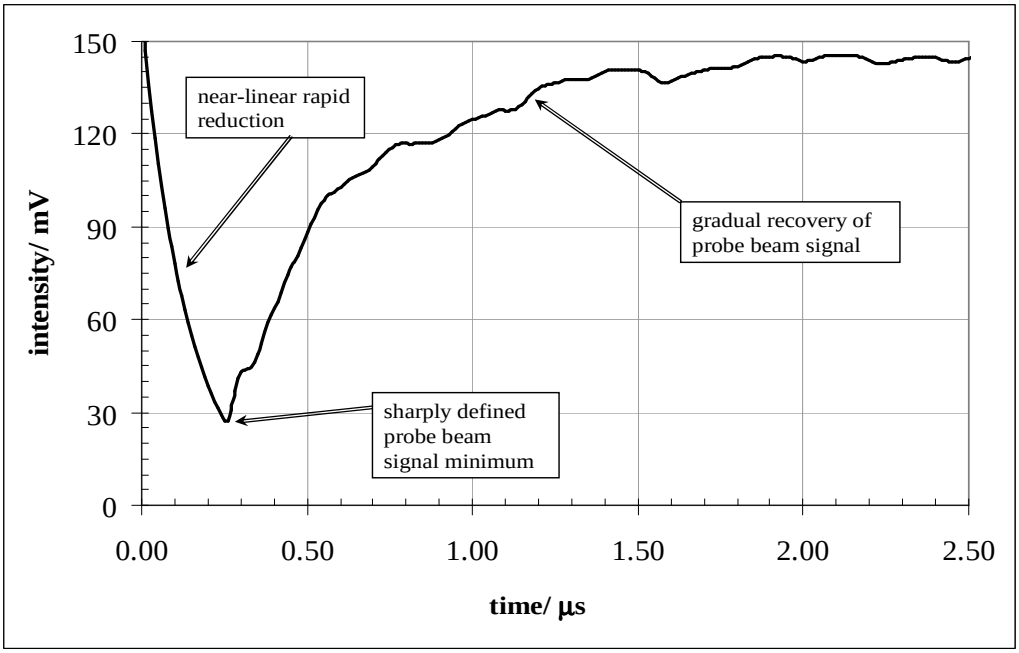

Figure 4.12 Typical Probe Beam Deflection Profile after Passage through Cavitation Bubble

From the recorded probe beam intensity profiles three fundamental parameters were measured: *i*. maximum change (decrease) in probe beam signal intensity; *ii*. time taken

for probe beam signal to recover to a pre-set percentage of its initial (undisturbed) intensity; and, *iii*. time taken for initial deflection of probe laser beam. By careful interpretation of these measurements the following characteristics were inferred: *i*. maximum primary bubble radius; *ii*. primary cavitation bubble lifetime; and, *iii*. bubble wall rate of expansion.

4.3.3 High Speed Imaging Technique

High speed imaging (HSI) was the complementary method used for characterization of laser induced cavitation. In this technique the spatial and temporal behaviour of the primary cavitation bubble were directly measured. The experimental layout of this technique is shown schematically in Figure 4.13. The camera used (Vision Research Phantom v12.1) had a maximum frame rate of ~1x10^6 frames per second (fps) and a 1280Hx800V CMOS sensor. Control of the camera was via bespoke software installed on a dedicated laptop.

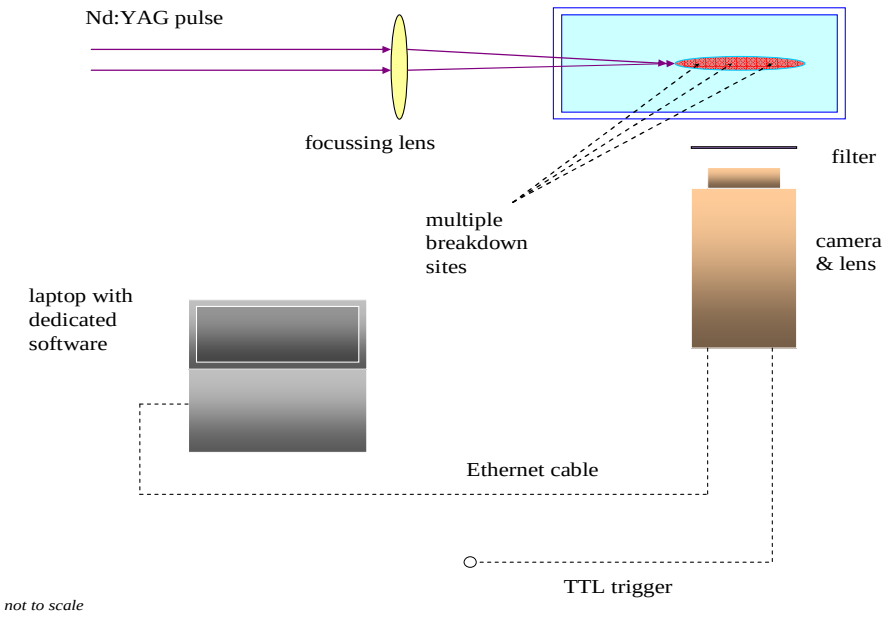

Figure 4.13 Schematic for High Speed Imaging Technique

The layout for this technique, indicating the positioning of principal elements of apparatus, is shown in the photograph in Figure 4.14.

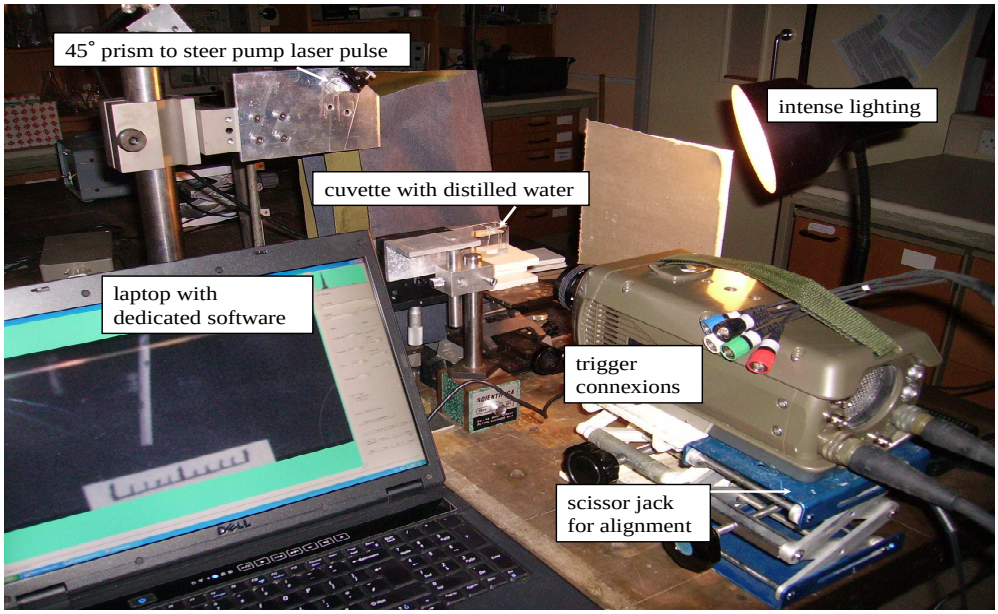

Figure 4.14 Photograph of High Speed Imaging Set-up

The key parameter for this technique was frame rate, the reciprocal of which allowed estimation of interval between frames. The original cine data (.avi format) was converted, using post-processing software, to individual frames (.bmp format). Due to the finite memory capacity of the camera imaging hardware, there was an inverse relationship between frame rate and size of individual images. Given the timescale of the primary cavitation bubble (in the order of hundreds of μs), a frame rate in the order of $5x10^5$ fps was preferred. This frame rate, however, generated images lacking sufficient contrast to differentiate with confidence between bubble wall and image background. The highest frame rate allowing sufficient resolution was ~$5x10^4$ fps, corresponding to an interval between images of ~20μs. Improved contrast was provided by illumination from a standard desk lamp (60W).

4.4 Optimization of Experimental Parameters for Increasing LIBS Sensitivity

For laser-induced plasma in the liquid bulk, 'quenching' is known to reduce the overall time scale for radiative emission processes. The intense *Bremsstrahlung* was typically emitted on a timescale in the order of 100s of nanoseconds. Atomic line emission from contaminant species was observed on a significantly longer timescale of typically several microseconds. By opening the time gate for detection after the *Bremsstrahlung* emission had reduced to a negligible level, and operating the gate for a duration sufficient to capture the majority of atomic line emission, LIBS signal-to-noise ratio (S/N) was increased.

The most critical LIBS temporal variables are delay time and gate width. The former equates to the delay between plasma formation and the electronic opening of the detection gate. The latter equates to the period for detection and accumulation of emitted radiation. Figure 4.15 is a sketch representing an idealized emission profile.

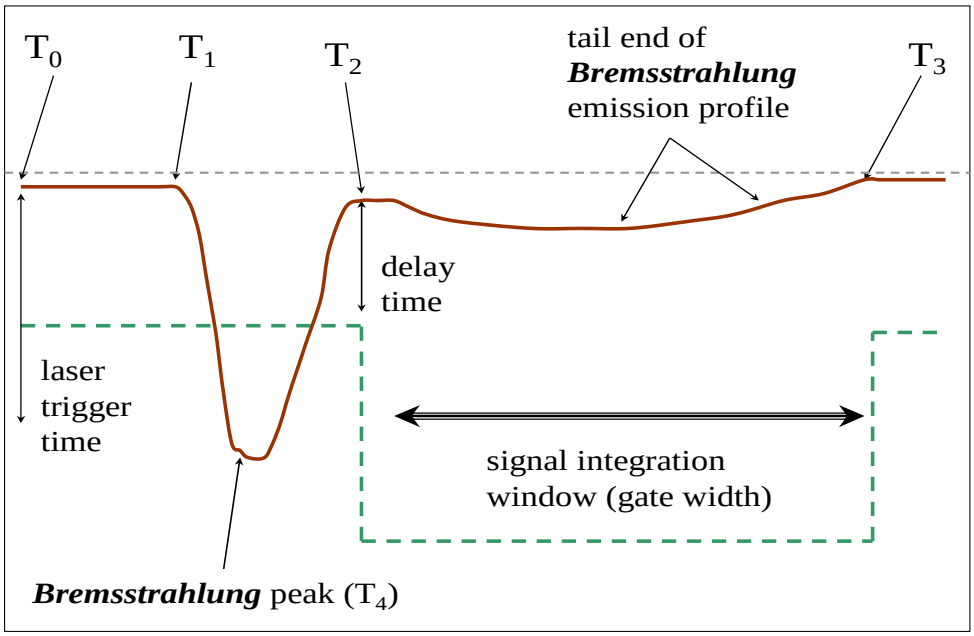

Figure 4.15 Sketch of an Idealized Representation of the Temporal Gating Sequence

Duration of emission profiles was referenced to a trigger pulse, taken to be the 'zero' time, and represented in Figure 4.16 by T_0. This is the point at which the laser flash lamp was initiated and was synonymous, for all intents and purposes, with plasma formation in the liquid bulk. The leading edge of the plasma emission, characterized by a *Bremsstrahlung* profile of rapidly increasing intensity, was recorded after a delay represented by T_1. The interval between T_0 and T_1 was typically in the order of 100s of ns, for plasma formation in the liquid bulk. The interval between T_1 and T_2 represented that period during which the majority of *Bremsstrahlung* emission occurred. The maximum intensity of the *Bremsstrahlung* profile occurred after a time represented by T_4. For times in excess T_2 the intensity of *Bremsstrahlung* had reduced to a negligible level. In the interval between T_2 and T_3 a significant proportion of detected radiation originated from atomic line emissions, line emissions from relaxation of molecular vibration manifolds, and relatively weak *continuum* emission from the cooling plasma. In order to prevent the majority of *Bremsstrahlung* emission from impinging upon the detector the delay time (t_d) was typically set to match T_2. In addition the gate width (t_g) was ideally matched to the period between T_2 and T_3 to maximize detection of radiation from atomic line emission.

The other important LIBS experimental parameter was the wavelength range over which radiation was dispersed by the monochromator grating, and the increment at which the grating was advanced ('stepped'). Estimation of S/N required a significant spectral range from which background signal mean and standard deviation calculations were statistically valid. The current research used a spectral range whereby the target line emission wavelength e.g. Na(I) at 589.00nm, was positioned one third of the way between the lower and upper limits of the spectral window. For the current research the spectral increment (grating 'step') was typically set at 0.05nm (0.5Å).

4.5 Alternative Techniques for Increasing LIBS Sensitivity

4.5.1 Electronic Time Gating

The 'conventional' technique used for discriminating discrete atomic emission lines from continuum background noise (*Bremsstrahlung*) was temporal gating. This entailed configuring the detection apparatus to selectively sample the emitted radiation envelope after a pre-determined time delay, beyond which *Bremsstrahlung* emission had reduced to negligible levels of intensity. To maximize detection of discrete atomic line emission the photo-multiplier tube (PMT) was exposed for a pre-set time interval. This temporal gate was activated by applying high tension (HT) to the PMT during this time period. The rapid application of HT generated electromagnetic noise interference in the detection system, which contributed to the overall noise budget.

4.5.2 Experimental Set-up for Mechanical Signal Gating

The 'mechanical gating' technique involved the recording of two independent LIBS spectra for each experimental run. The first spectrum was conventionally gated, and recorded a peak for the target atomic emission line, from which a S/N was calculated. A second spectrum was captured in the absence of plasma generation in the liquid medium, by physically blocking the laser pulse with the mechanical chopping blade. This spectrum represented the background signal profile for the chosen spectral waveband. By subtracting the latter spectrum from the former a 'background subtracted' LIBS spectrum was generated.

The experimental set-up for this work was practically the same as that previously described (Figure 4.1). A mechanical chopper was incorporated between the laser aperture and a plane mirror positioned above the sample cuvette. A fixed pulse energy of ~35mJ induced dielectric breakdown in the focused beam waist. Plasma collection and detection has been previously described and illustrated (Figures 4.2, 4.6 & 4.7). The location of the mechanical chopper between the Nd:YAG laser aperture and plane mirror is shown in Figure 4.16.

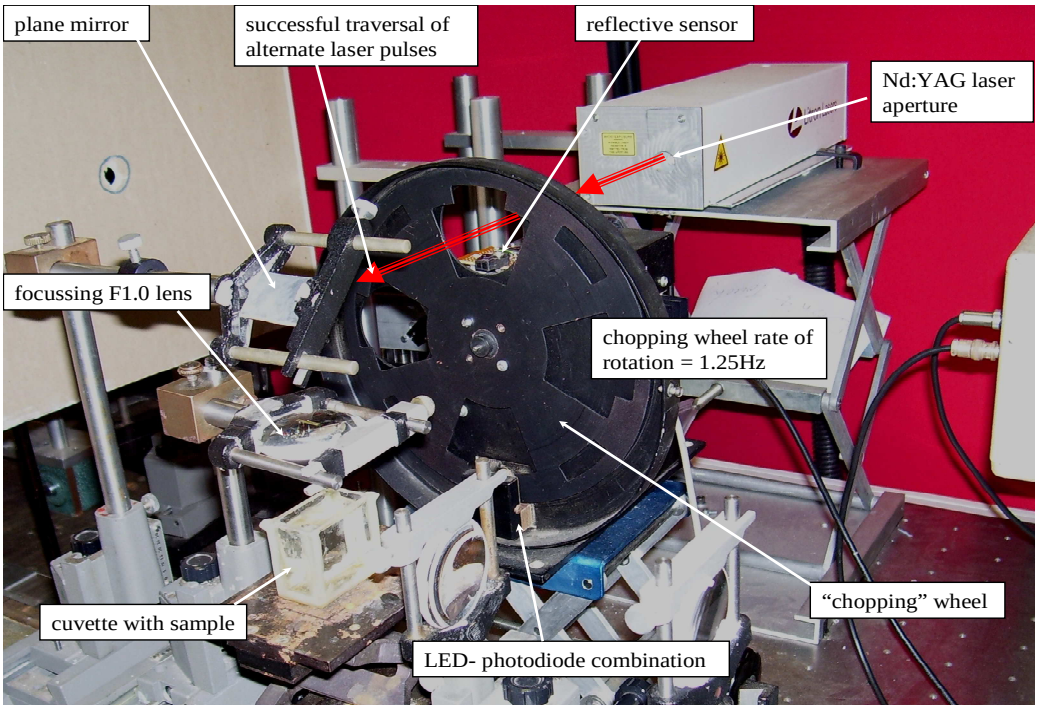

Figure 4.16: Photograph of the Mechanical Gating Set-up Showing Positioning of Chopping Apparatus Relative to Sample

The same Nd:YAG laser was used operating in a repetitive pulse mode. The pulse repetition rate was synchronized with the mechanical chopper rotation rate by means of a photodiode–LED sensor combination. This was placed at the lower periphery of the chopping wheel, and provided the trigger signal for the laser flash lamp. Eight signals per rotation were generated corresponding to the eight apertures coincident with the position of this sensor combination. The chopping wheel rate of rotation was fixed at 1.25Hz, which set the laser pulse repetition rate to 10Hz.

A reflective sensor, placed toward the centre of the chopping wheel, generated four signals per rotation. These signals corresponded to the four apertures coincident with the position of this sensor. For the fixed chopping wheel rate of rotation (1.25Hz) this sensor generated signals at 5Hz. Signals were 'high' for blocked pulses, corresponding to the

absence of plasma formation in the liquid medium. Alternate signals were 'low' for pulses successfully traversing an aperture, corresponding to plasma formation in the liquid bulk. These 'high' and 'low' signals were in sympathy with the duplex mode of the in-house software. This allowed simultaneous accumulation of background and conventionally gated spectra.

The main practical consideration for the current research was to set the maximum practicable pulse repetition rate at 10Hz. The *rationale* behind this upper limit was minimization of perturbations in the target liquid medium due to the mechanical effects of cavitation. An interval of 100ms between consecutive plasma formation in the liquid bulk was sufficient to reduce heterogeneities in laser pulse focusing to a negligible level.

Preliminary studies were carried out with plasma generated at the surface of an Al alloy target, with radiation propagating in air at STP (1atm pressure and ambient temperature of ~293K). The target emission line wavelength was 396.15nm, which dictated the use of the VIS grating with resolution of 1200 grooves mm^{-1}.

Initial liquid bulk sample presentation studies were undertaken with sodium chloride solution at fixed concentration of 10^3ppm, using the Na(I) emission line at 589.00nm. Spectrometer entrance slit width and PMT voltage were fixed at 300μm and ~1.8kV, respectively. Signal: noise ratio (S/N) for the target emission lines were calculated via *eqn.[3.14]*. Improvement in S/N was demonstrated by comparison of conventionally gated and background subtracted spectra.

4.5.3 Experimental Set-up for Plasma Blocking Technique

For surface generated plasma from a solid target the majority of *Bremsstrahlung* emission was observed to originate in a compact region directly above the target surface. The *Bremsstrahlung* intensity from this region was sufficient to over-expose the photo-detector in the time period prior to the activation of the temporal gate. The technique of

'plasma blocking' involved placing a rigid barrier between the principal *Bremsstrahlung* emission site and the collection optics. By incrementally increasing the height of the upper horizontal edge of this barrier, the proportion of intense *Bremsstrahlung* emission incident at the spectrometer entrance slit was gradually reduced. The barrier was positioned as close to the leading edge of the target as possible, without fouling the edge of the barrier.

Preliminary experiments were performed with an aluminium alloy target with plasma generation at the target leading edge. The experimental set-up, showing the position of the physical barrier in relation to the leading edge of the aluminium alloy target, is illustrated in Figure 4.17.

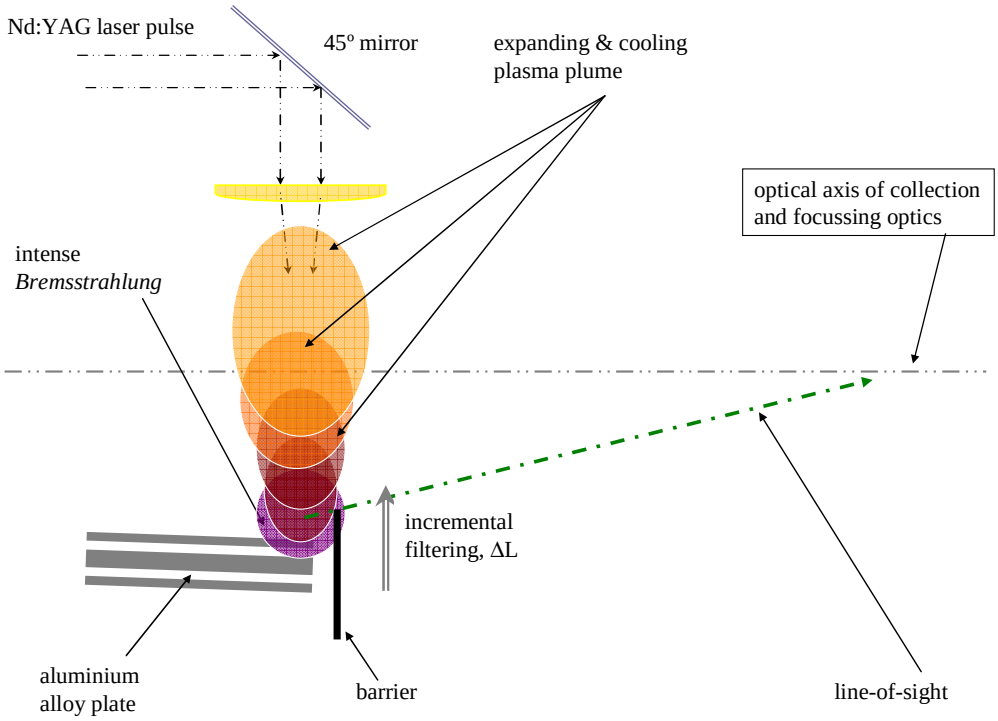

Figure 4.17: Schematic for Plasma Blocking Technique for Reduction in *Bremsstrahlung* Emission

The position of the physical barrier, in relation to the aluminium alloy target and the collection optics, is illustrated in Figure 4.18.

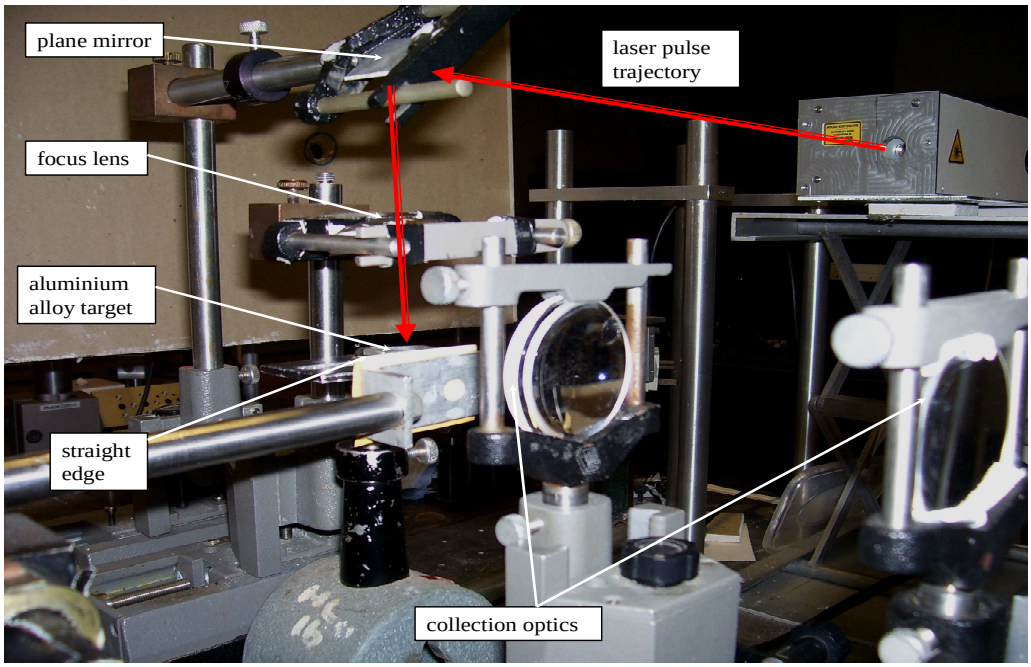

Figure 4.18: Photograph Showing Positioning of Physical Barrier in Relation to Target and Optics

A baseline height for the upper edge of the physical barrier was established, based on the criterion that a reduction in this height was observed to have no significant effect on the recorded *Bremsstrahlung* emission profile. The reciprocal criterion was that an increase in height from this baseline position, commensurate with blocking an increased proportion of the intense *Bremsstrahlung* source, caused a measureable change in recorded *Bremsstrahlung* emission profile. The height of the upper horizontal edge of the barrier was incremented (ΔL) with a vernier scale. The height was incremented by $\sim{}^{1}/_{16}$ of a complete rotation of a knurled adjustment screw, which corresponded to an increase of ~43±4μm. This was calculated by previously measuring the translation in the vertical plane (~6.9mm) as a result of 10 complete rotations of the adjustment screw.

The effect of ‘plasma blocking’ on *Bremsstrahlung* emission was characterised with respect to changes in magnitude of specific features of the *Bremsstrahlung* emission profile. These features were: *i*. maximum *Bremsstrahlung* emission intensity; *ii*. time elapsed between laser trigger and maximum *Bremsstrahlung* intensity; and, *iii*. full width at half maximum (FWHM) of the *Bremsstrahlung* emission profile. Similarly the effect of ‘plasma blocking’ on line emission was characterised with respect to changes in magnitude of specific features of the line emission profile. These features were: *i*. maximum line emission intensity; *ii*. time elapsed between laser trigger and maximum emission line intensity; *iii*. full width at half maximum (FWHM) of the line emission profile; and, *iv*. normalized equivalent energy encapsulated within the line emission profile.

A potential problem was anticipated due to material ablation at the leading edge of the aluminium alloy target. The formation of a crater of significant depth, would cause inconsistency in the proportion of *Bremsstrahlung* emission captured by the collection optics. To overcome this problem the aluminium alloy target was translated by a pre-set distance, following exposure to a specific number of laser shots. The direction of translation was mutually orthogonal to both the laser pulse trajectory and the axis of the collection optics. By refreshing the target surface in this way, variation in the proportion of captured *Bremsstrahlung* emission was minimized. The increment of target translation was set at an order of magnitude greater than the calculated focussed laser beam waist. For the parameters used (wavelength = 1064nm, nominal beam diameter = 5mm, lens focal length = 50mm) the focussed beam waist was estimated to be ~26μm. The separation between new laser focus sites was therefore set at ~260μm. This was sufficient to overcome the problem of inconsistency in signal detection from laser generated craters in the sample surface.

An upper limit for the number of laser shots incident upon each new target site was estimated from a consideration of the bulk physical properties of the aluminium alloy

target (specific heat capacity and melting point). The limiting assumption was made that incident laser pulse energy was entirely manifest in removal of target material. The mass of ablated material was estimated to be ~9μg for each 50mJ laser pulse. By assuming a cylindrical volume of ablated material, with circular cross-section of diameter 10x the nominal focussed beam waist, the depth of ablated material was estimated to be ≤ 50μm for each laser pulse. Based upon these calculations each new plasma formation site was exposed to 50 laser pulses.

THIS PAGE INTENTIONALLY BLANK

Chapter Five

RESULTS AND ANALYSIS

"Once and for all, I wish to record my unbounded admiration for the work of the experimenter in his struggle to wrest interpretable facts *from an unyielding Nature who knows so well how to meet our theories with a decisive* No *– or with an inaudible* Yes*."*
Hermann Weyl

The results and analysis of a series of individual experiments are sequentially described in this chapter, as follows: *i*. effect of scattering centre concentration on dielectric breakdown threshold; *ii*. spatial and temporal characterization of laser induced cavitation bubble; *iii*. demonstration of the data averaging technique for smoothing of *Bremsstrahlung* profile; *iv*. dependence of *Bremsstrahlung* emission on incident photon flux and analyte scattering concentration; *v*. optimization of various LIBS experimental parameters to achieve maximum LIBS sensitivity; *vi*. application of optimized LIBS experimental parameters for detection of weakly emitting metallic species in aqueous solution; *vii*. demonstration of alternative techniques for improving LIBS sensitivity.

5.1 Dependence of Dielectric Breakdown Threshold on Scattering Centre Concentration

5.1.1 Experimental Procedure

The layout for this experiment has been previously shown (see Figure 4.5). In this configuration the laser pulse train was focussed vertically into the water bulk. At the outset laser pulse energy was selected to be sufficient to provide consistent shot-to-shot dielectric breakdown of the distilled water target. Pulse energy was reduced at a fixed increment, and the number of audible shockwaves (an indication of dielectric breakdown) recorded for 100 laser pulses. Pulse energy was reduced to a level at which no dielectric breakdown was observed, over a series of 100 laser pulses. The process was repeated, with the same experimental parameters, for a tap water sample.

Probability of dielectric breakdown was calculated by dividing the number of breakdown events, as indicated by the emission of an audible shockwave, by the total number of delivered laser pulses i.e. 100. The dielectric breakdown threshold was defined as that irradiance at which there is a 50% chance of generating an audible shockwave. Laser irradiance was calculated by dividing pulse power by the focussed laser pulse waist area, for pulse duration fixed at 7ns. In the idealized case of a Gaussian pulse energy profile the waist area would be ~$5.3 \times 10^{-6} cm^2$, based upon estimated diffraction limited spot size (d_{spot}) of ~26μm (lens of focal length = 50mm, laser beam diameter = 5mm, wavelength = 1064nm).

5.1.2 Dependence of Dielectric Breakdown Probability on Laser Irradiance

Probability of dielectric breakdown was plotted against delivered laser irradiance, for samples of distilled and tap water, as shown in Figure 5.1.

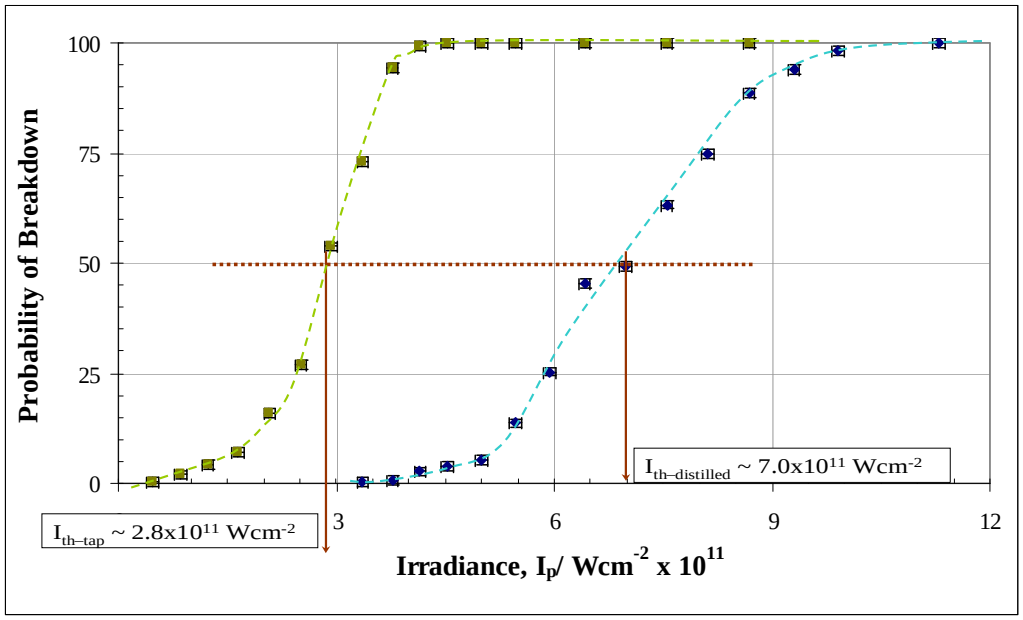

Figure 5.1: Probability of Dielectric Breakdown *vs.* Laser Irradiance for Distilled and Tap Water Samples

As indicated Figure 5.1, dielectric breakdown thresholds for the distilled water ($I_{th\text{-}distilled}$) and tap water ($I_{th\text{-}tap}$) samples were estimated to be $7.0x10^{11}Wcm^{-2}$ & $2.8x10^{11}Wcm^{-2}$, respectively.

The same experimental procedure was carried out with 50ppm, 5ppm and 500ppb $NaCl_{(aq)}$ samples i.e. covering two orders of magnitude for concentration. Based on the criterion of an audible shockwave, the percentage probability of dielectric breakdown was calculated, for laser pulse energy in the range from 22.0mJ to 37.0mJ. These data are presented in Table 5.1.

Table 5.1: Probability of Dielectric Breakdown as a Function of Laser Pulse Energy and Irradiance: $NaCl_{(aq)}$ Samples

Laser Pulse Parameters		Probability (%) of Dielectric Breakdown		
Energy/ mJ	Irradiance/ Wcm^{-2} ($x10^{11}$)	500ppb	5ppm	50ppm
22.0	5.93	23	18	26
24.0	6.47	36	34	49
26.5	7.14	51	49	62
29.0	7.82	60	64	73
31.5	8.49	60	73	87
34.0	9.16	67	81	95
37.0	9.97	70	92	98

Probability of dielectric breakdown as a function of delivered laser irradiance is shown in Figure 5.2. Data are included for the three concentrations of $NaCl_{(aq)}$ used.

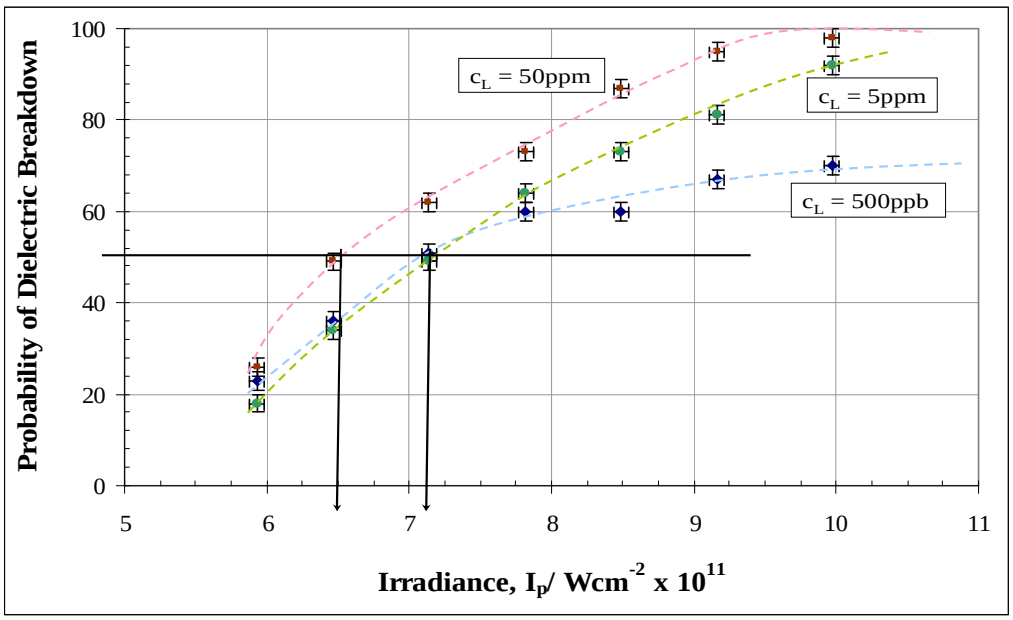

Figure 5.2: Probability of Dielectric Breakdown *vs*. Laser Irradiance for Aqueous Sodium Chloride Samples

From the data shown in Figure 5.2, and using the same 50% probability criterion for dielectric breakdown, a dielectric breakdown threshold of 6.5×10^{11} Wcm^{-2} was estimated for $NaCl_{(aq)}$ at 50ppm concentration. An equivalent dielectric breakdown threshold of 7.2×10^{11} Wcm^{-2} was estimated for $NaCl_{(aq)}$ at both 5ppm and 500ppb concentrations. Dielectric breakdown threshold estimates for $NaCl_{(aq)}$ samples are compared to equivalent data for distilled and tap water in Table 5.2.

Table 5.2: Summary of Dielectric Breakdown Thresholds

Samples	Water		Concentration of $NaCl_{(aq)}$		
	Distilled	Tap	500ppb	5ppm	50ppm
Threshold/ Wcm^{-2} x 10^{11}	7.0	2.8	7.2	7.2	6.5

5.1.3 Analysis of Calculated Dielectric Breakdown Thresholds

The estimated dielectric breakdown threshold for tap water was ~60% lower than that for distilled water. A further quantitative comparison was made between the tap and distilled water samples by measuring (from Figure 5.1) the range of irradiance, ΔI_p, which corresponded to the 25^{th} and 75^{th} percentiles for dielectric breakdown. Values of ΔI_p were measured at $2.2 \times 10^{11} Wcm^{-2}$ & $0.9 \times 10^{11} Wcm^{-2}$ for distilled and tap water, respectively. These values represent a reduction of ~59% for tap water compared to distilled water. The correspondence between these two comparison criteria i.e. dielectric breakdown threshold and $25^{th}/75^{th}$ percentile range for delivered irradiance, were indicative of a single factor influencing dielectric breakdown in the two target media i.e. concentration of scattering centres.

Dielectric breakdown thresholds for aqueous sodium chloride were not significantly different to the breakdown threshold for the distilled water sample. Further, they demonstrated a weak correlation with analyte concentration, for concentrations representing a range of two orders of magnitude i.e. between 50ppm and 500ppb.

5.2 Dynamics of Laser Induced Cavitation in Liquid

5.2.1 Preamble

The aim of this experimental work was to investigate the dynamics of the formation and expansion of laser induced cavitation bubbles in the liquid bulk. The two independent techniques used have been previously described i.e. probe beam deflection (PBD) and high speed imaging (HSI). It was envisaged that by characterizing the spatial and temporal properties of the cavitation bubble, additional pulses from the ionization (pump) laser may be targeted within the bubble volume. The required pulse repetition rate to realise this aim is a function of the primary cavitation bubble oscillation period. Information regarding the buoyancy of the bubble was also required, in order to facilitate accurate aiming of subsequent laser pulses.

5.2.2 Characterization of Cavitation Bubble Dynamics Using Probe Beam Deflection Technique

Two experimental configurations (I & II) were used in the application of the PBD technique. The set-up applicable to both configurations has been previously described in Figures 4.10, 4.11 & 4.12.

a. Experimental Configuration I

Using the principle of ray optics, the probe beam diameter in the focal plane of the pump laser, D*, referred to hereafter as 'de-focussed probe beam diameter', was estimated as illustrated in Figure 5.3. Probe beam diameter, D, was ~2000μm, based on the measured probe beam intensity profile, as previously reported (see Figure 4.9). Focal length of the convex lens, f, was measured at 100mm.

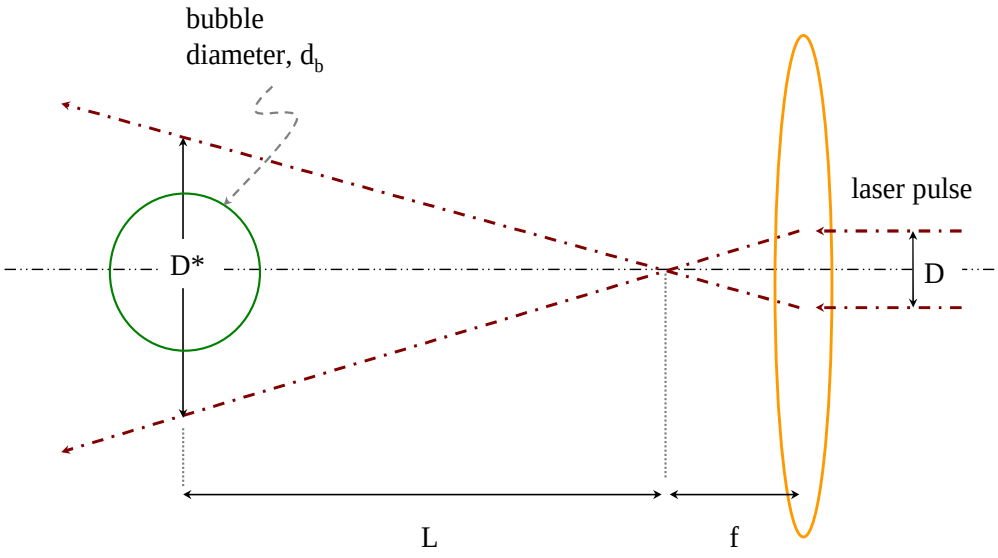

Figure 5.3: Geometry for Estimation of De-focussed Probe Beam Diameter

The convex lens was initially positioned such that the focal point of the lens was coincident with the centre of the cavitation bubble. The separation, L, between convex lens focal point and the cavitation bubble centre was increased in increments of 5mm. By using a vernier scale, the precision in L was ±10μm (0.01mm). For each value of L, de-focussed probe beam diameter, D*, was calculated, as follows:

$$D^* = L \cdot (D / f) \qquad \ldots \quad \ldots \quad [5.1]$$

The decrease in recorded probe beam intensity, ΔS_{pb}, was anticipated to be proportional to the relative amount of blocking of the probe beam by the expanding cavitation bubble. Based upon this hypothesis, for those values of bubble diameter, d_b, in excess of de-focussed probe beam diameter, D*, measured values of ΔS_{pb} would tend to a maximum. This would correspond with negligible transmission of the probe beam through the cavitation bubble volume. Based on *eqn(5.1)* it follows there will exist a lower limit of separation, L, for which ΔS_{pb} will tend to a maximum. By interpreting the decrease in probe beam intensity, ΔS_{pb}, for higher values of separation, L, the maximum bubble diameter, d_b, was inferred.

Temporal histories of probe beam signal intensity, for representative values of separation, L, are shown in Figure 5.4. A complete record of probe beam deflection traces, for the full range of L used, is presented at Appendix V.

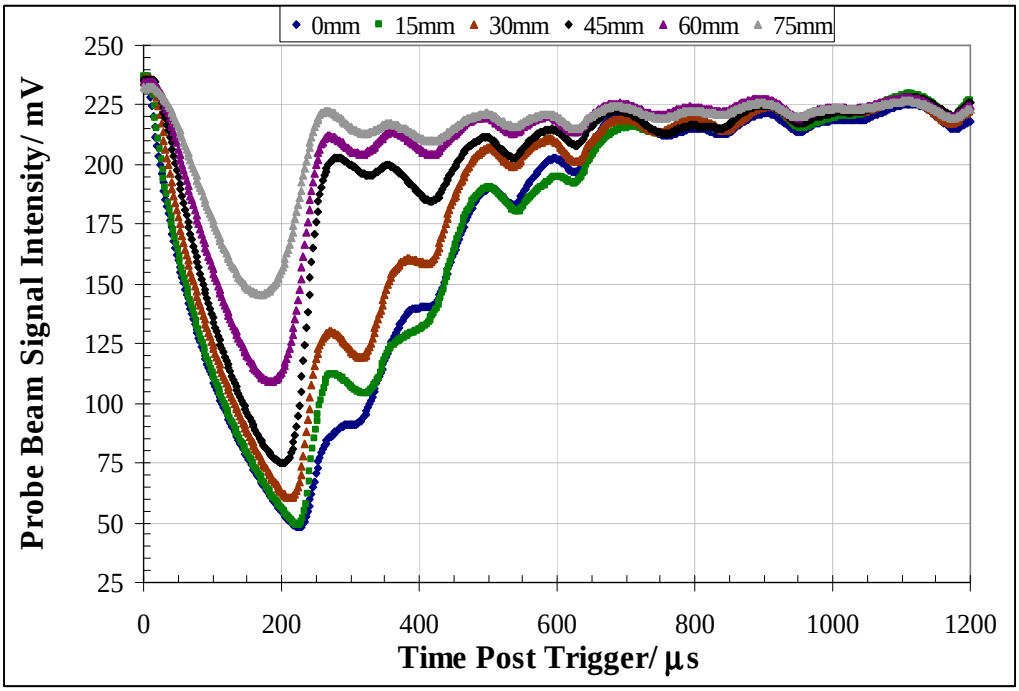

Figure 5.4: Probe Beam Deflection Traces for L = 0, 15, 30, 45, 60 & 75mm

Data for decrease in probe beam intensity, ΔS_{pb}, as a function of de-focussed probe beam diameter, D*, and separation, L, are summarized in Tables 5.3a & 5.3b. NB. For L = 0 the value of D* based on *eqn.[5.1]* is zero. A more reasonable estimate for D* is given as the diffraction limited spot size, d_{spot}, for the specific lens focal length (f), beam width (D) and wavelength (λ) used. For the present research f = 100mm, D = 2mm and λ = 632nm, resulting in an estimated value for d_{spot} of ~77µm (0.08mm).

Table 5.3a: Reduction of Probe Beam Intensity with Increasing De-focussed Probe Beam Diameter: 0 ≤ L ≤ 45mm

L/ mm (±0.01mm)	D*/mm (±10%)	ΔS_{pb} /mV (±3mV)	Normalized ΔS_{pb} (±5%)
0	0.08[a]	191	1.00
5	0.10	190	0.99
10	0.20	186	0.97
15	0.30	190	0.99
20	0.40	186	0.97
25	0.50	184	0.96
30	0.60	177	0.93
35	0.70	172	0.90
40	0.80	165	0.86
45	0.90	164	0.86

[a]: diffraction limited spot size ~ 77μm

Table 5.3b: Reduction of Probe Beam Intensity with Increasing De-focussed Probe Beam Diameter: 50 ≤ L ≤ 90mm

L/ mm (±0.01mm)	D*/mm (±10%)	ΔS_{pb} /mV (±3mV)	Normalized ΔS_{pb} (±5%)
50	1.00	159	0.83
55	1.10	149	0.78
60	1.20	135	0.71
65	1.30	128	0.67
70	1.40	112	0.59
75	1.50	89	0.47
80	1.60	81	0.42
85	1.70	34	0.18
90	1.80	32	0.17
95	-	-	-

Normalized reduction in transmitted probe beam intensity, as a function of de-focussed probe beam diameter, is shown at Figure 5.5.

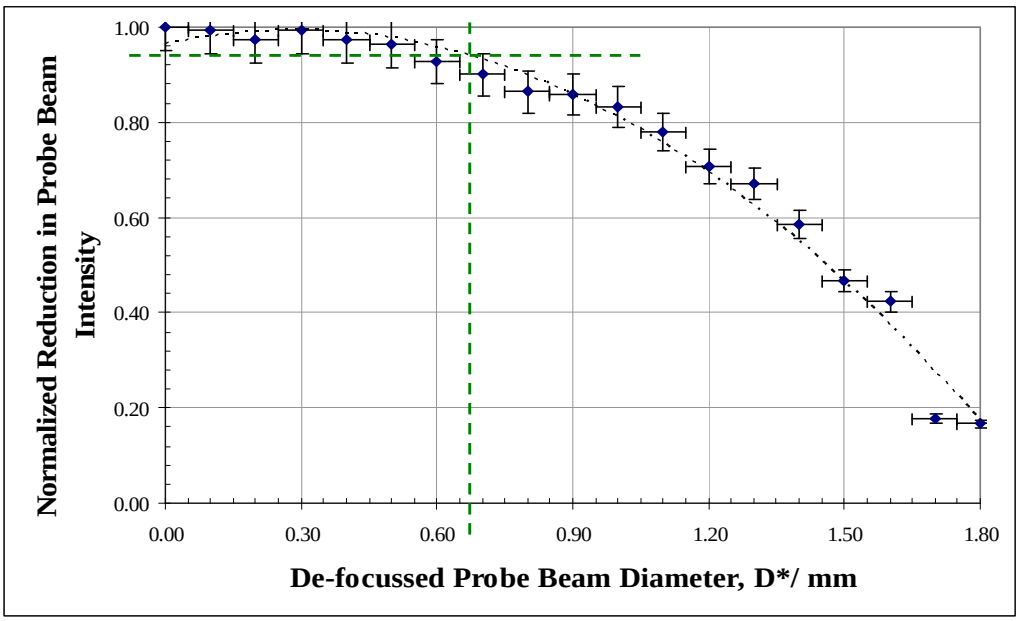

Figure 5.5: Dependence of Decrease in Probe Beam Intensity on De-focussed Probe Beam Diameter

The reduction in probe beam intensity tended toward a maximum at the limit where maximum bubble diameter exceeded the de-focussed probe beam diameter. Deviation from this maximum value indicated that de-focussed probe beam diameter had exceeded maximum bubble diameter. Despite using a fixed experimental parameter set (pulse energy, repetition rate, data average number), variations in maximum bubble diameter were anticipated. Such variations were attributed to deviations in laser pulse energy from the pre-set (and fixed) value, as well as variation in focussed laser beam waist due to inconsistencies in properties of the water bulk. To account for these inconsistencies a 95% criterion was invoked for estimation of maximum bubble diameter. According to this criterion maximum bubble diameter, d_b, was defined as numerically equal to de-focussed probe beam diameter, D*, which corresponded to a 95% reduction in probe

beam signal intensity. Application of this criterion to the data shown in Figure 5.5, enabled an estimate to be made for maximum bubble diameter, d_b, of 0.67mm ±10%.

Interpretation of the temporal probe beam deflection traces (see Figure 5.4) provided insight into bubble lifetime, τ_b. Examination of the probe beam deflection traces revealed a significant variation in signal intensity following maximum deflection. This phenomenon was typically observed in the period 500μs to 1200μs after bubble formation. Due to the limited measurement precision imposed by this phenomenon, a criterion of recovery to 75% of unaffected signal intensity was used for estimation of bubble lifetime. Based on this criterion, and an unaffected probe beam intensity of ~236mV, the bubble duration was estimated to be 460±30μs.

b. Experimental Configuration II

The probe beam was fixed in the horizontal plane, and initially aligned to the centre of the cavitation bubble i.e. the focal point of the lens focussing the Nd:YAG pulse train. The separation parameter, z, was defined as the distance between the bubble centre and the central axis of the probe beam. The separation, z, was adjusted at fixed increments, by altering the vertical position of the pump laser focus. Reduction in probe beam signal intensity (ΔS_{pb}) was recorded for each separation. This was carried out for bubble centre above and below the central axis of the probe beam. Assuming that probe beam diameter is smaller than the maximum bubble diameter (i.e. $D < d_b$), the effect of the expanding cavitation bubble on probe beam intensity was described within the context of two critical values of separation, z_{min} & z_{max}, illustrated as follows:

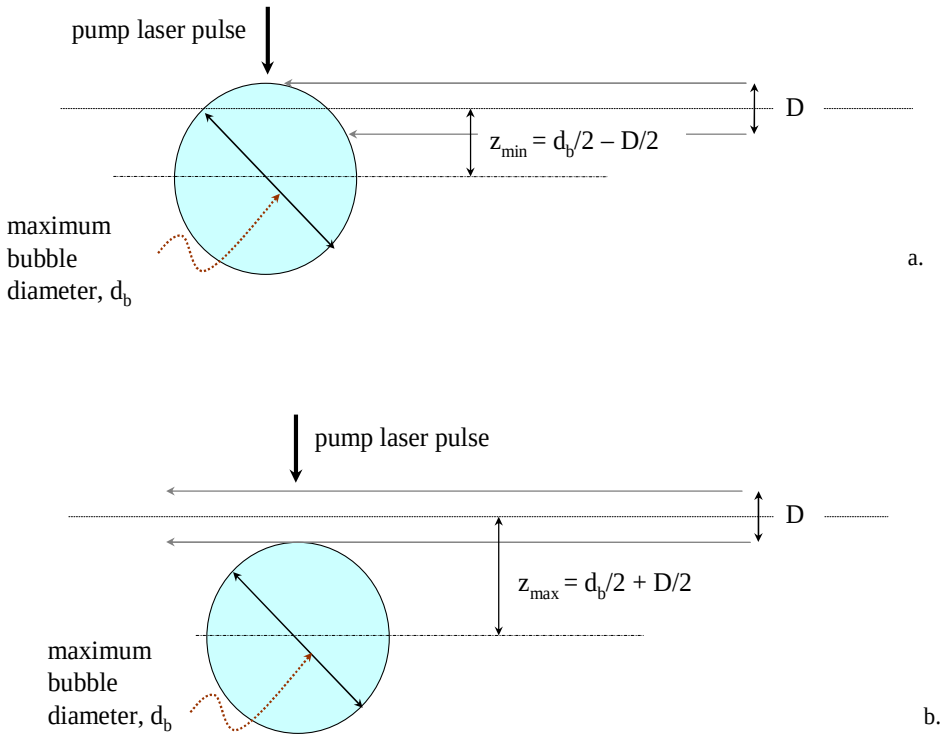

Figure 5.6: Relationship between Bubble Diameter, d_b, Probe Beam Diameter, D and Probe Beam Separation Parameter, z

As illustrated in Figure 5.6, the critical separation, z_{min}, was defined as that separation (z) such that the probe beam is completely encapsulated within the maximum cavitation bubble volume. Similarly, the critical separation, z_{max}, was defined as that separation (z) such that the probe beam is not affected by the cavitation bubble at maximum volume. The critical separation limits (z_{min} & z_{max}) allowed reduction in probe beam intensity (ΔS_{pb}) to be interpreted with respect to three regimes, described as follows:

For $|z| < z_{min}$: $\Delta S_{pb} \rightarrow$ maximum … *[i.]*

For $z_{min} < |z| < z_{max}$: maximum $> \Delta S_{pb} >$ zero *[ii.]*

For $|z| > z_{max}$: $\Delta S_{pb} \rightarrow$ zero … … *[iii.]*

Where $z_{min} = (d_b - D) / 2$ … … *[iv.]*

$z_{max} = (d_b + D) / 2$ … … *[v.]*

In the case of condition *[i.]* it was anticipated that the reduction in probe beam intensity would tend to a maximum, due to refractive effects within the cavitation bubble. In the case of condition *[iii.]* it was anticipated that reduction in probe beam intensity would be negligible, in the absence of significant diffraction effects. In the case of condition *[ii.]* it was anticipated that reduction in probe beam signal intensity would continuously change between maximum and minimum limits. Interpretation of probe beam intensity temporal histories for separation, z, in the range defined by condition *[ii]*, allowed estimates of both d_b and D to be made.

Temporal variation in probe beam signal intensity, corresponding to a representative set of values of separation, z, is shown in Figures 5.7 and 5.8. These represent bubble formation above and below the fixed probe beam laser, respectively. A complete record of probe beam deflection traces, for all values of z used, is presented in Appendix VI.

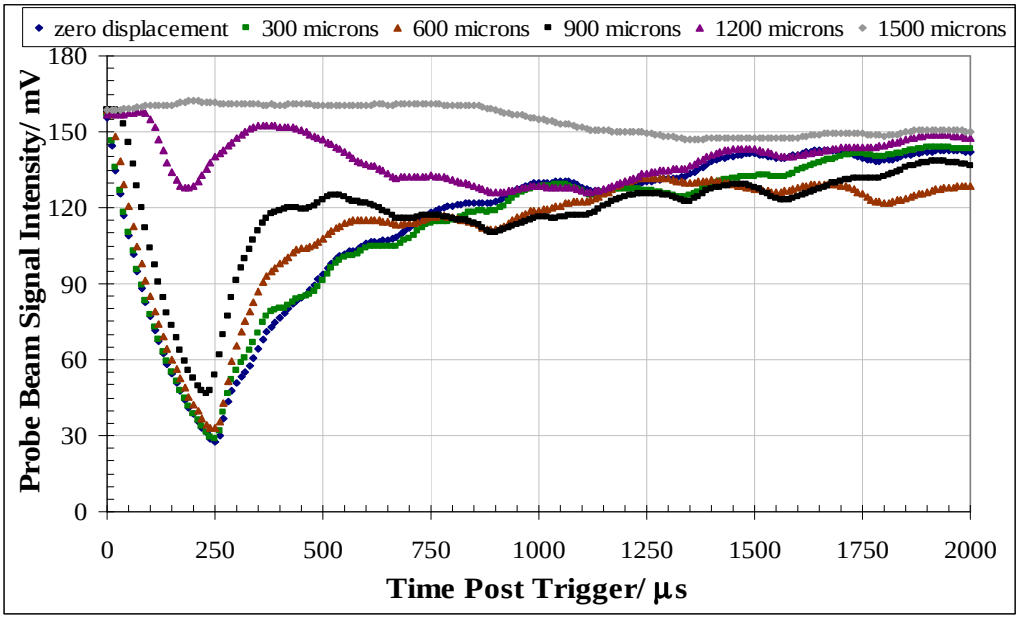

Figure 5.7: Probe Beam Deflection Traces for Separations of 0, 300, 600, 900, 1200 & 1500µm Above Fixed Probe Beam Position

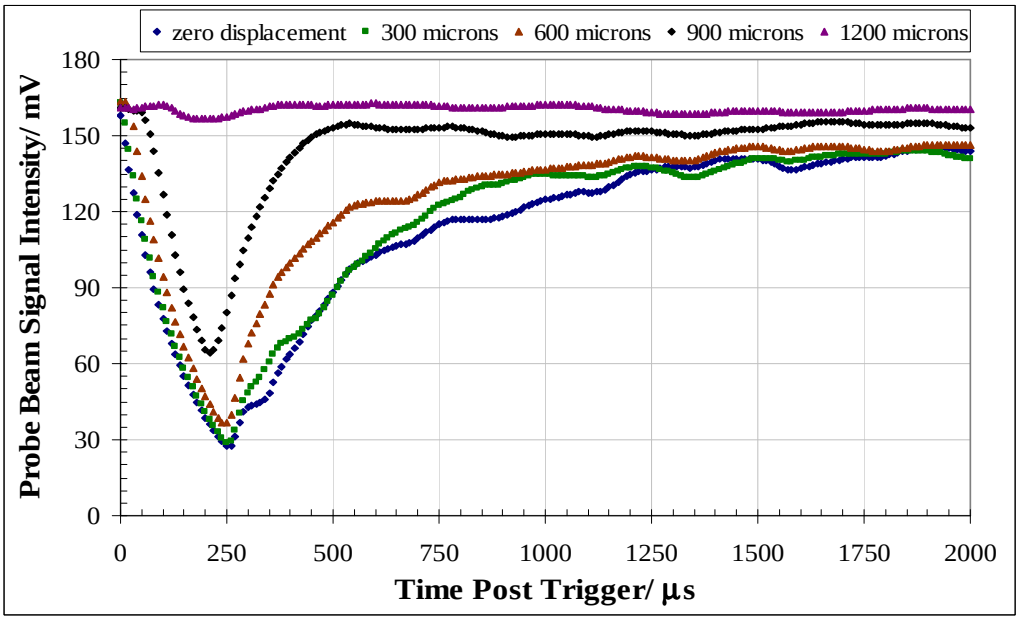

Figure 5.8: Probe Beam Deflection Traces for Separations of 0, 300, 600, 900 & 1200µm Below Fixed Probe Beam Position

From the temporal traces shown in Figures 5.7 & 5.8, the minimum values of probe of beam intensity were measured, for each separation, z. Reduction in probe beam intensity was calculated by subtraction from the maximum (unaffected) probe beam intensity (161mV), corresponding to t = 0 i.e. prior to delivery of laser pulse and subsequent bubble formation. These data are summarised in Table 5.4, including normalised reduction in probe beam intensity.

Table 5.4: Reduction in Probe Beam Intensity for Full Range of Separations

Pump Laser Pulse Focussed Below Probe Laser Beam			Pump Laser Pulse Focussed Above Probe Laser Beam		
z/ μm (±5μm)	ΔS_{pb}/ mV (±3mV)	Normalized ΔS_{pb} (±2%)	z/ μm (±5μm)	ΔS_{pb}/ mV (±3mV)	Normalized ΔS_{pb} (±2%)
-1500	0	0.00	1500	0	0.00
-1400	0	0.00	1400	0	0.00
-1300	5	0.04	1300	2	0.01
-1200	32	0.24	1200	5	0.04
-1100	77	0.57	1100	35	0.26
-1000	104	0.76	1000	65	0.48
-900	115	0.85	900	99	0.73
-800	127	0.93	800	116	0.85
-700	128	0.94	700	117	0.86
-600	130	0.96	600	121	0.89
-500	133	0.98	500	131	0.96
-400	133	0.98	400	133	0.98
-300	136	1.00	300	135	0.99
-200	136	1.00	200	135	0.99
-100	136	1.00	100	136	1.00
0	136	1.00	0	136	1.00

To illustrate the effect of the expanding cavitation bubble on the probe beam signal, normalized probe beam intensity, S_{pb} (as opposed to reduction in probe beam intensity,

ΔS_{pb}), was plotted as a function of separation, z. This relationship, for bubble formation above and below the fixed probe beam, is shown in Figure 5.9.

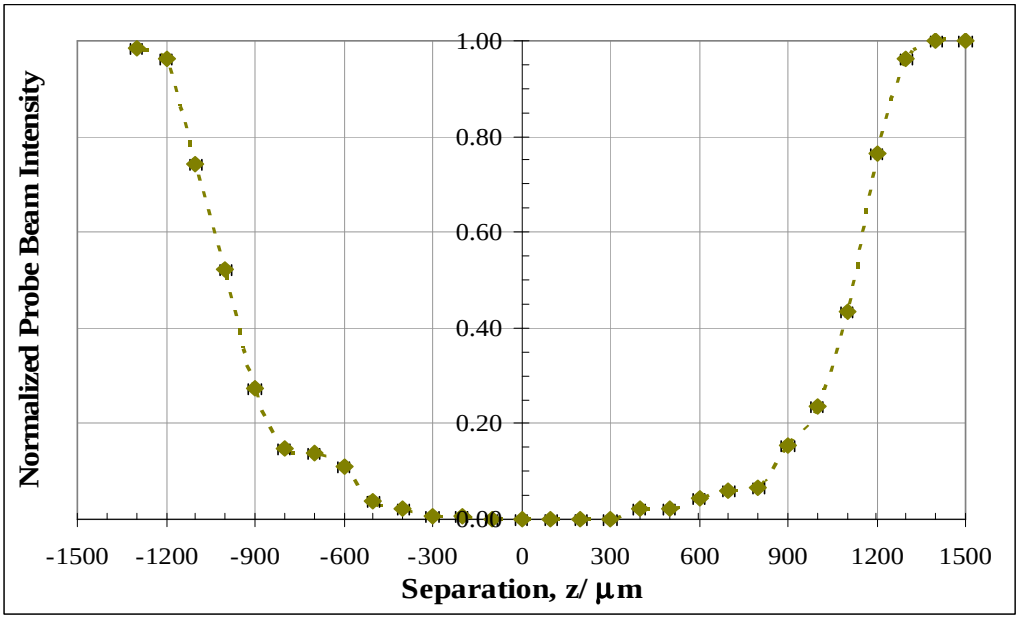

Figure 5.9: Normalized Probe Beam Intensity *vs*. Separation

From the data shown in Figure 5.9, the values of separation, z (positive and negative) which represented the critical limit, z_{max} i.e. probe beam signal intensity tending to a maximum value, were identified. The values of separation, z (positive and negative) which represented the critical limit z_{min} i.e. probe beam intensity tending to zero, were similarly identified.

As previously mentioned, differences in maximum cavitation bubble diameter were anticipated, due to variations in delivered laser pulse energy, and inconsistencies in focussing precision in the water bulk. For this reason a similar criterion was invoked for estimation of critical limits (z_{min} & z_{max}), based on the data shown in Figure 5.9. The critical limit represented by condition *[iv]* (z_{min}) was estimated as that separation for which probe beam intensity is equal to 10% of maximum value (equivalent to a

normalized value of 0.10). Similarly, the critical limit represented by condition *[v]* (z_{max}) was estimated as that separation for which probe beam intensity is equal to 90% of maximum value (equivalent to a normalized value of 0.90). Based on these conditions, z_{min} and z_{max} were estimated to be 715±50μm and 1225±50μm, respectively. These represented the mean of estimates for z_{min} and z_{max}, for bubble formation above and below the probe beam axis. By simple manipulation of conditions *[iv]* & *[v]*, maximum cavitation bubble diameter (d_b) was estimated to be 1940±70μm.

As with configuration I of the PDB technique, interpretation of the temporal probe beam deflection profiles (see Figures 5.7 & 5.8) allowed estimation of bubble lifetime, τ_b. The same inconsistency of signal intensity was apparent, during the period of signal recovery following maximum deflection. This phenomenon was typically observed in the period 750μs to 1500μs after bubble formation. Due to the limited measurement precision imposed by this phenomenon, the criterion of recovery to 75% of unaffected signal intensity was used. Based on this criterion, and an unaffected probe beam intensity of ~160mV, bubble lifetimes were estimated to be 760±60μs and 910±60μs, for bubble formation above and below the probe beam axis, respectively.

c. Expansion of the Bubble Wall

Probe beam signal temporal profiles were produced, with expanded time scales in the period immediately following delivery of the laser pulse. This was represented on oscilloscope traces as t = 0, and was synonymous with the onset of laser induced cavitation. The expanded probe beam traces were used to measure the time delay (t_b) before the onset of probe beam deflection.

Using these values, the speed of bubble wall expansion (v_b) was calculated for a set of separation (z) values. Bubble wall expansion speeds were calculated from original data (t_b and z) averaged over 16 laser shots. Calculations were made for positive separation (+z)

and negative separation (-z), corresponding to cavitation bubble formation above and below the fixed probe beam, respectively.

Expanded probe beam temporal histories are shown, for representative incremental separations above and below the fixed probe beam position, in Figures 5.10 and 5.11, respectively. Oscilloscope traces corresponding to expanded probe beam deflection profiles for all separations used, for bubble formation above and below the fixed probe beam axis, are presented in Appendix VII.

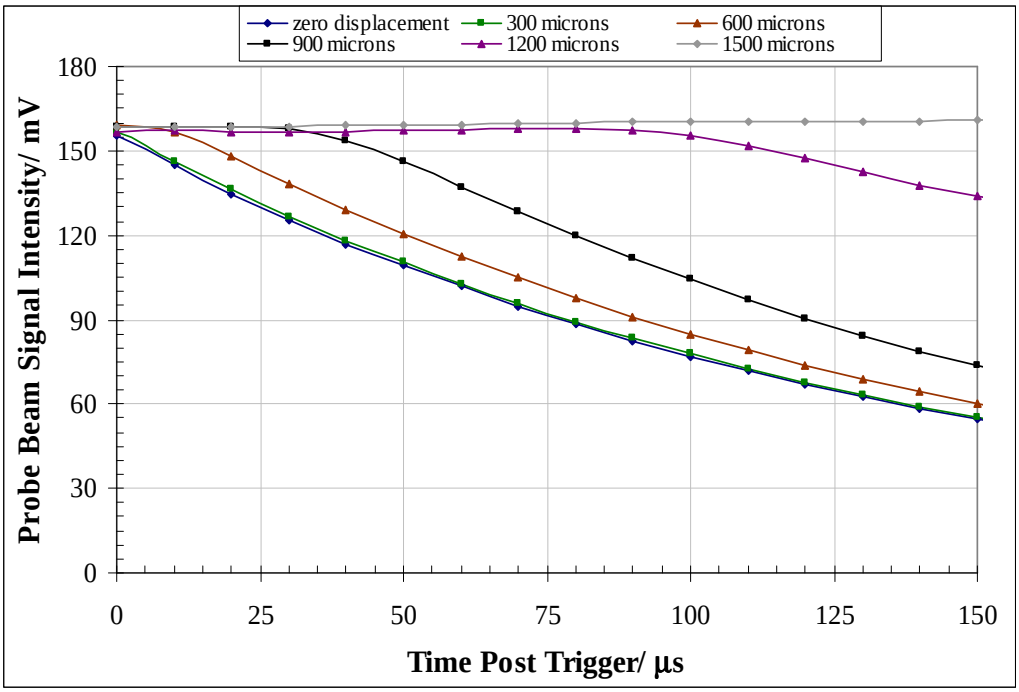

Figure 5.10: Probe Beam Deflection *vs*. Time Post-Trigger: Bubble Formation Above Probe Beam Axis (NB. Expanded Time Scale)

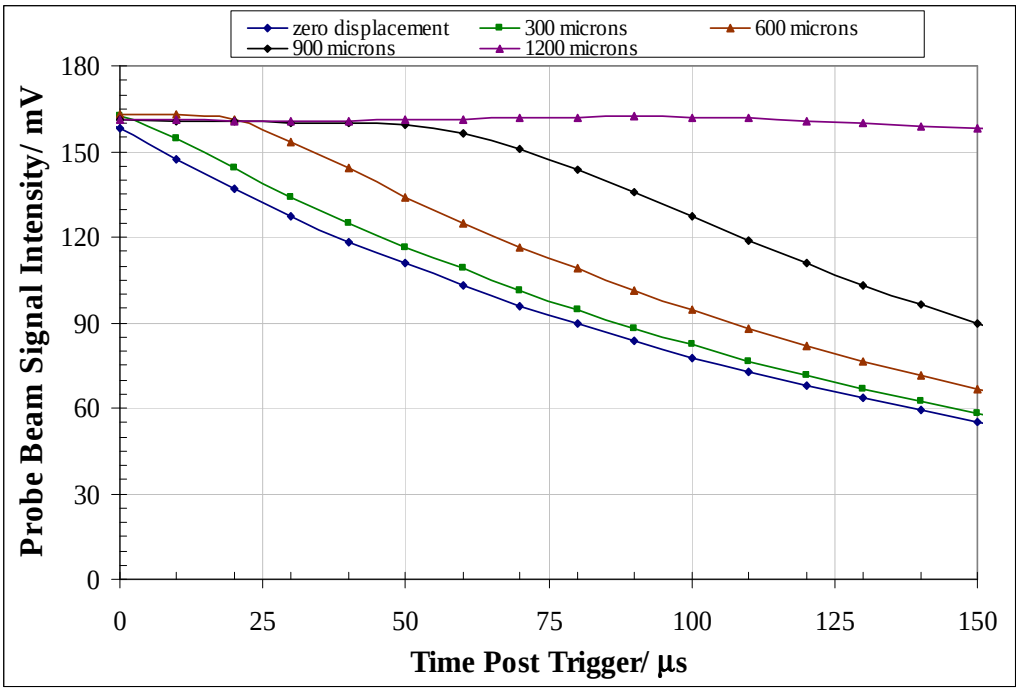

Figure 5.11: Probe Beam Deflection *vs*. Time Post-Trigger: Bubble Formation Below Probe Beam Axis (NB. Expanded Time Scale)

The expanded probe beam deflection profiles in Figures 5.10 & 5.11 demonstrated a non-linear positive correlation between separation (z) and time for onset of deflection (t_b). The gradient of the deflection curves were unchanged with z, within the limits of experimental error, for times in excess of t_b. Data for incremental separation (z), time delay to onset of probe beam deflection (t_b), and bubble wall expansion velocity (v_b), are summarized in Table 5.5.

Table 5.5: Time Delay for the Onset of Probe Beam Deflection and Derived Rate of Bubble Wall Expansion

Pump Laser Pulse Focussed Above Probe Laser Beam			Pump Laser Pulse Focussed Below Probe Laser Beam		
z/ μm (±5μm)	t_b/ μs (±5μs)	v_b/ ms^{-1} (±10%)	z/ μm (±5μm)	t_b/ μs (±5μs)	v_b/ ms^{-1} (±10%)
0	0	-	0	0	-
100	2	50.0	100	2	50.0
200	6	33.3	200	4	50.0
300	11	27.3	300	9	33.3
400	17	23.5	400	12	33.3
500	23	21.7	500	17	29.4
600	30	20.0	600	22	27.3
700	42	16.7	700	28	25.0
800	52	15.4	800	34	23.5
900	70	12.9	900	47	19.1
1000	87	11.5	1000	68	14.7
1100	102	10.8	1100	84	13.1
1200	122	9.8	1200	111	10.8
1300	-	-	1300	117	11.1

Bubble wall expansion rate, v_b, as a function of separation, z, is shown in Figure 5.12, for cavitation bubble formation above and below the fixed probe beam axis.

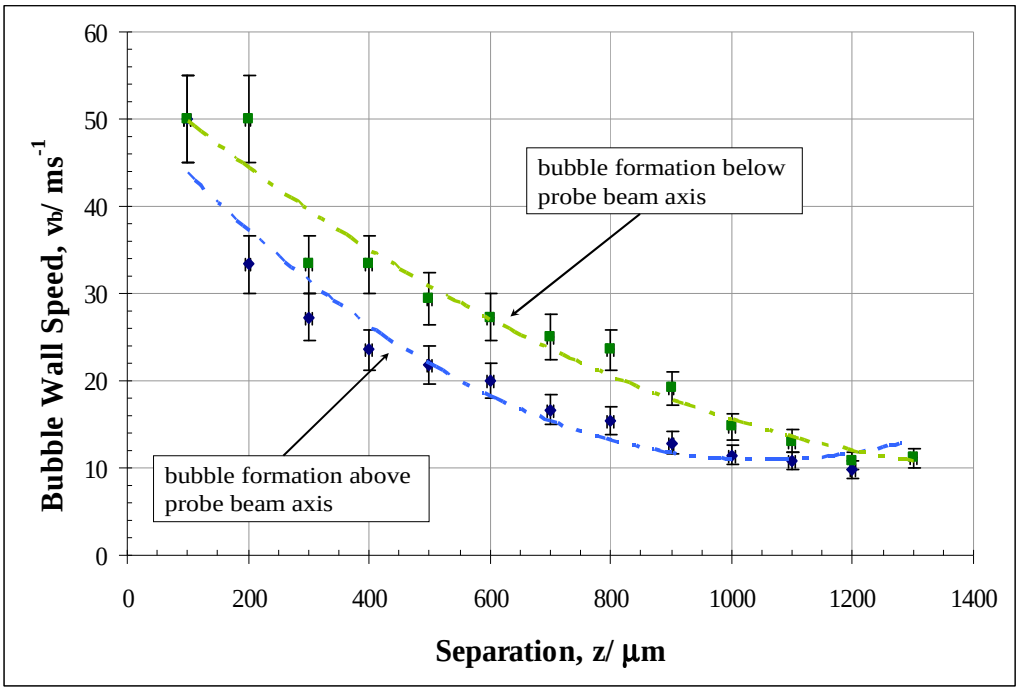

Figure 5.12: Estimated Bubble Wall Speed *vs*. Separation

Examination of the data in Table 5.5 revealed significant differences in time to onset of probe beam deflection, and hence derived bubble wall expansion rate, between cavitation above and below the probe beam axis. This effect was hypothesized to be due to the effect of buoyancy of the expanding bubble. Buoyancy was assumed to act uni-directionally i.e. upward, and to have a fixed magnitude, and therefore had the effect of decreasing the time to onset of probe beam deflection for bubble formation below the probe beam axis. The same buoyancy phenomenon had the converse effect of increasing the time for onset of probe beam deflection for bubble formation above the probe beam axis.

d. Interpretation of Bubble Buoyancy

Arrival times of the expanding bubble wall were higher for pump laser focussed above the fixed probe beam than those for below, for each separation, z, due to the effect of bubble buoyancy. The derived parameter of bubble wall expansion speed (v_b – as summarized in Table 5.5) was re-interpreted to represent the 'apparent' bubble wall speed i.e. the combination of the 'actual' rate of bubble wall expansion, $v_{b'}$, and the rate of motion due to bubble buoyancy, v_{bcy}. The combination of 'actual' rate of bubble wall expansion ($v_{b'}$), and rate of motion due to bubble buoyancy (v_{bcy}) is illustrated in Figures 5.13, for cavitation bubble centre above and below the probe beam.

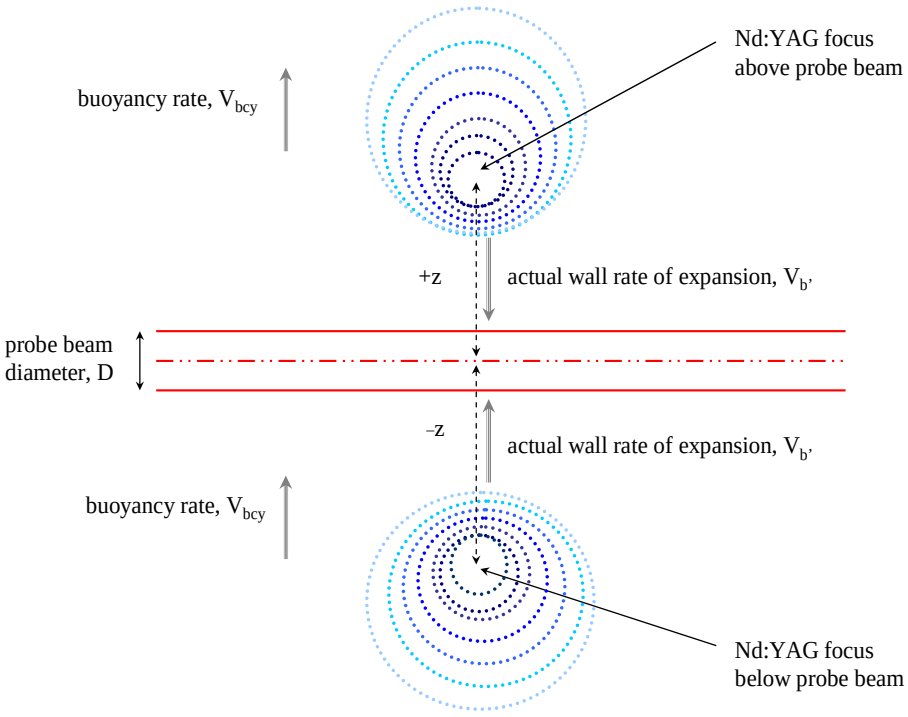

Figure 5.13: Bubble Expansion and Buoyancy Effects for Cavitation Formation Above and Below the Probe Beam Axis

The rate of motion due to bubble buoyancy (v_{bcy}), and the actual rate of bubble wall expansion ($v_{b'}$), were independent parameters. Given that these two independent rates of motion were applied to the cavitation bubble in a common direction i.e. vertically, their mutually effect was calculated by summation of their respective magnitudes, without recourse to vector addition.

The additive relationship between 'apparent' rate of bubble wall expansion (v_b), 'actual' rate of bubble wall expansion ($v_{b'}$), and rate of motion due to bubble buoyancy (v_{bcy}) is summarized as follows:

For bubble centre above probe beam:

$$v_b = v_{b'} - v_{bcy} \quad \ldots \quad \ldots \quad \ldots \quad \textit{[vi.]}$$

For bubble centre below probe beam:

$$v_b = v_{b'} + v_{bcy} \quad \ldots \quad \ldots \quad \ldots \quad \textit{[vii.]}$$

For each separation, z:

$$v_{b(below)} - v_{b(above)} = 2v_{bcy} \quad \ldots \quad \ldots \quad \textit{[viii.]}$$

Further: $$v_{b(below)} + v_{b(above)} = 2v_{b'} \quad \ldots \quad \ldots \quad \textit{[ix.]}$$

In defining conditions *[vi.-ix.]* the assumption was made that the magnitude of bubble buoyancy was constant, over the time intervals corresponding to the full range of separation, z. Estimates were made for 'actual' rate of bubble wall expansion ($v_{b'}$), and rate of motion due to buoyancy (v_{bcy}), based on empirically measured rates of bubble wall expansion (v_b). These data are summarized in Table 5.6, for the range $100\mu m \leq z \leq 1200\mu m$.

Table 5.6: Estimated 'Actual' Rate of Bubble Wall Expansion and Rate of Motion Due to Buoyancy

z/ μm (±5μm)	v_b/ ms^{-1} (±10%)[a]	v_b/ ms^{-1} (±10%)[b]	$v_{b'}$/ ms^{-1} (±14%)	v_{bcy}/ ms^{-1} (±14%)
100	50.0	50.0	50.0	0.0
200	33.3	50.0	41.7	8.4
300	27.3	33.3	30.3	3.0
400	23.5	33.3	28.4	4.9
500	21.7	29.4	25.6	3.9
600	20.0	27.3	23.7	3.7
700	16.7	25.0	20.9	4.2
800	15.4	23.5	19.5	4.1
900	12.9	19.1	16.0	3.1
1000	11.5	14.7	13.1	1.6
1100	10.8	13.1	12.0	1.2
1200	9.8	10.8	10.3	0.5

[a]: bubble formation above probe beam axis
[b]: bubble formation below probe beam axis

Estimates for 'actual' rate of bubble wall expansion and rate of motion due to bubble buoyancy are shown in Figure 5.14.

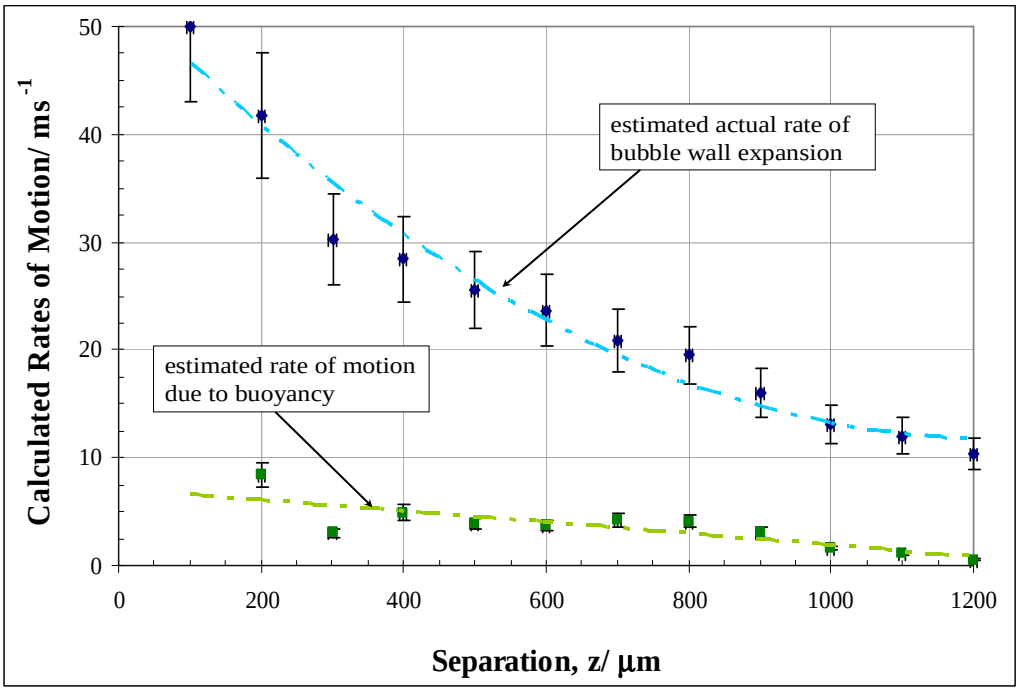

Figure 5.14: Variation in Bubble Motion with Increasing Separation

The data shown in Figure 5.14 indicated the rate of motion due to bubble buoyancy was an order of magnitude lower than the 'actual' rate of expansion of the bubble wall. The rate of expansion of the bubble reduced asymptotically to a minimum value, for separation (z) in the region of 1200µm. The non-zero value of this limit was attributed to limitation in the accuracy of the original probe beam deflection traces, which prevented inference with regard to the maximum bubble diameter. The decrease in the rate of bubble motion due to buoyancy is approximately linear, as a function of separation, within the limits of experimental error.

e. Comparison with Theory

The original Rayleigh Equation relating the bubble wall velocity, v_{Ray}, with bubble radius, R_b, is given as follows:

$$v_{Ray} = \{(^2/_3)p_\infty/\rho_l \cdot [(R_0/R_b)^3 - 1]\}^{0.5} \quad \ldots \quad [5.2]$$

where

R_0 = maximum bubble radius
ρ_l = density of the fluid medium (kgm^{-3})
p_∞ = pressure in the infinite liquid (Nm^{-2})

Taking natural logarithms of both sides of *eqn.[5.2]* gives the expression:

$$\ln(v_{Ray}) = 0.5\ln\{(^2/_3)p_\infty/\rho_l\} + 0.5\ln\{(R_0/R_b)^3 - 1\}$$
$$= 0.5\ln\{(R_0/R_b)^3 - 1\} + k \quad \ldots \quad [5.3]$$

The constant, $k = 0.5\ln\{2p_\infty/(3\rho_l)\}$, and is therefore independent of the oscillating bubble radius.

Greater accuracy was possible for measurement and analysis of probe beam deflection profiles for elapsed times significantly greater than the zero (trigger) time i.e. in excess of ~100μs. With respect to the radius of the expanding cavitation bubble, this time regime is synonymous with bubble radius (R_b) significantly greater than zero, and of the same order of magnitude as the maximum bubble radius (R_0).

Bubble radius for times in excess of ~100μs following the onset of cavitation are characterized by the condition:

$$0 << R_b < R_0 \quad \ldots \quad \ldots \quad \ldots \quad [x.]$$

Condition *[x.]* may be used to derive an approximation to *eqn.[5.2]*, applicable to this specific range of bubble radius, as follows:

For $R_0 > R_b \rightarrow (R_0/R_b)^3 >> 1$ ... ... *[xi.]*

Hence $\ln\{(R_0/R_b)^3 - 1\} \approx \ln(R_0/R_b)^3 = 3\ln(R_0/R_b)$ *[xii]*

With reference to *eqn.[5.3]*:

$$\ln(v_{Ray}) \approx 1.5\ln(R_0 / R_b) + k \quad \ldots \quad [5.4]$$

By plotting the experimentally measured $\ln(v_{Ray})$ against $\ln(R_0/R_b)$, the gradient and y-intercept were measured, and compared with those predicted by *eqn.[5.4]*. These data are summarized in Table 5.7, and shown in Figure 5.15.

In the interests of clarity, the following are noted:

i. the bubble wall velocity which appears in the Rayleigh Equation, denoted by v_{Ray}, is synonymous with the 'actual' rate of bubble wall expansion, denoted by $v_{b'}$ (see Table 5.6, column #4).

ii. the maximum bubble radius, R_0, was fixed at half the estimated maximum bubble diameter, obtained using configuration II of the PBD technique.

Table 5.7: Comparison of Empirical and Approximated Rayleigh Data

$v_{b'}$/ ms^{-1} (±10%)	R_b[a]/ μm (±5μm)	$(R_0/R_b)^b$	$\ln(v_{b'})$	$\ln(R_0/R_b)$
50.0	83	12.00	3.91	2.48
41.7	167	6.00	3.73	1.79
30.3	250	4.00	3.41	1.39
28.4	333	3.00	3.35	1.10
25.6	417	2.40	3.24	0.88
23.7	500	2.00	3.17	0.69
20.9	583	1.71	3.04	0.54
19.5	667	1.50	2.97	0.41
16.0	750	1.33	2.77	0.29
13.1	833	1.20	2.57	0.18
12.0	917	1.09	2.48	0.09
10.3	1000	1.00	2.33	0.00

[a]: *normalized w.r.t. empirically measured R_0 (see note 'b')*
[b]: *$R_0 \leq 1000\mu m$ based on empirical data, as described above*

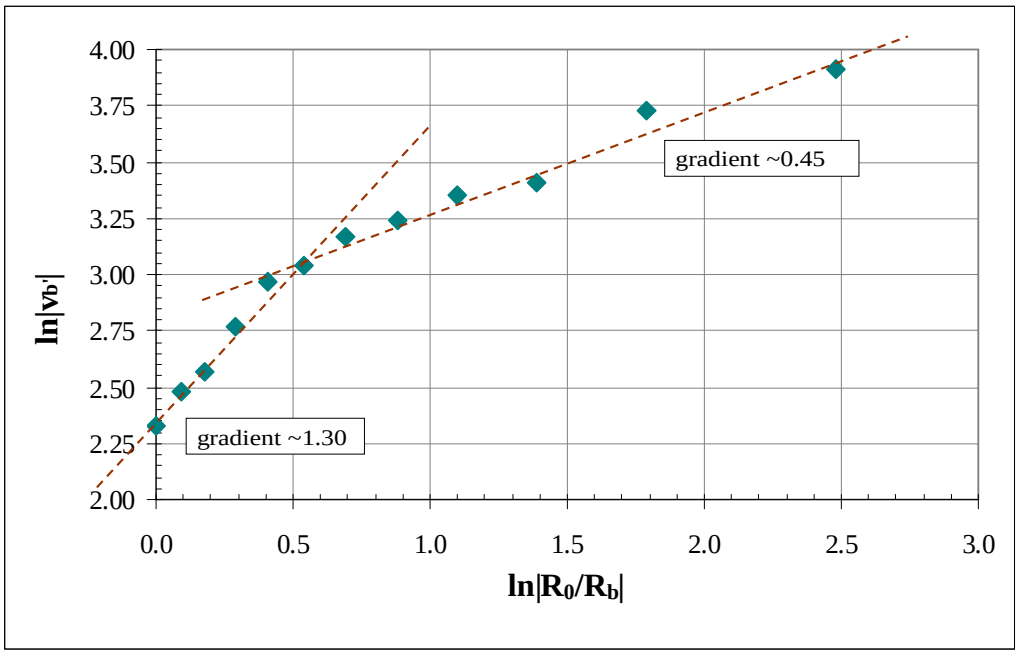

Figure 5.15: Rayleigh Bubble Expansion Velocity *vs*. Normalized Bubble Radius Satisfying the Condition $(R_0/R_b)^3 >> 1$

The data shown in Figure 5.15 demonstrated two distinct functional relationships corresponding to two distinct regions separated by the value $\ln(R_0/R_b) \approx 0.55$. The relationship between $\ln(v_b)$ and $\ln(R_0/R_b)$ is approximately linear for both regions. The gradients were ~1.30 & 0.45, for $\ln(R_0/R_b) < 0.55$ and $\ln(R_0/R_b) > 0.55$, respectively.

The lower gradient in the region corresponding to $\ln(R_0/R_b) > 0.55$ was interpreted as evidence of fundamental changes in the processes occurring in the material encapsulated within the expanding bubble. Further, the apparent discontinuous change of gradient implies a sudden change in these processes, for bubble *radii* corresponding to ~580μm.

5.2.3 Evaluation of Cavitation Dynamics by High Speed Imaging

The set-up for the high speed imaging technique has been previously illustrated in Figures 4.14 & 4.15. Still images were created to allow direct measurement of the dynamic evolution of the cavitation bubble volume. The frame rate was fixed at $\sim 5.4 \times 10^4$ frames per second (fps) which fixed an interval between images (τ_{int}) of ~20μs. Still images were generated using the dedicated software provided with the camera. A series of post-processing procedures (including enlargement, clipping of extraneous background, and contrast enhancement) were carried out, to facilitate accurate bubble measurements. The sequence of images in Figure 5.16 shows the evolution of the cavitation bubble over the primary oscillation period. The stated times represent the interval following delivery of the laser pulse. The onset of cavitation in the liquid bulk was considered to be equivalent, for all intents and purposes, with the generation of laser induced plasma. The millimetre scale was added in post-processing. A complete record of images, covering the time period from 200μs to 660μs post-trigger, is presented in Appendix VIII.

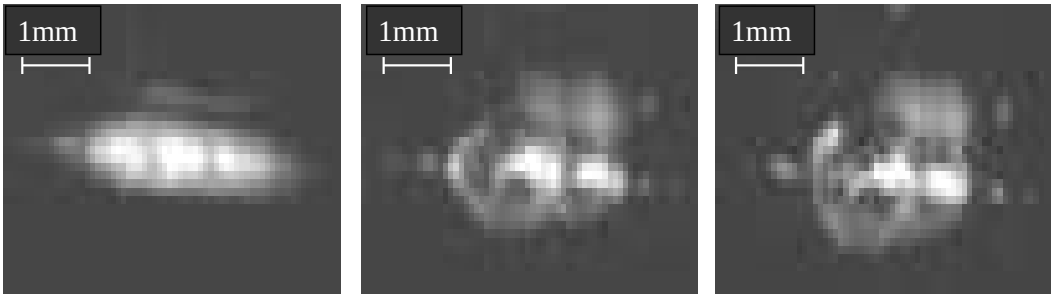

a. 200μs b. 240μs c. 280μs

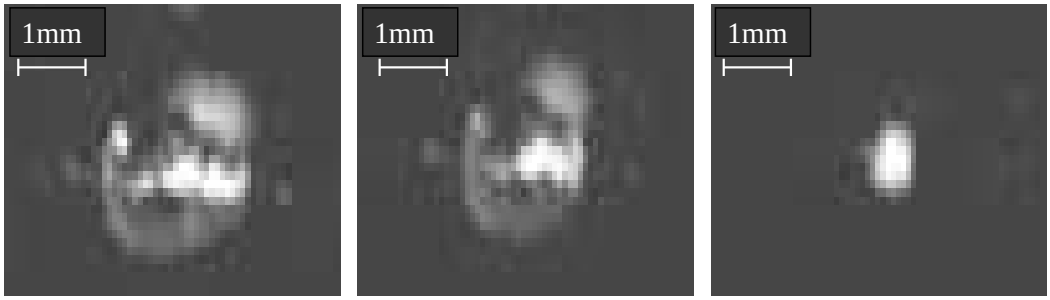

d. 320μs e. 360μs f. 420μs

Figure 5.16. Dynamics of Cavitation Bubble at Selected Times after Delivery of Pump Laser Pulse

The primary, secondary and tertiary bubble oscillation lifetimes (τ_b) were estimated by visual inspection of post-processed images, based on the criterion of time taken for the bubble to oscillate between sequential states of minimum volume. The bubble collapse time (τ_c) was classically defined (Lord Rayleigh) as the time taken for a cavitation bubble to collapse from maximum to minimum volume. No data were available in the interval between delivery of the laser pulse (zero time i.e. t = 0) and 200μs post-trigger, due to over-exposure of the imaging apparatus by significant spectral emission which accompanied dielectric breakdown of the target medium.

For estimation of bubble volume ($\mathbf{V}_B$) over the duration of the oscillation period spatial symmetry was assumed in the plane orthogonal to the trajectory of the delivered pulse. This assumption was justified by the knowledge that the sole impulse to the cavitation region was provided by mechanical effects (including cavitation and shock wave emission) resulting from dielectric breakdown. Given a reasonably high degree of homogeneity of the physical properties in the water bulk in the vicinity of the cavitation region, this assumption was deemed valid.

Examination of the bubble images indicated substantial non-uniformity of bubble morphology, as well as multiple bubble formation sites, during the primary oscillation cycle. Initially there were multiple (smaller) bubbles in the cavitation region, which exhibited lateral motion toward the centre of this region as they increased in volume. As the bubble radius (R_b) approached a maximum (R_0), individual bubbles gradually coalesced to form a single bubble with a high level of sphericity i.e. negligible eccentricity.

Three regimes were identified with respect to estimation of the total bubble volume in the cavitation region. These regimes are particular to the time scale of bubble evolution, and are described as follows:

Multiple bubbles with negligible overlap - see images (Appendix IX) pertaining to 200μs to 260μs inclusive *[xiii.]*

Two distinct bubbles with varying degrees of overlap - see images (Appendix IX) pertaining to 280μs to 340μs inclusive *[xiv.]*

Single distinct bubble - see images (Appendix IX) pertaining to 360μs to 420μs inclusive *[xv.]*

Bubble volumes were estimated over the primary oscillation cycle, based on measurements from contrast enhanced and enlarged bubble images. The eccentricity, ε, of the cavitation region was defined as the ratio between minor and major axes. The major axis was co-linear to the trajectory of the incident laser pulse. The minor axis was any axis in the plane orthogonal to the trajectory of the laser pulse. The change in eccentricity during the primary oscillation cycle is shown in Figure 5.17.

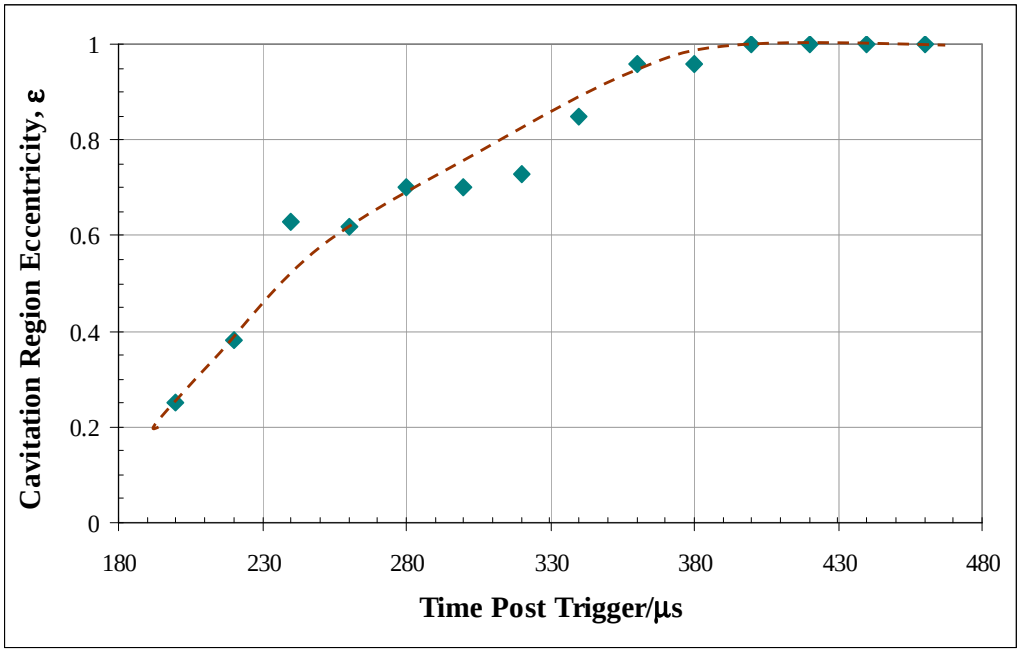

Figure 5.17. Eccentricity of Cavitation Bubble During Primary Oscillation Cycle

The trend shown in Figure 5.17 corroborated the previously noted observation of multiple cavitation bubbles in the early stages of the primary oscillation cycle, which coalesced toward the centre of the cavitation region. Translation of multiple cavitation bubbles along the trajectory of the incident laser pulse was coincident with a tendency to sphericity of the resultant (single) bubble i.e. tendency of eccentricity towards unity, as shown in Figure 5.17.

Errors in bubble volume were estimated based upon the difficulty in resolving the bubble wall from the ambient background in the post-processed still images. Equivalent bubble radii ($R_{b'}$) were derived, based upon a single bubble with volume equal to that of the cumulative individual bubble volumes in the cavitation region. These data are summarized in Table 5.8, and shown in Figure 5.18. A complete record of measurements in support of estimation of bubble volume is presented at Appendix IX.

Table 5.8: Bubble Volume and Equivalent Radius: Primary Oscillation Cycle

time/ μs	$\mathbf{V}_B$/ mm^3	error in $\mathbf{V}_B$/ %	eccen-tricity, ε	$R_{b'}$/ mm	error in $R_{b'}$/ %
200	0.62	40	0.25	0.53	3.4
220	1.58	20	0.38	0.72	2.7
240	3.16	15	0.63	0.91	2.5
260	4.13	10	0.62	1.00	2.2
280	5.25	10	0.70	1.08	2.2
300	5.74	10	0.70	1.11	2.2
320	4.87	10	0.73	1.05	2.2
340	4.92	10	0.85	1.06	2.2
360	4.42	10	0.96	1.02	2.2
380	3.35	20	0.96	0.93	2.7
400	1.53	20	1.00	0.71	2.7
420	0.22	40	1.00	0.37	3.4
440	0.20	75	1.00	0.36	4.2
460	0.20	75	1.00	0.36	4.2

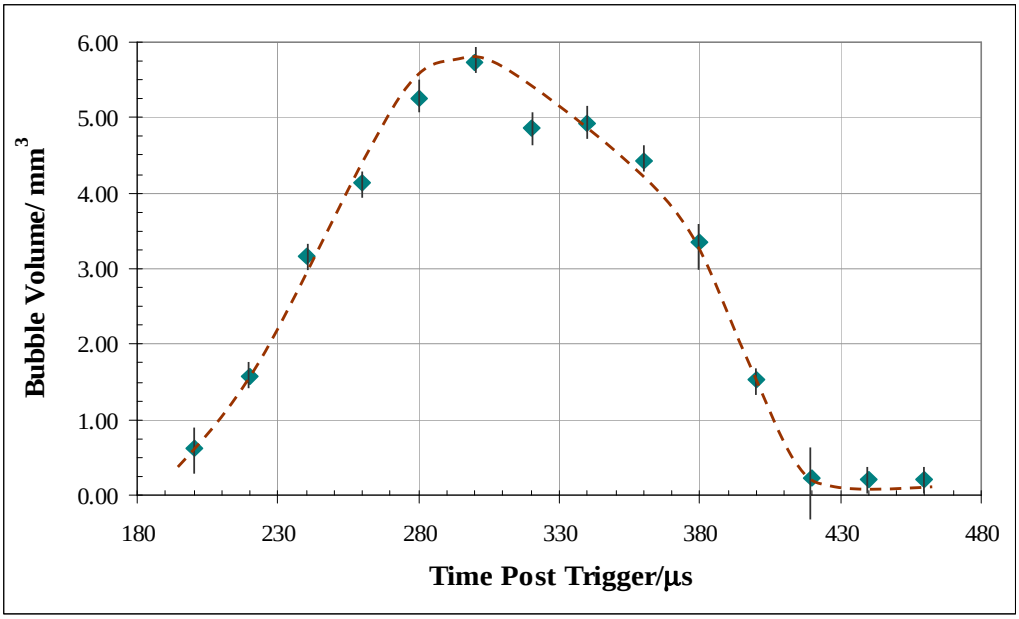

Figure 5.18. Bubble Volume Profile During Primary Oscillation Cycle

From the data shown in Figure 5.18, maximum bubble volume, $\mathbf{V}_0$, was estimated to be 5.8mm^3 ±10%. This corresponded to an equivalent maximum (spherical) bubble radius, R_0, of ~1.1mm (1100µm). Maximum volume was reached ~310µs after the onset of cavitation. The bubble volume profile exhibited a minor degree of asymmetry during the primary oscillation period.

The primary bubble oscillation time, τ_b, was estimated to be ~240µs, notwithstanding the non availability of data in the time period <200µs following the onset of cavitation. Secondary and tertiary oscillation lifetimes, based upon examination of the still image sequences representing these time periods (see Figures H4, H5 & H6, Appendix VIII), were estimated to be ~130µs & ~90µs, respectively. The total bubble lifetime, incorporating the three complete imaged oscillation cycles, and the period representing the initial 200µs after bubble formation, was estimated to be 660µs. The precision of this estimate was limited by the interval between images i.e. ~20µs.

By reprising the integrated form of *eqn.[3.3]* (Rayleigh Equation), a comparison was made between theoretical and experimental values. On substituting oscillation time (τ_b) for collapse time (τ_c), the integrated form of the Rayleigh Equation takes the following form:

$$\tau_b = 1.83R_0 \cdot (\rho_l/p_\infty)^{0.5} \qquad \ldots \quad \ldots \quad \ldots \quad [5.5]$$

On transposing *eqn.[5.5]* followed by substitution for estimated oscillation time (τ_b) and maximum radius (R_0), the value of (ρ_l/p_∞) was calculated to be ~$1.40\text{x}10^{-2}$ $kgm^{-1}N^{-1}$. This compared with an value of ~$1.0\text{x}10^{-2}$ $kgm^{-1}N^{-1}$, based on values of bulk density (ρ_l) and pressure (p_∞) of $1000kgm^{-3}$ and $1\text{x}10^5Nm^{-2}$, respectively (atmospheric pressure is three orders of magnitude higher than fluid pressure). The agreement within an order of magnitude, between values based on the first principles theory and empirically measurement, lends validation to the *a priori* assumptions implicit in the original derivation of the Rayleigh Equation.

5.2.4 Comparison of Estimates by Different Witnessing Techniques

Estimates of spatial and temporal bubble characteristics obtained by the probe beam deflection (PBD) and high speed imaging (HIS) techniques were compared. These estimates are summarised in Table 5.9.

Table 5.9: Comparison of Estimates for Critical Bubble Parameter

Bubble Characteristic	Technique		
	PBD(I)	PBD(II)	HSI
Maximum Radius, R_0/ μm	335±10%	900±50	1100±50
Bubble Lifetime, τ_b/ μs	460±30	835±60	660±20

The data in Table 5.9 indicated reasonable agreement for estimates of maximum bubble radius and bubble lifetime between the HIS and PBD(II) techniques. Estimates of these critical bubble parameters obtained using the PBD(I) technique, however, displayed significant differences compared to the other two techniques.

The fundamental difference between the probe beam deflection (PBD) and high speed imaging (HSI) techniques was the direct witnessing of the latter, in contrast to the indirect witnessing of the former. For this reason it was concluded that interpretation of data acquired by the HSI technique was intrinsically more accurate than that acquired by the PBD technique. Of the two configurations of the PBD technique, configuration (II) was considered to have superior precision than configuration (I), due to the fixed nature of the probe laser beam. A further advantage with PBD(II) was the facility to discretely infer the separation (z) at which the maximally expanded cavitation bubble wall impinged upon the edge of the probe beam.

5.3 Shot Noise Considerations Relating to *Bremsstrahlung* Emission

5.3.1 Preamble

The aim of this experimental work was to demonstrate the efficacy of data averaging for reducing the shot noise component in the *Bremsstrahlung* emission profile, which was a ubiquitous emission feature in the post-dielectric breakdown phase. The successful application of a data averaging algorithm to line emission signal data was considered to have significant potential for improving LIBS sensitivity.

5.3.2 Results and Analysis

The set-up for plasma generation and collection of emitted radiation were illustrated previously (see Figure 4.5). Radiative emissions from the laser induced plasma were dominated by continuum *Bremsstrahlung*, with a contribution from discrete atomic emission lines. The contribution from statistical noise was reduced using a box car

integrator unit, which accumulated plasma emission signal over a pre-set temporal window. Data averaging was performed over an accumulated number (N) of *Bremsstrahlung* profiles with fixed experimental parameters i.e. laser pulse energy ~80mJ, pulse repetition rate = 10Hz, spectrometer entrance slit width ~200μm, and pulse duration = 7ns.

The intrinsic inconsistency in intensity of *Bremsstrahlung* emission was demonstrated by recording five separate profiles corresponding to a single laser shot i.e. N=1. With respect to data averaging this represented the 'null' case, and served as a *datum* to which profiles averaged over larger values of N were compared. Three separate emission profiles were recorded for N = 2, with two being recorded for N = 4. Averaged profiles were then recorded for higher values of data average number i.e. N = 8, 16, 32, 64, 128, 256, 512 & 1024 to demonstrate the significant reduction in shot noise component of the *Bremsstrahlung* emission profiles. By using a range of N covering two orders of magnitude it was intended to demonstrate optimization of data average number with respect to reduction in shot noise component.

The data shown in Figure 5.19 represent *Bremsstrahlung* emission profiles, normalized with respect to peak emission intensity, for a representative selection of data average number i.e. N = 4, 16 & 256. *Bremsstrahlung* emission profiles for the complete range of data average numbers (N) used are presented at Appendix X.

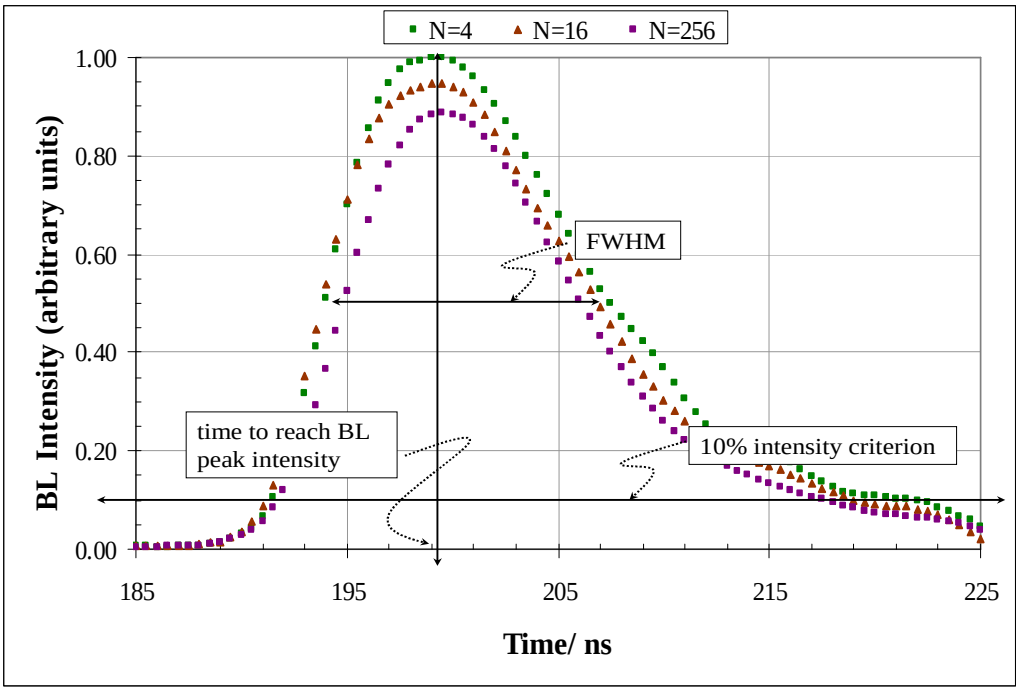

Figure 5.19: Data Averaged *Bremsstrahlung* Emission Profiles

For each *Bremsstrahlung* emission profile the peak intensity, S_{max}, was measured. Key temporal characteristics of the *Bremsstrahlung* profiles were also measured: *i*. time between plasma generation and peak *Bremsstrahlung* intensity, t_{peak}; *ii*. full width at half maximum of *Bremsstrahlung* profile, t_{FWHM}; and, *iii*. duration of *Bremsstrahlung* profile during which *Bremsstrahlung* intensity is greater than 10% of peak intensity, t_{Bremss}. *Bremsstrahlung* profile characteristics are summarized in Table 5.10. Data for N = 1, 2, & 4 represent mean values calculated from multiple recorded spectra, as previously described.

Table 5.10: Measured Properties of Data Averaged *Bremsstrahlung* Emission Profiles

Data Average Number, N	*Bremsstrahlung* Properties			
	S_{max}/ ±0.04V	t_{peak}/ ±2ns	t_{FWHM}/ ±4ns	t_{Bremss}/ ±4ns
1	-1.43	199.0	14.0	31.0
2	-1.40	199.0	13.0	29.5
4	-1.46	200.0	13.5	28.5
8	-1.36	199.5	13.0	34.5
16	-1.38	199.5	14.0	31.5
32	-1.32	199.5	12.0	30.0
64	-1.30	199.5	11.5	28.5
128	-1.24	200.0	12.5	28.0
256	-1.28	200.0	12.5	28.0
512	-1.28	200.0	12.5	28.0
1024	-1.30	200.0	12.5	28.0

Examination of the data in Table 5.10 indicated consistency of *Bremsstrahlung* profile temporal characteristics, within the limits of experimental error, over the complete range of data averaging used. It was noted, however, that peak *Bremsstrahlung* intensity (S_{max}) was consistent only for $N \geq 8$. This suggested a lower limit of N for which the effect of data averaging for smoothing *Bremsstrahlung* peak emission intensity was demonstrable.

By integrating the plasma emission intensity over the duration of the profile envelope, with reference to the previously defined 10% criterion, the energy encapsulated within the *Bremsstrahlung* profile (E_{net}) was estimated. The effect of data averaging on the standard deviation (σ) of *Bremsstrahlung* intensity was also investigated. The temporal period between 300ns and 500ns after plasma generation was chosen, to demarcate the

region of the *Bremsstrahlung* profile with emission intensity significantly lower than peak intensity. Data for E_{net} and σ are summarized in Table 5.11.

Table 5.11: Net Emission and Standard Deviation Characteristics of Data Averaged *Bremsstrahlung* Profiles

N	log(N)	*Bremsstrahlung* Emission, E_{net} ±1%	Standard Deviation, σ
1	0.000	20.66	0.0100
2	0.301	21.74	0.0081
4	0.602	21.65	0.0091
8	0.903	20.83	0.0112
16	1.204	20.20	0.0089
32	1.505	17.79	0.0078
64	1.806	17.43	0.0076
128	2.107	16.66	0.0075
256	2.408	17.45	0.0074
512	2.709	17.16	0.0076
1024	3.010	17.47	0.0072

The efficacy of data averaging for reduction in the standard deviation (σ) of the residual *Bremsstrahlung* emission intensity is shown in Figure 5.20. A natural logarithmic scale was used to improve clarity for lower values of N.

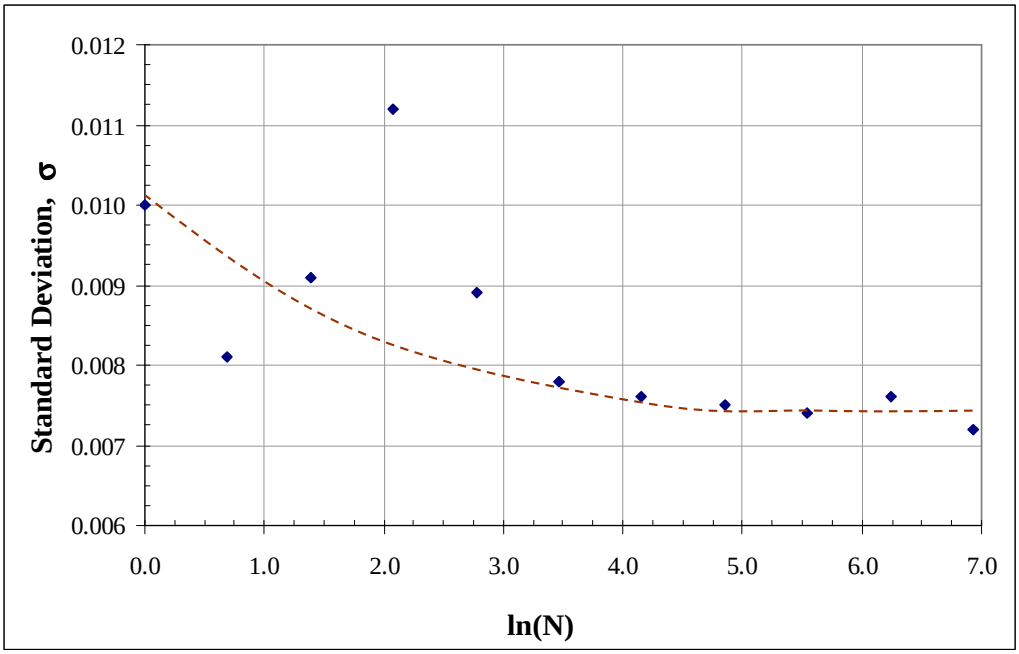

Figure 5.20: Natural Log-Linear Plot of Reduction in Standard Deviation of Residual *Bremsstrahlung* Intensity

The standard deviation of *Bremsstrahlung* emission intensity, as shown in Figure 5.32, tended to a minimum for values of ln(N) in excess of ~4. This asymptotic trend demonstrated a lower limit for N at which shot noise contribution was reduced to a minimum.

Reduction of shot noise contribution from the *Bremsstrahlung* emission profile was considered advantageous for improving LIBS sensitivity. This was demonstrated by calculating signal-to-noise ratio (S/N) for the data averaged *Bremsstrahlung* profiles. As previously shown (see Table 5.10), measured peak *Bremsstrahlung* intensity (S_{max}) was unchanged for $N \geq 8$. The S/N was calculated using *eqn[3.18]*, for *Bremsstrahlung* profiles averaged for $N \geq 8$, using standard deviation (σ) values previously calculated (see Table 5.11). These S/N data are summarized in Tables 5.12.

Table 5.12: Signal-to-Noise Ratio for Data Averaged *Bremsstrahlung* Profiles

N	8	16	32	64	128	256	512	1024
σ	0.0112	0.0089	0.0078	0.0076	0.0075	0.0074	0.0076	0.0072
S/N	120	151	172	176	179	181	176	186

Normalized S/N estimates, as a function of data average number, N, are shown in Figure 5.21.

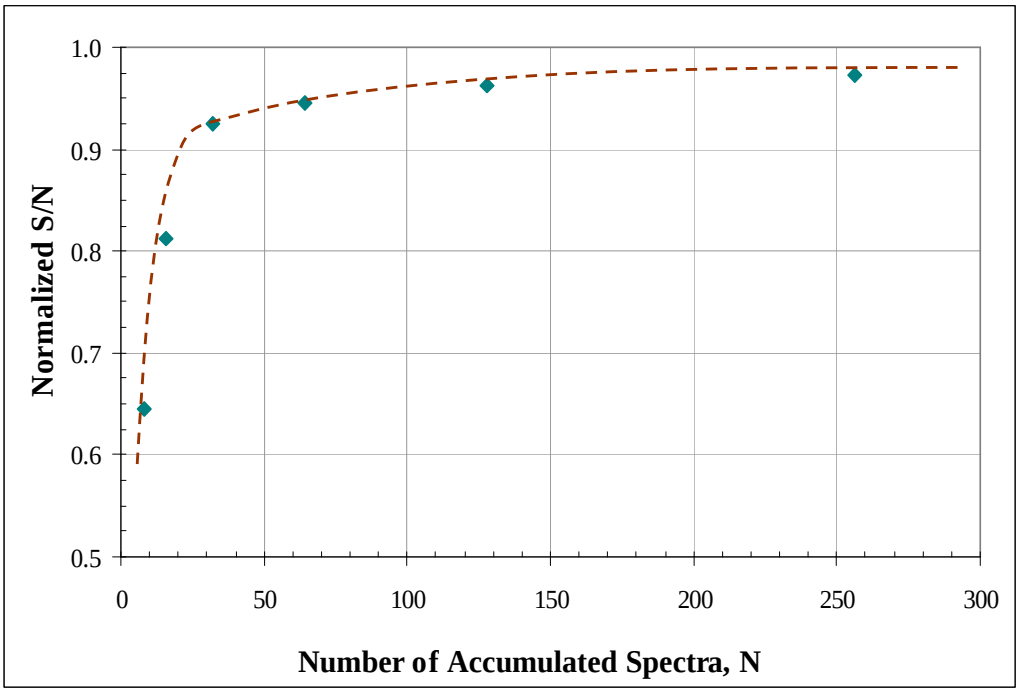

Figure 5.21: Normalized Signal-to-Noise Ratio for *Bremsstrahlung* Profiles as a Function of Data Average Number

The trend shown in Figure 5.21 demonstrated the efficacy of using a data averaging algorithm for increase in S/N, by reduction of the *rms* contribution of shot noise in plasma emission. Further, the asymptotic trend shown in Figure 5.21 indicated an optimum value for data average number, N, in the region of 120.

5.4 Dependence of *Bremsstrahlung* Emission Parameters on Contaminant Concentration and Photon Flux

5.4.1 Preamble

The aim of this experimental work was to quantitatively demonstrate the effect on the *Bremsstrahlung* emission profile of two experimental parameters: *i*. scattering centre concentration; and, *ii*. laser photon flux. These parameters are independent and synonymous with analyte concentration and pulse energy, respectively. Characterization of *Bremsstrahlung* emission profiles, with respect to analyte concentration and pulse energy, was considered important for understanding critical processes taking place during plasma formation and expansion.

5.4.2 Results and Analysis

The experimental set-up for this series of experiments was previously illustrated (see Figure 4.5). Experimental parameters were fixed, and included laser pulse energy ~100mJ, pulse duration = 7ns, pulse repetition rate = 10Hz, and monochromator entrance slit width ~200μm.

In the first part of this experiment *Bremsstrahlung* emission was investigated as a function of scattering centre concentration. The target media chosen for the first phase of this investigation was aqueous sodium chloride, diluted from stock solution to represent an order of magnitude range of concentration. The *Bremsstrahlung* emission profile from a sample of distilled water was used as a reference standard. A sample of tap water was used to provide a further comparative *Bremsstrahlung* emission profile. A series of equivalent tests was also undertaken with aqueous mercury II chloride, similarly diluted from stock solution to represent an order of magnitude range of concentration. As with the $NaCl_{(aq)}$ samples *Bremsstrahlung* emission profiles were recorded for distilled and tap water samples for comparison.

In the second part of this experiment *Bremsstrahlung* emission was investigated as a function of laser pulse energy, for a target medium consisting of 500ppm $NaCl_{(aq)}$. Seven pulse energies were used in the approximate range 85-165mJ, separated by an increment of typically 12-16mJ. Comparative *Bremsstrahlung* emission profiles were also recorded for distilled and tap water samples.

a. Effect of $NaCl_{(aq)}$ on Bremsstrahlung Emission

The temporal window of interest was between 175ns and 225ns after plasma formation. Typical *Bremsstrahlung* emission profiles are shown in Figure 5.22 for $NaCl_{(aq)}$ concentrations of 112ppm and 1100ppm. Emission profiles for distilled and tap water are shown for comparison. *Bremsstrahlung* emission profiles for the full range of $NaCl_{(aq)}$ concentrations used are reproduced at Appendix XI.

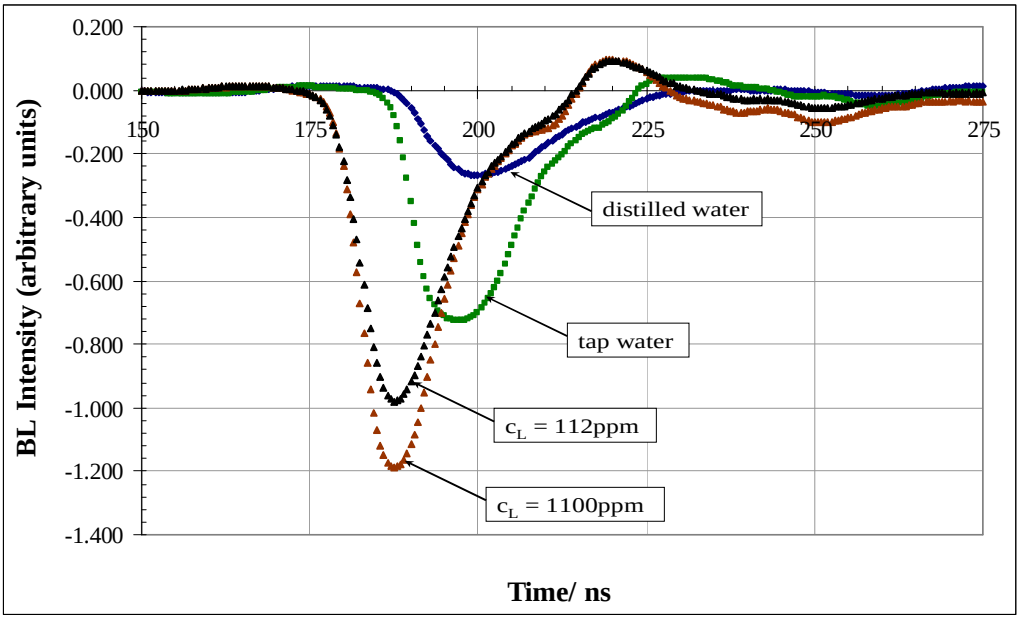

Figure 5.22: Temporal History of *Bremsstrahlung* Profiles for Sodium Chloride, Distilled Water and Tap Water Samples

The presence of ppm concentrations of $NaCl_{(aq)}$ were demonstrated, on examination of the data shown in Figure 5.22, to significantly increase the peak intensity of *Bremsstrahlung* emission. Increases of approximately 38% and 67% were calculated for 112ppm and 1100ppm concentrations, respectively, compared to peak *Bremsstrahlung* intensity for the tap water sample.

Bremsstrahlung emission profiles for $NaCl_{(aq)}$ were integrated over the duration of the profile in order to quantify the radiated energy associated with *Bremsstrahlung* emission. A 10% criterion was used which limited integration to the temporal range within the *Bremsstrahlung* profile for which intensity was >10% of peak intensity. Results for all concentrations of $NaCl_{(aq)}$ are summarized in Table 5.13 and shown in Figure 5.23. Normalized *Bremsstrahlung* emissions for distilled and tap waters were calculated to be 0.28 & 0.71, respectively.

Table 5.13: Normalized *Bremsstrahlung* Emission Energy as a Function of Sodium Chloride Concentration

$NaCl_{(aq)}$ Conc./ ppm	Normalized Area
1100	1.00
550	0.96
225	0.99
112	0.86
56	0.69

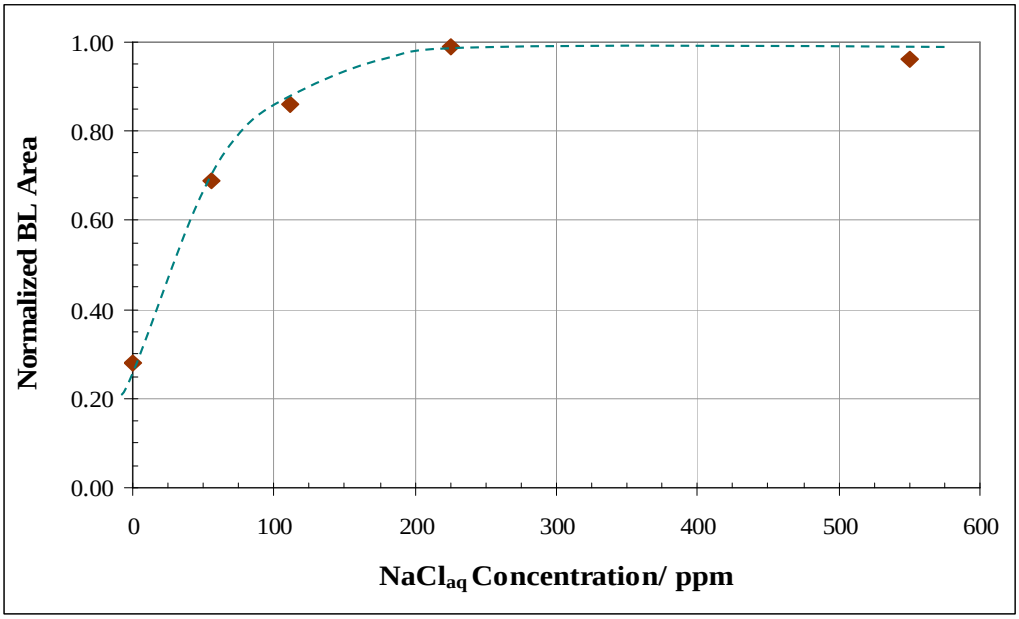

Figure 5.23 Saturation of *Bremsstrahlung* Profile with Increasing Concentration of Aqueous Sodium Chloride

Radiative emission associated with the *Bremsstrahlung* emission profile increased linearly with increasing $NaCl_{(aq)}$ concentration, up to a limit of ~75ppm. For higher analyte concentrations the rate of increase of *Bremsstrahlung* emissions reduced asymptotically, reaching a saturation maximum for analyte concentration of ~225ppm. No significant change in *Bremsstrahlung* emission was demonstrated for higher analyte concentrations in excess of ~225ppm.

b. Effect of $HgCl_{2(aq)}$ on Bremsstrahlung Emission

The temporal window of interest was between 200ns & 250ns following plasma formation. Typical *Bremsstrahlung* emission profiles are shown in Figure 5.24 for $HgCl_{2(aq)}$ concentrations of 50ppm and 500ppm. Emission profiles for distilled and tap water are shown for comparison. *Bremsstrahlung* emission profiles for the full range of $HgCl_{2(aq)}$ concentrations used are reproduced at Appendix XI.

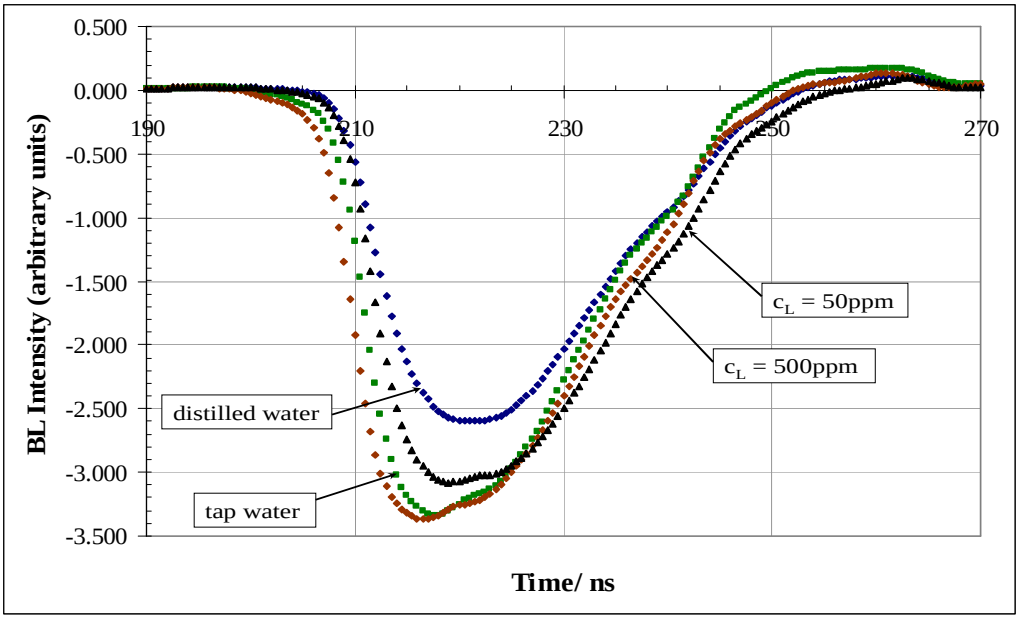

Figure 5.24: Temporal History of *Bremsstrahlung* Profiles for Mercury II Chloride, Distilled Water and Tap Water Samples

The presence of ppm concentrations of $HgCl_{2(aq)}$ were demonstrated, on examination of the data shown in Figure 5.24, to increase the peak intensity of *Bremsstrahlung* emission. Increases of approximately 19% and 31% were estimated for 50ppm and 500ppm concentrations, respectively, compared to peak *Bremsstrahlung* intensity for the distilled water sample.

Bremsstrahlung emission peak intensity displayed greater sensitivity to increases in $NaCl_{(aq)}$ concentration than equivalent increases in $HgCl_{2(aq)}$ concentration. Based on data shown in Figure 5.22 *Bremsstrahlung* peak intensity increased by ~21% for an order of magnitude increase in $NaCl_{(aq)}$ concentration (112ppm to 1000ppm). An equivalent increase in $HgCl_{2(aq)}$ concentration (50ppm to 500ppm), based on data shown in Figure 5.24, generated at increase in *Bremsstrahlung* peak intensity of ~10%.

Bremsstrahlung emission profiles for $HgCl_{2(aq)}$ were integrated over the duration of the profile in order to quantify the radiated energy associated with *Bremsstrahlung* emission. A 10% criterion was used, which limited integration to the temporal range within the *Bremsstrahlung* profile for which intensity was >10% of peak intensity. Results for all concentrations of $HgCl_{2(aq)}$ are summarized in Table 5.14, and shown in Figure 5.25. Normalized *Bremsstrahlung* emissions areas for distilled and tap waters were calculated to be 0.64 & 0.96, respectively.

Table 5.14: Normalized *Bremsstrahlung* Emission Energy as a Function of Mercury II Chloride Concentration

$HgCl_{2(aq)}$ Concentration	1000	500	100	50
Normalized Area	0.96	1.00	0.94	0.91

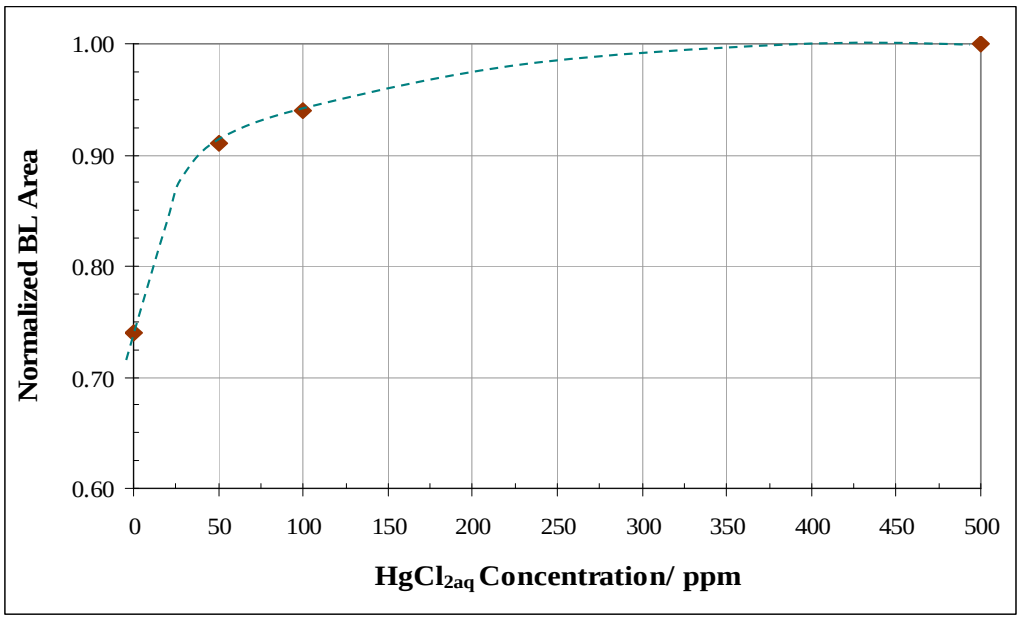

Figure 5.25 Saturation of *Bremsstrahlung* Profile with Increasing Concentration of Aqueous Mercury II Chloride

As with the equivalent data for $NaCl_{(aq)}$, radiative emissions associated with the *Bremsstrahlung* emission profile were positively correlated with increasing $HgCl_{2(aq)}$ concentration up to a limit of ~30ppm. For higher analyte concentrations the rate of increase of *Bremsstrahlung* emissions reduced asymptotically, reaching a saturation maximum for analyte concentration of ~400ppm. No significant change in *Bremsstrahlung* emission was demonstrated for analyte concentrations in excess of ~400ppm.

c. Effect of Laser Pulse Energy on Bremsstrahlung Emission

The temporal window of interest was between 160ns & 220ns following plasma formation. Typical *Bremsstrahlung* emission profiles are shown in Figures 5.26 for three representative pulse energies. A complete set of *Bremsstrahlung* emission profiles for the range of pulse energy used is presented at Appendix XII.

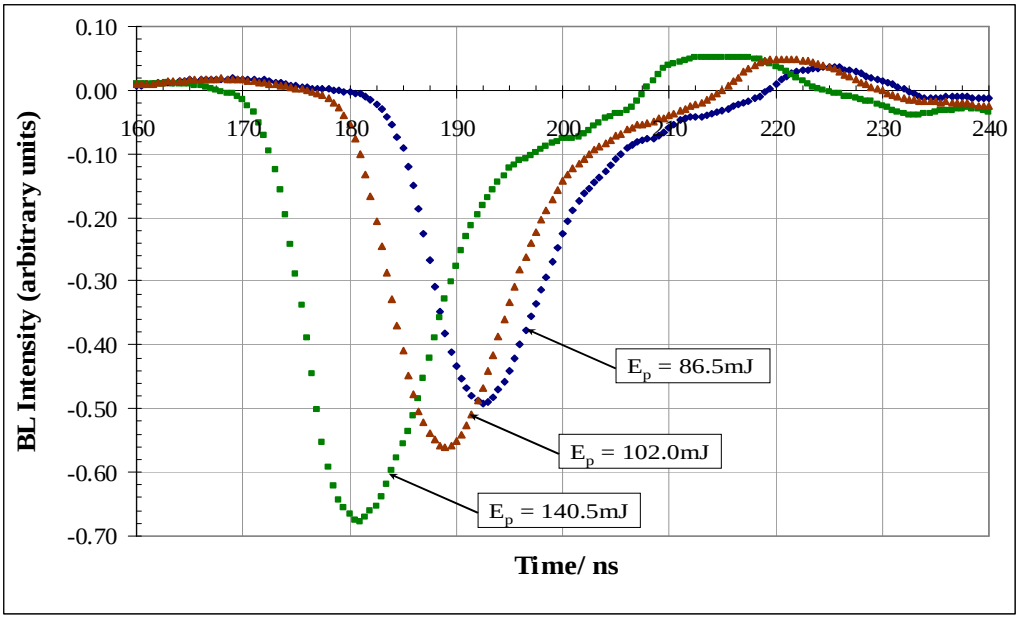

Figure 5.26: Temporal History of *Bremsstrahlung* Profiles for Different Pulse Energies

The data shown in Figure 5.26 demonstrated significant increase in *Bremsstrahlung* emission peak intensity as a result of increase in pulse energy. Increases of approximately 17% and 40% were recorded for pulse energies of 102.0mJ and 140.5mJ, respectively, compared to pulse energy of 86.5mJ.

Bremsstrahlung emission profiles were integrated over the duration of the profile in order to quantify the radiated energy associated with *Bremsstrahlung* emission. A 10% criterion was (again) used, which limited integration to the temporal range within the *Bremsstrahlung* profile for which intensity was >10% of peak intensity. Results for each pulse energy are summarized in Table 5.15, and shown in Figure 5.27.

Table 5.15: Normalized *Bremsstrahlung* Emission Energy as a Function of Laser Pulse Energy

Pulse Energy, E_p/ mJ	86.5	102.0	116.5	127.5	140.5	153.0	164.5
Normalized Area	0.34	0.66	0.76	0.85	0.93	0.88	1.00

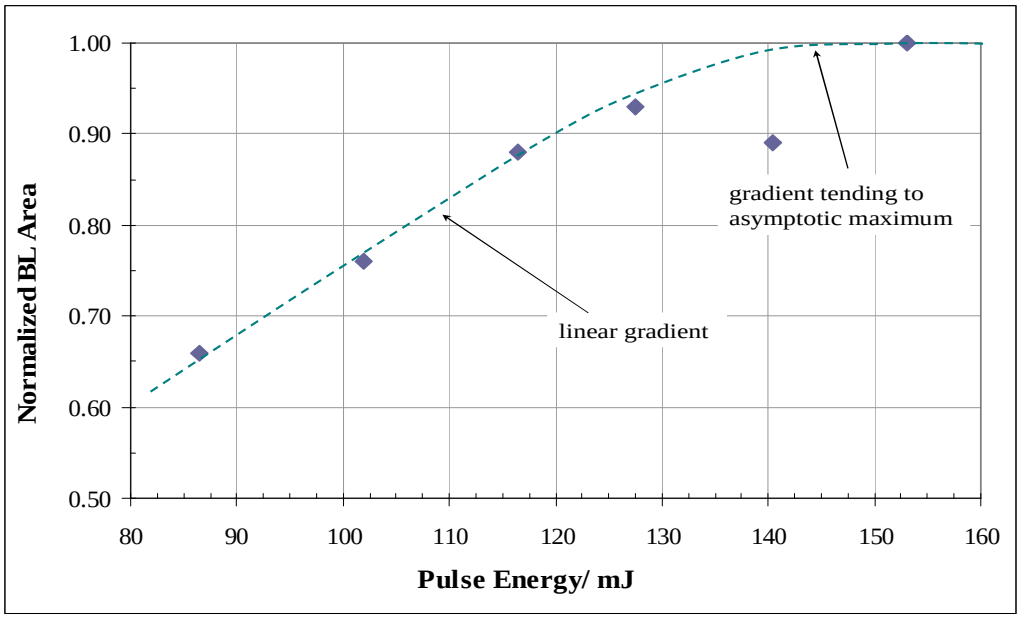

Figure 5.27 Saturation of *Bremsstrahlung* Profile with Increasing Pulse Energy

The data shown in Figure 5.27 demonstrated a linear increase in normalized *Bremsstrahlung* emission intensity with pulse energy up to a limit of ~130mJ. For higher pulse energies the *Bremsstrahlung* emission intensity tended asymptotically to an upper limit, reaching a saturation maximum at ~150mJ.

5.4.3 Dependence of *Bremsstrahlung* Emission Parameters on Concentration of Target Species and Laser Pulse Energy

The gradient (G_1) of the linear portion of the *Bremsstrahlung* profile was measured, for increasing *Bremsstrahlung* intensity, for profiles corresponding to different concentrations of $NaCl_{(aq)}$ and $HgCl_{2(aq)}$ (see Figures 5.22 & 5.24 and Appendix XI), and different pulse energies (see Figure 5.26 and Appendix XII). The temporal region (Δt_1) over which the rate of increase in *Bremsstrahlung* intensity was linear was also measured. In addition peak *Bremsstrahlung* intensity (S_{max}) and the time taken to reach this value (t_{peak}) were measured. Finally the duration of *Bremsstrahlung* emission based on the 10% intensity criterion (t_{Bremss}), and FWHM of the continuum emission envelope (t_{FWHM}) were measured. These properties are shown in Figure 5.28.

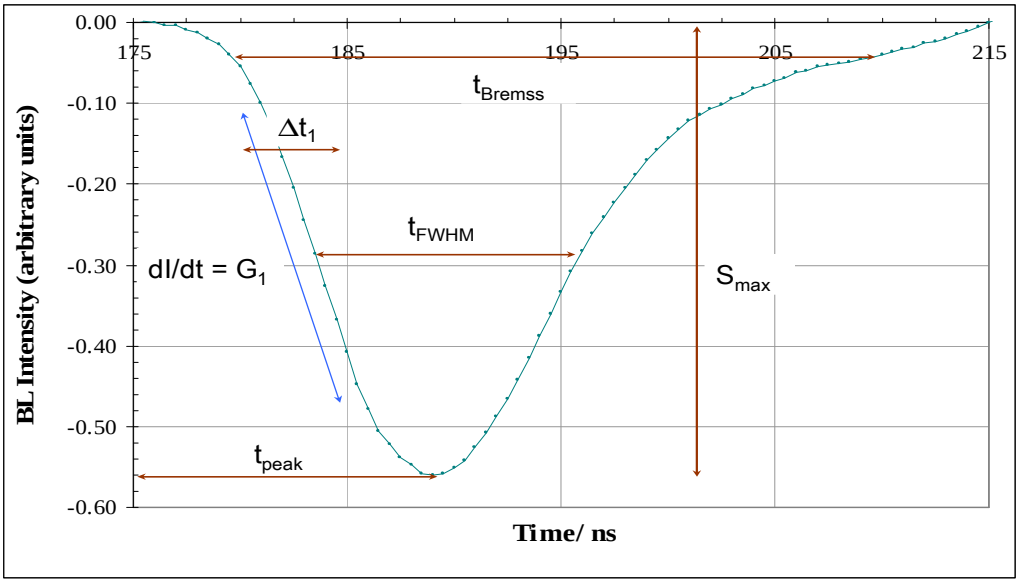

Figure 5.28 Sketch of Key Characteristics for Typical *Bremsstrahlung* Profile

These *Bremsstrahlung* emission profile characteristics, corresponding to changes in aqueous sodium and mercury concentration, are summarized in Tables 5.16 & 5.17, respectively. Equivalent data corresponding to changes in laser pulse energy are summarized in Table 5.18.

Table 5.16: *Bremsstrahlung* Profile Properties for Different NaCl Concentrations

Target Solution	Characteristics		Emission Properties			
	Δt_1/ ±0.5ns	G_1/ $mVns^{-1}$ ±15%	S_{max}/ ±40mV	t_{peak}/ ±2ns	t_{FWHM}/ ±4ns	t_{Bremss}/ ±4ns
56ppm	4.5	100	750	190	16.0	33.5
112ppm	4.5	125	990	187.5	14.0	31.0
225ppm	4.0	152	1130	188	14.0	32.0
550ppm	5.0	152	1140	187.5	13.0	31.0
1100ppm	4.5	182	1190	187.5	14.0	29.5
tap water	3.5	123	730	197	17.0	32.5
distilled water	4.5	31	270	200	20.5	36.0

Table 5.17: *Bremsstrahlung* Profile Properties for Different $HgCl_2$ Concentrations

Target Solution	Characteristics		Emission Properties			
	Δt_1/ ±0.5ns	G_1/ $mVns^{-1}$ ±15%	S_{max}/ ±50mV	t_{peak}/ ±2ns	t_{FWHM}/ ±4ns	t_{Bremss}/ ±4ns
50ppm	4.5	478	3100	219	26.5	39.0
100ppm	4.0	520	3200	218	25.0	39.5
500ppm	4.0	575	3350	216	25.0	39.5
1000ppm	4.0	563	3400	215	21.5	35.5
tap water	4.5	533	3350	217	23.0	37.0
distilled water	5.0	330	2600	222	24.0	38.0

Table 5.18: *Bremsstrahlung* Profile Properties for Different Laser Pulse Energies

Pulse Energy, E_p/ mJ	Characteristics		Emission Properties			
	Δt_1/ ±0.5ns	G_1/ $mVns^{-1}$ ±15%	S_{max}/ ±50mV	t_{peak}/ ±2ns	t_{FWHM}/ ±4ns	t_{Bremss}/ ±4ns
86.5	4.0	62	490	192.5	13.0	27.5
102.0	5.5	75	560	189.0	13.0	27.5
116.5	4.5	93	670	185.0	12.5	30.0
127.5	5.0	88	680	183.5	12.5	28.0
140.5	4.5	96	675	182.5	13.5	28.0
153.0	4.5	119	720	179.0	13.5	27.5

From the above data it was concluded that the temporal characteristics t_{peak}, t_{FWHM} and t_{Bremss} were unchanged, for all intents and purposes, with respect to analyte concentration (for both sodium and mercury) and pulse energy. Examination of the data in Tables 5.16 & 5.17 suggested positive correlations between peak *Bremsstrahlung* intensity (S_{max}) and analyte concentrations, as shown in Figure 5.29.

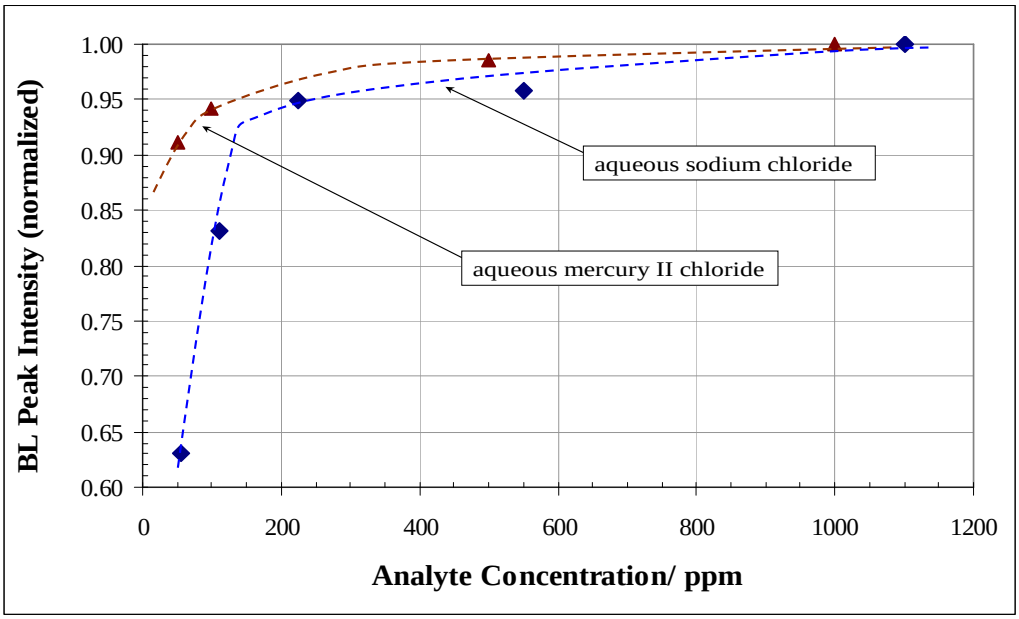

Figure 5.29 Correlation between Peak *Bremsstrahlung* Intensity and Analyte Concentration

For both aqueous sodium and mercury species the increase in *Bremsstrahlung* peak intensity was linear for concentrations below ~100ppm. For higher analyte concentrations the rate of increase in *Bremsstrahlung* peak intensity decreased asymptotically, and reached a saturation limit for concentrations in excess of ~750ppm.

Review of the data in Table 5.18 suggested a similar correlation between S_{max} and pulse energy, as shown in Figure 5.30.

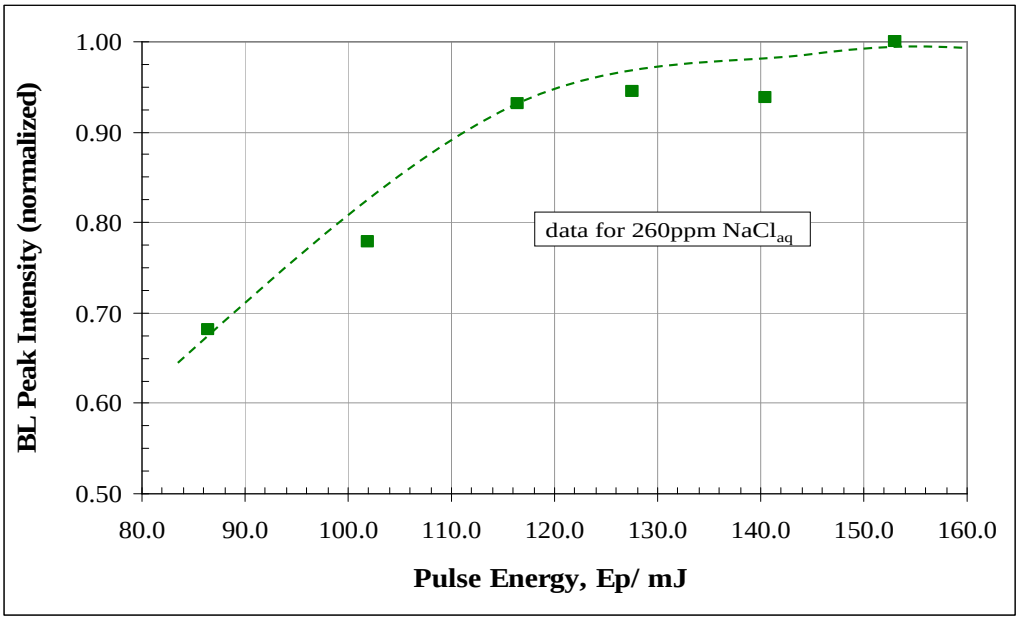

Figure 5.30 Correlation between Peak *Bremsstrahlung* Intensity and Pulse Energy

Increase in *Bremsstrahlung* peak intensity was linear for pulse energy between ~85mJ and ~115mJ. At higher pulse energies the *Bremsstrahlung* peak intensity tended to a saturation limit. No increase in *Bremsstrahlung* peak intensity was demonstrated for pulse energy in excess of ~150mJ.

Examination of the data in Tables 5.16 & 5.17 indicated no significant change in time period (Δt_1) for which *Bremsstrahlung* intensity increased linearly as a function of increase in analyte concentration. This was demonstrated for both chloride solutions (sodium and mercury), as well as *Bremsstrahlung* emission profiles corresponding to distilled and tap water samples. Examination of the data in Table 5.18 indicated a similar insensitivity for changes in pulse energy.

A correlation was apparent, however, between the rate of change of *Bremsstrahlung* intensity (G_1) and analyte concentration (Tables 5.16 & 5.17), as well as pulse energy (Table 5.18). These correlations are shown in Figures 5.31 and 5.32, respectively.

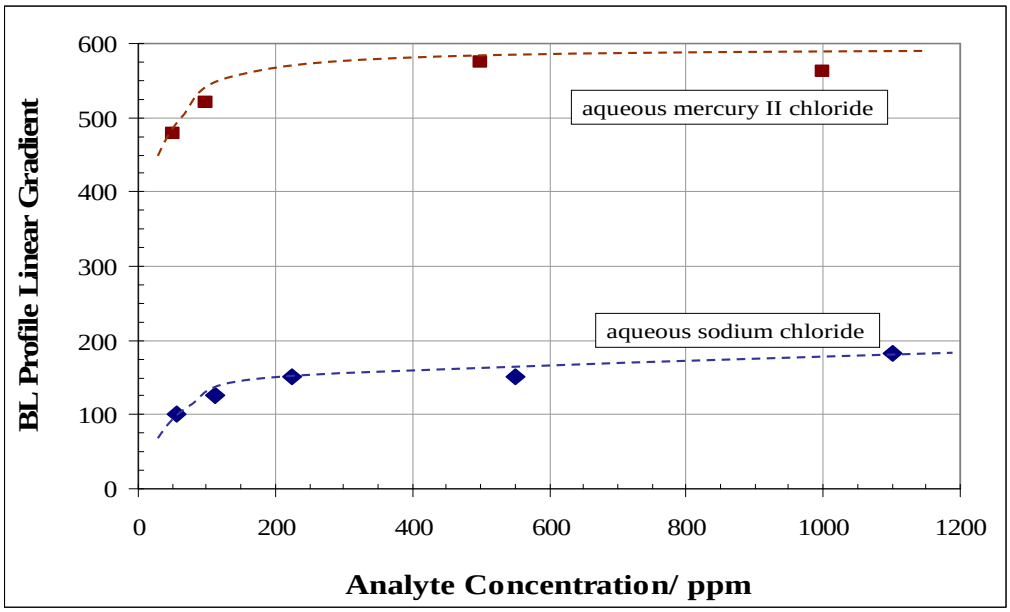

Figure 5.31 Rate of Increase in Linear *Bremsstrahlung* Profile Intensity as a Function of Analyte Concentration

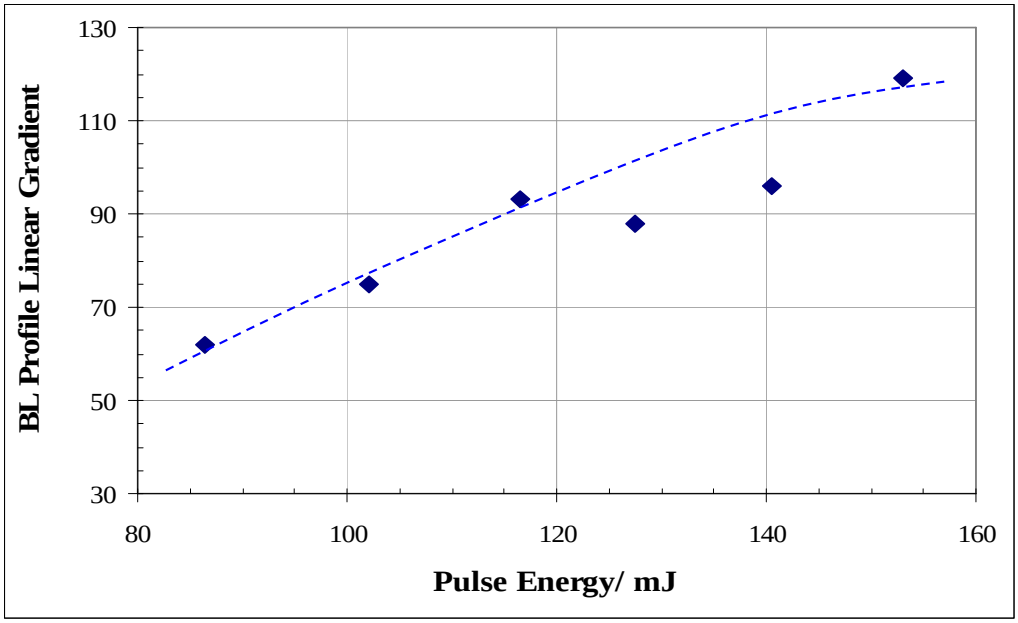

Figure 5.32 Rate of Increase in Linear *Bremsstrahlung* Profile Intensity as a Function of Pulse Energy

The linear gradient of the *Bremsstrahlung* emission profiles reached a saturation limit for analyte concentration in the order of 200ppm (for both Na and Hg species). Interpretation of the relationship between gradient and concentration below 200ppm was limited due to the lack of data for lower analyte concentrations. No saturation limit for *Bremsstrahlung* gradient was evident as a function of increasing laser pulse energy. Detailed interpretation of this relationship was similarly limited by the absence of data at higher pulse energies.

5.5 Optimization of Experimental Parameters to Increase LIBS Sensitivity

5.5.1 Rationale

The research reported in this section was undertaken to improve the sensitivity of the LIBS system through optimization of specific experimental parameters. These parameters were delay time, gate width, data average number and laser pulse energy. LIBS system sensitivity was quantified by the signal-to-noise ratio (S/N) for the target atomic emission line, which has been previously defined (*eqn.[3.12]*). The conventional equation for calculating sensitivity of a LIBS system, D_L, based on the construction of a calibration curve covering an order of magnitude of analyte concentration (number of atomic species per unit volume), is expressed as follows:

$$D_L = 3\sigma_{bkgnd} / \Gamma \quad \ldots \quad \ldots \quad \ldots \quad [5.6]$$

σ_{bkgnd} = *standard deviation of background signal*
Γ = *gradient of calibration curve*

A comprehensive review of the concept of 'limit of quantitation' has been reported (Mermet: 2008). In the idealized case where the calibration curve intercepts the origin i.e. mean background intensity tends to zero, *eqn.[5.6]* may be expressed (Charfi & Harith: 2002) as follows:

$$D_L = 3c_L / (S/N) \quad \ldots \quad \ldots \quad \ldots \quad [5.7]$$

c_L = *analyte concentration*
S/N = emission line signal-to-noise ratio

5.5.2 Temporal Gating of Emission Signals

The principle of temporal gating for increasing emission line S/N was demonstrated with respect to the contribution to emission profiles from *Bremsstrahlung* and discrete atomic line emissions. Emission profiles were recorded using a sample of $NaCl_{(aq)}$ at 100ppm

concentration. The spectrometer grating was initially set to the strong Na(I) emission line at 589.00nm, and subsequently to a wavelength a significant spectral distance from the Na(I) emission wavelength i.e. 590.10nm. These emission profiles are shown in Figure 5.33.

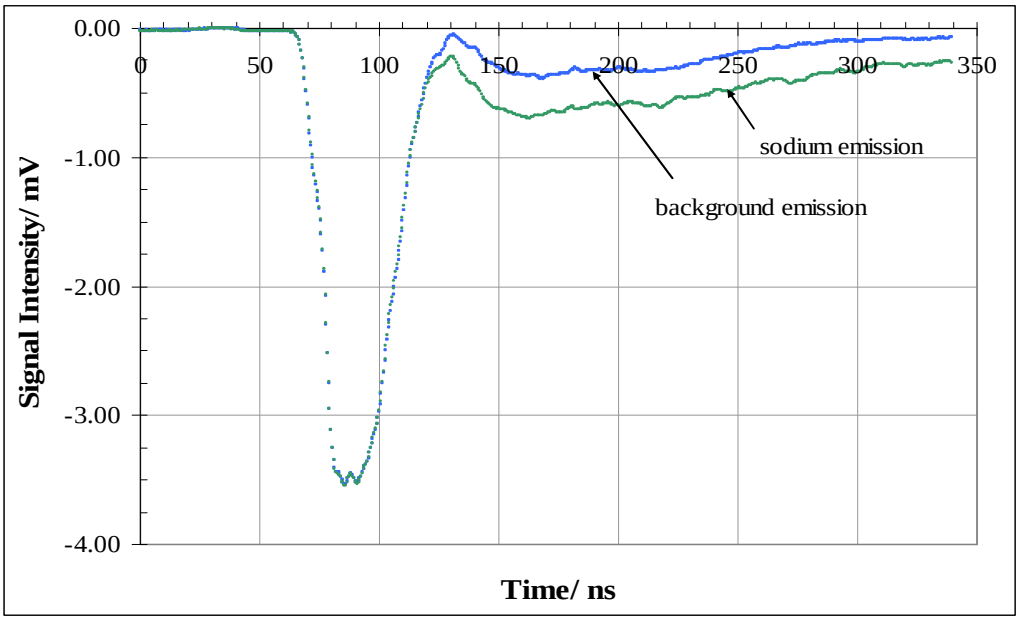

Figure 5.33: Temporal Emission Profiles for Strong Na(I) Emission Line and Representative Background Wavelength

As shown in Figure 5.33 the *Bremsstrahlung* profiles were unchanged for the wavelengths used. The principal difference between the emission profiles was the significant increase in radiated energy for spectrometer grating set to 589.00nm, in the period after *Bremsstrahlung* continuum had reduced to negligible intensity i.e. for times in excess of ~130ns after plasma formation. This increase was attributed to the specific atomic line emission at 589.00nm. Using a suitable delay time, guided by the temporal profiles shown in Figure 5.33, emission spectra were recorded over a time period (gate

width) during which *Bremsstrahlung* contribution to the total emission profile was minimal.

a. Optimum Delay Time

For analysis of the dependence of detection sensitivity on gating delay time, t_d, laser parameters were set, as follows: pulse energy = 32mJ, pulse repetition rate = 10Hz and spectrometer entrance slit = 250μm. The delay time was increased from 200ns to 362ns in steps of 10ns, with gate width fixed at 400ns. Optimized emission spectra for delay times of 220, 252 & 296ns are shown in Figure 5.34. A complete record of LIBS emission spectra for the full set of delay times used is presented in Appendix XIII.

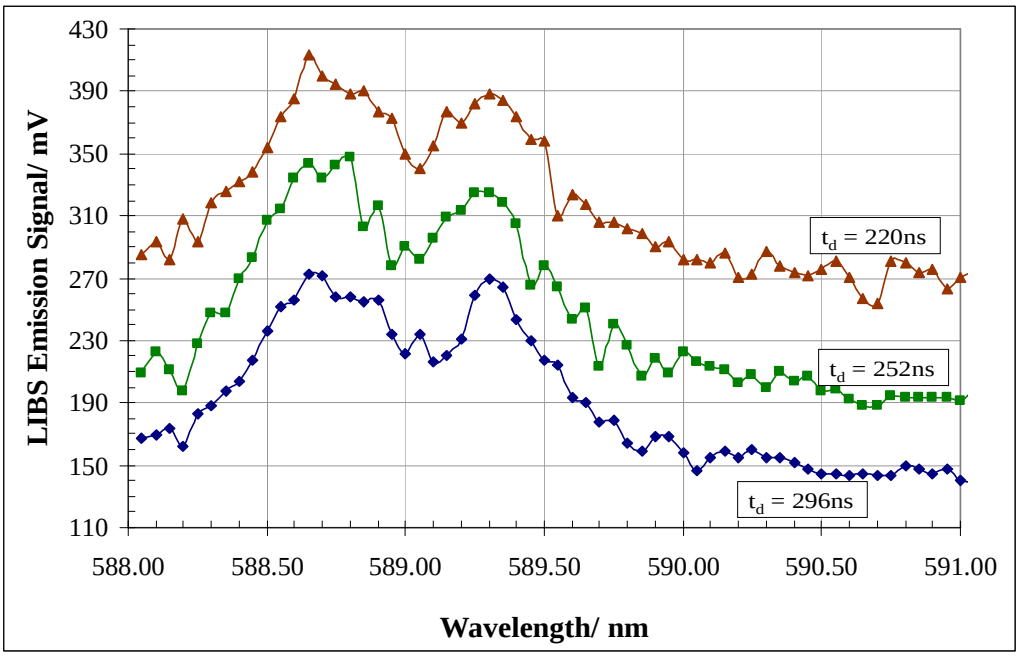

Figure 5.34: LIBS Emission Spectra for Delay Times of 220, 252 & 296ns

Data for Na(I) emission line intensity, S_{Na}, mean background intensity, m_{bkgnd}, standard deviation of the background, σ_{bkgnd}, and signal-to-noise ratio, S/N, are summarized in

Table 5.19. Values for m_{bkgnd} and σ_{bkgnd} were calculated over the spectra range 590.00nm to 591.00nm inclusive, at an increment of 0.05nm.

Table 5.19: Measured and Calculated LIBS Data *w.r.t.* Delay Time

t_d/ ns (±4ns)	S_{Na} (±5%)	m_{bkgnd} (±5%)	σ_{bkgnd}	ΔS (±5%)	S/N (±7%)
200	586.36	444.92	14.64	141.44	9.7
212	476.65	348.26	8.81	128.39	14.6
220	399.58	274.52	8.54	125.06	14.6
228	384.86	237.41	10.25	147.45	14.4
240	340.70	212.26	8.40	128.44	15.3
252	334.23	200.97	9.79	133.26	13.6
262	315.69	193.14	4.79	122.55	25.6
274	325.84	173.21	8.06	152.63	18.9
284	294.07	165.28	8.37	128.79	15.4
288	275.97	151.34	7.77	124.63	16.0
296	271.09	149.39	5.97	121.70	20.4
310	337.80	185.11	7.09	152.69	21.5
318	308.20	180.74	7.30	127.46	17.5
324	309.08	173.67	5.76	135.41	23.5
334	263.58	149.90	5.38	113.68	21.1
340	255.28	146.34	6.38	108.94	17.1
348	256.90	142.05	5.86	114.85	19.6
354	253.14	138.06	4.66	115.08	24.7
362	250.00	134.53	5.56	115.47	20.8

Figure 5.35 shows the influence of delay time on Na(I) emission line and mean background intensities.

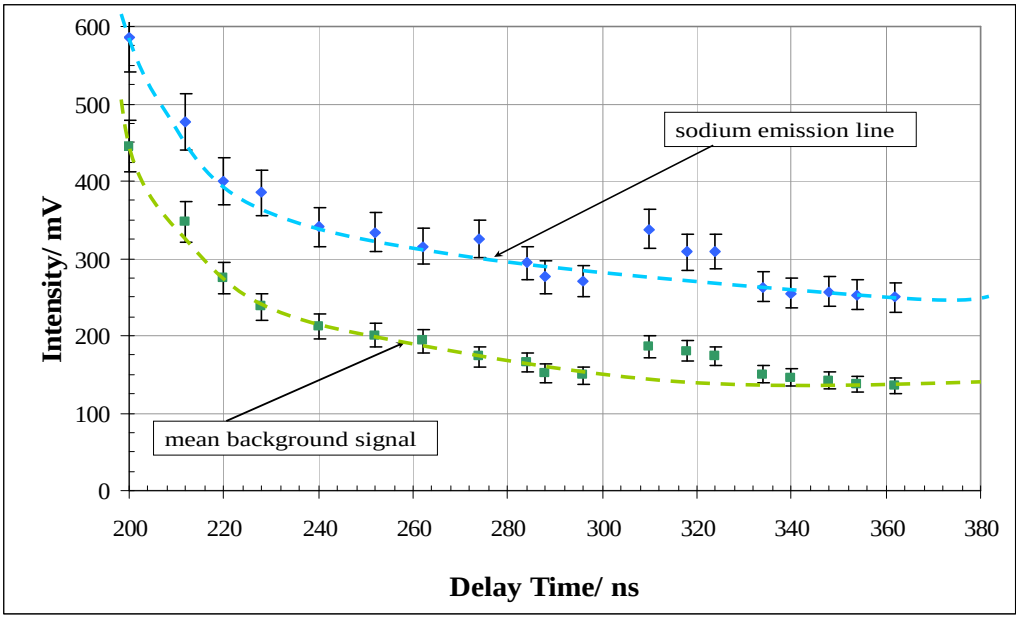

Figure 5.35: Emission Line & Mean Background Intensities *vs.* Delay Time

The profiles shown in Figure 5.35 demonstrate a slowly decreasing relationship between delay time and both emission line intensity and mean background intensity, for value of delay time between ~200ns & ~360ns. This was commensurate with the gradual decrease in overall radiative emission from the cooling plasma. The significant increase in intensity for delay times less than ~230ns reflected the rapid change in emission line and background radiated energy as the signal accumulation window was 'gated into' the trailing edge of the decaying *Bremsstrahlung* profile.

Figure 5.35 included three pairs of data points, corresponding to delay times of 310ns, 318ns and 324ns, which indicated intensities significantly higher than estimated values interpolated from the overall trend. The reason for these high intensity readings was attributed to fluctuations in the HT applied to the PMT during accumulation of emitted radiation. Evidence for a systemic source of anomalous data was based on the ratio of these outlying data pairs i.e. S_{Na}: m_{bkgnd}, which was equal (within the limits of experimental error) to the ratio of equivalent data which were consistent with the overall

trend. This was demonstrated as follows: for delay times of 310ns, 318ns and 324ns, S_{Na}: m_{bkgnd} were 1.82, 1.71 & 1.78, respectively; for delay times in the range 334ns to 362ns, the mean S_{Na}: m_{bkgnd} was 1.80; for delay times in the range 240ns to 296ns, the mean S_{Na}: m_{bkgnd} was 1.73.

Figure 5.36 shows the effect of delay time on S/N for the Na(I) emission line at 589.00nm.

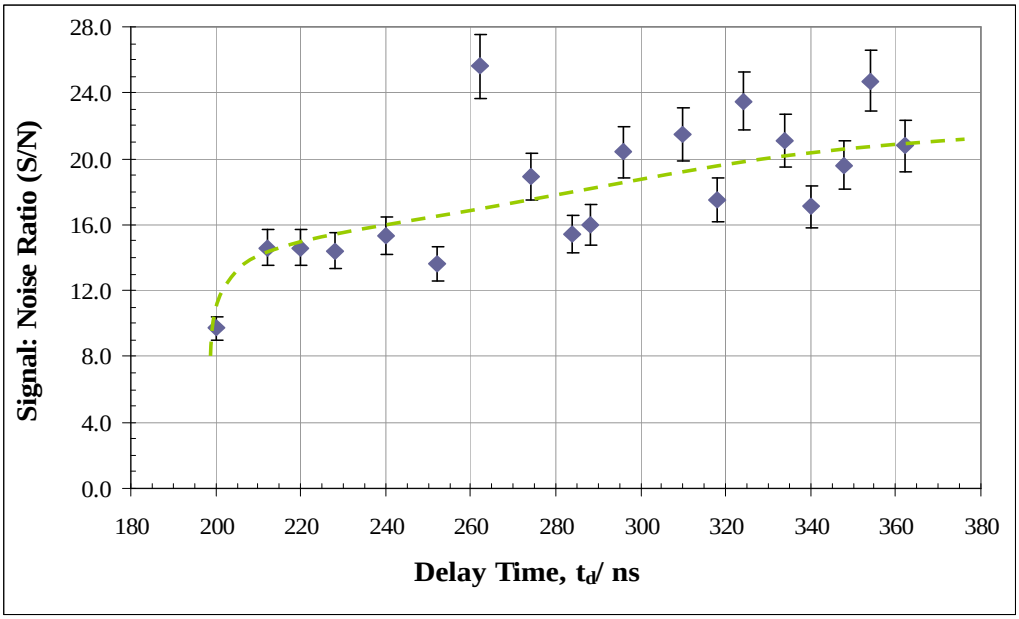

Figure 5.36: Signal-to-Noise Ratio *vs.* Delay Time

The data is Figure 5.36 showed an increase in S/N with increasing delay time over the range of delay times used. The correlation was stronger for shorter delay times i.e. <260ns. For delay times up to ~360ns the correlation was significantly weaker. There was an indication of the onset of S/N saturation for delay times in the range 310ns to 360ns.

b. Optimum Gate Width

For investigation of optimum gate width, t_g, with respect to S/N of Na(I) emission line, LIBS spectra were generated for the same experimental parameters as previously described. The gate width was increased from 280ns to 430ns in steps of 10ns. Delay time was fixed at 320ns based on the data shown in Figure 5.36. Emission spectra for gate widths of 310ns, 390ns & 1000ns are shown in Figure 5.37. A complete record of emission spectra for the full range of gate widths used is presented in Appendix XIV.

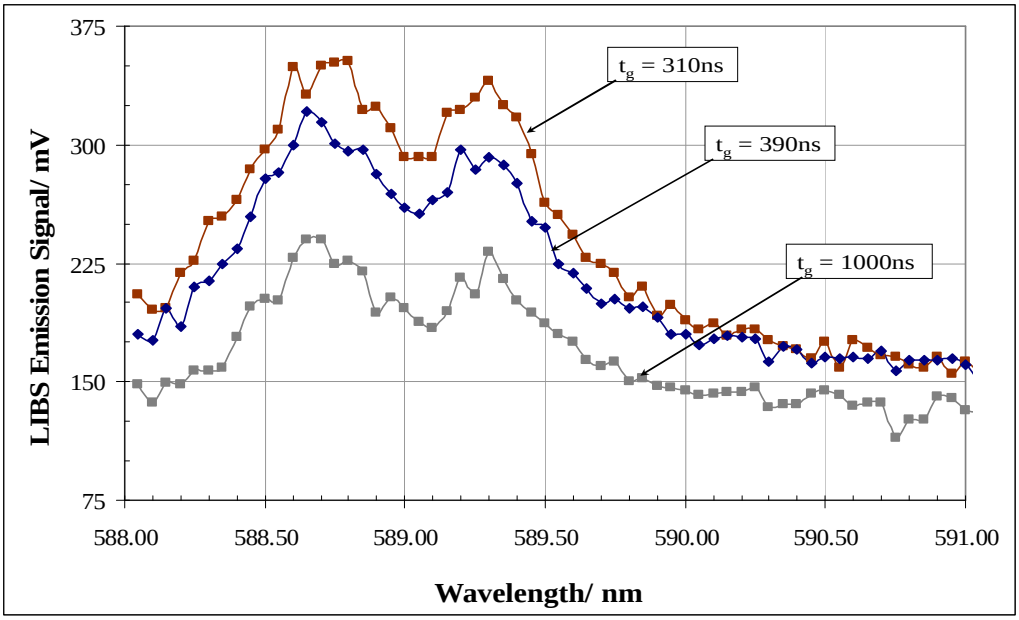

Figure 5.37: LIBS Emission Spectra for Gate Widths of 310, 390 & 1000ns

Data for Na(I) emission line intensity, S_{Na}, mean background intensity, m_{bkgnd}, standard deviation of the background, σ_{bkgnd}, and signal-to-noise ratio, S/N, are summarized in Table 5.20. Values for m_{bkgnd} and σ_{bkgnd} were calculated over the spectra range 590.00nm to 591.00nm inclusive, at an increment of 0.05nm.

Table 5.20: Measured and Calculated LIBS Data *w.r.t.* Gate Width

t_g/ ns (±4ns)	S_{Na} (±5%)	m_{bkgnd} (±5%)	ΔS (±5%)	σ_{bkgnd}	S/N (±7%)
280	386.66	184.69	201.97	10.75	18.8
290	359.25	176.77	182.48	11.97	15.2
300	369.17	174.00	195.17	10.26	19.0
310	349.64	171.76	177.88	9.95	17.9
320	348.94	169.14	179.80	11.64	15.4
330	343.99	166.93	177.06	10.44	17.0
340	339.75	161.15	178.60	9.75	18.3
350	339.97	158.32	181.65	9.35	19.4
360	313.51	162.46	151.05	9.36	16.1
370	301.54	171.84	129.70	8.35	15.5
380	306.21	170.75	135.46	8.55	15.8
390	314.34	168.48	145.86	6.78	21.5
400	334.93	179.66	155.27	8.80	17.6
410	308.17	182.69	125.48	7.23	17.4
420	316.28	185.84	130.44	6.81	19.2
430	311.86	189.89	121.97	6.56	18.6
1000	240.36	137.32	103.04	7.68	13.4

Figure 5.38 shows the influence of gate width on Na(I) emission line and mean background intensities.

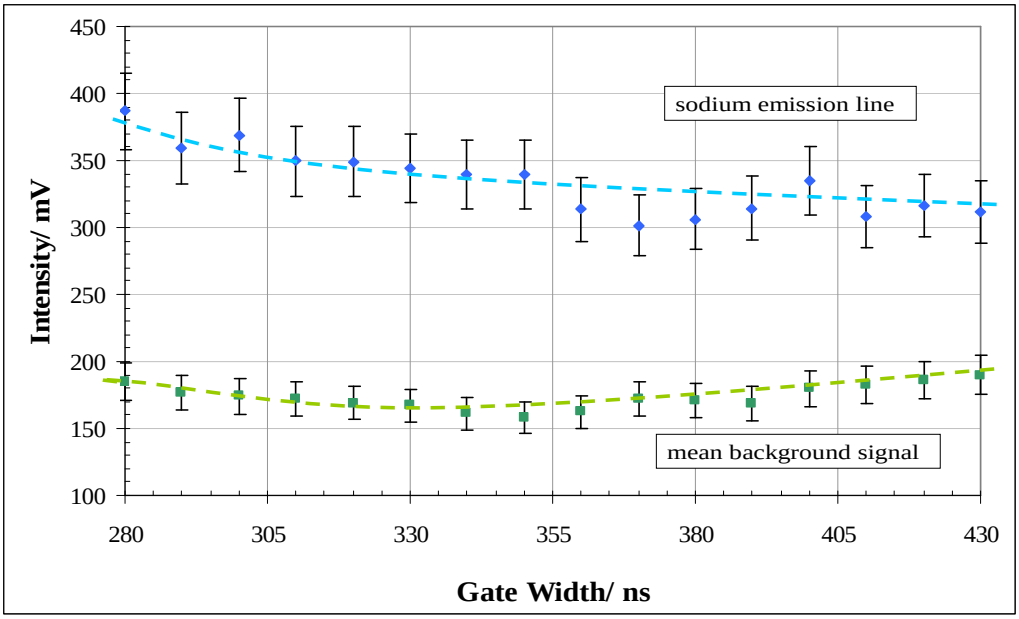

Figure 5.38: Emission Line & Mean Background Intensities *vs*. Gate Width

The data in Figure 5.38 showed a reduction of ~15% in emission line signal intensity for gate widths between 280ns and 430ns. This was attributed to the averaging effect of signal accumulation in the box car integrator as the gate width was increased. This decrease reflected the gradual decrease in emission line intensity in the temporal region between 600ns and 750ns (i.e. the sum of delay time and gate width) after plasma formation. No statistically significant variation in mean background intensity was indicated by the data shown in Figure 5.38.

Figure 5.39 shows the effect of changing gate width on S/N for the Na(I) emission line at 589.00nm.

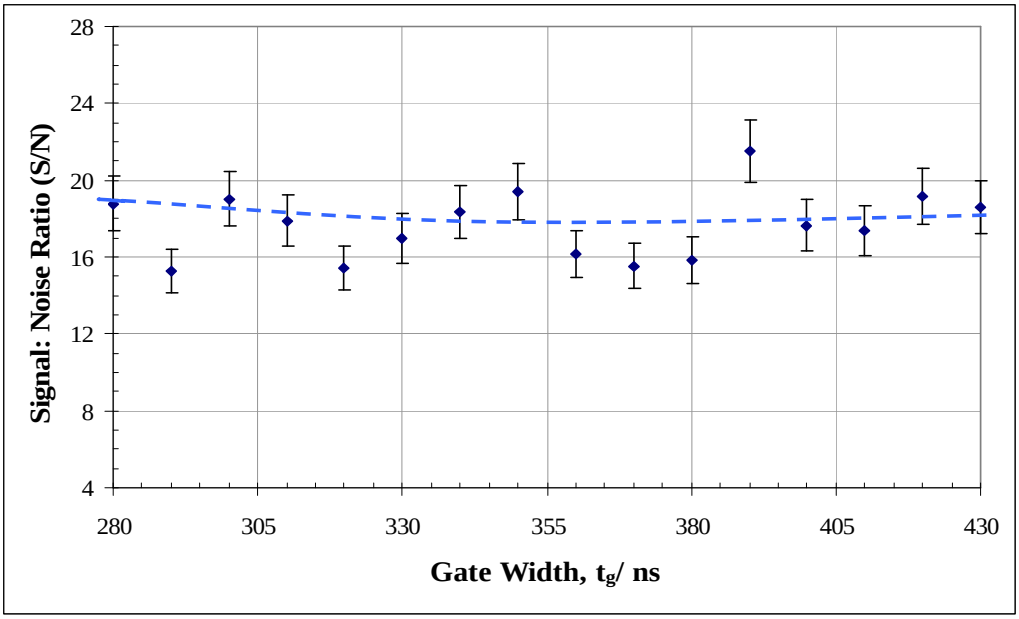

Figure 5.39: Signal-to-Noise Ratio *vs*. Gate Width

The data in Figure 5.39 showed that there is no reduction in S/N, within the limit of experimental error, over the range of gate widths used. No change in S/N as a function of gate width, in the range 280ns to 430ns, was anticipated. Given the previously demonstrated decrease of ~15% in emission line intensity (Figure 5.38) over this range of gate widths, the consistency of estimates for S/N was attributed to an equivalent decrease in standard deviation of the background signal over this range of gate widths.

c. Optimum Data Averaging

For analysis of the dependence of detection sensitivity on data averaging number (N) pulse energy was fixed at 31.7mJ, with a pulse repetition rate of 10Hz. Guided by the previous research for optimizing temporal parameters, delay time was fixed at 320ns, with gate width fixed at 400ns. LIBS spectra for data average numbers of 48 & 112 are shown in Figure 5.40. A complete set of optimized emission spectra for the full range of N used is presented in Appendix XV.

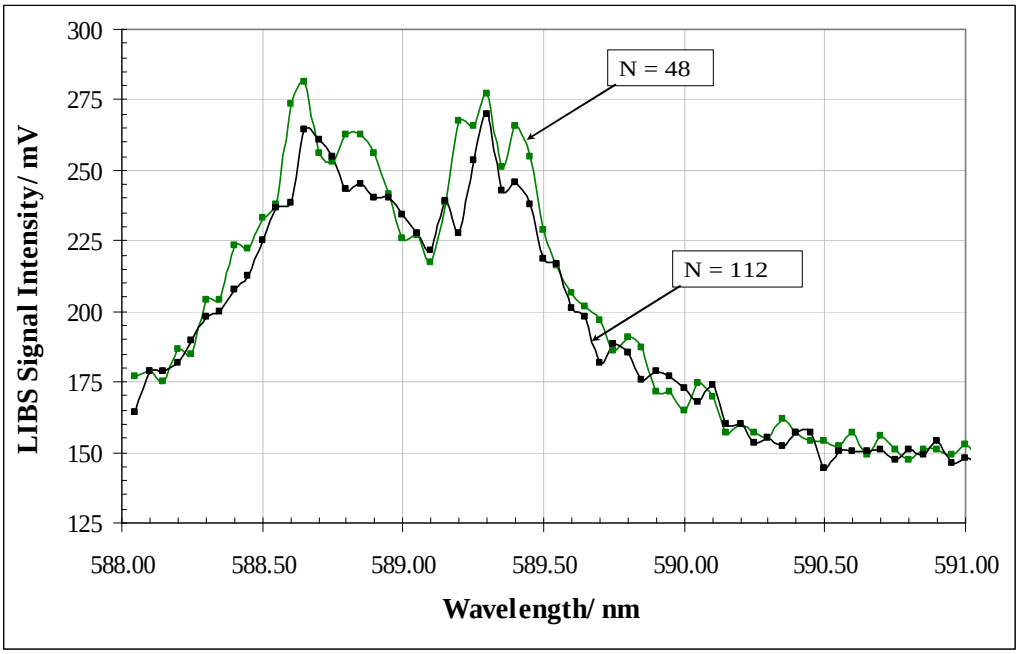

Figure 5.40: Optimized LIBS Emission Spectra for N = 48 & 112

Data for Na(I) emission line intensity, S_{Na}, mean background intensity, m_{bkgnd}, standard deviation of the background, σ_{bkgnd}, and signal-to-noise ratio, S/N, are summarized in Table 5.21. These data were acquired using the 'static scan' software mode NB. in this mode the grating is fixed at a specific wavelength, and multiple spectra are accumulated to generate an averaged spectrum.

The wavelengths used for generation of Na(I) line emission and background spectra were 589.00nm & 590.90nm, respectively. The default setting for the data averaging algorithm was 16 (accumulated spectra). By incrementing this default setting between 2 and 10 inclusive data averaged spectra were obtained for N increasing arithmetically between 32 and 160, respectively.

Table 5.21: Measured and Calculated LIBS Data *w.r.t.* Data Average Number

N	S_{Na} (±5%)	m_{bkgnd} (±5%)	ΔS (±5%)	σ_{bkgnd}	S/N (±7%)
16	258.85	150.73	108.12	2.90	37.3
32	292.71	149.24	143.47	4.32	33.2
48	255.87	151.68	104.20	3.09	33.7
64	267.20	151.12	116.08	3.56	32.6
80	276.95	160.57	116.38	1.68	69.2
96	272.18	163.36	120.11	5.11	23.5
112	261.02	149.30	111.72	2.32	48.1
128	280.52	114.22	166.30	3.20	52.0
144	274.08	109.35	164.73	4.66	35.3
160	271.10	107.20	163.91	3.90	42.1

Figure 5.41 shows Na(I) emission line and mean background intensities as a function of data average number, N.

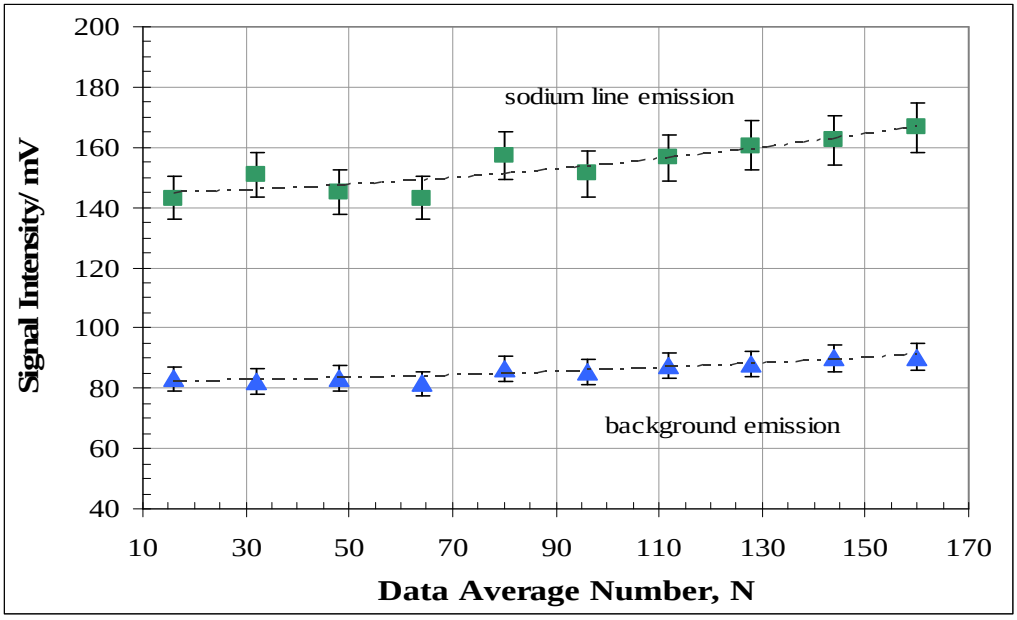

Figure 5.41: Emission Line & Mean Background Intensities *vs.* Data Average Number

The data in Figure 5.41 showed an increase of ~15% in emission line intensity as data average number was increased from 16 to 160. Increase in emission line intensity indicated an increase in the population of a higher energy level in the emitting (Na) species. With reference to *eqn.[3.7]* this indicated an increase in plasma temperature in the emitting plasma volume. Such an increase in plasma temperature was consistent with delivery of increased net laser energy into the plasma volume for emission spectra accumulated over higher values of N.

An increase of ~13% in mean background intensity was demonstrated for the same increase in data average number. The conventional gating technique measured background data originating from the decaying 'tail' of the *Bremsstrahlung* emission profile. With reference to *eqn.[3.9]* the main source of *Bremsstrahlung* was attributed to radiative re-combination between free electrons and ionized species in the plasma volume. As such the *Bremsstrahlung* intensity was considered to be primarily a function of the concentration of ionized species.

As described above an increase in the concentration of emitting species was attributed to an increase in temperature in the plasma volume. The measured increase in mean background intensity, as a result of increasing data average number by an order of magnitude, was therefore consistent with the measured increase in emission line intensity.

Figure 5.42 shows the influence of data average number on S/N for the Na(I) emission line at 589.00nm.

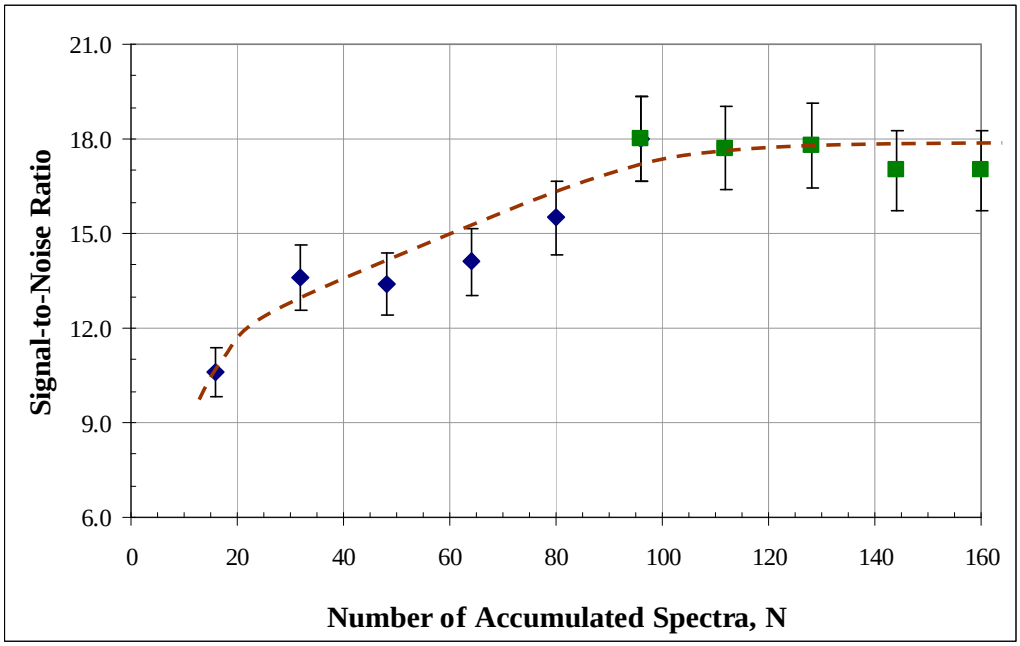

Figure 5.42: Signal-to-Noise Ratio *vs.* Data Average Number

The data shown in Figure 5.42 was characterized by two distinct regions. For lower values of N an non-linear increase in S/N was indicated. For values of N >100 the S/N reached a saturation maximum of ~18. Optimum data average number was estimated to be ~100. The changing trend between signal-to-noise ratio and data average number, as shown in Figure 5.42, was consistent with reduction in the shot noise contribution to the overall noise budget.

d. Optimum Laser Pulse Energy

For analysis of the dependence of detection sensitivity on laser pulse energy, E_p, delay time and gate width were fixed at 320ns and 400ns, respectively, based upon previous optimization of LIBS temporal parameters. The spectrometer entrance slit was fixed at 250μm, with pulse repetition fixed at 10Hz. LIBS spectra were averaged over 48 laser shots. Pulse energy in the range 10.5mJ to 88.0mJ were used increased at a step of ~4.5mJ. Plasma was generated in sodium chloride solution at a concentration of 260ppm.

Emission spectra for selected laser pulse energies (24.0, 37.7 & 64.0mJ) are shown in Figures 5.43. A complete record of LIBS emission spectra for the full range of pulse energies used is presented in Appendix XVI.

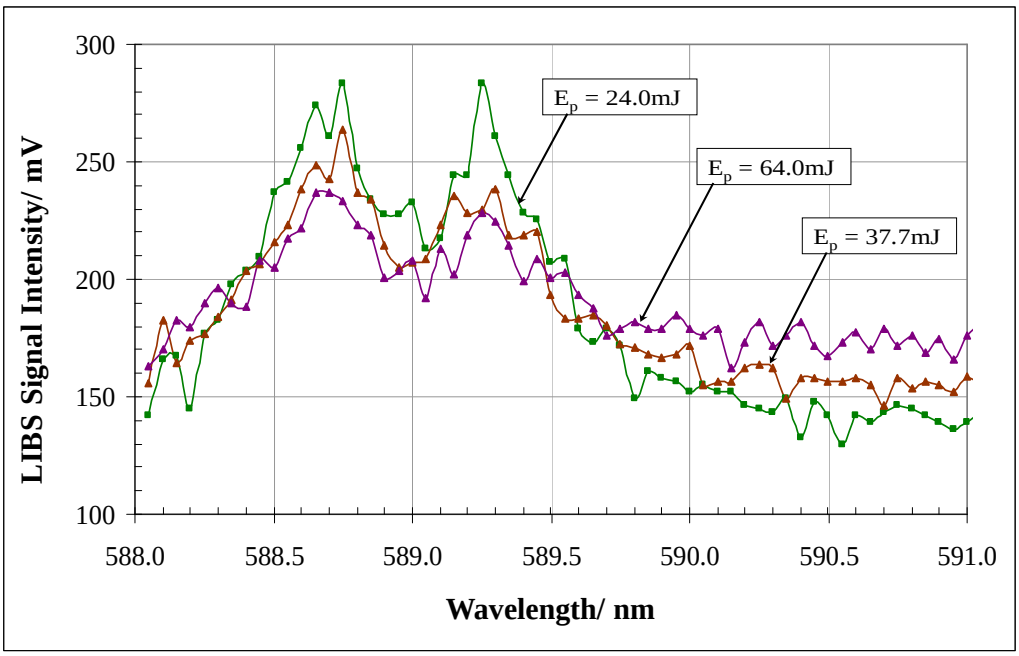

Figure 5.43: LIBS Emission Spectra for Pulse Energies of 24.0, 37.7 & 64.0mJ

Data for Na(I) emission line intensity, S_{Na}, mean background intensity, m_{bkgnd}, standard deviation of the background, σ_{bkgnd}, and signal-to-noise ratio, S/N, are summarized in Table 5.22. Values for m_{bkgnd} and σ_{bkgnd} were calculated over the spectral range from 590.00nm to 591.00nm, inclusive, at an increment of 0.05nm.

Table 5.22: Measured and Calculated LIBS Data *w.r.t.* Pulse Energy

Ep/ mJ (±0.5mJ)	S_{Na} (±5%)	m_{bkgnd} (±5%)	ΔS (±5%)	σ_{bkgnd}	S/N (±7%)
10.5	111.04	79.54	31.50	14.69	2.1
14.5	196.30	125.03	71.27	10.01	7.1
16.8	235.15	136.65	98.50	11.26	8.7
19.0	263.61	141.70	121.91	8.84	13.8
21.5	260.67	141.35	119.32	11.70	10.2
24.0	260.68	143.74	116.94	6.51	18.0
26.5	245.65	148.51	97.14	5.49	17.7
29.0	259.12	149.27	109.85	5.91	18.6
31.7	262.13	154.77	107.36	6.09	17.6
34.5	259.11	155.37	103.74	5.24	19.8
37.7	242.65	157.22	85.43	5.22	16.4
41.0	260.64	160.77	99.87	5.62	17.8
43.7	242.71	161.79	80.92	4.88	16.6
46.5	247.16	166.30	80.86	6.27	12.9
49.5	232.22	166.86	65.36	4.99	13.1
52.5	251.72	168.71	83.01	8.00	10.4
55.5	236.74	171.28	65.46	6.49	10.1
58.5	233.70	173.62	60.08	5.06	11.9
64.0	236.63	174.01	62.62	5.21	12.0
76.0	230.70	177.07	53.63	5.92	9.1
88.0	212.77	178.98	33.79	4.63	7.3

Dependence of the Na(I) emission line and mean background intensities on laser pulse energy is shown in Figure 5.44.

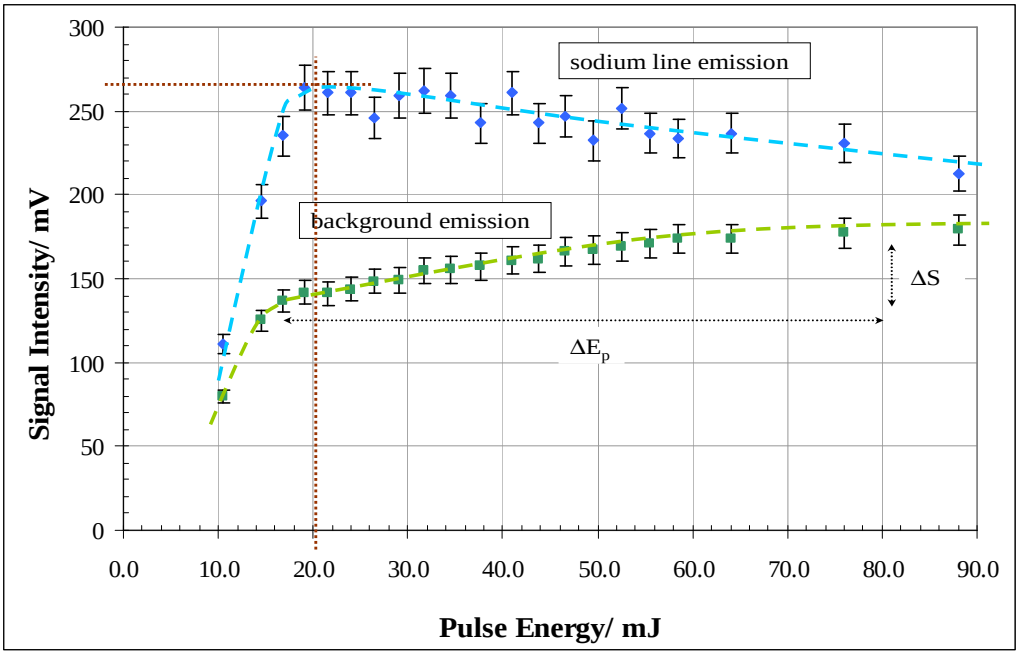

Figure 5.44: Emission Line & Mean Background Intensities *vs*. Pulse Energy

The data in Figure 5.44 showed an initially rapid increase in Na(I) emission line intensity with increase in pulse energy, at an estimated rate of 21mV/mJ. Maximum emission line intensity was reached in the region of 18mJ. Na(I) emission line intensity subsequently decreased at higher pulse energies up to ~90mJ, at an estimated rate of 0.72mV/mJ. Mean background emission intensity also displayed an initially rapid increase for lower pulse energies, at an estimated rate of 8mV/mJ. Maximum intensity was reached in the region of 16mJ. Mean background intensity continued to increase, at a reduced estimated rate of 1.0mV/mJ, at higher pulse energies up to ~90mJ.

The difference in intensity (ΔS) between the Na(I) emission line and mean background intensities, as a function of laser pulse energy, is shown in Figure 5.45.

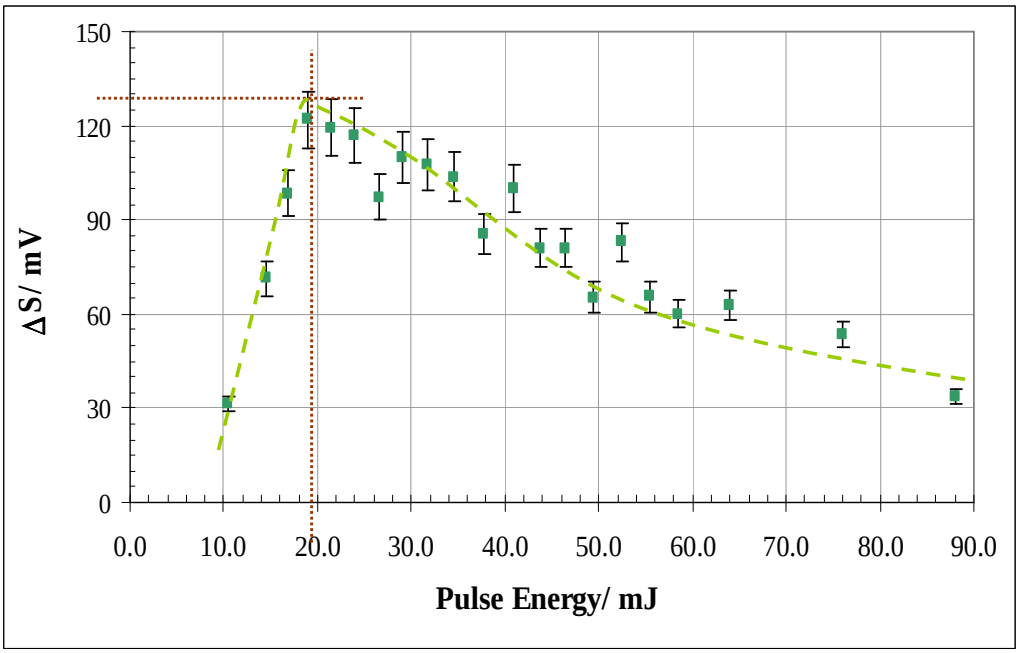

Figure 5.45: Difference between Emission Line and Mean Background Intensities *vs*. Pulse Energy

The data in Figure 5.45 showed maximum background corrected Na(I) emission intensity at ~19mJ. This was consistent with the peak Na(I) emission intensity shown in Figure 5.44. The rapid increase in background corrected Na(I) emission intensity at lower values of pulse energy had an estimated rate of 11mV/mJ. This corresponded approximately to the average of the rates of increase previously calculated (Figure 5.44) for Na(I) emission line and mean background intensities. The reduction in background corrected Na(I) emission intensity was commensurate with the trends previously shown (Figure 5.44) for Na(I) emission line and mean background intensities.

Figure 5.46 shows the relationship between S/N and pulse energy for the Na(I) emission line at 589.00nm.

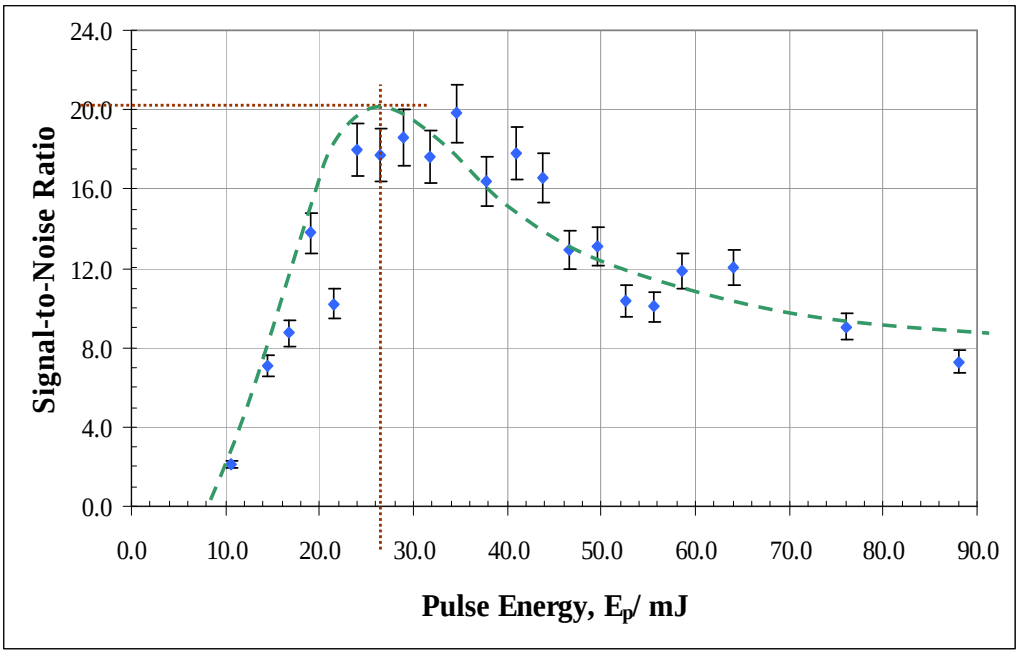

Figure 5.46: Signal-to-Noise Ratio *vs*. Pulse Energy

The data in Figure 5.46 showed an initially rapid increase in S/N for lower pulse energies. A maximum of S/N was reached for pulse energy in the region between ~25mJ and ~29mJ. A gradual decrease in S/N was shown for higher pulse energies up to ~90mJ.

Comparison of the data shown in Figures 5.45 and 5.46 revealed a significant difference in the pulse energy corresponding to peaks in background corrected Na(I) emission intensity and signal-to-noise ratio. The pulse energies corresponding to these peaks were ~19mJ and ~26mJ, respectively. This was explained with respect to the competing and complementary mechanisms for ionization in the liquid bulk i.e. cascade and multi-photon ionization. As previously discussed (section 3.3) these two mechanisms are distinct in terms of their *modus operandi*, but are related in terms of critical free electron densities for their respective onset. At sufficiently high incident photon flux the mechanism of multi-photon ionization has the potential to generate free electron density of sufficient magnitude to trigger the onset of cascade ionization, in the focussed laser

beam waist. It was suggested that an increase in photon flux, commensurate with increased pulse energy and derived laser irradiance, caused the S/N peak to occur at a higher pulse energy compared to the previously demonstrated peak for background corrected Na(I) intensity (Figure 5.45).

5.5.3 LIBS System Sensitivity for Characterization of Species in Aqueous Solution

a. Sodium Chloride Solution

Having optimized delay time, pulse energy and data average number for the strong Na(I) emission line at 589.00nm, LIBS system sensitivity was investigated for $NaCl_{(aq)}$ at concentrations of 260ppm & 50ppm. Pulse energy and repetition rate were fixed at ~29mJ and 10Hz, respectively. Delay time and gate width were fixed at 300ns & 400ns, respectively. LIBS emission spectra were accumulated over 48 laser shots. This relatively low number of data averaged spectra was deemed adequate due the relative strength of the Na(I) emission line. Optimized spectra for these concentrations are in Figure 5.47.

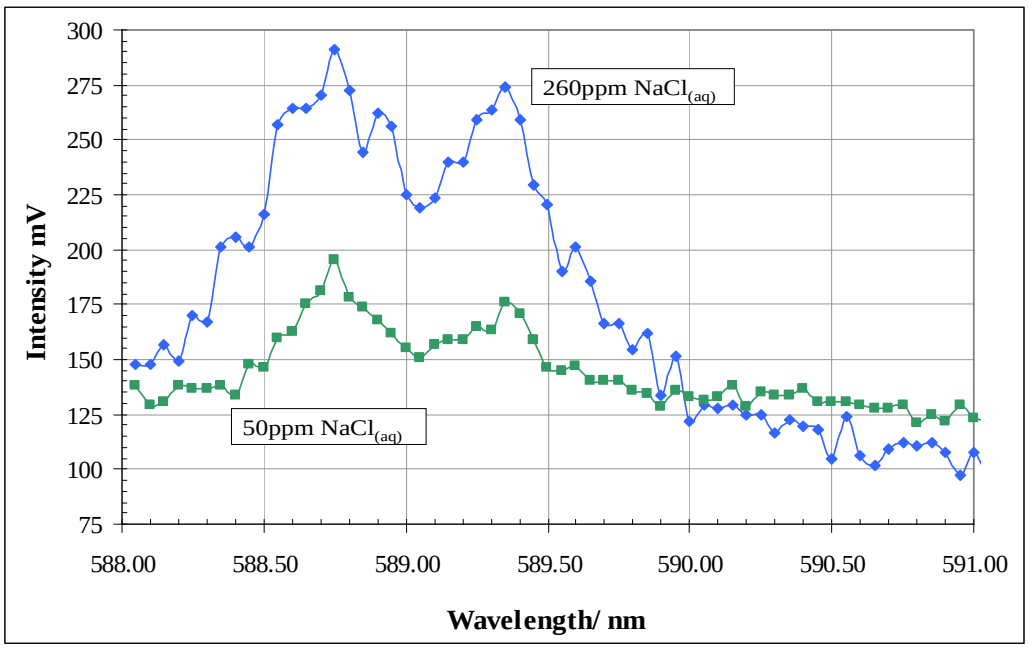

Figure 5.47: Optimized LIBS Spectra for Sodium Chloride Solution at Concentrations of 50ppm & 260ppm

Table 5.23 summarizes Na(I) emission line intensity (S_{Na}), mean background intensity (m_{bkgnd}), standard deviation of background (σ_{bkgnd}), difference between line emission and mean background intensities (ΔS), and S/N for these solutions.

Table 5.23: LIBS Statistical Data for Sodium Chloride Solution at 260ppm & 50ppm Concentration

	Concentration (ppm)	
Parameter	260	50
S_{Na} (±5%)	291.35	195.16
m_{bkgnd} (±5%)	114.35	131.58
ΔS (±7.5%)	177.00	63.58
σ_{bkgnd}	4.19	2.98
S/N (±7.5%)	42.2	21.3
D_L/ppm	18.5	9.6

Applying *eqn[5.7]* to the data summarized in Table 5.23 the detection sensitivity, D_L, for Na, using the current LIBS system, was estimated to be ~10ppm.

b. Lead Acetate Solution

Having estimated LIBS system sensitivity for detection of Na in aqueous solution the same technique was applied to the detection of lead. Targeting the Pb(I) emission line at 405.78nm, LIBS spectra were generated from plasma generated in lead acetate solution, for a range of concentrations in the ppm range. Pulse energy and repetition rate were fixed at ~29mJ and 10Hz, respectively. Delay time and gate width were fixed at 300ns & 400ns, respectively. Spectra were accumulated over 80 laser shots. A higher number of data average spectra was required due to the relative weakness of the Pb(I) emission line (compared to Na(I) in the previous section).

An optimized LIBS emission spectrum for 250ppm lead acetate solution is shown in Figure 5.48. A complete set of optimized emission spectra for the concentrations used is presented in Appendix XVII.

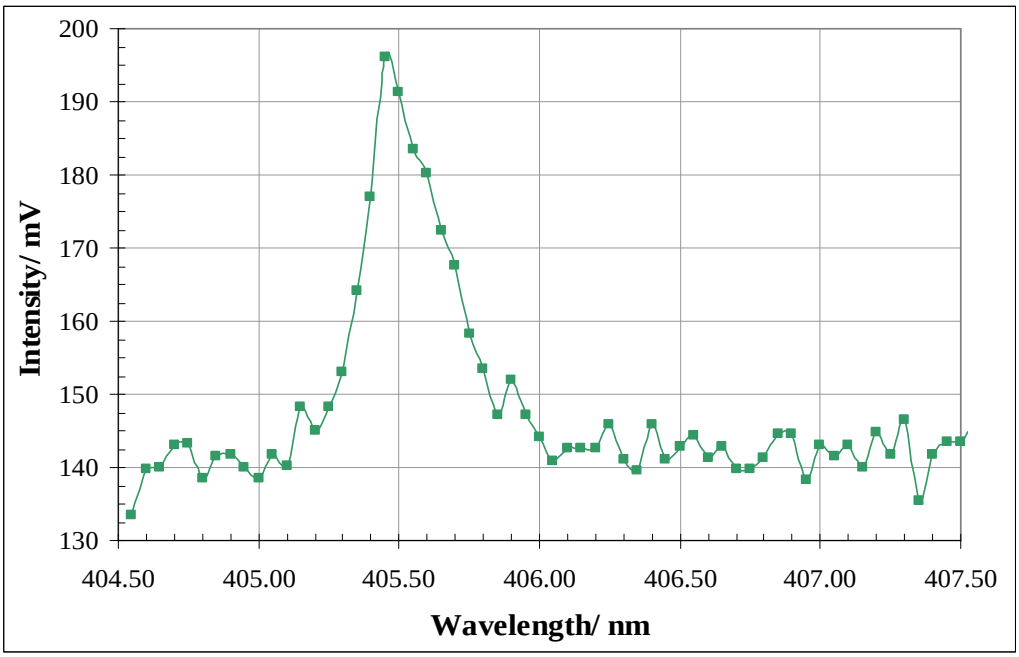

Figure 5.48: Optimized LIBS Spectrum for Lead Acetate Solution at Concentration of 250ppm

Figure 5.49 shows lead emission line intensity (S_{Pb}), difference between lead emission line and mean background intensities (ΔS), and standard deviation of background signal (σ_{bkgnd}) as a function of concentration of Pb species.

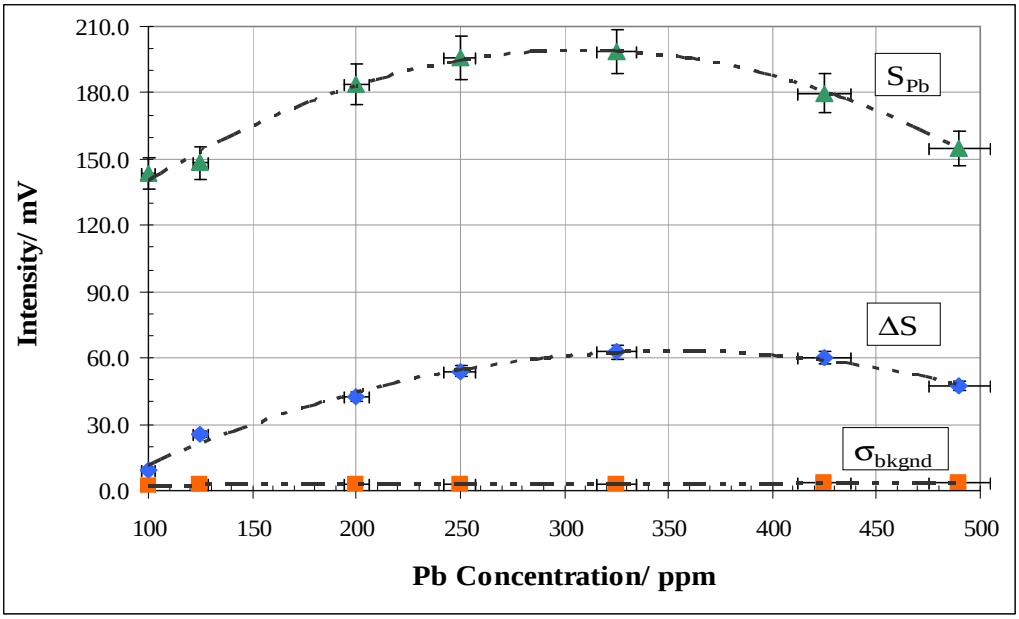

Figure 5.49: LIBS Statistical Parameters *vs.* Concentration of Lead Emitters

Figure 5.50 shows the influence of analyte concentration on estimated S/N for the Pb(I) emission line at 405.78nm.

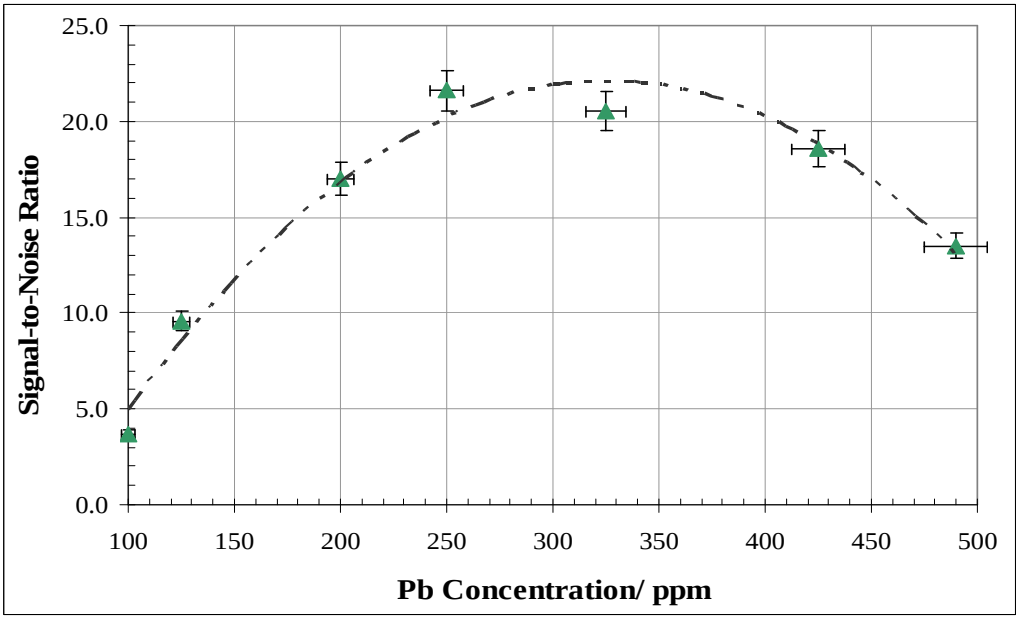

Figure 5.50: Signal-to-Noise Ratio *vs.* Concentration of Lead Emitters

Based on the data shown in Figure 5.50 maximum emission line S/N is achieved for Pb concentration in the approximate range 250ppm to 350ppm.

Table 5.24 summarizes lead emission line intensity (S_{Pb}), mean background intensity (m_{bkgnd}), standard deviation of background (σ_{bkgnd}), difference between line emission and mean background intensities (ΔS), and signal-to-noise ratio (S/N) for the concentrations used.

Table 5.24: LIBS Statistical Data for Different Concentrations of Lead Acetate Solution

Parameter	Concentration (ppm)						
	490	425	325	250	200	125	100
S_{Pb} (±5%)	154.80	179.78	198.73	196.09	183.98	148.45	143.37
m_{bkgnd} (±5%)	107.48	119.66	135.89	142.12	141.61	123.03	134.47
ΔS (±7.5%)	47.32	60.12	62.84	53.97	42.37	25.42	8.90
σ_{bkgnd}	3.51	3.23	3.07	2.50	2.49	2.65	2.38
S/N (±7.5%)	13.5	18.61	20.47	21.6	17.02	9.6	3.7
D_L/ppm	109	69	48	35	35	39	81

Applying *eqn[5.7]* to the data summarized in Table 5.24 the detection sensitivity, D_L, for Pb, using the current LIBS system, was estimated to be ~40ppm. The relationship between concentration (C_L) of lead acetate solution and derived detection limit (D_L) is shown in Figure 5.51.

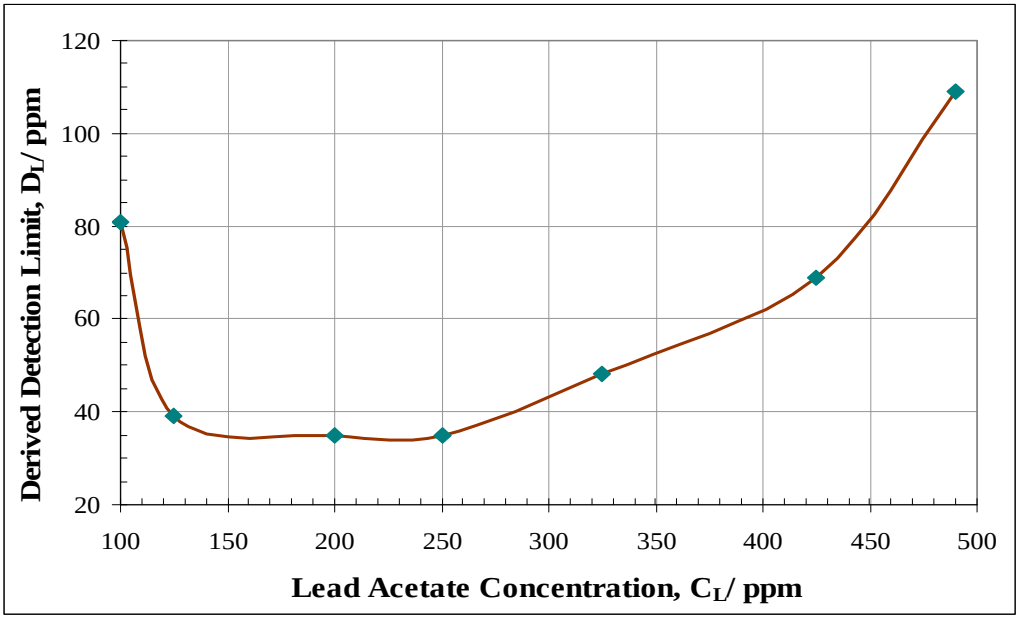

Figure 5.51: Derived Detection Limit *vs*. Concentration of Lead Emitters

Maximum detection sensitivity of ~35ppm has been demonstrated for analyte concentration in the approximate range between 125ppm & 250ppm. Detection sensitivity is progressively weaker for higher concentrations, up to a maximum of ~500ppm. The anomalous detection limit for 100ppm solution (D_L~80ppm) is attributed to a combination of potential factors: these include an error in dilution of the 100ppm solution from the original stock solution, and inconsistency of focussed laser volume in the liquid bulk due to splashing of the focussing optics.

5.6 Signal-to-Noise Ratio Improvement by Mechanical Filtering

5.6.1 Surface Plasma Expanding in Air

In order to demonstrate improvement of LIBS sensitivity using this technique initial tests were carried out with a solid Al alloy target. The spectrometer grating was set to the target strong Al(I) emission line at 396.15nm. Plasma generated at the target surface expanded in air at STP. An advantage of plasma expansion in a gaseous medium,

compared to the liquid bulk, was the relative lack of plasma 'quenching'. The experimental set-up for this technique was previously illustrated in Figure 4.17.

As with previous LIBS experimental research optimization of delay time to maximize emission line S/N was performed. Pulse energy was fixed at ~35mJ and pulse repetition rate fixed at 10Hz. Conventionally gated and 'background subtracted' LIBS spectra were generated for delay times (t_d) between 328ns & 488ns at a step of 20ns. Gate width (t_g) was fixed at 350ns. A representative LIBS spectra is shown in Figure 5.52. Emission spectra for the full range of delay times used are presented at Appendix XVIII.

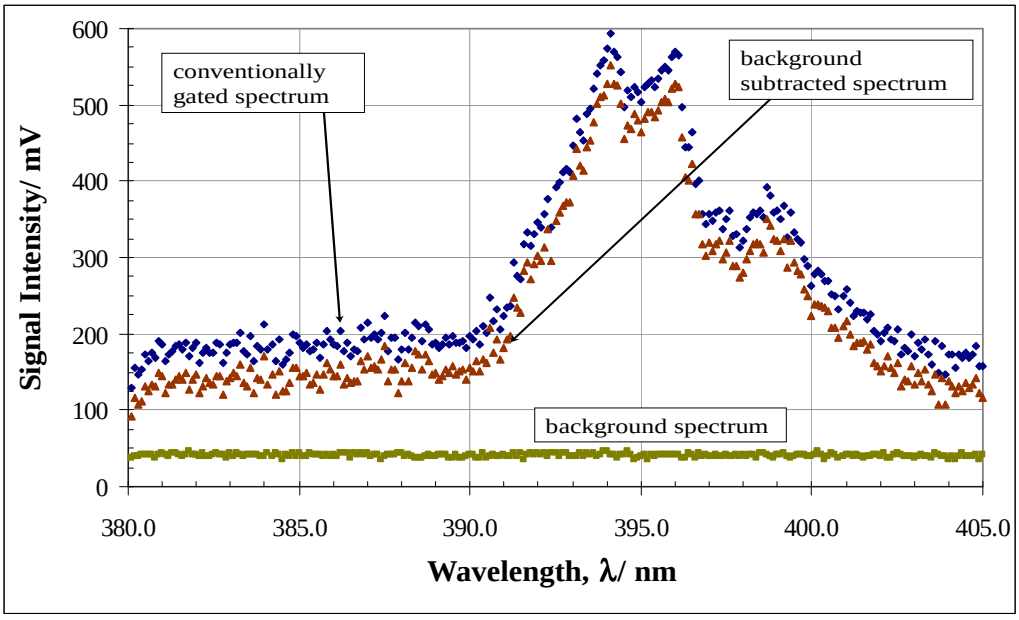

Figure 5.52: LIBS Spectra using Mechanical Filtering Technique: Delay Time = 432ns

For each value of time delay S/N were calculated for temporally gated and 'background subtracted' emission spectra (S/N_{temp} and S/N_{mech}, respectively). Consistency was maintained for statistical analysis by using a fixed spectral range between 380.7nm and

390.2nm for calculation of mean and standard deviation of background emission signal. Delay time was optimized with respect to S/N for the range of delay times used, as shown in Figure 5.53, for conventionally gated and "background subtracted" LIBS spectra.

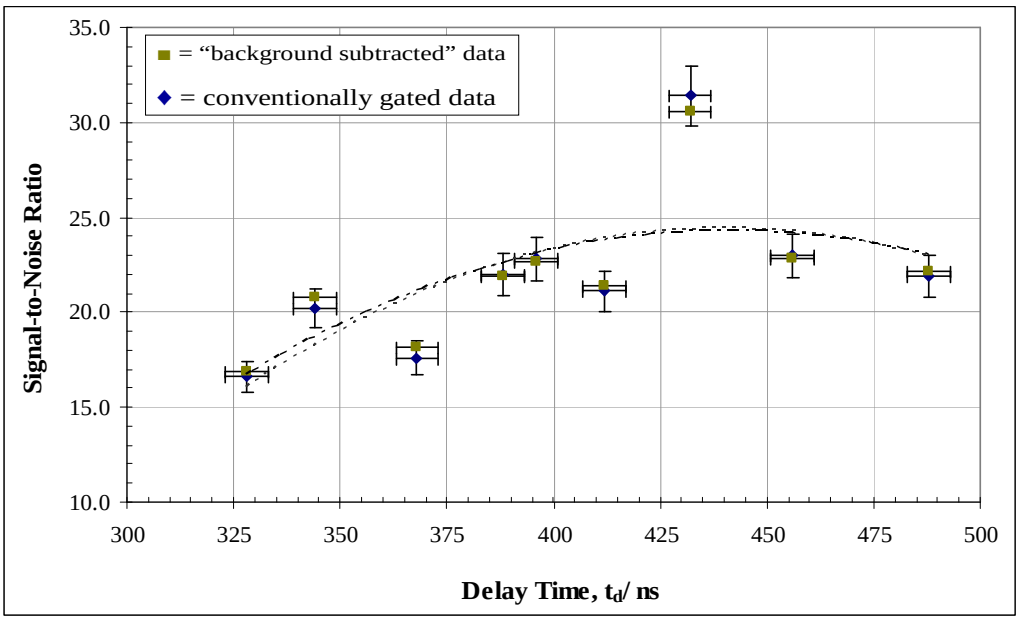

Figure 5.53: Influence of Delay Time on S/N for Conventionally Gated and Background Subtracted LIBS Spectra

Signal-to-noise ratio for both gating configurations displayed a weak non-linear relationship with respect to delay time, and indicated a maximum of ~25 for t_d ~ 435±50ns. The data in Figure 5.53 showed no statistically significant difference between S/N_{temp} and S/N_{mech} over the range of delay times used. Improvement in LIBS sensitivity by the technique of mechanical filtering was concluded to not have been conclusively demonstrated.

Initial LIBS spectra obtained were generated using a single laser pulse. The next stage of experimental work took advantage of the optimum delay time (t_d ~ 435ns) shown in

Figure 5.53, and generated data averaged conventionally gated and 'background subtracted' LIBS emission spectra. Four spectra were generated in this way of which Figure 5.54 is a representative example, corresponding to data average number, N = 10. A complete set of data averaged spectra are presented at Appendix XVIII.

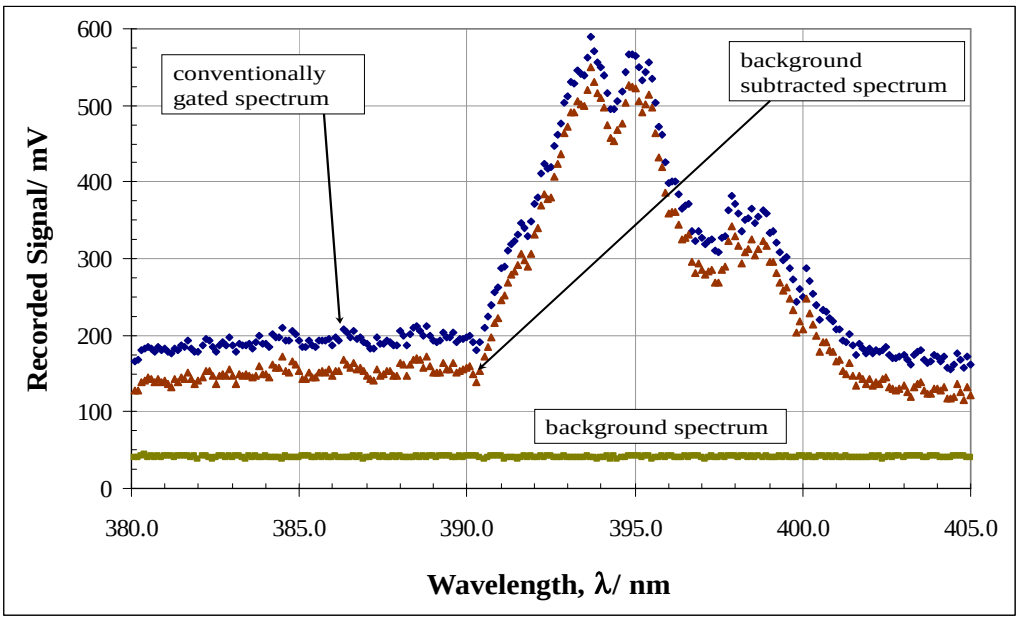

Figure 5.54: Data Averaged LIBS Spectra using Mechanical Filtering Technique: Surface Plasma on Solid Target

Consistency was maintained for calculation of mean background intensity (m_{bkgnd}) and standard deviation of background (δ_{bkgnd}) by using a fixed spectral region between 381.0nm and 390.2nm. Statistical data for data averaged conventionally gated and 'background subtracted' spectra are presented in Tables 5.25a and 5.25b, respectively.

Table 5.25a: Statistical Analysis of Data Averaged Conventionally Gated LIBS Spectra: Surface Generated Metal Plasma

Parameters	Data Average Number			
	3	10	20	30
S_{Na}	614.32	538.91	132.36	206.05
m_{bkgnd}	190.80	192.44	45.14	60.03
σ_{bkgnd}	10.61	8.25	2.23	4.23
ΔS	423.52	346.47	87.22	146.02
S/N_{temp}	39.9	42.0	39.2	34.5

Table 5.25b: Statistical Analysis of Data Averaged Background Subtracted LIBS Spectra: Surface Generated Metal Plasma

Parameters	Data Average Number			
	3	10	20	30
S_{Na}	571.53	498.02	114.59	176.27
m_{bkgnd}	150.14	151.82	31.69	32.88
σ_{bkgnd}	10.84	8.48	1.62	3.34
ΔS	421.39	346.20	82.90	143.39
S/N_{temp}	38.9	40.8	51.2	42.9

Improvement in S/N between conventionally gated and 'background subtracted' LIBS spectra was demonstrated by simple subtraction of data in Tables 5.25a and 5.25b. No significant improvement in S/N was demonstrated for data averaging over 3 & 10 laser shots. Improvements in S/N of ~30% and ~25% were demonstrated, however, for data averaging over 20 and 30 laser shots, respectively.

5.6.2 Plasma Generation in the Liquid Bulk

The mechanical filtering technique was subsequently used to improve LIBS sensitivity for plasma generation in the liquid bulk. The experimental set-up used was previously illustrated in Figures 4.6 & 4.17. The target medium was $NaCl_{(aq)}$ at 100ppm concentration. Emission spectra were generated targeting the strong Na(I) emission line

at 589.00nm. Pulse energy, repetition rate and spectrometer entrance slit width were fixed at ~35mJ, 10Hz and 250μm, respectively. A series of LIBS spectra were generated with fixed delay time (t_d) of 300ns, and fixed gate width (t_g) of 400ns. A data average algorithm was used to accumulate emission spectra over 37, 67 & 91 laser shots. A pair of conventionally gated and 'background subtracted' LIBS spectra averaged over 67 laser shots are shown in Figure 5.55. Spectra pairs for the full range of data average numbers used are presented at Appendix XIX.

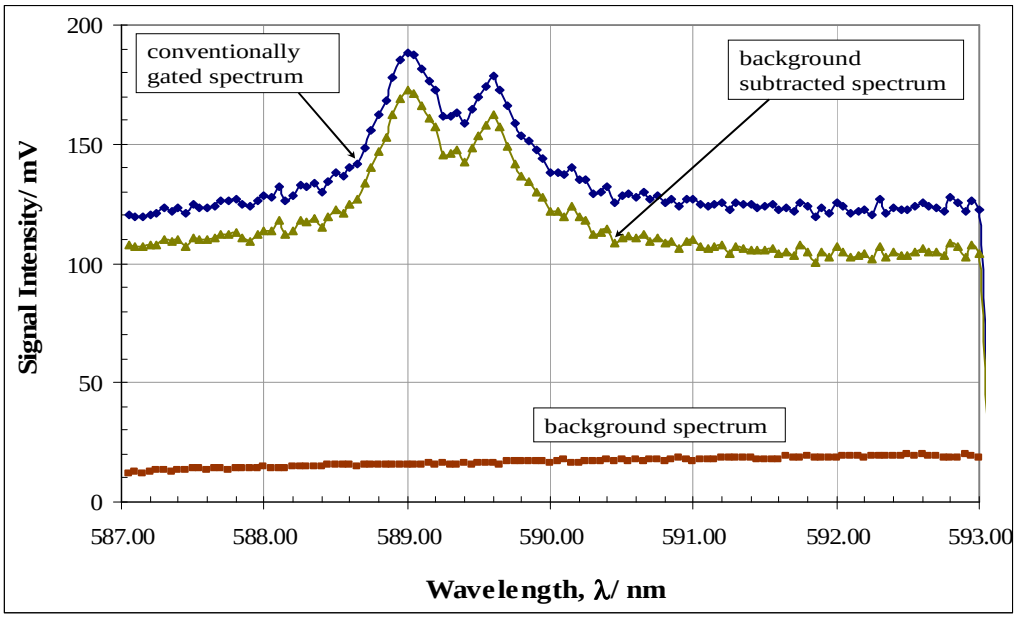

Figure 5.55: Data Averaged LIBS Spectra using Mechanical Filtering Technique: Plasma Generated in the Liquid Bulk

Signal intensity was measured for the Na(I) emission line. Mean background intensity (m_{bkgnd}) and standard deviation of background (δ_{bkgnd}) were calculated with consistency being maintained by using a fixed spectral region between 590.65nm and 592.50nm. Signal-to-noise ratio was calculated using *eqn.[3.18]*. Statistical data for data averaged conventionally gated and 'background subtracted' spectra are presented in Tables 5.26a and 5.26b, respectively.

Table 5.26a: Statistical Analysis of Data Averaged Conventionally Gated LIBS Spectra: Liquid Bulk Sample Configuration

Parameter	Data Average Number, N		
	37	67	91
m_{bkgnd}	133.44	123.67	130.76
σ_{bkgnd}	4.24	1.82	3.40
S_{Na}	223.15	187.96	186.31
ΔS	89.71	64.29	55.55
S/N_{temp}	21.2	35.4	16.3

Table 5.26b: Statistical Analysis of Data Averaged 'Background Subtracted' LIBS Spectra: Liquid Bulk Sample Configuration

Parameter	Data Average Number, N		
	37	67	91
m_{bkgnd}	110.04	105.10	108.59
σ_{bkgnd}	4.38	2.08	3.59
S_{Na}	200.38	172.67	165.07
ΔS	90.34	67.57	56.48
S/N_{temp}	20.6	32.4	15.7

Improvement in S/N between mechanically and conventionally gated LIBS spectra was demonstrated by simple subtraction of data in Tables 5.26a and 5.26b. No significant improvement in S/N was demonstrated for the data average numbers used i.e. N = 37, 67 & 91. The was attributed to significant quenching in the liquid bulk, with the subsequent effect of reduction in plasma temperature. Reduction in plasma temperature had significant implications for emission line intensity, as demonstrated with reference to *eqn[3.7]*. The reduction of LIBS sensitivity as a result of quenching in the liquid bulk was concluded to be more significant than potential improvements in LIBS sensitivity from application of the mechanical filtering technique.

5.7 Signal-to-Noise Ratio Improvement by Plasma Blocking

5.7.1 Optimization of Temporal Parameters

In order to demonstrate the principle of spatial filtering of *Bremsstrahlung* emissions for improvement of LIBS sensitivity, initial tests were carried out with an Al alloy target. Plasma generated at the target surface expanded in air at STP. The set-up for this experimental technique was illustrated in Figures 4.18 & 4.19. This series of tests was carried out with laser pulse energy ~35mJ, pulse repetition rate = 10Hz and spectrometer entrance slit width ~250μm. Emission profiles were recorded using a digitising oscilloscope (Agilent Technologies model DSO5054A) utilising a data averaging algorithm accumulating over 64 individual spectra.

The delay time (t_d) and gate width (t_g) were fixed at 3.2μs & 8.0μs, respectively, as shown in Figure 5.56. The emission line profile for the strong Al(I) 396.15nm wavelength is superimposed, as is the temporal profile for the (12.5μs) TTL laser flash lamp trigger pulse. The temporal profile for this emission line was sensitive to small changes in the spectrometer grating setting, specifically the time taken to reach peak intensity after the onset of plasma emission.

The sensitivity of the Al(I) emission line profile to changes in the spectrometer grating setting is demonstrated by a series of images (complementary to Figure 5.56) in Appendix XX.

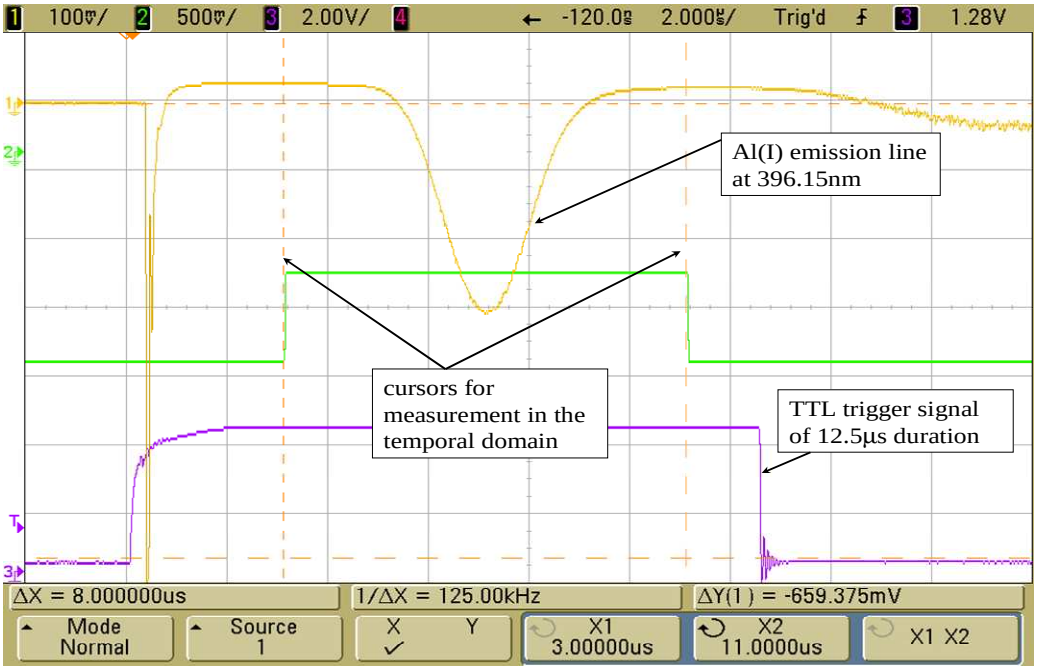

Figure 5.56: Tuning of Temporal Window to Al(I) Emission Line Profile

A key difference between plasma emission in the liquid bulk (section 5.6.2), and surface plasma expanding in air was the order of magnitude difference in time taken for the appearance of emission line profiles. This was illustrated by the delay times used for these sample presentation configurations i.e. in the order of hundreds of ns for liquid bulk compared to 3.2µs for surface plasma. The time scale for surface plasma emissions in air at STP is shown in Figure 5.57. This emission profile represented negligible blocking of *Bremsstrahlung* emission.

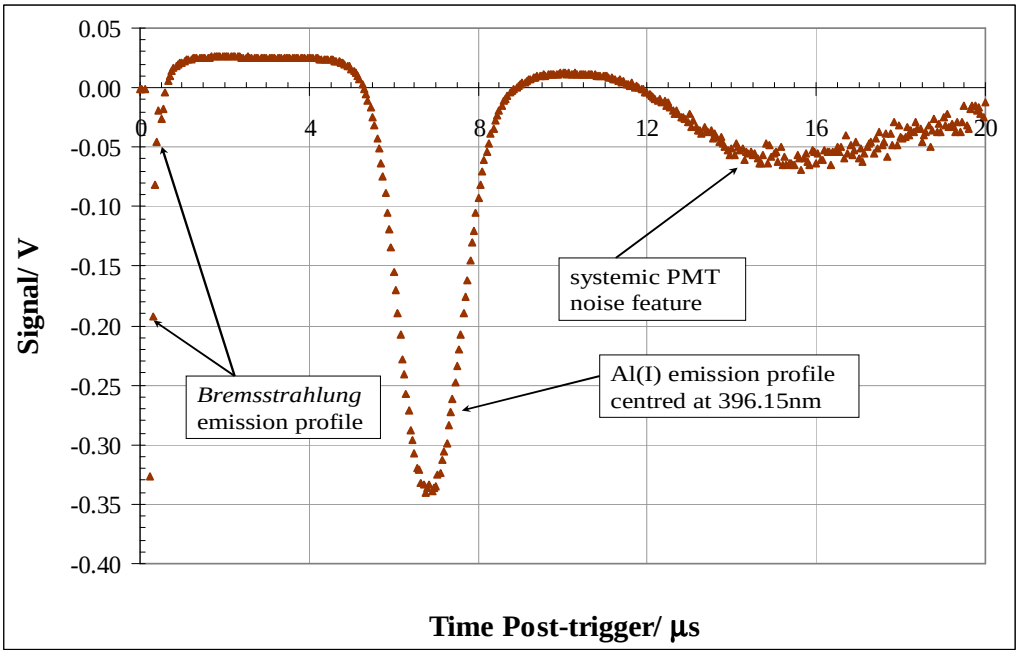

Figure 5.57: Emission Line Profile: Surface Generated Metal Plasma

5.7.2 Effect of Plasma Blocking on *Bremsstrahlung* and Line Emission Profiles

Having identified the emission line of interest, and optimized delay time and gate width, a series of measurements were performed during which the principal plasma emission region was incrementally (ΔL) blocked. The initial objective was to investigate the effect of increased plasma blocking on *Bremsstrahlung* and emission line profiles.

a. Bremsstrahlung Emission Profiles

The effect on *Bremsstrahlung* emission profiles of increased blocking of plasma emissions is shown in Figure 5.58. The *Bremsstrahlung* profiles shown represent a range of blocking from ~22% to ~67%, and include the 'null' case of negligible plasma blocking. A complete set of *Bremsstrahlung* emission profiles for the full range of plasma blocking is presented in Appendix XXI.

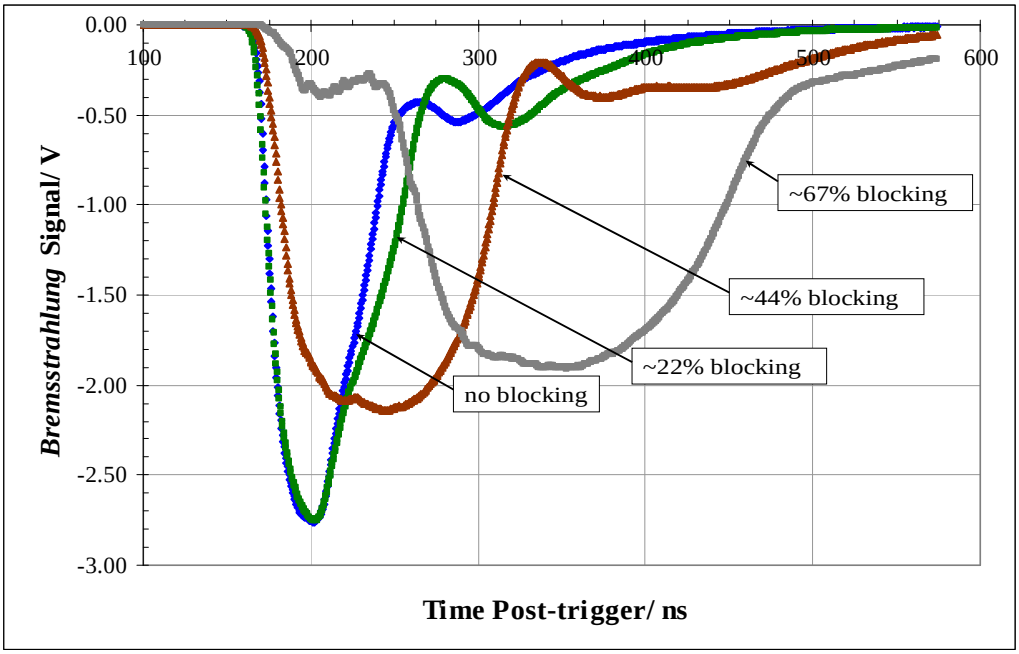

Figure 5.58: Effect of Plasma Blocking on *Bremsstrahlung* Emission Profiles

Quantitative comparison of *Bremsstrahlung* emission profiles, subject to the effect of increasing plasma blocking, was undertaken by defining and measuring key profile characteristics. These characteristic were maximum *Bremsstrahlung* emission intensity (S_{max}), time between plasma formation and onset of maximum *Bremsstrahlung* emission intensity (t_{peak}) and full width at half maximum (t_{FWHM}) of the *Bremsstrahlung* emission profile. These criteria are shown in Figure 5.59 for a *Bremsstrahlung* emission profile subject to negligible plasma blocking.

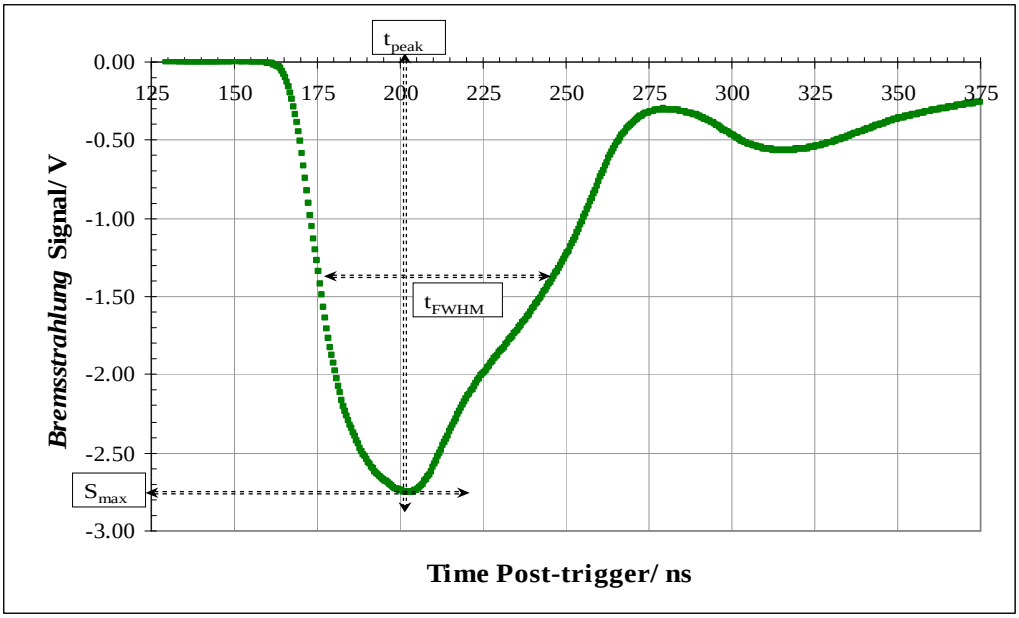

Figure 5.59: Critical Features of *Bremsstrahlung* Emission Profile

Measured *Bremsstrahlung* emission profile characteristics are summarized in Tables 5.27a and 5.27b for the full range of plasma blocking used. The increment between successive recorded profiles, ΔL, was fixed at ~45μm.

Table 5.27a: *Bremsstrahlung* Profile Characteristics: $0 \leq \Delta L \leq 360\mu m$

ΔL ±8μm	S_{max} ±0.05V	t_{peak} ±10ns	t_{FWHM} ±10ns
0	2.77	198	49
45	2.77	198	51
90	2.77	198	53
135	2.77	199	50
180	2.77	199	53
225	2.77	199	53
270	2.80	196	53
315	2.80	196	56
360	2.73	202	60

Table 5.27b: *Bremsstrahlung* Profile Characteristics: 405µm ≤ ΔL ≤ 720µm

ΔL ±8µm	S_{max} ±0.05V	t_{peak} ±10ns	t_{FWHM} ±10ns
405	2.77	200	63
450	2.74	203	72
495	2.56	206	96
540	2.12	246	125
585	2.34	278	114
630	1.90	353	191
675	1.44	584	410
720	1.06	745	1027

The influence of increased plasma blocking at fixed increment, ΔL, on t_{peak} and t_{FWHM} is shown in Figure 5.60.

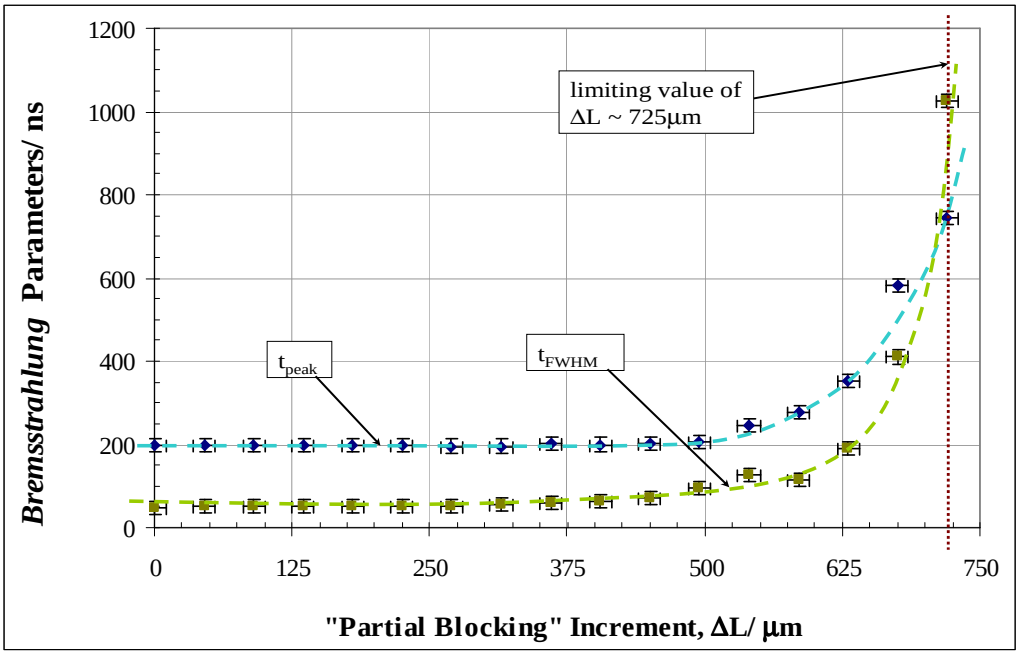

Figure 5.60: Effect of Plasma Blocking on *Bremsstrahlung* Temporal Characteristics

The data shown in Figure 5.60 demonstrated that the *Bremsstrahlung* parameters of t_{peak} and t_{FWHM} do not change with increase in blocking of the plasma for ΔL in the range 0 to ~500μm. For ΔL in excess of ~500μm both t_{peak} and t_{FWHM} demonstrated a rapid non-linear increase, tending towards convergence for ΔL ~725μm. The convergence of t_{peak} and t_{FWHM} was consistent with dispersion of the energy encapsulated within the *Bremsstrahlung* profile to such an extent that residual *Bremsstrahlung* emissions were, for all intents and purposes, of negligible intensity.

The influence of increased plasma blocking at fixed increment, ΔL, on S_{max} is shown in Figure 5.61.

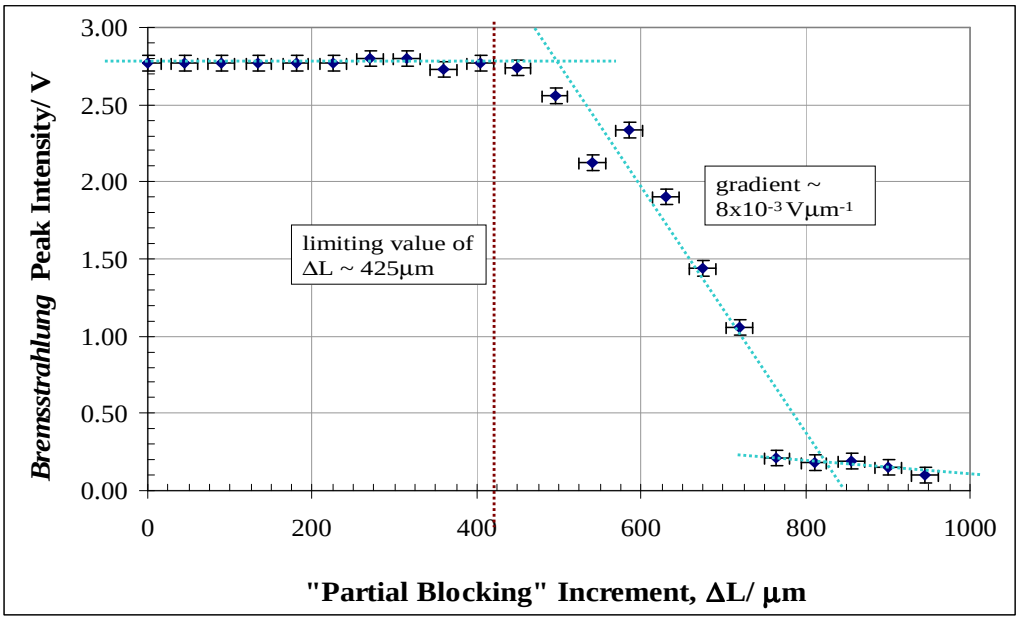

Figure 5.61: Effect of Plasma Blocking on Maximum *Bremsstrahlung* Intensity

Peak *Bremsstrahlung* emission intensity was found to remain unchanged with increase in plasma blocking for ΔL between 0 and ~425μm. For larger values of ΔL a rapid and approximately linear decrease in S_{max} was demonstrated with an estimated rate of 8×10^{-3}

$V\mu m^{-1}$. Peak intensity, S_{max}, reduced to minimum intensity for ΔL ~750µm, and tended to negligible levels as ΔL tended towards 1000µm. The approximately linear decrease in S_{max} in the region 425µm < ΔL < 750µm is consistent with the gradual blocking of a compact plasma region, within which the radiative energy flux is approximately homogeneous. The clear demarcation of the *Bremsstrahlung* peak intensity profile into three distinct regions as described is consistent with the plasma region having a boundary which tended towards discontinuity with respect to radiative flux.

b. Line Emission Profiles

The effect on the target Al(I) emission line profile of increased blocking of plasma emissions is shown in Figure 5.62. The profiles shown represent the full range of blocking as characterized by reduction of the peak intensity of the emission line profile. A complete set of emission line profiles for the full range of plasma blocking is presented in Appendix XXII.

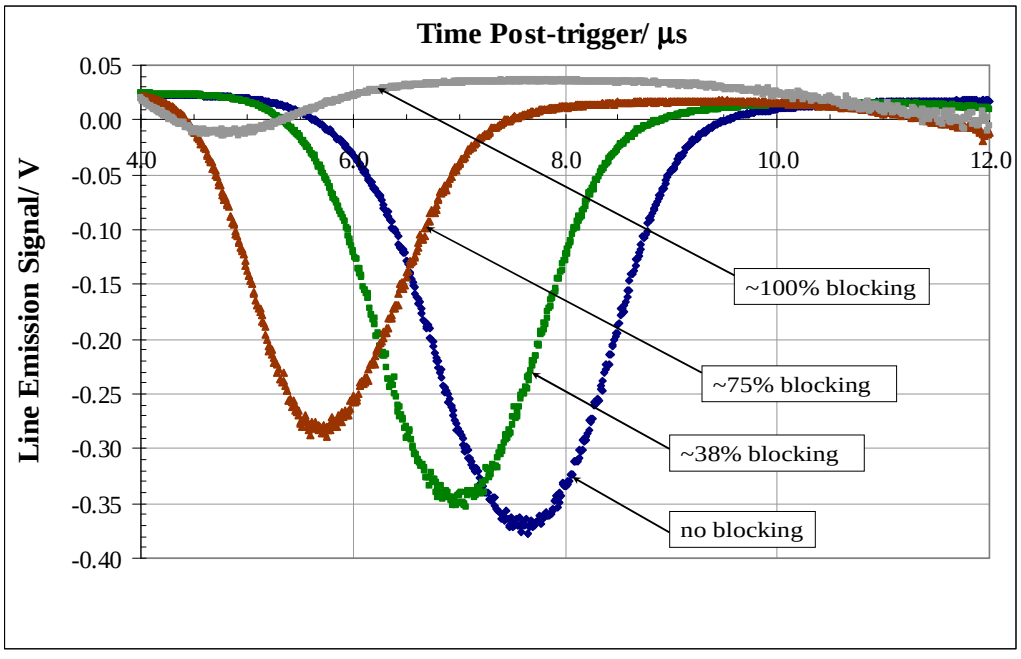

Figure 5.62: Effect of Plasma Blocking on Emission Line Profiles

Initial examination of the incrementally blocked line emission profiles (Figure 5.62) demonstrate a steady reduction in the area encapsulated within the emission profile. This was interpreted as an inverse (negative) correlation between blocking increment and line emission energy incident upon the detection apparatus. The gradual decrease in the time taken for the line emission profile to achieve maximum intensity also demonstrated an inverse (negative) correlation to the degree of plasma blocking i.e. 7.6μs, 7.0μs, 5.7μs & 4.9μs corresponding to 0%, 38%, 75% & 100% blocking, respectively.

Based upon the assumption of a homogeneous density of line emitting species within the plasma volume, these data were interpreted as an artefact of the detection and charge accumulation apparatus.

Quantitative comparison of emission line profiles, subject to the effect of increased plasma blocking, was undertaken by defining and measuring key profile characteristics. These characteristic were maximum emission line intensity (S_{max}), time between plasma formation and onset of maximum emission line intensity (t_{peak}) and full width at half maximum (t_{FWHM}) of the emission line profile, as shown in Figure 5.62.

The area beneath the emission line profile was also calculated, in order to estimate radiated energy (E_{line}) encapsulated within the emission line profile. A 10% criterion was used for estimation of E_{line} i.e. summation over the temporal range for which emission intensity was ≥10% of peak emission. These criteria are shown in Figure 5.63 for an emission line profile subject to negligible plasma blocking..

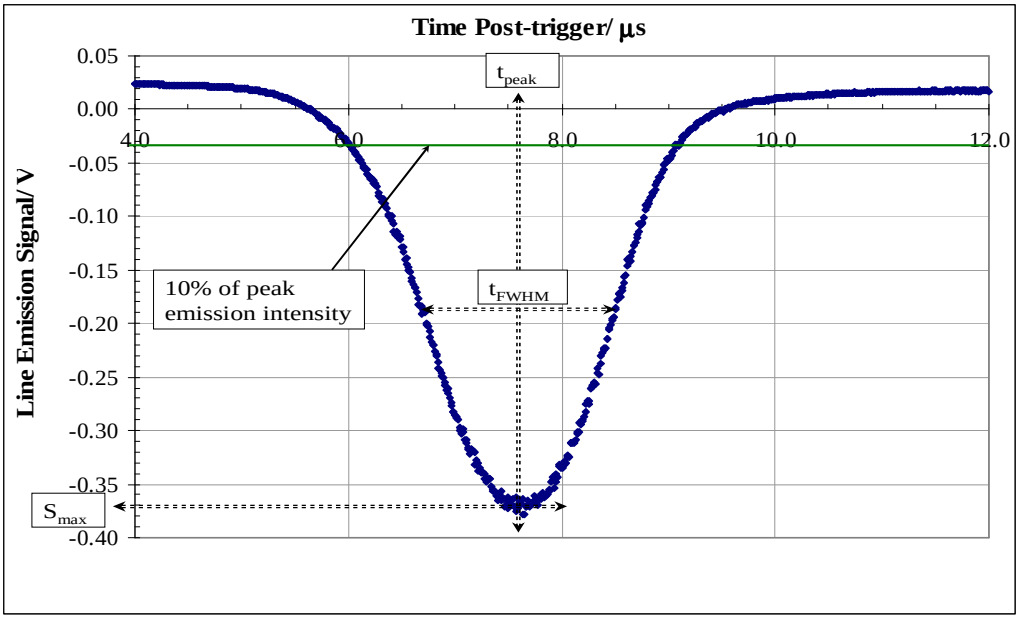

Figure 5.63: Critical Features of Emission Line Profile

Principal emission line profile characteristics are summarized in Table 5.28, including normalized line emission energy (E_{norm}), for the full range of plasma blocking used. The increment between successive recorded profiles, ΔL, was fixed at ~45µm.

Table 5.28: Line Emission Profile Characteristics

ΔL ±8µm	S_{max} ±0.05V	t_{peak} ±0.1µs	t_{FWHM} ±0.1µs	E_{line}	E_{norm}
0	0.380	7.63	1.84	67.74	1.00
45	0.350	7.63	1.79	65.43	0.97
90	0.355	7.40	1.76	62.64	0.92
135	0.350	6.99	1.66	58.49	0.86
180	0.335	6.73	1.64	56.15	0.83
225	0.320	6.27	1.58	50.38	0.74
270	0.280	5.74	1.48	42.20	0.62
315	0.265	5.35	1.43	39.35	0.58
360	0.014	4.81	0.67	0.85	0.01

The influence of increased plasma blocking at fixed increment, ΔL, on t_{peak} and t_{FWHM} is shown in Figure 5.64.

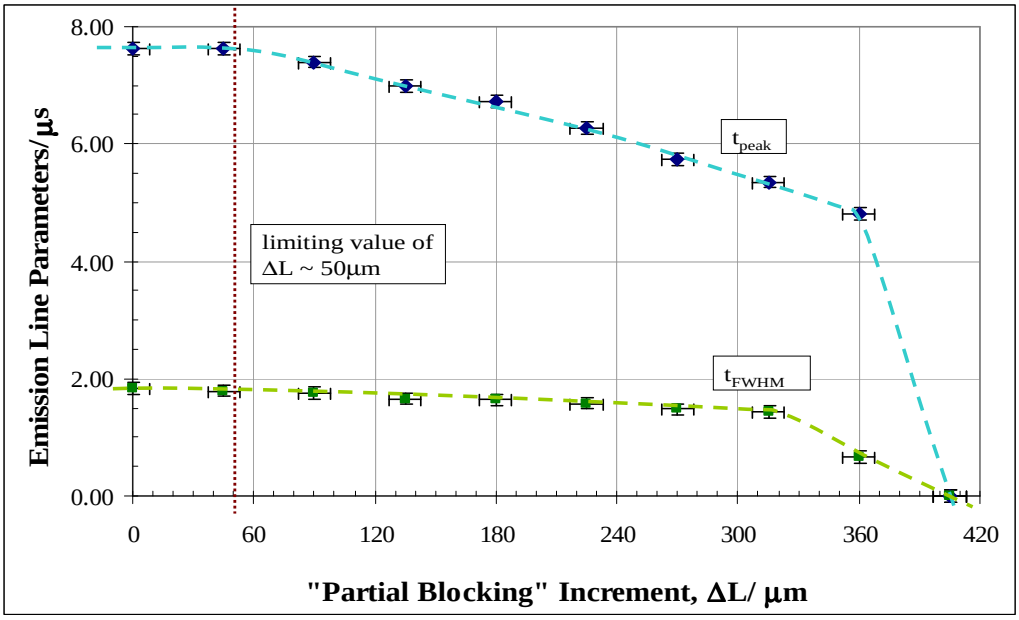

Figure 5.64: Effect of Plasma Blocking on Emission Line Temporal Characteristics

The limiting value of ΔL ~50µm, as shown in Figure 5.63, corresponded to minimum plasma blocking below which no significant effect on t_{peak} was recorded. A linear decrease of ~35% in t_{peak} was demonstrated for ΔL in the range ~50µm to ~370µm. A sharp decrease in t_{peak} was demonstrated for values of ΔL in excess of ~370µm, reducing to zero for ΔL ~405µm. Reduction in t_{FWHM} was less pronounced, reducing by ~20% for ΔL in the range ~50µm and ~315µm. A sharp decrease in t_{FWHM} was also measured as ΔL tended to an upper limit of 405µm. The linear decrease in both t_{peak} and t_{FWHM} are consistent with a compact region from which atomic emission lines are radiated, this region being characterized by a radiative flux that is approximately homogeneous.

The influence of increased plasma blocking at fixed increment, ΔL, on S_{max} and E_{norm} is shown in Figure 5.65.

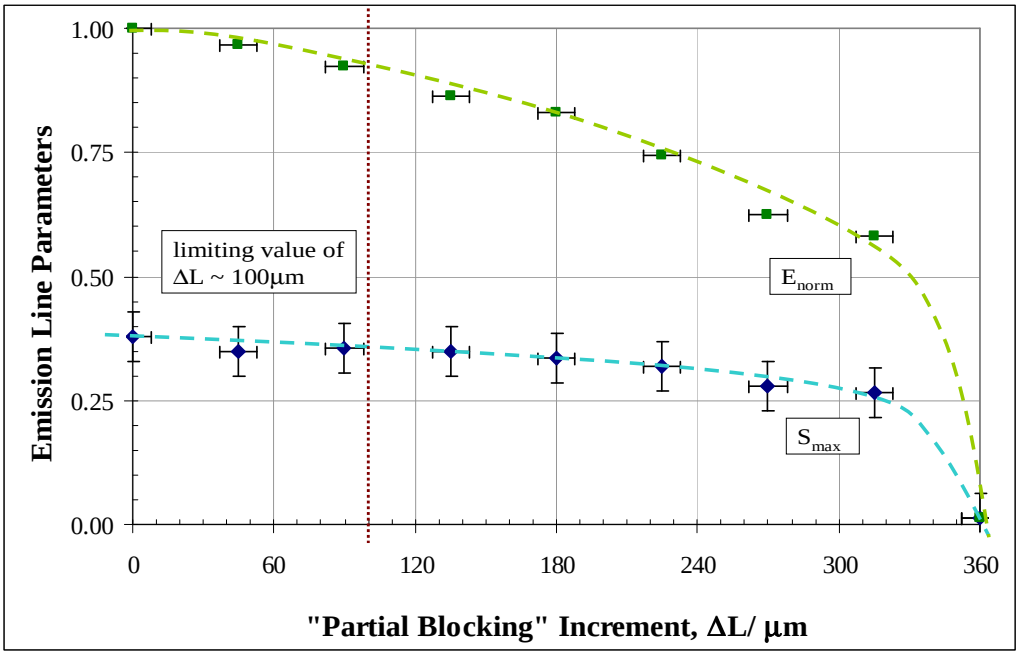

Figure 5.65: Effect of Plasma Blocking on Maximum Emission Line Intensity and Normalized Emission Profile Energy

The value of S_{max} was found to be unchanged, within the limits of experimental error, for plasma blocking, ΔL, up to ~100μm. For plasma blocking up to ~320μm a linear reduction in S_{max} of ~25% was demonstrated. The measure of net energy encapsulated within the emission line profile, E_{norm}, displayed a linear decrease of ~40% for plasma blocking up to ~320μm. The estimated changes in S_{max} and E_{norm} are consistent with a compact source of atomic emissions line, characterized by a flux which is approximately homogeneous across the emitting surface area. The rapid reduction to zero of these two parameters, for plasma blocking, ΔL, between ~320μm and ~360μm, indicated an emitting region with a well defined boundary.

Examination of the variation in critical emission parameters (S_{max}, t_{peak} and t_{FWHM}), for plasma blocked *Bremsstrahlung* and emission line profiles, revealed a significant difference in the blocking value, L_0, at which these parameters tended towards zero. For plasma blocked *Bremsstrahlung* profiles L_0 was estimated to be in the region of 750μm. This is significantly higher than the equivalent estimate of 400μm for plasma blocked emission line profiles.

These figures are consistent with the interpretation that the majority of line emission signals originate from a region of the laser induced plasma relatively close to the target surface. Examination of these data also lead to the inference that the volume for *Bremsstrahlung* emissions is considerably larger than the volume from which the majority of line emissions originate.

5.7.3 Improvement in LIBS Sensitivity using the Plasma Blocking Technique

LIBS spectra were recorded for the strong Al(I) emission line at 396.15nm for the range of plasma blocking previously described. A typical LIBS emission spectrum, representing approximately 15% plasma blocking, is shown in Figure 5.66. The mean and standard deviation of background signal intensity (m_{bkgnd} and σ_{bkgnd}, respectively) were calculated over the fixed spectral range between 397.00nm and 399.50nm. The data averaging algorithm accumulated 80 individual spectra. A complete set of LIBS spectra for the full range of plasma blocking is presented in Appendix XXIII.

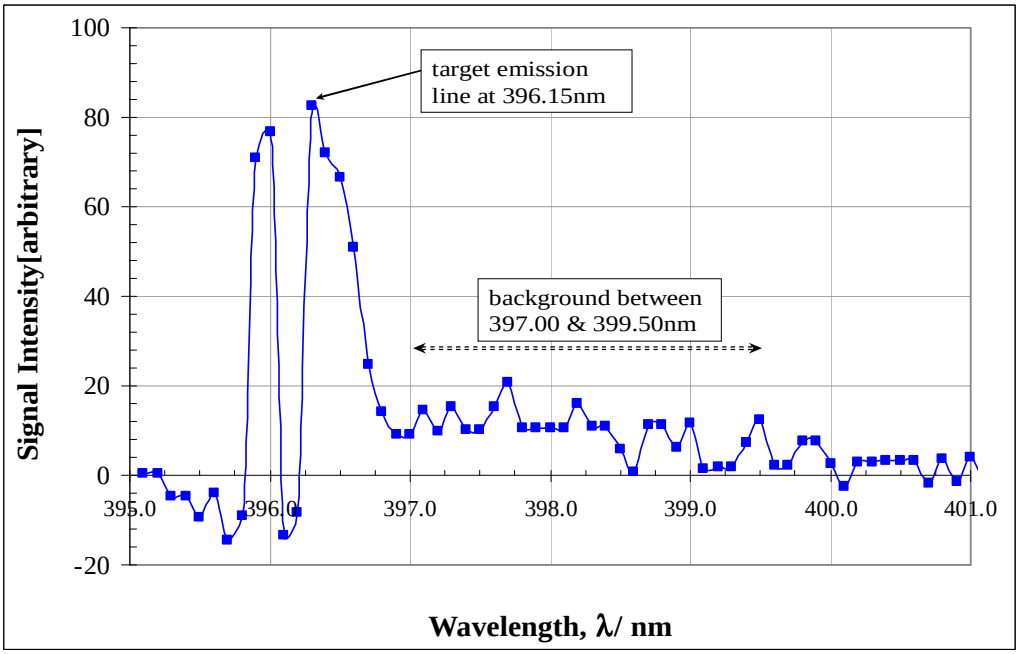

Figure 5.66: LIBS Emission Spectrum for ~15% Plasma Blocking

Signal-to-noise ratios (S/N_{blk}) for plasma blocked LIBS emission spectra were calculated using *eqn[3.18]*. Statistical parameters for these spectra are summarized in Table 5.29.

Table 5.29: Statistical Analysis of Plasma Blocked LIBS Spectra

ΔL ±8μm	S_{peak} ±2%	m_{bkgnd} ±2%	σ_{bkgnd}	S/N_{blk} ±5%
43	82.40	9.88	4.86	14.9
86	66.53	-11.72	3.84	20.4
129	87.13	7.56	4.95	16.1
172	66.53	3.91	5.02	12.5
258	60.73	23.86	9.25	4.0

The influence of increased plasma blocking at fixed increment, ΔL, on S/N_{blk} is shown in Figure 5.67.

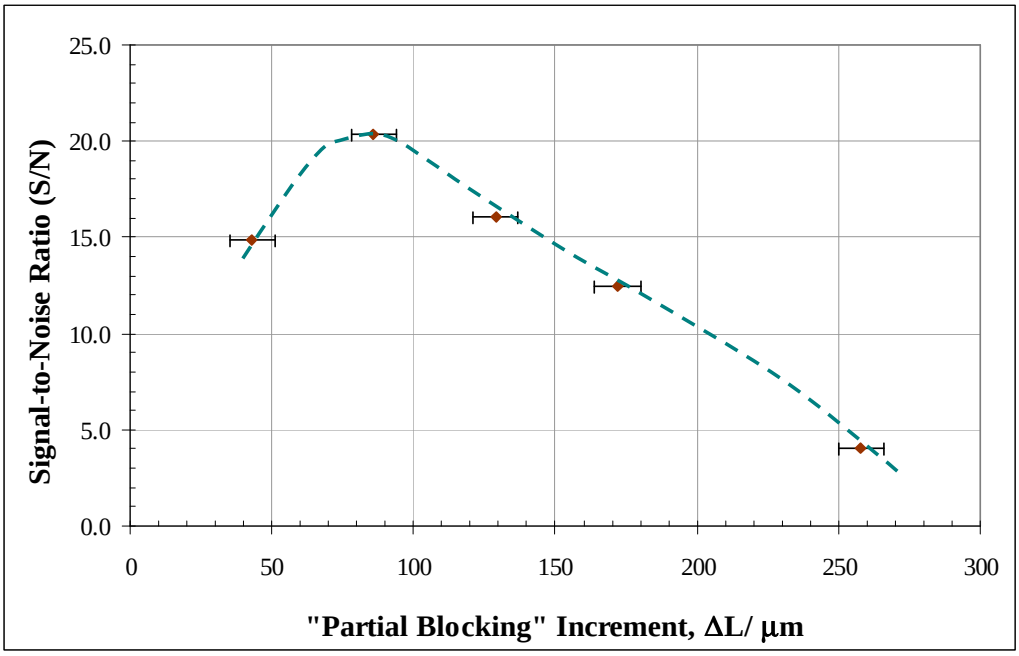

Figure 5.67: Influence of Plasma Blocking on LIBS Signal-to-Noise Ratio

The data shown in Figure 5.67 demonstrated a well defined maximum S/N of ~20 for plasma blocking increment, ΔL, in the region of 80μm. The optimum ΔL inferred from Figure 5.67 corresponded approximately to the range of plasma blocking during which peak emission line intensity was sustained (see Figure 5.64). The S/N decreased linearly for higher values of ΔL up to the maximum value of ~260μm. This was consistent with the trends previously described (see Figures 5.63 and 5.64) for the temporal and peak intensity parameters of plasma blocked emission line profiles. This consistency added weight to the hypothesis that the majority of atomic emission lines originated from a compact region which was separated from the target surface by a distance in the order of tens of microns.

References

Charfi B & Harith MA. Panoramic Laser Induced Breakdown Spectrometry of Water. Spectrochimica Acta B 57 1141-1153 (2002)

Mermet Jean-Michel. Limit of Quantitation in Atomic Spectrometry: An Unambiguous Concept? Spectrochimica Acta B 63 166-182 (2008)

THIS PAGE INTENTIONALLY BLANK

Chapter Six

DISCUSSION AND CONCLUSIONS

"Intellect is a magnitude of intensity, not a magnitude of extension."
Arthur Schœpenhauer

6.1 Dielectric Breakdown in Liquid Bulk

The difference between estimated breakdown thresholds for tap water ($2.8x10^{11}$ Wcm^{-2}) and distilled water ($7.0x10^{11}$ Wcm^{-2}) samples was demonstrated to be ~60%. This may be understood within the context of cascade ionization, which is the dominant mechanism for laser induced dielectric breakdown in the nanosecond pulse regime. This occurs through the collision process facilitated by the presence of free (solvated) electrons in the probed volume. Relatively high concentration of dissolved compounds normally found in tap waters (see Table 4.1) provided higher concentrations of solvated electrons compared to the availability of negligible concentrations of free electrons in distilled water. The relative abundance of free electrons in the tap water sample allowed onset of cascade ionization at significantly reduced photon flux (i.e. pulse energy), leading to a correspondingly lower breakdown threshold compared to that for the distilled water sample. A detailed theoretical model of multi-photon and cascade ionization in aqueous solutions has been reported (Kennedy: 1995), which included a mathematical derivation of thresholds for these respective mechanisms with regard to free electron density. The conclusions included in this report (Kennedy: 1995) support the significant reduction in dielectric breakdown threshold for tap water compared to distilled water, as reported in the present research.

Estimated breakdown thresholds for distilled water containing dissolved sodium chloride at different concentrations were similar to that of the distilled water sample. The difference between maximum and minimum breakdown thresholds in $NaCl_{(aq)}$ was ~11% for concentrations in the range 50ppm to 0.5ppm ($6.5x10^{11}Wcm^{-2}$ and $7.2x10^{11}Wcm^{-2}$, respectively). The relatively small difference (~11%) in breakdown threshold, for

$NaCl_{(aq)}$ samples representing two orders of magnitude of concentration, indicated a relatively weak dependence of breakdown threshold on singly ionized solvated species e.g. Na^+, Cl^- etc.

The estimated breakdown threshold for tap water was ~57% lower than that of the highest concentration (50ppm) of $NaCl_{(aq)}$. This may also be explained with reference to the cascade ionization mechanism for dielectric breakdown, and the relative abundance of solvated free electrons (for the tap water sample) in the focussed laser volume. In addition to the reported concentration of heavy metal species in the tap water sample (see Table 4.1), this sample also contained trace concentrations (in the order of parts per million) of other atomic and molecular species (see Appendix III: Thames Water Utilities Water Quality Report). The cumulative concentration of the four most abundant contaminant species i.e. Cl^-, Na^+, SO_4^{2-}, NO_3^- was in excess of 100ppm. This is significantly higher than the highest concentration (50ppm) of $NaCl_{(aq)}$ tested. Higher concentration of solvated electrons for tap water is consistent with the lower breakdown threshold for this sample. It was also concluded that dielectric breakdown threshold exhibited a significantly stronger dependence on molecular species and species of higher ionization e.g. SO_4^{2-} and NO_3^- than singly ionized atomic species e.g. Na^+ and Cl^-.

During dielectric breakdown in liquid bulk a proportion of laser energy is manifest as mechanical effects. These include the formation of a dynamically oscillating bubble in a process referred to as ‘cavitation’. Analysis of the dynamic behaviour of the laser induced bubble was necessary to evaluate the potential of using repeated pulses for enhancement of atomic emission line S/N in LIBS analysis.

6.2 Characterization of Laser Induced Cavitation

Experimental estimates for maximum bubble radius, obtained by two different techniques i.e. probe beam deflection (PBD – Configuration II) and high speed imagery (HSI), were

in good agreement i.e. 900 ± 50μm and 1100 ± 50μm, for PBD and HSI techniques, respectively. Estimates for the bubble lifetime were significantly different for the two techniques i.e. 835 ± 60μs and 660 ± 20μs, for PBD and HSI techniques, respectively. It is noted that PBD is an in-direct technique *insofar* as dynamic behaviour of the oscillating bubble is inferred from the reduction in probe beam signal intensity. The HSI technique, in contrast, allows direct imaging of the oscillating cavitation bubble for measurements in the spatial and temporal domains.

Estimation of maximum bubble diameter utilizing the PBD technique was dependent on the *a priori* estimation of two critical separation limits (denoted z_{min} and z_{max}). These limits represented the separation between the bubble centre and probe beam axis which corresponded to maximum and minimum (zero) effect on probe beam signal intensity, respectively (see Figure 5.6). These two separation limits were estimated from the graph showing the reduction in probe beam signal intensity with increasing separation between the bubble centre and probe beam axis. The principal sources of error for estimation of these two boundary limits were due to errors in the original measured data (for reduction in probe beam signal intensity), and the rapid change of gradient in the regions of the graph corresponding to z_{min} and z_{max} (see Figure 5.9).

Estimation of bubble oscillation period in the PBD technique was made by analysis of the probe beam signal intensity profile for zero separation between the bubble centre and probe beam axis. The bubble lifetime was considered to be equivalent to the time taken for the probe beam signal intensity to recover to its original (unaffected) value. A 75% criterion was used for this estimate to allow for inconsistency in probe beam signal intensity in the time period following maximum probe beam deflection. These inconsistencies were the main source of systematic error in estimation of bubble lifetime.

The principal source of error in the HSI technique was the limited contrast between the relatively luminous expanding bubble wall and the darker background. This problem was

especially apparent when individual images of the oscillating bubble were imported into standard PC software for post-processing (expansion, cropping and contrast enhancement). The resolution of individual images was inversely proportional to the frame rate of the camera. An attempt to utilize the maximum frame rate of ~$1x10^6$ frames per second (fps) was unsuccessful due to the limited byte size of single images (~2 kbytes), which rendered discrimination between bubble wall and background difficult, and therefore prone to relatively large errors. As previously noted (see section 5.2.4) a compromise between frame rate and image resolution resulted in the use of a frame rate of $5.4x10^4$ fps (corresponding to ~20μs between images), which generated still images each of ~8 kbytes. These images provided sufficient contrast to discriminate between the illuminated bubble wall and darker background with significantly reduced error.

Accurate estimation of expanding bubble volume from still images was limited by another source of error. This resulted from the presence of multiple bubbles in the cavitation region, which coalesced into a single bubble of negligible eccentricity over approximately the first half of the primary bubble oscillation cycle. Estimation of total cavitation bubble volume was performed by summation of the series of (assumed) spherical bubbles within the expanding cavitation region, whilst correcting for the estimated degree of overlap between adjacent bubbles. The assumption was made of a circular bubble cross-section in the plane orthogonal to the incident laser pulse trajectory. This assumption is consistent with a previously reported (Kennedy *et al*: 1997) model of plasma formation, with particular reference to the 'moving breakdown model' of plasma expansion.

Estimation of bubble diameter and oscillation lifetime has been reported (Petkovšek & Gregorčič: 2007, Petkovšek *et al*: 2007, Gregorčič & Možina: 2007, Gregorčič *et al*: 2008) using the PBD technique. Principal experimental parameters were similar to those of the present research i.e. laser wavelength = 1064nm, pulse duration = 7ns and focussed laser beam diameter ~60μm. The major difference was that these authors used

significantly lower laser pulse energies i.e. 4.7mJ and 8.6mJ, compared to in the order of 100mJ used in the present research. These authors quoted values of approximately 1150μm and 1550μm for the maximum radius of the cavitation bubble, and bubble lifetimes of approximately 330μs and 480μs for the same respective pulse energies. These values are significantly different from equivalent estimates of ~450μm & 835μs, obtained utilizing configuration II of the PBD technique, as reported in the present research.

Other estimates of laser induced cavitation bubble parameters have been reported (Lazic *et al*: 2007). These authors also used experimental parameters similar to that used for the present research i.e. laser wavelength = 1064nm and pulse repetition rate = 10Hz (no value was quoted by these authors for pulse duration). These authors investigated the time between generation of plasma in the liquid bulk and the first collapse of the cavitation bubble, for 10 pulse energies between ~25mJ and ~280mJ. This range of pulse energy included the value used in the present research i.e. ~140mJ. These authors measured bubble collapse period indirectly from the scattering of probe laser beam radiation from the surface of the oscillating bubble, and reported a complex relationship between pulse energy and primary bubble collapse time. A significant feature of this relationship was a rapid linear increase in collapse time from ~240μs to ~320μs for lower pulse energies in the range from 25mJ to 65mJ. For higher pulse energies (up to ~230mJ) an approximately linear and slowly decreasing change in collapse time from ~320μs to ~285μs was quoted. This trend was reversed for the highest pulse energy (~280mJ) for which a small increase in collapse time (to ~290μs) was quoted. By interpolating the trend reported by these authors it was estimated that the pulse energy used for the present research (~140mJ) corresponded to a collapse time (for the primary bubble) of 295μs. This value is 25% higher than the value (~220μs) obtained in the present research. For pulse energy of 280mJ these authors quoted approximate bubble lifetimes of 245μs, 140μs & 45μs for primary, secondary and tertiary oscillation cycles, respectively. These figures allow an estimate for bubble lifetime of 430μs. This compares to estimates of

bubble lifetime for the present research of 460±30, 835±60 and 660±20μs for PBD(I), PBD(II) and HSI techniques, respectively.

Other data for maximum bubble *radii* and collapse time have been reported (Zhao *et al*: 2007) for research investigating the behaviour of laser induced cavitation bubbles near a solid boundary. These authors used similar experimental parameters to that used for the present research i.e. laser wavelength = 1064nm and pulse duration = 10ns, and they also used a PBD technique. Quoted values were approximately 520μs, 210μs and 180μs for primary, secondary and tertiary bubble collapse times, respectively, for laser pulse energy of 25mJ. These figures allow an estimate for bubble lifetime of 910μs. Corresponding maximum bubble *radii* for this pulse energy were quoted to be approximately 2600μm, 1100μm and 900μm, respectively, for the three bubble oscillation cycles. The primary bubble radius was shown to increase non-linearly from ~800μm to ~3200μm with increase in pulse energy from ~2mJ and ~34mJ, with the indication of a saturation maximum for bubble radius at considerably higher pulse energies.

Previously reported research for characterization of laser induced cavitation bubble dynamics used similar experimental parameters to those of the present research. It follows that the significant differences in quoted values for maximum (primary) bubble radius and bubble lifetime cannot be adequately explained with reference to differences in laser pulse energy, pulse duration or laser wavelength. It is also noted that the specifications of the probe beam apparatus used to estimate bubble parameters were similar i.e. a HeNe probe beam operating in *cw* mode and emitting at 632nm was typically used. On close examination of the aforementioned research it was noted that there was a significant difference in the specifications of the focussing optics used to generate dielectric breakdown in the liquid bulk. A summary of the focussing optics is as follows: pre-expansion by a 50mm focal length concave lens followed by focussing with a 150mm focal length convex lens (Zhao *et al*: 2007); focussing with a double convex lens arrangement with an effective focal length of 25mm (Lazic *et al*: 2007); and,

focussing with a single 50mm focal length convex lens for the present research. No figure was quoted for the focal length of the convex lens in the papers issues by Petkovšek, Gregorčič *et al*. These authors did, however, quote a value for focussed laser spot size (i.e. ~60μm). By assuming an unfocussed laser beam width of 5mm (equal to that for the present research), and using the conventional formula for calculation of 'diffraction limited spot size', the focal length of the convex lens used by these authors was estimated to be ~100mm. The focussing lens focal length influences two important cavitation bubble parameters: *i*. the size of the focussed laser beam waist in the liquid bulk; and, *ii*. the cone angle for focussed radiation in the plasma forming region. The laser beam waist places a lower limit on the initial size of the cavitation bubble, whilst the cone angle influences the morphology of the bubble in the early stages of expansion. It is suggested that the significant differences in laser beam waist and cone angle in the liquid bulk, as inferred from the diverse range of focussing optics reported in the present and earlier research, was a major factor behind the differences in values of maximum bubble diameter and bubble lifetime.

The implications of accurate characterization of primary cavitation bubble properties for improving LIBS sensitivity are clear. By setting the pulse repetition rate high enough such that the inter-pulse separation matches the primary bubble lifetime, a second laser pulse may be focussed within the plasma formation volume. This aim has been realised in the established technique of double pulse (DP-) LIBS. The complementary effect of two pulses focussed within the cavitation bubble is to maintain/ increase the plasma temperature, and thus maintain the population of excited atomic states for a longer period and/ or increase the population of the upper level(s) of the emitting species.

Quantitative analysis of cavitation bubble spatial and temporal characteristics allows optimization of pulse repetition rate that could be used to increase emission line S/N for signals accumulated over a fixed temporal window. A pre-requisite to further improvement in LIBS sensitivity, however, is the elimination (or reduction to negligible

intensity levels) of the contribution from *Bremsstrahlung* to the emission profile. It was therefore necessary to investigate the dependence of the *Bremsstrahlung* emissions on both laser pulse energy and analyte concentration.

6.3 Characterization of *Bremsstrahlung* Emission

The results of the present research demonstrated no change in the temporal parameters of *Bremsstrahlung* emission profiles over a wide range of both laser pulse energies and analyte concentrations. Temporal *Bremsstrahlung* profile parameters considered here were time interval between plasma formation and the onset of maximum *Bremsstrahlung* signal intensity, full width at half-maximum of the *Bremsstrahlung* profile, and duration of the *Bremsstrahlung* profile (subject to a 10% signal intensity criterion). These parameters did not vary, within the limits of experimental error, for $NaCl_{(aq)}$ and $HgCl_{2(aq)}$ for concentrations covering a range of two orders of magnitude, and pulse energy over a range representing a factor of two. Consistency of temporal *Bremsstrahlung* emission parameters allows the setting of a fixed delay time prior to activation of a temporal window over which radiative signals may be accumulated. This provided the justification for the temporal gating technique for improvement of LIBS sensitivity.

The present research has also demonstrated a consistent relationship between emission parameters of the *Bremsstrahlung* profiles, and both laser pulse energy and analyte concentration. The *Bremsstrahlung* emission parameters considered here were peak intensity of the emission continuum, and the integrated emission energy within the *Bremsstrahlung* profile. For lower pulse energy and analyte concentrations (less than ~120mJ & ~100ppm, respectively) these parameters were demonstrated to increase linearly, tending asymptotically towards a saturation maximum at higher values. The saturation phenomenon is ubiquitous in all LIBS measurements and has been reported both in terms of analyte concentration (Knopp *et al*: 1996, Koch *et al*: 2004) and pulse energy (Michel *et al*: 2006, 2007).

These findings may be understood by consideration of the principal source of *Bremsstrahlung* emission from the expanding plasma i.e. acceleration of quasi-free electrons by the laser electromagnetic field. The intensity of *Bremsstrahlung* emission is therefore a function of both the free electron density in the plasma volume, as well as the photon flux (synonymous with laser pulse energy). The free electron density is a function of the rate at which species in the focussed laser volume are ionized, as well as the density of target species in this volume (synonymous with analyte concentration). It is important to appreciate that ionization of target species, and acceleration of quasi-free electrons, can only occur for the duration of the laser pulse. Saturation of *Bremsstrahlung* emission intensity has been demonstrated for a combination fixed laser pulse energy and variable analyte concentration, as well as fixed analyte concentration and variable pulse energy. These saturation effects reflect the influence of both pulse energy (photon flux) and analyte concentration (scattering centre concentration) on the intensity of *Bremsstrahlung* emission.

Emission line S/N may be further increased by optimization of principal LIBS experimental parameters, including temporal delay and gate width. This involves identifying a time domain for accumulation of emission signals which represents the optimum compromise between minimal intensity in the decaying *Bremsstrahlung* emission profile and the intensity of analyte emission line signals.

6.4 Optimization of Temporal Gating Parameters

Data presented in the present research has demonstrated optimization of laser pulse energy, delay time and data average number for maximizing of emission line signal-to-noise ratio (S/N). For each of these (independent) parameters S/N was found to slowly reach a maximum value at an upper limit. Additionally, the saturation phenomenon was observed for S/N with respect to these three parameters.

Temporal gating was introduced to take advantage of the differential rate of decay between *Bremsstrahlung* and atomic emission lines. The onset of emission corresponded to delivery of the laser pulse and was synonymous (for all intents and purposes) with plasma generation in the focussed volume. Triggering of detection apparatus in sympathy with delivery of the laser pulse was used to set the 'zero' time for recorded emission spectra. Atomic emission lines were masked by the intense *continuum* emission in the time period between delivery of the laser pulse and the reduction of *Bremsstrahlung* signal intensity to negligible levels. By setting an appropriate delay time, with respect to delivery of the laser pulse, the accumulated radiative emissions were dominated by emission lines from the target species. Experimental investigation into maximization of emission line S/N as a function of delay time demonstrated a S/N maximum for delay times in excess of ~290μs. Optimized S/N for the strong Na(I) emission line at 589.00nm was relatively insensitive to change in delay time in the range between ~270ns & ~370ns.

A significant contribution to the noise budget in LIBS spectra was the shot noise component of the background (*Bremsstrahlung*) signal. Reduction of shot noise was demonstrated by application of a data averaging algorithm. The effect of data average was demonstrated with regard to reduction of the shot noise component in the trailing edge of the residual *Bremsstrahlung* emission profile. The criterion by which the shot noise component was measured was the standard deviation of *Bremsstrahlung* signal intensity. An increase of data average number by a factor of 10 (from 1 to 100) reduced the standard deviation of the residual *Bremsstrahlung* emission signal by ~25%. No improvement in shot noise reduction was measured for higher values of N, which was interpreted as evidence of the saturation phenomenon.

The present LIBS research also demonstrated significant reduction in the *rms* magnitude of shot noise by the accumulation, within an optimized temporal window for signal accumulation, of a statistically significant number of emission spectra. Investigation into the maximization of S/N as a function of data average number demonstrated a S/N

maximum for data average number in the region of 100. The saturation phenomenon was also demonstrated *insofar* as no change, within the limits of experimental error, was shown for higher values of N. Additionally, a linear increase in S/N was demonstrated for lower values of data average number. The optimum value of N for the present research (i.e. ~100) is consistent with previously reported research. Comparative examples include: accumulation of 100 spectra (Diaz Pace *et al*: 2006) for estimation of detection limits for metal species, including lead and cadmium, contained within a solid matrix; averaging over 20 spectra (Hussain & Gondal: 2008) for detection of strontium using liquid surface sample presentation configuration; averaging over 20 spectra (Gondal & Hussain: 2007) for detection of strontium and titanium in liquid samples absorbed onto an solid organic matrix; and, averaging over 100 spectra (Fang *et al*: 2008) for detection of mercury in solid organic samples with surface plasma generation.

In the present research a rapid linear increase in S/N for pulse energy in the range ~10mJ to ~25mJ was demonstrated. An increase in S/N by a factor of 10 was found for this range of pulse energy. The maximum atomic emission line S/N corresponded to pulse energy of ~27mJ. At higher pulse energies the S/N showed a gradual reduction, before reaching a steady value for energy in excess of ~80mJ. It was also demonstrated that the difference between emission line and mean background signal intensities decreased by ~61% for pulse energy between ~27mJ and ~90mJ. This compared to a decrease of ~58% in S/N over the range of same pulse energy. This difference of 3% was not significant within the limits of experimental error. Reference to *eqn.[3.14]* led to the conclusion that there was no significant change in standard deviation of the background signal for pulse energy in the range ~27mJ to ~90mJ.

The demonstration of maximum S/N for relatively low laser pulse energy is explained by consideration of the timescale for absorption of focussed laser radiation by the liquid medium. Timescales for multi-photon absorption of laser radiation, photolysis in the liquid bulk, and hydrolysis of free electrons are in the picosecond and femtosecond

regimes (Longtin & Tien: 1997, Crowell & Bartels: 1996, Giacomo *et al*: 2007). These time scales are at least three orders of magnitude shorter than the nanosecond pulse duration used for the present research. The main implication of this significant difference in time scales is the utilization of only a fraction of the available pulse energy for initiating dielectric breakdown. The majority of pulse energy is therefore utilized (through absorption by photolysis products, particularly quasi-free electrons and hydroxyl radicals) in rapid heating of the expanding plasma. Dielectric breakdown threshold is more accurately considered, therefore, as a function of the gradient of the laser pulse intensity profile, as opposed to the pulse energy *per se*. As has been demonstrated by the present research the intensity profile of the Nd:YAG pulse is non-linear and has maximum gradient at the leading edge pulse of the incident laser pulse.

Optimized delay time, data average value and pulse energy were used to generate LIBS spectra for sodium and mercury in aqueous solution. The maximum measured S/N for Pb(I) emission lines at 405.78nm was ~22 (analyte concentration ~250ppm with data averaging over 80 spectra), compared to ~43 for Na(I) emission line at 589.00nm (analyte concentration ~260ppm with data averaging over 48 spectra). These data corresponded to LIBS detection limits of ~35ppm and ~10ppm, for lead and sodium, respectively. The lower value of S/N for lead was explained by the relative weakness of the Pb(I) emission line. The Payling and Larkins database (v1.5.7) quoted relative emission line strengths for neutral sodium (Na I at 589.00nm) and neutral lead (Pb I at 405.78nm) to be $1.7x10^8$and $2.7x10^6$, respectively. The Na(I) emission line is therefore ~63 times stronger than that of Pb(I). The attempt to obtain an experimentally significant S/N for aqueous mercury species utilizing the same optimized experimental parameters was unsuccessful. This was due to the weakness of the Hg(I) emission line compared to those of Pb(I) and Na(I). The Payling and Larkins database (v1.5.7) quoted relative emission line strength for neutral mercury (Hg I at 253.65nm) to be $1.7x10^5$. The Hg(I) emission line is therefore 1000 times weaker than that of Na(I), and ~16 times weaker than that of Pb(I).

The detection limits for lead as demonstrated in the present research (i.e. ~40ppm) compared favourably with other reported detection limits for this species, which were obtained using an equivalent sample presentation configuration (liquid bulk) e.g. 12.5ppm (Knopp *et al*: 1996). The detection limit quoted for the present research also compared favourably with reported detection limits for lead using alternative sample presentation configurations. Examples include: 4ppm for surface generated plasma (Cheri & Tavassali: 2011); 60ppm for liquid jet sample presentation configuration (Feng *et al*: 2010); 201ppm for liquid jet sample presentation configuration (Chang *et al*: 2010); 50ppm for surface generated plasma (Wu *et al*: 2008); 100ppm for surface generated plasma (Charfi & Harith: 2002); and, 40ppm for liquid jet sample presentation configuration (Samek *et al*: 1998).

Optimization of emission line S/N for improvement of LIBS sensitivity had thus far been demonstrated using spectral and temporal gating techniques. It was deemed prudent to investigate alternative techniques for improving LIBS sensitivity which are grouped under the description 'mechanical filtering'.

6.5 Mechanical Filtering for Improvement in Signal-to-Noise Ratio

6.5.1 'Background Subtraction' Technique

Before comments are made and conclusions drawn with regard to background subtracted (mechanically filtered) LIBS emission spectra, it is important to stress the generic nature of the mechanical filtering description. An earlier report (Miles & Barlow: 2000) described a mechanical filtering technique in which the spectrometer entrance slit was replaced with a sophisticated rotating wheel, which incorporated differentially rotating primary and secondary wheels. The authors reported an optimized exposure time of 9.1μs in combination with an 800μm entrance slit, which took advantage of the attributes (including high quantum efficiency and spatial resolution) of a back illuminated CCD detector. A later report (Mueller *et al*: 2007) used a chopping wheel with a single aperture

placed at the entrance slit of an Échelle spectrometer. The context of the authors' research was characterization of trace elements (molybdenum, copper etc.) in steel samples. The authors compared the performance of non-filtered iCCD and filtered CCD detection systems under identical experimental conditions, and reported no statistically significant differences in limits of detection. A more recent paper (Fang *et al*: 2008) compared LIBS performance of a conventionally gated double monochromator spectrometer coupled to an iPDA/ OMA detection system, and a mechanically filtered detection system comprising an Échelle grating spectrometer coupled to a CCD detector. In these authors' mechanically filtered experimental arrangement the chopping wheel was placed in front of the spectrometer entrance slit. The authors reported detection limits for mercury in soil samples to be ~50ppm and ~20ppm for the conventionally gated and mechanically chopped systems, respectively. These authors also reported significant interference between the target Hg(I) emission line at 253.65nm and a strong Fe(I) emission line at 253.68nm. These authors noted that the difference between these wavelengths (0.03nm) was comparable to the resolution limit (~0.05nm) of the conventionally gated system.

The mechanical filtering technique used in the present research utilized a rotating mechanical chopping wheel positioned between the pump laser aperture and the plane mirror which reflected the pulse into the liquid sample. This difference in experimental set-up differentiated the present research from those previously reported. A significant difference was demonstrated in emission timescales between liquid bulk sample presentation and surface generated plasma.

Initial data obtained with a surface generated plasma configuration demonstrated significant improvement in S/N, for detection of the Al(I) emission line at 396.15nm, for mechanically filtered (compared to conventionally gated) LIBS spectra, with data averaging over 20 laser shots. Conventionally gated LIBS spectra yielded an emission line S/N of ~39 compared to ~51 for mechanically filtered spectra. This represented an increase in LIBS sensitivity of ~31%. The attempt to demonstrate the efficacy of

mechanical gating for the liquid bulk sample presentation was unsuccessful. This was attributed to the increased effect of quenching in the liquid bulk compared to that for surface generation of plasma expanding in air.

6.5.2 'Plasma Blocking' Technique

The background subtraction technique showed improvement in LIBS sensitivity by direct comparison of emission line S/N for conventionally gated and mechanically filtered LIBS spectra. The plasma blocking technique similarly demonstrated improvement in LIBS sensitivity by comparison of S/N for progressively blocked LIBS spectra to the 'null case', which corresponded to no blocking of the plasma source. To the best of the Author's knowledge there is no research in the peer reviewed literature demonstrating improvement in LIBS sensitivity using an equivalent technique.

The present research demonstrated maximum emission line S/N of ~20 for plasma blocking increment of ~90μm relative to the 'point of origin' of the plasma. A linear decrease in S/N from ~20 to ~4 was shown for values of plasma blocking between ~90μm and ~270μm. By extrapolating measured data for plasma blocking increment <90μm, S/N was estimated to be ~6 for the condition of 'null' plasma blocking. (NB. extrapolation was limited by the presence of a single data point for the lower range of plasma blocking). Reduction in S/N was approximately the same for plasma blocking in the range 45μm to 135μm, centred on 90μm i.e. the degree of plasma blocking which corresponded to maximum S/N. This suggested a plasma emission region which was approximately symmetrical in the plane orthogonal to the axis represented by the 'line-of-sight' between the upper edge of the blocking medium and the collection optics.

6.6 Further Research

6.6.1 Improvements in LIBS System Sensitivity

Plasma generation is characterized by an intense continuum *Bremsstrahlung* emission profile which must be suppressed in order to maximize emission line S/N. The present research has demonstrated three techniques for suppression of *Bremsstrahlung*: *i*. conventionally (electronic/ temporal) gated LIBS spectra; *ii*. mechanical filtering to achieve 'background subtracted' LIBS spectra; and, *iii*. incorporation of 'plasma blocking' as a preliminary stage before (conventional) temporal gating. Given the small physical size of mechanical filtering components used in the present as well as previously reported research, the incorporation of this technique into a fieldable LIBS system is considered practicable.

6.6.2 'Fieldable' LIBS Systems

A principal objective of future research is the development of a portable LIBS system for *in situ* applications, including environmental monitoring of water samples contaminated with toxic elements e.g. mercury, lead etc. The practicality of developing a portable LIBS system has been made possible only over the previous two decades, as a result of technological advances in two critical areas: *i*. optical components for delivery of laser pulse and collection of plasma radiation; and, *ii*. size and mass reduction of three main LIBS system components i.e. laser, spectrometer and detector.

The rapid development of fieldable LIBS technology has given rise to a specific *nomenclature* within the LIBS research community, which differentiates between three categories of fieldable systems: *i*. 'portable' LIBS systems typically use a lens for delivery of the laser pulse; *ii*. 'remote' LIBS systems typically use an optical fibre for delivery of the laser pulse; and, *iii*. 'stand-off' LIBS systems typically use telescopic means for delivery of the laser pulse. Collection of plasma emissions by optical fibre is generally common to all fieldable LIBS system. For environmental applications in non-hostile environments a portable LIBS system is typically deemed the more suitable.

Given the general requirement of environmental applications for the generation of multi-element data in a spectrum extending from the UV to the N-IR, one of the main constraints for fieldable LIBS systems is the compromise between miniaturization of components and spectral resolution. A review of the development of fieldable LIBS systems has been recently reported (Fortes & Laserna: 2010).

References

Beddows DCS *et al*. Single Pulse Laser Induced Breakdown Spectroscopy of Samples Submerged in Water using a Single Fibre Light Delivery System. Spectrochimica Acta B 57 (9) 1461-1471 (2002)

Chang L *et al*. Analysis of Metals in Liquid by Laser Induced Breakdown Spectroscopy. High Power Laser and Particle Beams 22 (6) 1369-1372 (2010)

Charifi B & Harith MA. Panoramic Laser Induced Breakdown Spectroscopy of Water. Spectrochimica Acta B 57 (7) 1141-1153 (2002)

Cheri MS & Tavassoli SH. Quantitative Analysis of Toxic Metals Lead and Cadmium in Water Jet by Laser Induced Breakdown Spectroscopy. Applied Optics 50 (9) 1227-1233 (2011)

Crowell RA & Bartels DM. Multi-Photon Ionization of Liquid Water with 3.0-5.0eV Photons. Journal of Physical Chemistry 100 17940-17949 (1996)

Cuňat J *et al*. Real Time and *in situ* Determination of Lead in Road Sediments using a Man Portable Laser Induced Breakdown Spectroscopy Analyzer. Analytica Chimica Acta 633 (1) 38-42 (2009)

De Giacomo A *et al*. Spectroscopic Investigation of Laser-Water Interaction Beyond the Breakdown Threshold Energy. Spectrochimica Acta B 62 87-93 (2007)

Diaz Pace DM *et al*. Analysis of Heavy Metals in Liquid using Laser Induced Breakdown Spectroscopy by Liquid-to-Solid Matrix Conversion. Spectrochimica Acta B 61 929-933 (2006)

Fang X *et al.* Elemental Analysis in Soil by LIBS – a Comparison of Performance of a Chopper - Échelle based and a Conventional System. (2008)

Feng Y *et al*. Investigation of Laser Induced Breakdown Spectroscopy of a Liquid Jet. Applied Optics 49 (13) C70-C74 (2010)

Fortes FJ & Laserna JJ. The Development of Fieldable Laser Induced Breakdown Spectrometer: No Limits on the Horizon. Spectrochimica Acta B 65 975-990 (2010)

Gondal A & Hussain T. Determination of Poisonous Metals in Wastewater Collected from Paint Manufacturing Plant using Laser Induced Breakdown Spectroscopy. Talanta 71 (1) 73-80 (2007)

Gregorčič P *et al*. Measurements of Cavitation Bubble Dynamics based on a Beam Deflection Probe. Applied Physics A 93 901-905 (2008)

Gregorčič P & Možina J. Optodynamic Characterization of Laser Induced Bubbles. Acta Physica Polonica A 112 (5) 1137-1143 (2007)

Hussain T & Gondal A. Detection of Toxic Metals in Waste Water from Dairy Products Plant using Laser Induced Breakdown Spectroscopy. Bulletin of Environmental Contamination and Toxicology 80 561-565 (2008)

Kennedy PK. A First-Order Model for Computation of Laser-Induced Breakdown Thresholds in Ocular and Aqueous Media: Part I – Theory. IEEE Journal of Quantum Electronics 31 (12) 2241-2249 (1995)

Kennedy PK *et al*. Laser-Induced Breakdown in Aqueous Media. Progress in Quantum Electronics 21 (3) 155-248 (1997)

Knopp R *et al*. Laser Induced Breakdown Spectroscopy [LIBS] as an Analytical Tool for the Detection of Metal Ions in Aqueous Solution. Fresnius Journal of Analytical Chemistry 355 16-20 (1996)

Lazic V *et al*. Efficient Plasma and Bubble Generation Underwater by an Optimized Laser Excitation and its Application for Liquid Analyses by Laser Induced Breakdown Spectroscopy. Spectrochimica Acta B 62 1433-1442 (2007)

Longtin JP & Tien C-L. Efficient Laser Heating of Transparent Liquids using Multiphoton Absorption. International Journal of Heat and Mass Transfer 40 (4) 951-959 (1997)

Michel APM *et al*. Evaluation of Laser Induced Breakdown Spectroscopy (LIBS) as a New *in-situ* Chemical Sensing Technique for the Deep Ocean. Oceans 4098930 (2006)

Michel APM *et al*. Laser Induced Breakdown Spectroscopy for Bulk Aqueous Solutions at Oceanic Pressure: Evaluation of Key Measurement Parameters. Applied Optics 46 (13) 2507-2515 (2007)

Miles PC & Barlow RS. A Fast Mechanical Shutter for Spectroscopic Applications. Measurement Science and Technology 11 (4) 392-397 (2000)

Mueller M *et al*. Approach to Detection in Laser Induced Breakdown Spectroscopy. Analytical Chemistry 79 4419-4426 (2007)

Petkovšek R & Gregorčič P. A Laser Probe Measurement of Cavitation Bubble Dynamics Improved by Shock Wave Detection and Compared to Shadow Photography. Journal of Applied Physics 102 044909 (2007)

Petkovšek R *et al*. A Beam Deflection Probe as a Method for Optodynamic Measurements of Cavitation Bubble Oscillations. Measurement Science and Technology 18 (9) 2972-2978 (2007)

Samek O *et al*. Analysis of Liquid Samples using Laser Induced Breakdown Spectroscopy. Proceedings of SPIE 3504 299-308 (1998)

Wainner RT *et al*. Analysis of Environmental Lead Contamination: Comparison of LIBS Field and Laboratory Instruments. Spectrochimica Acta B 56 (6) 777-793 (2001)

Wu J-L *et al*. Detection of Metal Ions in Water Solution by Laser Induced Breakdown Spectroscopy. Spectroscopy and Spectral Analysis 28 (9) 1979-1982 (2008)

Yamamoto KY *et al*. Detection of Metals in the Environment using a Portable Laser Induced Breakdown Spectroscopy Instrument. Applied Spectroscopy 50 (2) 222-233 (1996)

Zhao R *et al*. Experimental Investigation of the Collapse of Laser Generated Cavitation Bubbles near a Solid Boundary. Optics & Laser Technology 39 968-972 (2007)

THIS PAGE INTENTIONALLY BLANK

BIBLIOGRAPHY

Walter Koechner. Solid-State Laser Engineering. 4th edition. Springer - Verlag 1996

Douglas A Skoog & James J Leary. Principles of Instrumental Analysis. Saunders College Publishing 1992

Wolfgang Demtröder. Laser Spectroscopy: Basic Concepts. 2nd corrected printing. Springer - Verlag 1982

MH Freeman. Optics. 10th edition. Butterworths 1990

John C Travis & Gregory C Turk. Laser Enhance Ionization Spectroscopy. John Wiley & Son Ltd. 1996

Joseph Sneddon, Terry L Thien and Jong-Ill Lee (editors). Lasers in Analytical Atomic Spectroscopy. VCH Publishers Inc. 1997

RCA Electro-Optics Handbook. Atlantic Books 1974

John F Ready. Effects of High Power Laser Radiation. Academic Press 1971

Kenichi Iga. Fundamentals of Laser Optics. Plenum Press 1994

J Wilson & JFB Hawkes. Optoelectronics: An Introduction. Prentice-Hall International Inc. 1983

J Watson. Optoelectronics. Van Nostrand Reinhold International 1988

THIS PAGE INTENTIONALLY BLANK

PUBLISHED PAPERS

Christopher S. Peel , Xiao Fang , S. Rafi Ahmad. Dynamics of laser-induced cavitation in liquid. Applied Physics A: Materials Science & Processing. DOI 10.1007/s00339-010-6056-7

Appendix I Operating Specification of Principal Items of Equipment

Litron Nd:YAG model Nano-L 200-20 class IV laser

maximum repetition rate	20 Hz
output energy at 1064nm	<200 mJ
pulse length at 1064nm	7ns
pulse to pulse stability	±2 %
beam diameter	5 mm
beam divergence	<0.8 mrad
timing jitter:	<0.5 ns

Uniphase He-Ne model 1125P: serial # 780893 class IIIb laser

minimum output power	5 mW cw
wavelength	632.8 nm
mode purity (TEM_{00})	>95 %
beam diameter	0.81 mm
beam divergence	±1 mrad
maximum noise	0.2 rms

SPEX 1404 double monochromator spectrometer

focal length	850mm
mirror diameter	120mm
grating resolution	1200 grooves mm^{-1}
spectral range	125nm - 375nm (UV)
	250nm - 750nm (VIS)
blaze wavelength	250nm (UV)
	500nm (VIS)
spectral purity	$<10^{-14}$ for $\Delta\lambda > 0.5$nm

Electron Tubes Limited model 9214QB photomultiplier tube

operating voltage	1.7kV
maximum QE	30% at 400nm
no. of dynodes	12
maximum gain	70×10^6
spectral range	160nm to 700nm
dark current	3nA
rise time (single pulse)	2ns
transit time	40ns
output impedance	50Ω

EG&G model 4420 charge integrator

gate range	2ns to 2ms
delay time	>50ns
input impedance	50Ω

Agilent Technologies model DSO5054A oscilloscope

bandwidth	500MHz
sample rate	4GSa/s
peak detection	250 ps
scope channels	4 channel simultaneous acquisition
range	2mV/div to 5V/div [1MΩ or 50MΩ]
input impedance	1 MΩ ±1%; 12 pF or 50MΩ ±1 %
noise	0.5% or 360μV rms

Centronic BPX65 series photodiode

rise time	10ns

Appendix II Reported Limits of Detection for LIBS in Aqueous Media

Table 1: Selected Group One Elements (SP-LIBS) - Different Sample Presentation Configurations

Element	Sample Presentation	LoD (ppm)	Experimental Parameters	*Remarks*	References
Li	Bulk	0.006 0.013	1064nm, 15ns, 9Hz, 260mJ 308nm, 28ns, 22mJ	*Order of magnitude difference in pulse energy*	Cremers (1984) Knopp (1996)
	Jet	0.009	1064nm, 10-15ns, 20Hz, <100mJ	*'Like-for-like' comparison between jet & nebulised*	Samek (1998)
	Nebulised	0.3	1064nm, 10ns, 10Hz, 90-100mJ		Archontaki & Crouch (1988)
Na	Bulk	0.014 0.008	1064nm, 15ns, 9Hz, 260mJ 308nm, 28ns, 22mJ	*See remark for bulk lithium*	Cremers (1984) Knopp (1996)
	Surface	0.7 2.0 1.0	532nm, 14ns, 1-10Hz, 60mJ 1064nm, 7ns, 10Hz, 180mJ 1064nm, 20ns, 10Hz, 10mJ	*Influence of wavelength stronger than influence of pulse energy*	Fichet (2001) Charfi & Harith (2002) Golik (2005)
	Jet	0.08 0.0004 50 0.23	1064nm, 10-15ns, 20Hz, <100mJ 193nm, 15ns, 40Hz, 16mJ 532nm, 12ns, 5-8Hz, 0.27mJ 193nm, 12ns, 5-8Hz, 0.27mJ	*Overall, jet data imply influence of wavelength, and poor LoD for micro-LIBS*	Samek (1998) Lo & Cheung (2002) Ho (1997) Ho (1997)
	Nebulised	2.2 0.6	1064nm, 10ns, 10Hz, 90-100mJ 355nm, 5-8ns, 10Hz, 12.6mJ	*Influence of wavelength out-weighs influence of pulse energy*	Archontaki & Crouch (1988) Huang (2002)
K	Bulk	1.2	1064nm, 15ns, 9Hz, 260mJ	*Implication of saturation at high pulse energy*	Cremers (1984)
	Jet	4	1064nm, 10-15ns, 20Hz, <100mJ		Samek (1998)
	Nebulised	2.7 1.2	355nm, 5-8ns, 10Hz, 12.6mJ 266nm, 5-8ns, 10Hz, 12.6mJ	*Advantage of lower wavelength*	Huang (2002) Huang (2002)

Table 2: Selected Group Two Elements (SP-LIBS) - Different Sample Presentation Configurations

Element	Sample Presentation	LoD (ppm)	Experimental Parameters	*Remarks*	References
Mg	Bulk	100	1064nm, 15ns, 9Hz, 260mJ	*Inferiority of bulk format*	Cremers (1984)
	Surface	1.0 1.0 0.7	532nm, 14ns, 1-10Hz, 60mJ 1064nm, 7ns, 10Hz, 180mJ 1064nm, 20ns, 10Hz, 10mJ	*Minimal influence of wavelength and pulse energy on LoD*	Fichet (2001) Charfi & Harith (2002) Golik (2005)
	Nebulised	1.9	1064nm, 10ns, 10Hz, 90-100mJ	*No disadvantage cf. surface configuration*	Archontaki & Crouch (1988)
Ca	Bulk	0.8 0.13	1064nm, 15ns, 9Hz, 260mJ 308nm, 28ns, 22mJ	*Dominance of wavelength over pulse energy*	Cremers (1984) Knopp (1996)
	Surface	0.3 0.9	1064nm, 7ns, 10Hz, 180mJ 1064nm, 20ns, 10Hz, 10mJ	*Advantage of larger pulse energy*	Charfi & Harith (2002) Golik (2005)
	Jet	0.6 0.003	1064nm, 10-15ns, 20Hz, <100mJ 193nm, 15ns, 40Hz, 16mJ	*Significant advantage of UV vs. IR wavelength, irrespective of pulse energy*	Samek (1998) Lo & Cheung (2002)
	Nebulised	0.4	1064nm, 10ns, 10Hz, 90-100mJ	*See remark for nebulised magnesium*	Archontaki & Crouch (1988)
Ba	Bulk	6.8	308nm, 28ns, 22mJ	*Influence of shorter wavelength off sets disadvantage of bulk format*	Knopp (1996)
	Surface	6.0	1064nm, 20ns, 10Hz, 10mJ		Golik (2005)
	Jet	0.007	193nm, 15ns, 40Hz, 16mJ	*Significant advantage of UV wavelength at high repetition rate*	Lo & Cheung (2002)

Table 3: Selected Metals (SP-LIBS) - Different Sample Presentation Configurations

Element	Sample Presentation	LoD (ppm)	Experimental Parameters	*Remarks*	References
Al	Bulk	20	1064nm, 15ns, 9Hz, 260mJ	*Superiority of surface vs. bulk configuration; Inferiority of low pulse energy*	Cremers (1984)
	Surface	10	1064nm, 7ns, 10Hz, 180mJ		Charfi & Harith (2002)
		500	1064nm, 20ns, 10Hz, 10mJ		Golik (2005)
		15	???		Chang *et al* (2010)
	Jet	18	1064nm, 10-15ns, 20Hz, 100mJ	*Inconclusive re. surface at same wavelength*	Samek (1998)
		62	???		Chang *et al* (2010)
	Nebulised	5.2	1064nm, 10ns, 10Hz, 90-100mJ	*IR advantageous cf. UV wavelength: in contradiction to other data*	Archontaki & Crouch (1988)
		43	355nm, 5-8ns, 10Hz, 38mJ		Huang (2002)
Pb	Bulk	12.5	308nm, 28ns, 22mJ	*UV at high repetition rate counters inferiority of bulk vs. surface configuration*	Knopp (1996)
	Surface	100	1064nm, 7ns, 10Hz, 180mJ		Charfi & Harith (2002)
		50	532nm, 10ns, 10Hz, ???		Wu *et al* (2008)
	Surface (Jet)	7	???		Chang *et al* (2010)
		4	1064nm, ???		Cheri & Tavassoli (2011)
	Jet	40	1064nm, 10-15ns, 20Hz, 100mJ	*Advantage of UV wavelength*	Samek (1998)
		0.3	193nm, 15ns, 40Hz, 16mJ		Lo & Cheung (2002)
		60	???		Feng Y *et al* (2010)
		201	???		Chang *et al* (2010)
Mn	Jet	10	1064nm, 10-15ns, 20Hz, <100mJ	*Equivalence of jet and nebulised configurations*	Samek (1998)
	Nebulised	7.2	1064nm, 10ns, 10Hz, 90-100mJ		Archontaki & Crouch (1988)
Cu	Surface	7	1064nm, 7ns, 10Hz, 180mJ	*Equivalence of surface and jet configurations*	Charfi & Harith (2002)
		31	532nm, 10ns, 10Hz, ???		Wu *et al* (2008)
	Jet	5	1064nm, 10-15ns, 20Hz, 100mJ		Samek (1998)

Table 4: Selected Metals (SP-LIBS) - Different Sample Presentation Configurations

Element	Sample Presentation	LoD (ppm)	Experimental Parameters	*Remarks*	References
Cr	Surface	10	1064nm, 7ns, 10Hz, 180mJ	*Superiority of surface vs. jet configuration*	Charfi & Harith (2002)
	Jet	200	1064nm, 10-15ns, 20Hz, <100mJ		Samek (1998)
Fe	Surface	30	1064nm, 7ns, 10Hz, 180mJ	*Advantage of higher pulse energies*	Charfi & Harith (2002)
		400	1064nm, 20ns, 10Hz, 10mJ		Golik (2005)
	Jet	148	???		Chang *et al* (2010)
	Surface	24	???		Chang *et al* (2010)
Zn	Surface	120	1064nm, 7ns, 10Hz, 180mJ	*Advantage of higher pulse energies*	Charfi & Harith (2002)
		600	1064nm, 20ns, 10Hz, 10mJ		Golik (2005)
Ni	Surface	36.4	1064nm, 8ns, 5-20Hz, 60mJ	*Minor influence of pulse energy in the 60mJ to 180mJ range; advantage of UV cf. IR wavelengths*	Berman & Wolf (1998)
		20.7	355nm, 8ns, 5-20Hz, 60mJ		Berman & Wolf (1998)
		20	1064nm, 7ns, 10Hz, 180mJ		Charfi & Harith (2002)
U	Surface	100	1064nm, 15ns, 10Hz, 125mJ	*Confirms typically high LoD for toxic heavy metal species*	Wachter & Cremers (1987)
Cd	Bulk	500	308nm, 28ns, 22mJ		Knopp (1996)
	Surface (Jet)	68	1064nm, ???		Cheri & Tavassoli (2011)
	Jet	207	???		Chang *et al* (2010)
	Surface	50	???		Chang *et al* (2010)
Sn	Surface	100	1064nm, 7ns, 10Hz, 180mJ		Charfi & Harith (2002)

Table 5: Comparison of LoD for DP-LIBS

Author(s)	wavelength λ/ nm	pulse duration τ_d/ ns	repetition rate f_p/ Hz	initial pulse E_1/ mJ	second pulse E_2/ mJ	inter-pulse separation $\Delta\tau$/ μs	LoD (ppm) element: DP and SP
Cremers *et al* (1984)	1064	15	10	30 - 76	125	<200	B: 80 *vs*. 1200
Kuwako *et al* (2003)	1064	3.5	10	201 (total)	201 (total)	8	Na: 0.1 [DP only]
Rai *et al* (2003)	532	5	10	<180	120	2 - 3	Mg: 0.370 *vs*. 0.970 Cr: 0.120 *vs*. 1.300
Koch *et al* (2004b)	532	6	5	106	94	80	Mn: 0.080 [DP only]
Lazic *et al* (2007b)	1064	?	10	92 72	214 144	75 75	DP-LIBS Mg: 0.210 Mn: 2.45 Cr: - Mg: 0.034 Mn: 0.390 Cr: 0.920

Table 6: Comparison of LoD for DP-LIBS

Author(s)	wavelength λ/ nm	pulse duration τ_d/ ns	repetition rate f_p/ Hz	initial pulse E_1/ mJ	second pulse E_2/ mJ	inter-pulse separation $\Delta\tau$/ μs	LoD (ppm) element: DP *cf.* SP
Yaroshchyk *et al* (2005b) (blended oil)	1064	7	1	95	170	1	Ag: 1 *cf.* 2 Al: 4 *cf.* 7 Cd: 4 *cf.* 7 Cr: 12 *cf.* 29 Cu: 1 *cf.* 4 Fe: 3 *cf.* 4 Mn: 3 *cf.* 4 Mo: 5 *cf.* 7 Ni: 7 *cf.* 20 Ti: 2 *cf.* 5 V: 2 *cf.* 5 Zn: 2 *cf.* 5 Pb: 3 *cf.* 18 Si: 11 *cf.* 19

Table 7: Comparison of LoD for Substrate Sample Presentation (SP-LIBS)

Author(s)	λ/ nm	E_p/ mJ	f_p/ Hz	LoD/ ppm
Arca *et al* (1996)	?	500	10	Cr: 0.010 Pb: 5.0 Cu: 0.005
Van der Wal *et al* (1999)	1064	155	single shot	Cr: 0.1 Fe: 0.01 Co: >0.1 Ni: 0.01 Cu: 0.01 Zn: 1.0 As: 5.0 Cd: 0.1 Hg: 10 Pb: 2.0
Schmidt & Goode (2002)	1064	80	?	Cd: 0.21 Cr: 0.13 Cu: 0.0042 Pb: 1.1 Hg: 2.0 Ni: 0.31 Zn: 0.85
Gondal & Hussein (2007)	1064	120	10	Cr: 2.0¶ Fe: 10.0¶ Cu: 2.0¶ Ni: 0.2¶ Pb: 3.0¶ Zn: 5.0¶
Alamelu *et al* (2008)	1064	<200	10	Sm: 1.3§ Eu: 1.9§ Gd: 2.3§
Chen *et al* (2008)	1064	100	5	Cr: 0.034 Cu: 0.029 Cd: 0.59 Pb: 0.074

¶ : LoD in μg/g
§ : LoD in ppm by weight

Appendix III Trace Chemical Composition of Local Water Supply

THAMES WATER UTILITIES
WATER QUALITY REPORT - 2009 DATA

Water Supply Zone S26 : SHRIVENHAM — Zone No. : 0291, Population: 5,908

Time Period: 01/01/2009 to 31/12/2009
Data extracted on :08/04/2010

Parameter	Units	PCV	Concentration or value (all samples) Min	Mean	Max	No. of Samples Total	Contravening	% of samples contravening PCV
Coliform bacteria	no/100ml	0	0	0	0	25	0	0
E. coli	no/100ml	0	0	0	0	25	0	0
Enterococci	no/100ml	0	0	0	0	8	0	0
Clostridium perfringens	no/100ml	0	0	0	0	217	0	0
Colony count 22C	no/ml	-	0	1.1	8	12	0	0
Colony count 37C	no/ml	-	0	2.9	33	12	0	0
Residual Disinfectant	mg/l	-	0.09	0.34	0.72	25	0	0
Colour (Pt/Co scale)	mg/lPt/Co	20.0	< 0.6	0.66	1.1	12	0	0
Hydrogen Ion	pH	6.5 to 9.5	7.2	7.3	7.6	12	0	0
Turbidity	FTU	4.00	< 0.09	0.098	0.18	12	0	0
Conductivity at 20C	uS/cm	2500	523	570	602	12	0	0
Ammonium as NH4	mg/l	0.50	< 0.05	< 0.05	< 0.05	13	0	0
Chloride as Cl	mg/l	250.0	19	33.1	45	8	0	0
Sodium as Na	mg/l	200.0	11	18	24.8	8	0	0
Sulphate as SO4	mg/l	250.0	18.6	49.7	77	8	0	0
Nitrate as NO3	mg/l	50.0	13.4	28.3	38.4	8	0	0
Nitrite as NO2	mg/l	0.500	< 0.01	< 0.01	< 0.01	8	0	0
Nitrate/Nitrite calculation	mg/l	1.00	< 0.3	0.57	0.77	8	0	0
Total Organic Carbon as C	mg/l	-	0.7	1.3	4.7	24	0	0
Total Hardness as CaCO3	mg/l	-	263	277	297	4	0	0
Odour (quantitative)	dilution no.	0	0	0	0	7	0	0
Taste (quantitative)	dilution no.	0	0	0	0	7	0	0
Iron as Fe	ug/l	200.0	< 1	10.2	57.7	13	0	0
Manganese as Mn	ug/l	50	< 1.5	1.6	2.5	13	0	0
Aluminium as Al	ug/l	200.0	< 6.5	12.3	65.6	13	0	0
Antimony as Sb	ug/l	5.0	< 0.2	0.21	0.3	8	0	0
Arsenic as As	ug/l	10.0	< 0.3	0.52	0.9	8	0	0
Cadmium as Cd	ug/l	5.0	< 0.2	< 0.2	< 0.2	8	0	0
Chromium as Cr	ug/l	50.0	< 1.4	< 1.4	< 1.4	8	0	0
Copper as Cu	mg/l	2.000	0.002	0.044	0.172	8	0	0
Lead as Pb	ug/l	25.0	< 0.3	0.62	1.6	8	0	0
Mercury as Hg	ug/l	1.00	< 0.12	< 0.12	< 0.12	20	0	0
Nickel as Ni	ug/l	20.0	< 1.6	< 1.6	< 1.6	8	0	0
Fluoride as F	mg/l	1.500	0.09	0.13	0.182	8	0	0
Selenium as Se	ug/l	10.0	< 0.8	0.82	1	8	0	0
Boron as B	mg/l	1.000	0.032	0.045	0.055	8	0	0
Bromate as BrO3	ug/l	10.0	< 0.2	0.23	0.6	20	0	0
Cyanide as CN	ug/l	50.0	< 2	< 2	< 2	20	0	0
Benzo 1.12 perylene	ug/l	-	< 0.001	< 0.001	< 0.001	8	0	0
Benzo 3.4 fluoranthene	ug/l	-	< 0.001	< 0.001	< 0.001	8	0	0
Benzo 11.12 fluoranthene	ug/l	-	< 0.001	< 0.001	< 0.001	8	0	0
Indeno(1,2,3-cd)pyrene	ug/l	-	< 0.001	< 0.001	< 0.001	8	0	0
PAHs (sum of 4 substances)	ug/l	0.100	0	0	0	8	0	0
Benzo (a) pyrene	ug/l	0.010	< 0.001	< 0.001	< 0.001	8	0	0
Trichloromethane	ug/l	-	0.4	1.2	2	8	0	0
Tribromomethane	ug/l	-	1.8	4	6.7	8	0	0
Dichlorobromomethane	ug/l	-	1	3	5.2	8	0	0

NOTE: PCV = Prescribed Concentration or Value

Page 1

THAMES WATER UTILITIES
WATER QUALITY REPORT - 2009 DATA

Water Supply Zone S26 : SHRIVENHAM — Zone No. : 0291 — Population: 5,908

Time Period: 01/01/2009 to 31/12/2009 — Data extracted on :08/04/2010

Parameter	Units	PCV	Concentration or value (all samples) Min	Mean	Max	No. of Samples Total	Contravening	% of samples contravening PCV
Dibromochloromethane	ug/l	-	2.4	6.6	11	8	0	0
Trihalomethanes	ug/l	100.0	5.6	14.7	24.4	8	0	0
Tetrachloroethene	ug/l	-	< 0.1	< 0.1	< 0.1	8	0	0
Trichloroethene	ug/l	-	< 0.1	< 0.1	< 0.1	8	0	0
Tetra- & Trichloroethene cal	ug/l	10.0	0	0	0	8	0	0
Tetrachloromethane	ug/l	3.0	< 0.1	< 0.1	< 0.1	8	0	0
1,2 dichloroethane	ug/l	3.0	< 0.1	< 0.1	< 0.1	8	0	0
Benzene	ug/l	1.0	< 0.1	< 0.1	< 0.1	8	0	0
Gross Alpha activity	Bq/l	0.10	< 0.02	0.022	0.04	12	0	0
Gross Beta activity	Bq/l	1.0	0.09	0.13	0.17	12	0	0
Atrazine	ug/l	0.100	< 0.006	< 0.006	< 0.006	20	0	0
Bentazone	ug/l	0.100	< 0.003	< 0.003	< 0.003	20	0	0
Bromoxynil	ug/l	0.100	< 0.002	< 0.002	< 0.002	20	0	0
Carbetamide	ug/l	0.100	< 0.006	< 0.006	< 0.006	20	0	0
Chlortoluron	ug/l	0.100	< 0.008	< 0.008	< 0.008	20	0	0
Clopyralid	ug/l	0.100	< 0.008	< 0.008	< 0.008	20	0	0
2,4-D	ug/l	0.100	< 0.004	< 0.004	< 0.004	20	0	0
Dicamba	ug/l	0.100	< 0.004	< 0.004	< 0.004	20	0	0
Dichlorprop	ug/l	0.100	< 0.003	< 0.003	< 0.003	20	0	0
Diuron	ug/l	0.100	< 0.006	< 0.006	< 0.006	20	0	0
Fluroxypyr	ug/l	0.100	< 0.004	< 0.004	< 0.004	20	0	0
Isoproturon	ug/l	0.100	< 0.004	< 0.004	< 0.004	20	0	0
Ioxynil	ug/l	0.100	< 0.001	< 0.001	< 0.001	20	0	0
Linuron	ug/l	0.100	< 0.017	< 0.017	< 0.017	20	0	0
Mecoprop	ug/l	0.100	< 0.003	< 0.003	< 0.003	20	0	0
MCPA	ug/l	0.100	< 0.002	< 0.002	< 0.002	20	0	0
MCPB	ug/l	0.100	< 0.002	< 0.002	< 0.002	20	0	0
Pentachlorophenol	ug/l	0.100	< 0.002	< 0.002	< 0.002	20	0	0
Propazine	ug/l	0.100	< 0.007	< 0.007	< 0.007	20	0	0
Prometryn	ug/l	0.100	< 0.013	< 0.013	< 0.013	20	0	0
Propyzamide	ug/l	0.100	< 0.015	< 0.015	< 0.015	20	0	0
Simazine	ug/l	0.100	< 0.005	< 0.005	< 0.005	20	0	0
2,3,6-TBA	ug/l	0.100	< 0.004	< 0.004	< 0.004	20	0	0
2,4,5-T	ug/l	0.100	< 0.002	< 0.002	< 0.002	20	0	0
Terbutryn	ug/l	0.100	< 0.013	< 0.013	< 0.013	20	0	0
2,4-DB	ug/l	0.100	< 0.002	< 0.002	< 0.002	20	0	0
Fenoprop	ug/l	0.100	< 0.002	< 0.002	< 0.002	20	0	0
Monuron	ug/l	0.100	< 0.004	< 0.004	< 0.004	20	0	0
Picloram	ug/l	0.100	< 0.01	< 0.01	< 0.01	20	0	0
Triclopyr	ug/l	0.100	< 0.002	< 0.002	< 0.002	20	0	0
Tebuthiuron	ug/l	0.100	< 0.004	< 0.004	< 0.004	20	0	0
Ametryne	ug/l	0.100	< 0.011	< 0.011	< 0.011	20	0	0
Carbendazim	ug/l	0.100	< 0.007	< 0.013	< 0.015	20	0	0
Dichlobenil	ug/l	0.100	< 0.001	< 0.001	< 0.001	12	0	0
Diflufenican	ug/l	0.100	< 0.005	< 0.005	< 0.005	12	0	0
Metazachlor	ug/l	0.100	< 0.002	0.003	0.008	12	0	0
Metaldehyde	ug/l	0.100	< 0.004	0.015	0.033	20	0	0

NOTE: PCV = Prescribed Concentration or Value

Page 2

THAMES WATER UTILITIES
WATER QUALITY REPORT - 2009 DATA

Water Supply Zone S26 : SHRIVENHAM — Zone No. : 0291, Population: 5,908

Time Period: 01/01/2009 to 31/12/2009
Data extracted on :08/04/2010

Parameter	Units	PCV	Concentration or value (all samples) Min	Mean	Max	No. of Samples Total	Contra-vening	% of samples contravening PCV
Total Pesticides	ug/l	0.500	0	0.013	0.033	20	0	0

THAMES WATER UTILITIES
WATER QUALITY REPORT - 2009 DATA

WATER SUPPLY ZONE:S26 : SHRIVENHAM — Zone No: 0291
FOR PERIOD 01/01/2009 to 31/12/2009 — Population: 5,908

Commentary on Water Quality :

Excellent quality water, no infringements to report.

NOTE

For some parameters, monitoring occurs at the supplying Water Treatment Works, rather than in the Water Supply Zone.

NOTE: PCV = Prescribed Concentration or Value

Appendix IV Spectrometer Grating Efficiency Curves

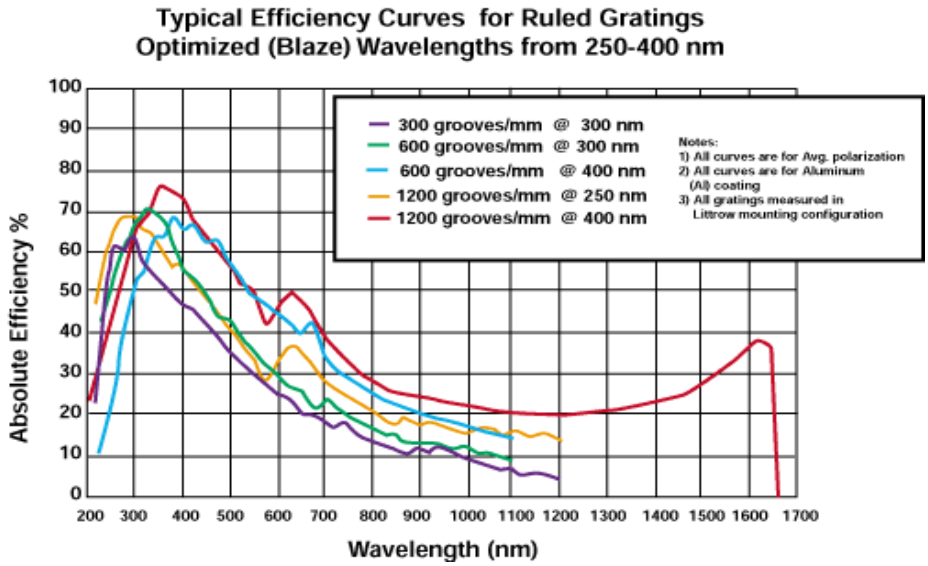

Figure 1 Dispersion Efficiency for UV Grating
source: http://www.horiba.com/uk/scientific/products/gratings/

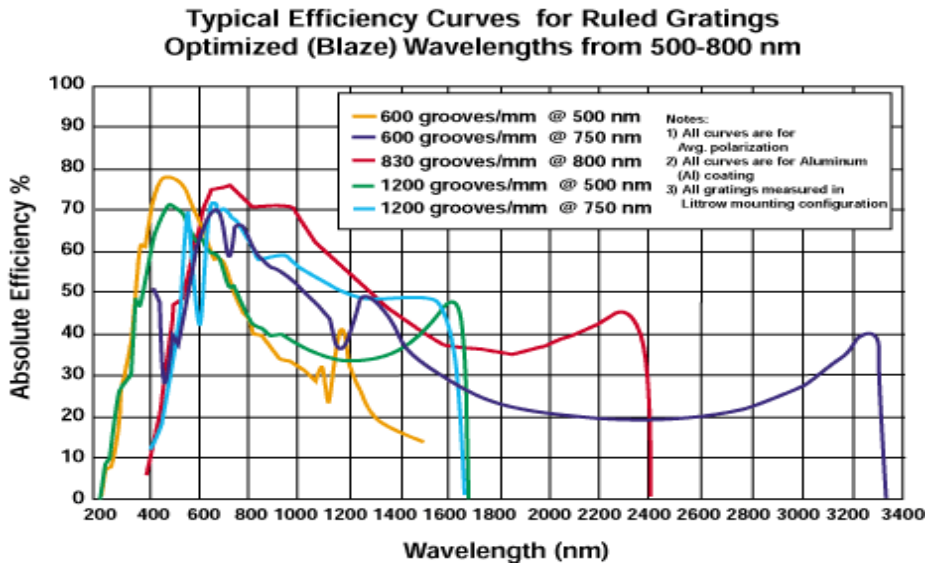

Figure 2 Dispersion Efficiency for VIS Grating
source: http://www.horiba.com/uk/scientific/products/gratings/

Appendix V Probe Beam Deflection Profiles: Configuration I

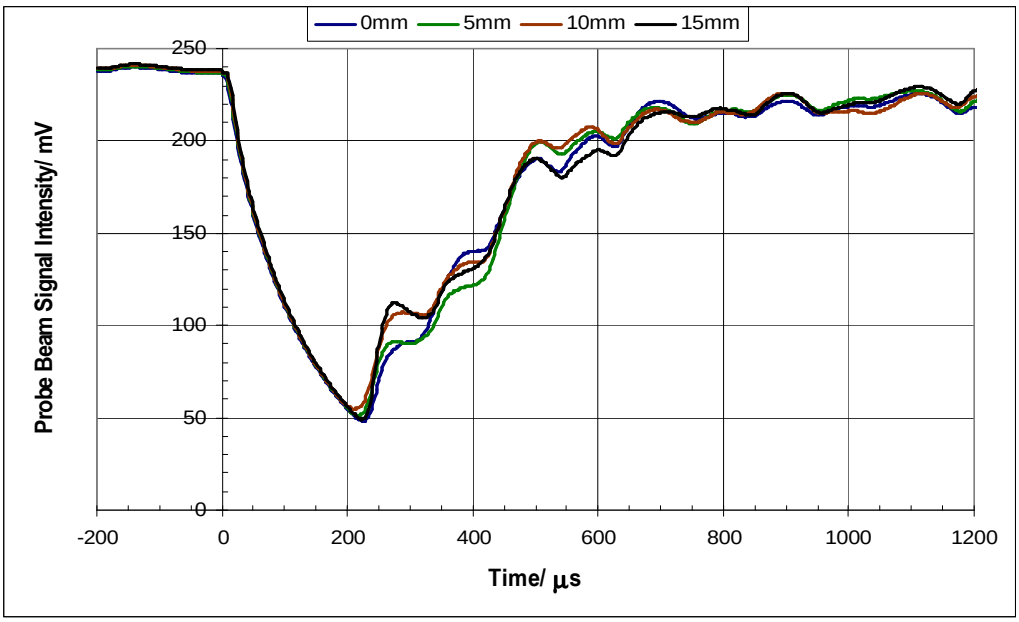

Figure 1: Probe Beam Deflection: 0mm<L<15mm

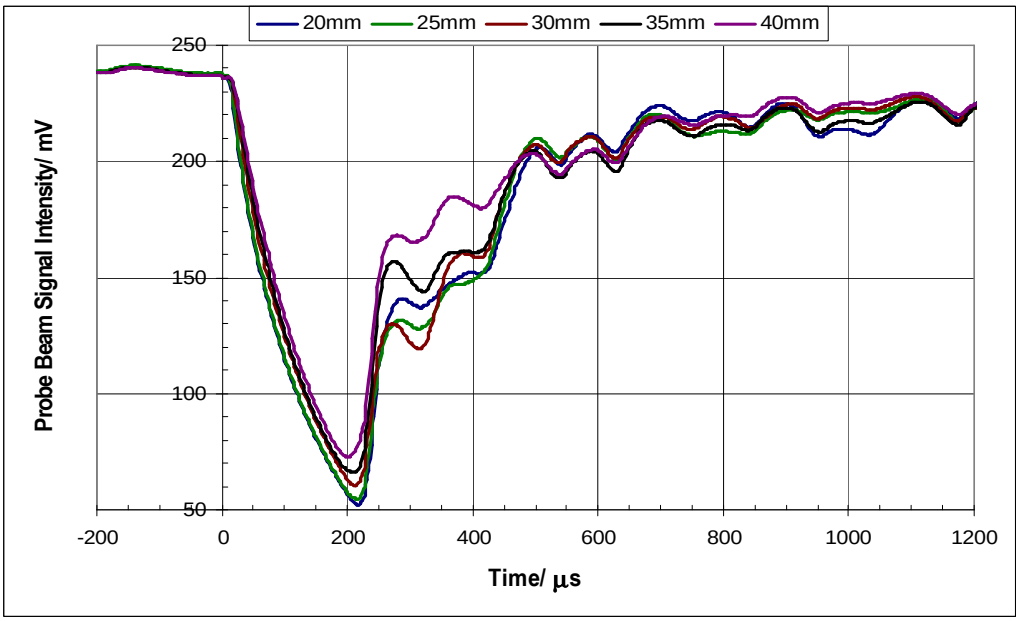

Figure 2: Probe Beam Deflection: 20mm<L<40mm

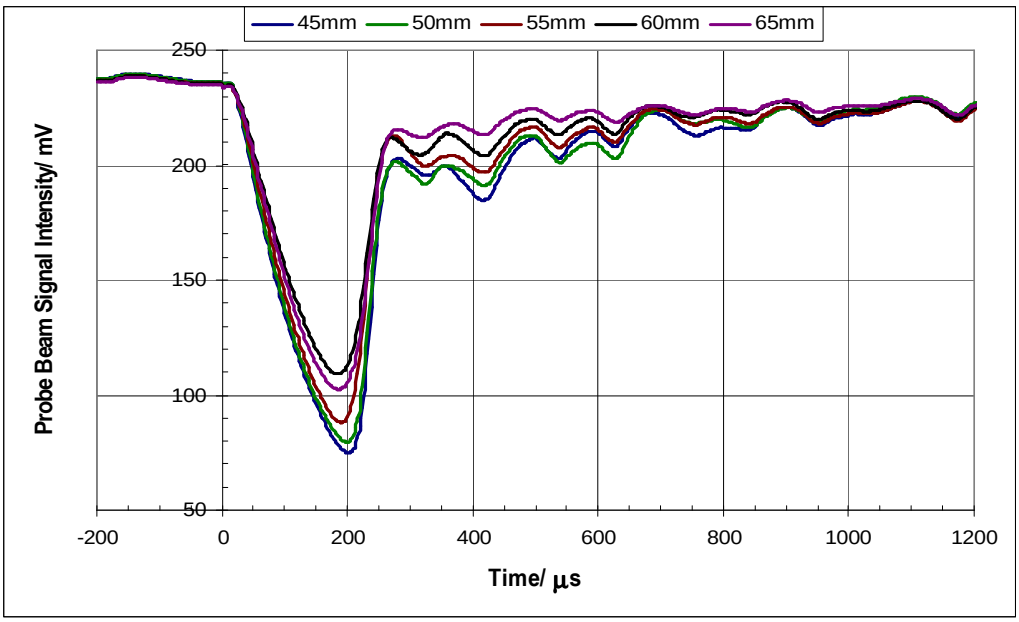

Figure 3: Probe Beam Deflection: 45mm<L<65mm

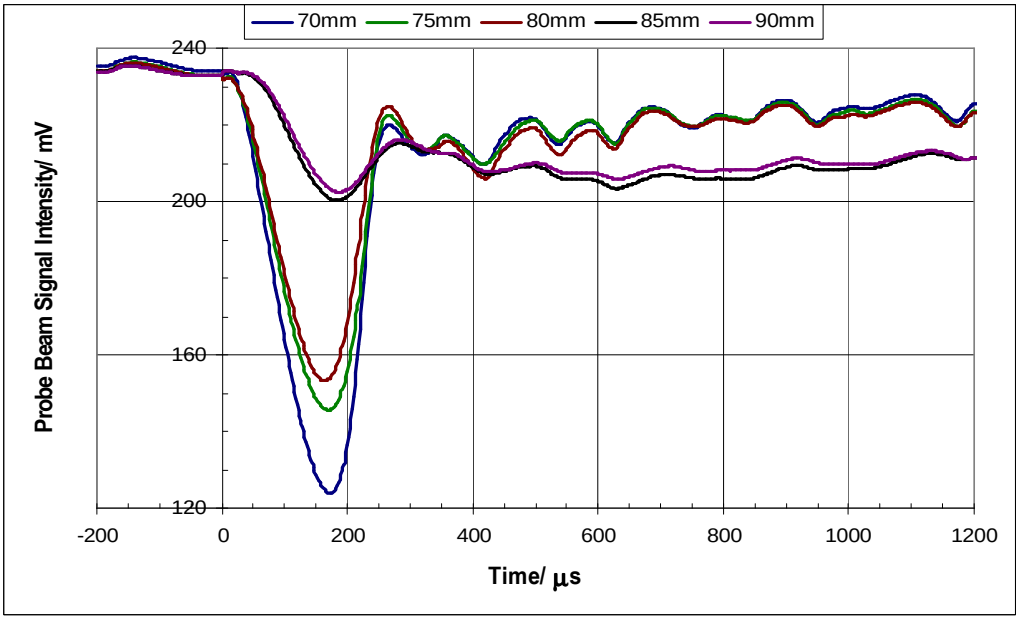

Figure 4: Probe Beam Deflection: 70mm<L<90mm

Appendix VI Probe Beam Deflection Profiles: Configuration II

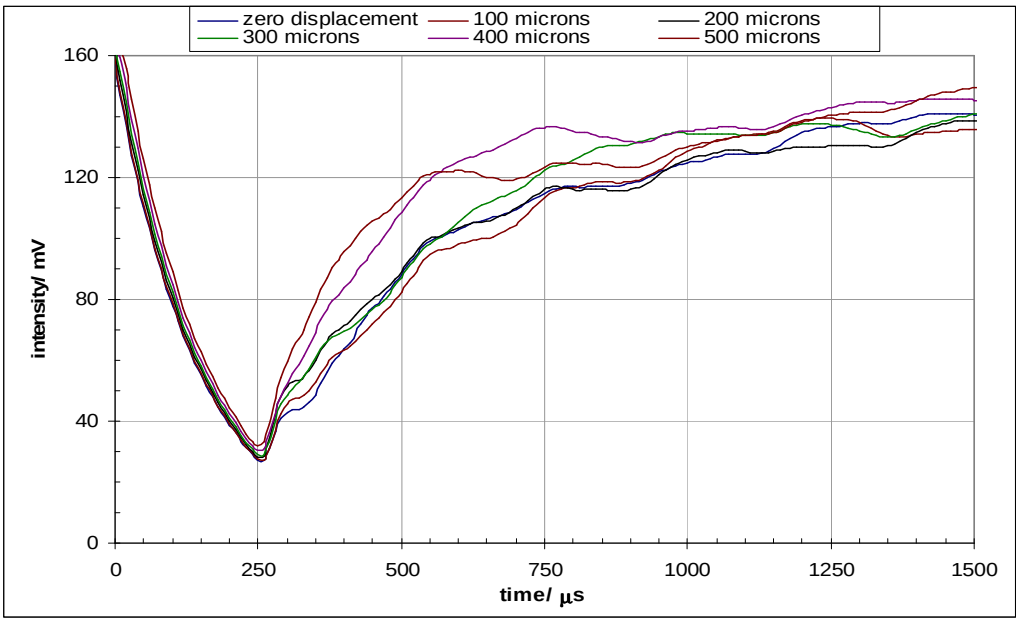

Figure 1: Probe Beam Deflection: 0<z< -500µm

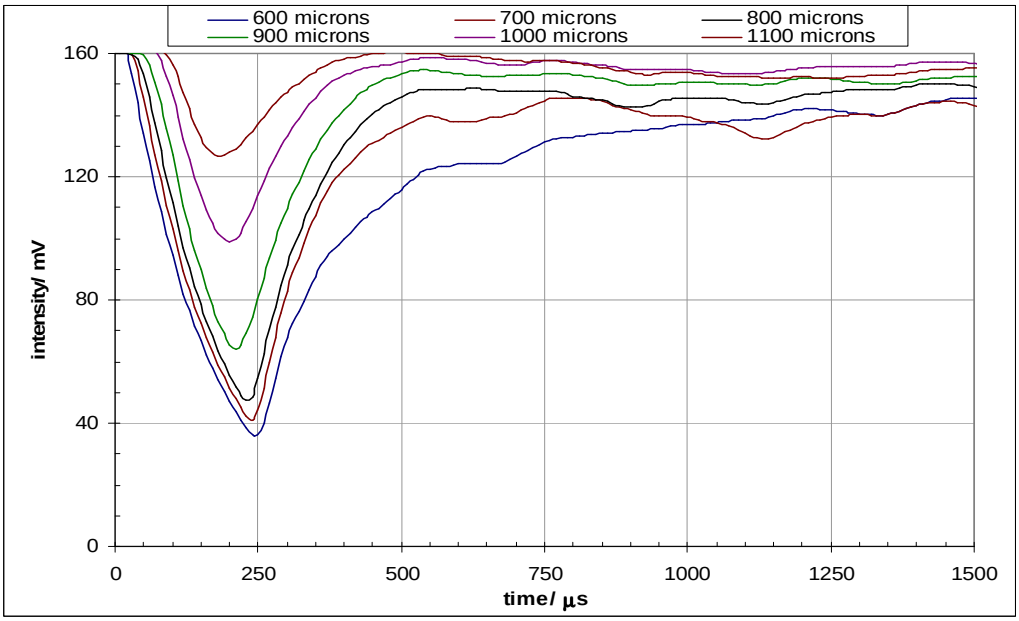

Figure 2: Probe Beam Deflection: -600<z< -1100µm

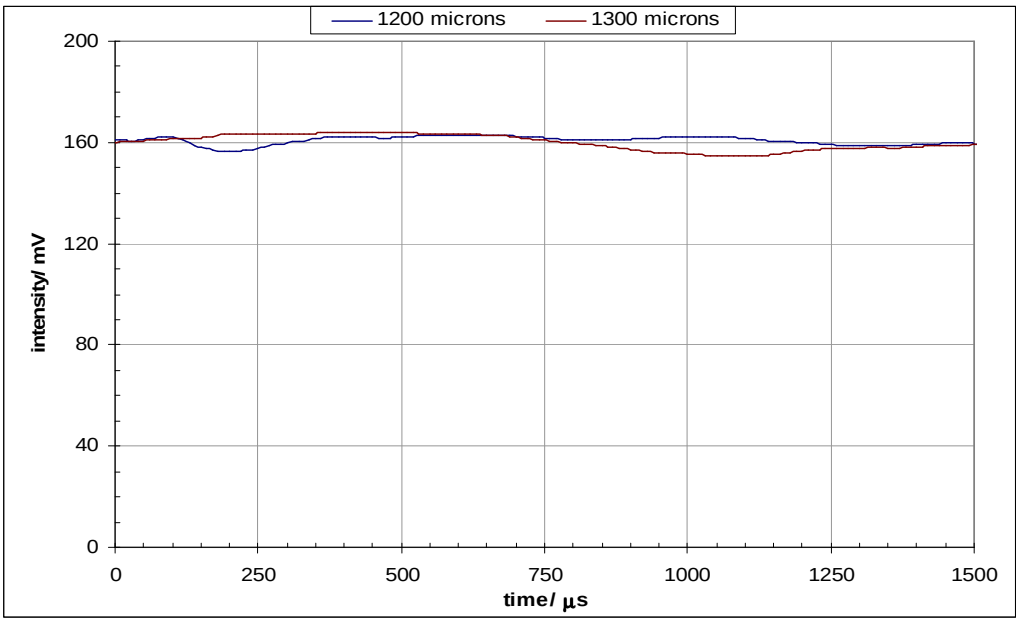

Figure 3: Probe Beam Deflection: z = -1200 & -1300µm

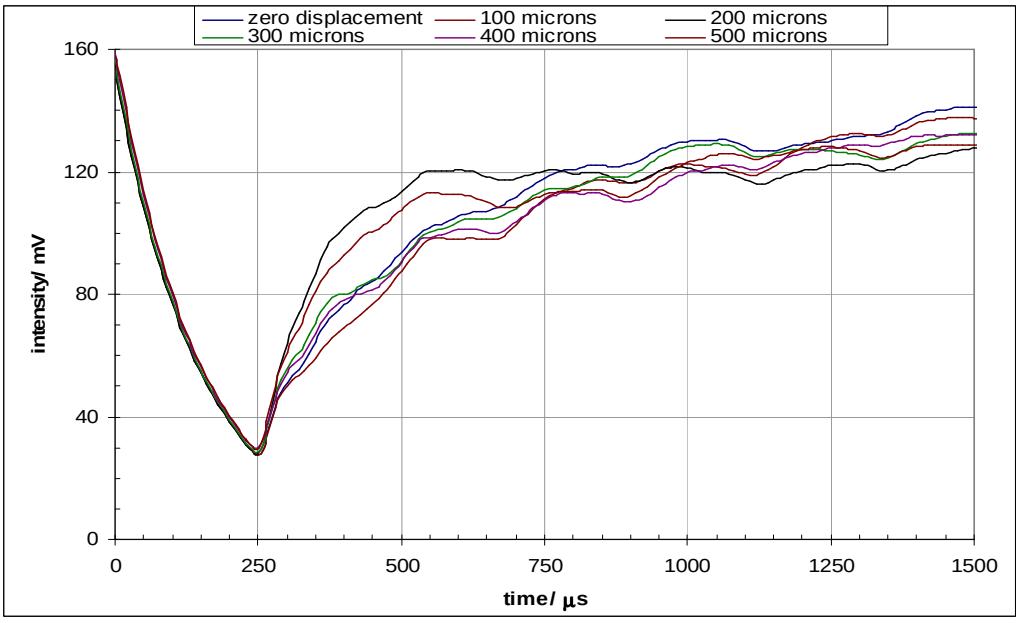

Figure 4: Probe Beam Deflection: 0<z< +500µm

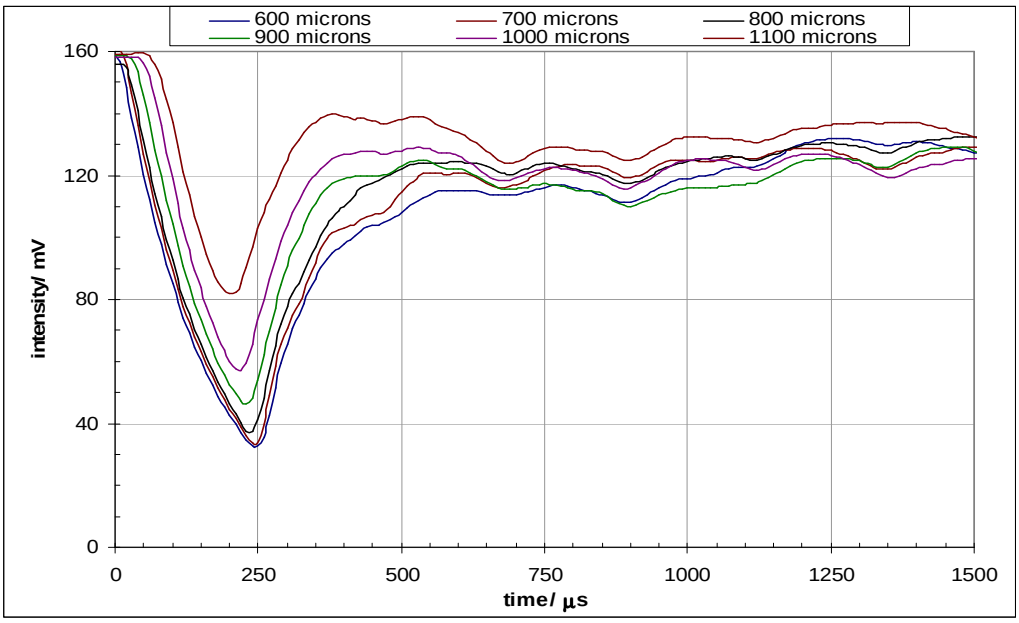

Figure 5: Probe Beam Deflection: +600<z< +1100µm

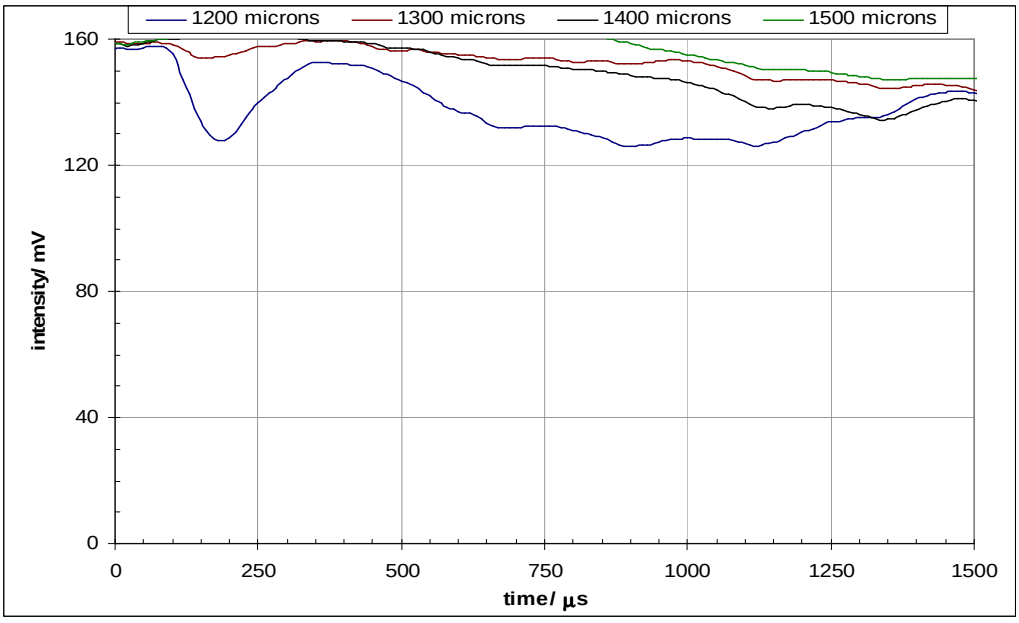

Figure 6: Probe Beam Deflection: +1200<z< +1500µm

Appendix VII Expanded Probe Beam Deflection Profiles: Configuration II

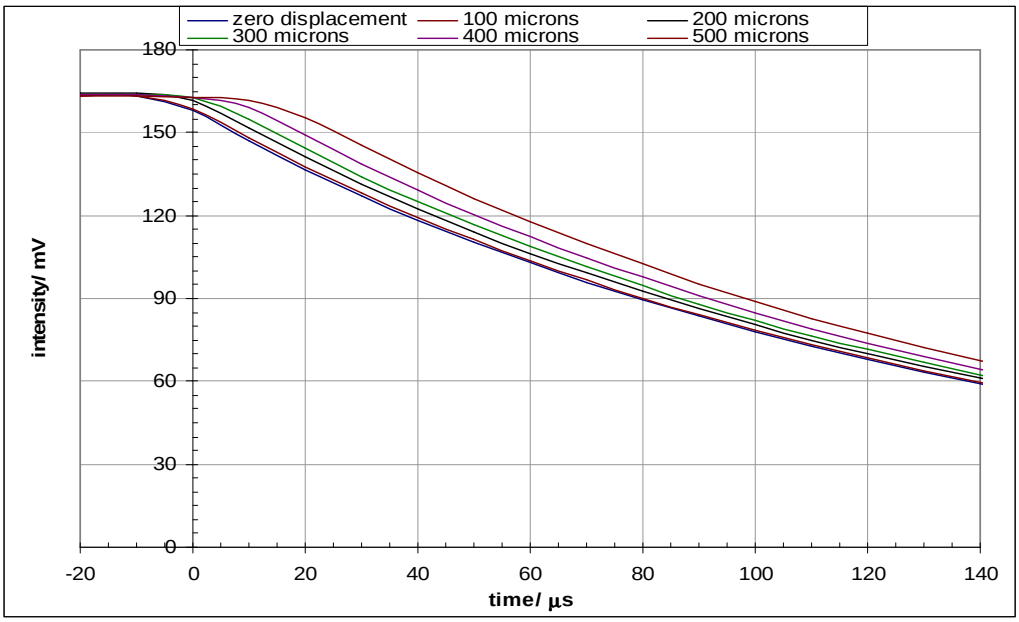

Figure 1: Expanded Time Base: 0<z< -500µm

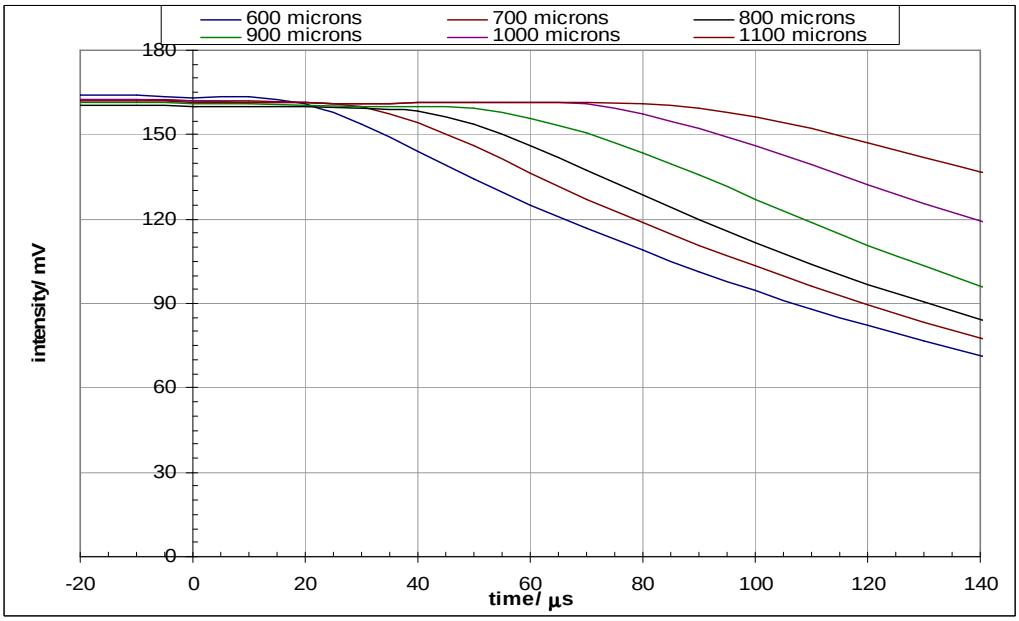

Figure 2: Expanded Time Base: -600<z< -1100µm

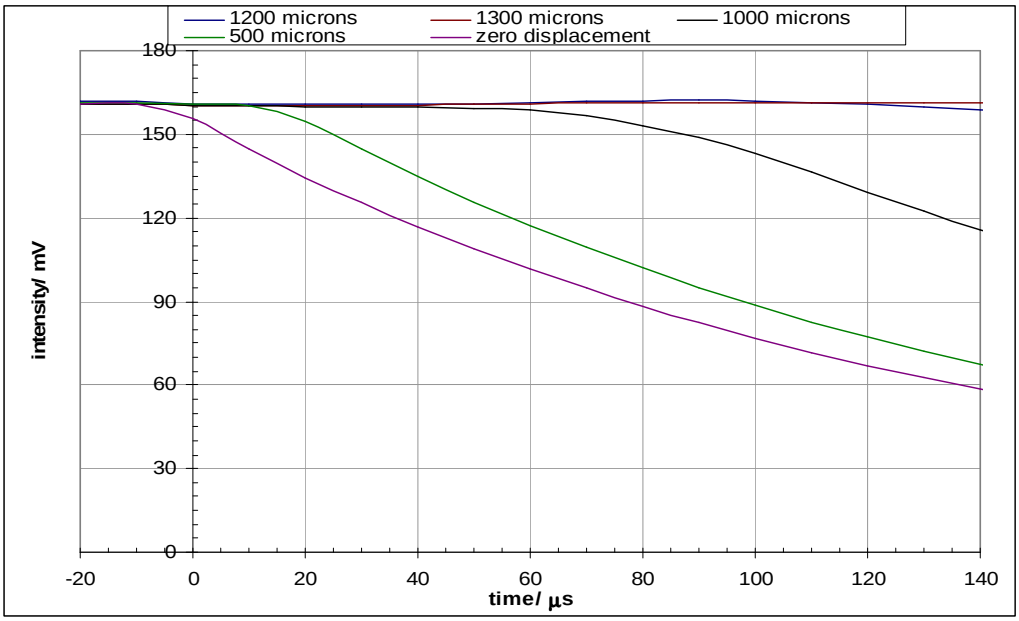

Figure 3: Expanded Time Base: z = -1200 & -1300µm

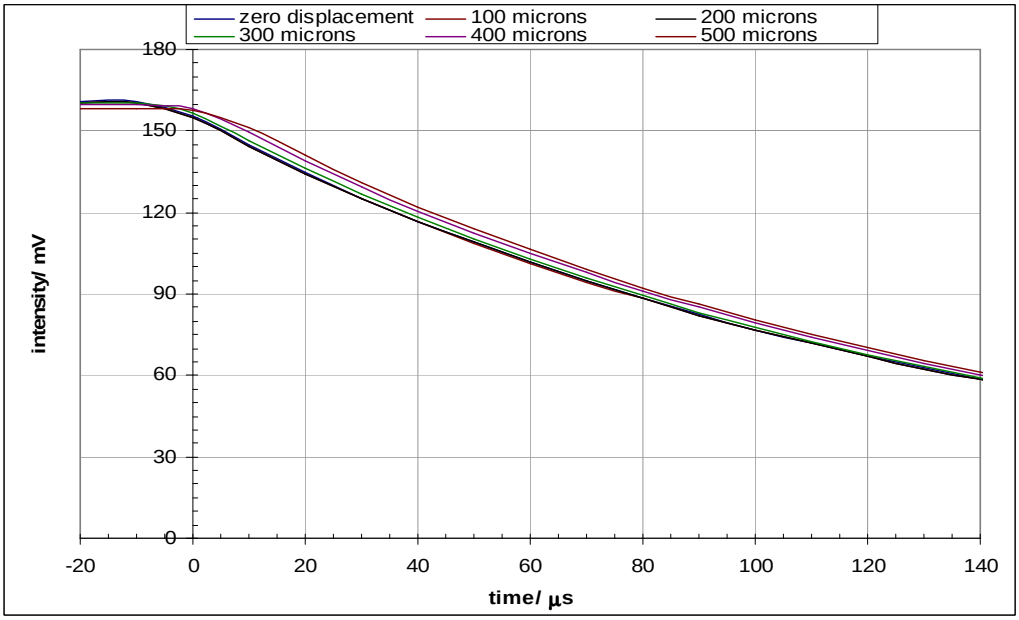

Figure 4: Expanded Time Base: 0<z< +500µm

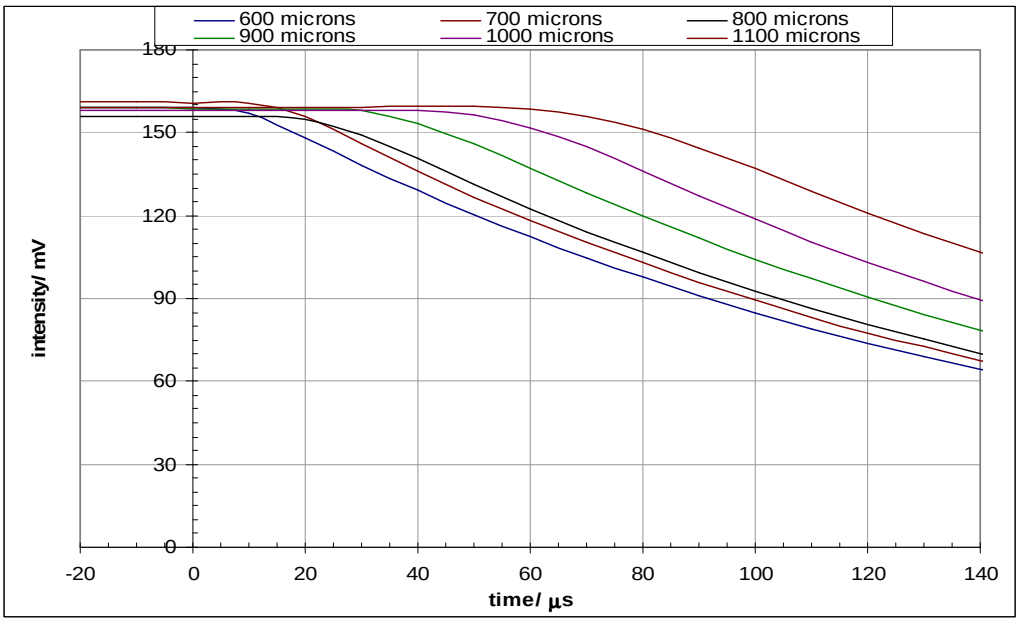

Figure 5: Expanded Time Base: +600<z< +1100µm

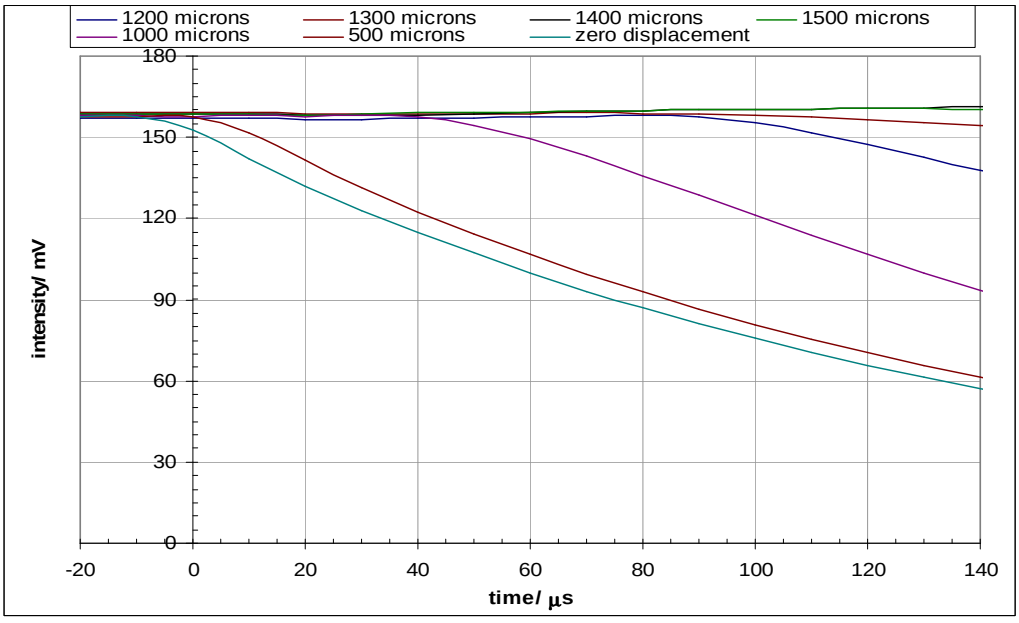

Figure 6: Expanded Time Base: +1200<z< +1500µm

Appendix VIII High Speed Imaging of Laser Induced Cavitation Bubble

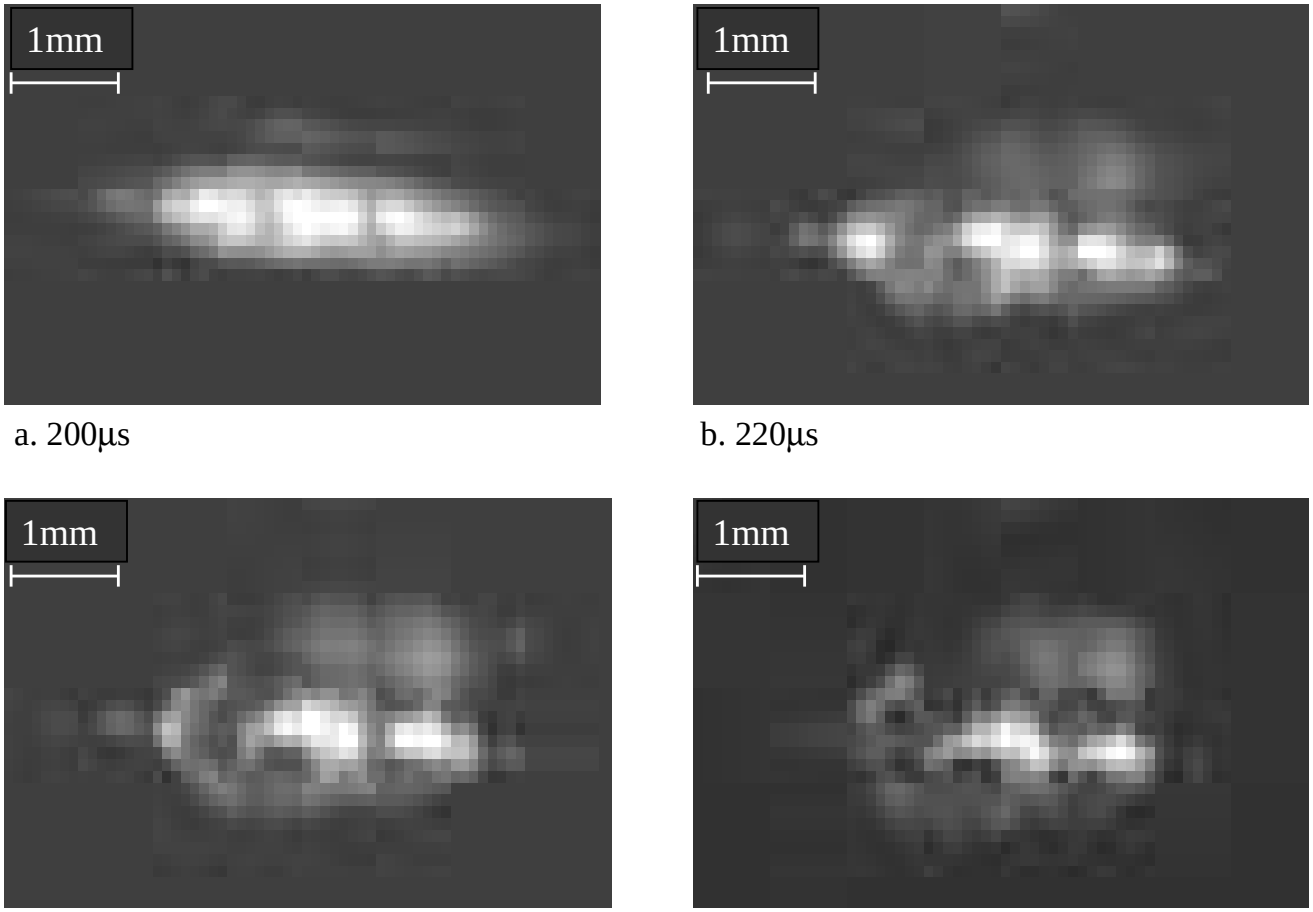

a. 200µs b. 220µs

c. 240µs d. 260µs

Figure 1: Contrast Enhanced Images of Primary Cavitation Bubble – 200µs to 260µs after Plasma Formation

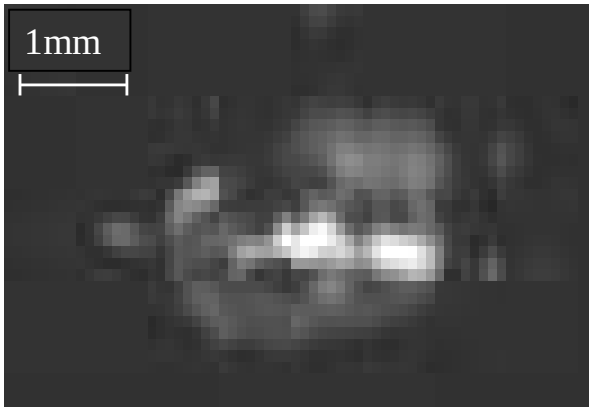

e. 280µs

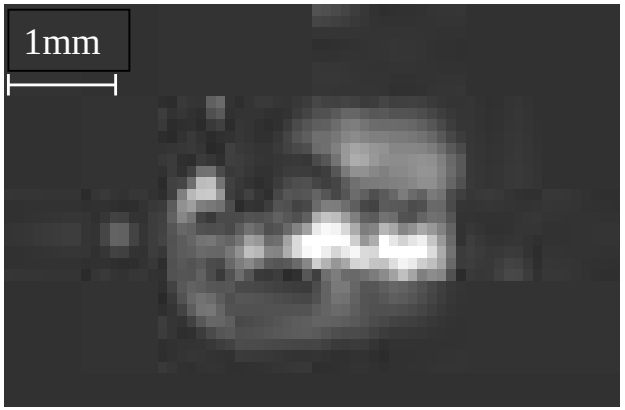

f. 300µs

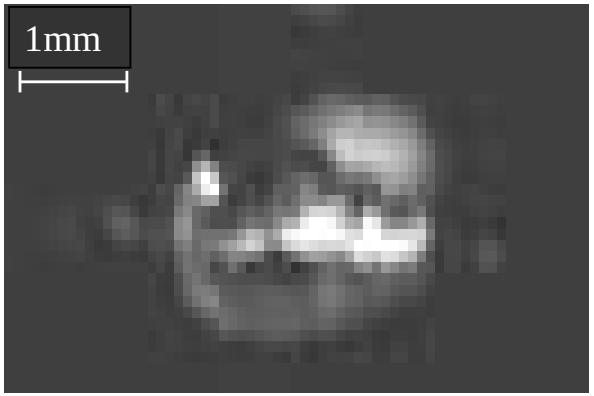

g. 320µs

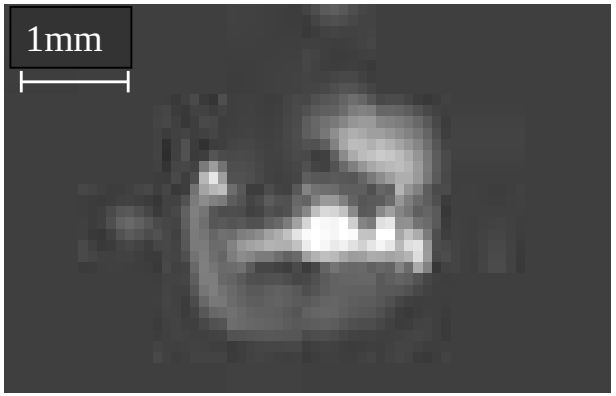

h. 340µs

Figure 2: Contrast Enhanced Images of Primary Cavitation Bubble – 280µs to 340µs after Plasma Formation

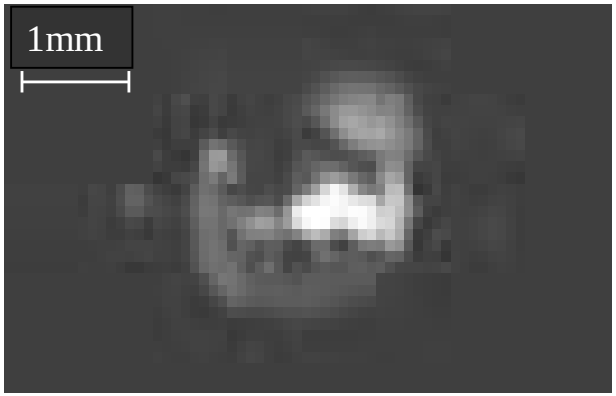

i. 360µs

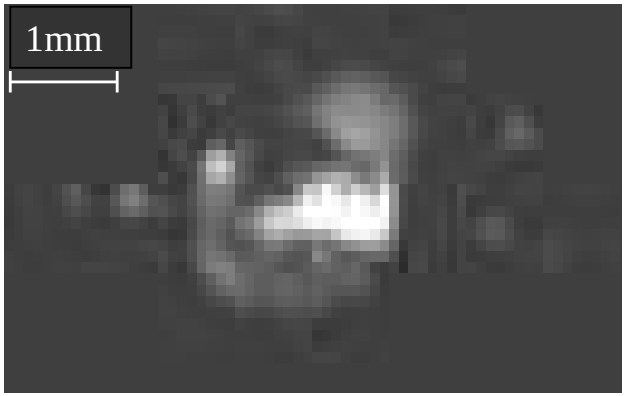

j. 380µs

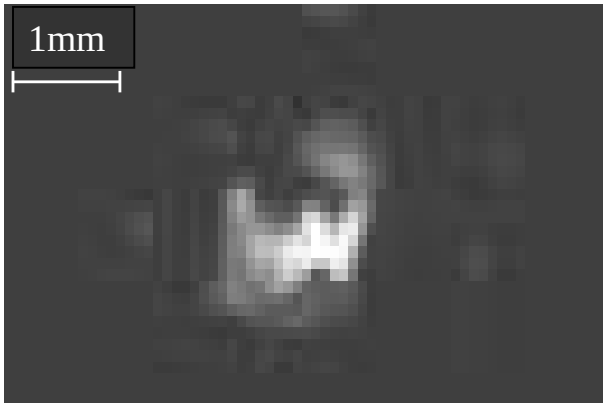

k. 400µs

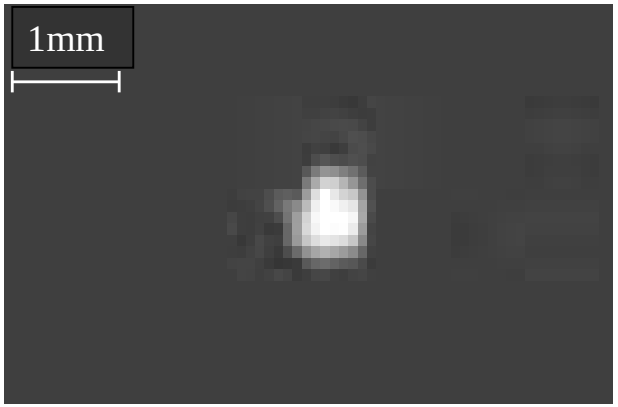

l. 420µs

Figure 3: Contrast Enhanced Images of Primary Cavitation Bubble – 360µs to 420µs after Plasma Formation

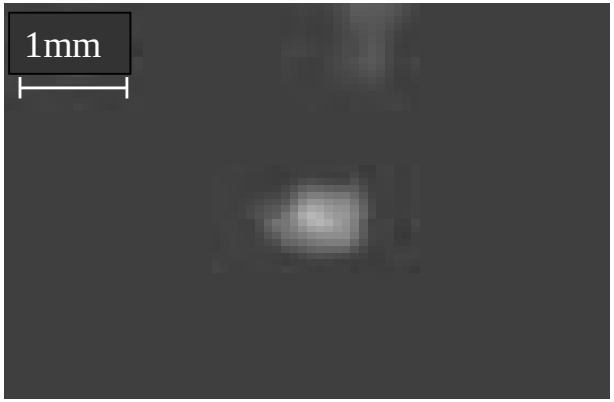

m. 440µs

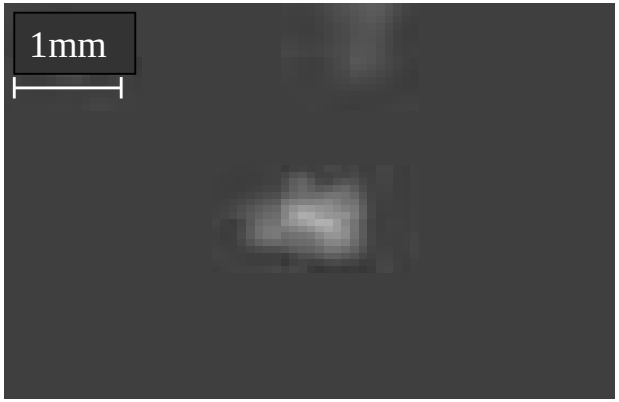

n. 460µs

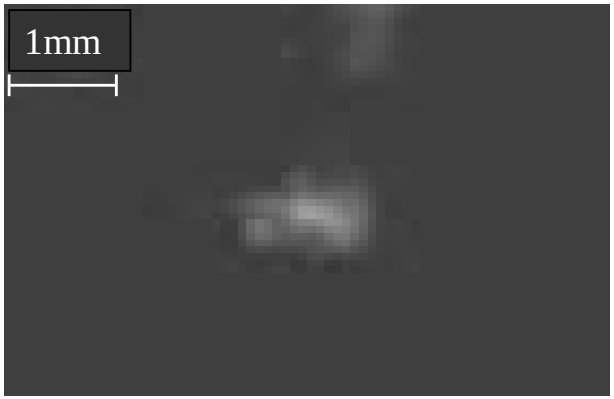

o. 480µs

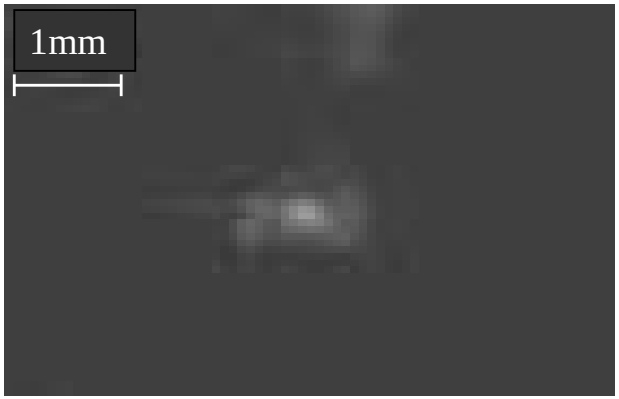

p. 500µs

Figure 4: Contrast Enhanced Images of Primary Cavitation Bubble – 440µs to 500µs after Plasma Formation

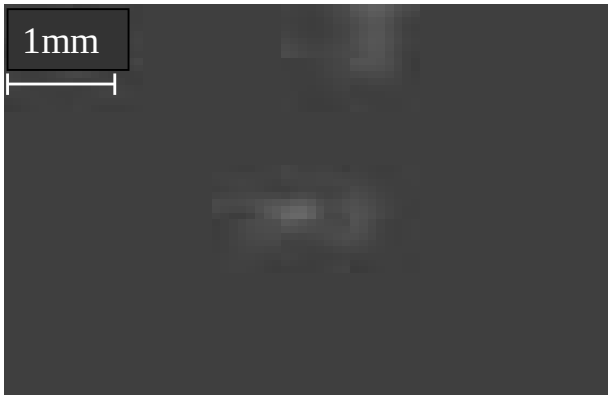

q. 520µs

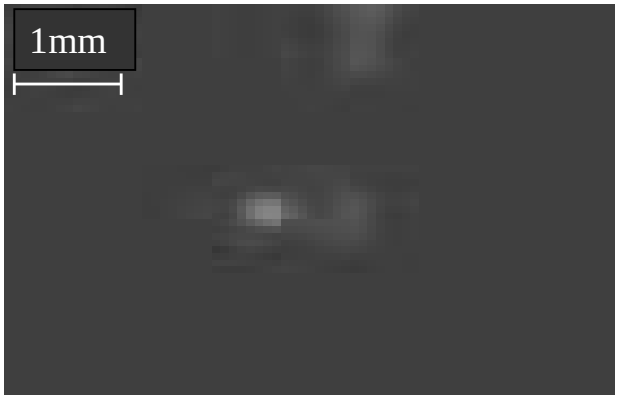

r. 540µs

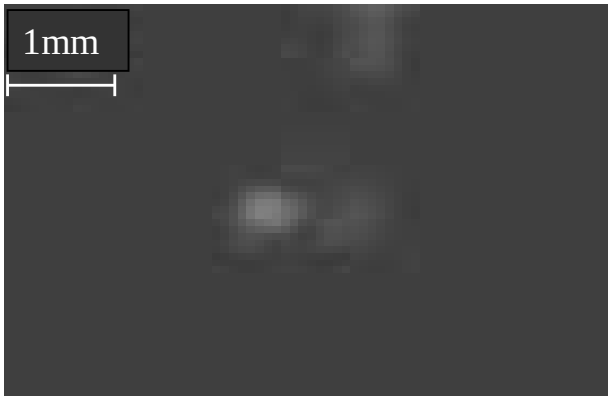

s. 560µs

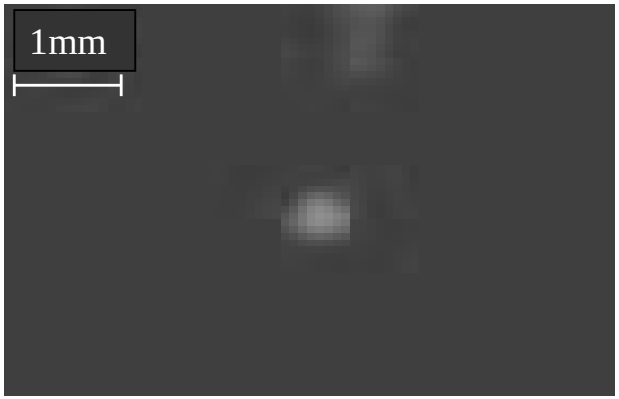

t. 580µs

Figure 5: Contrast Enhanced Images of Primary Cavitation Bubble – 520µs to 580µs after Plasma Formation

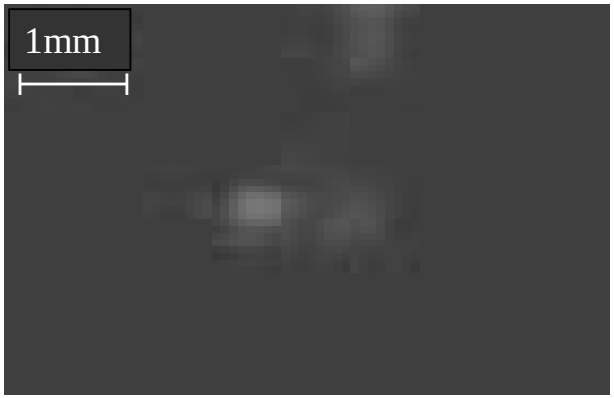

u. 600µs

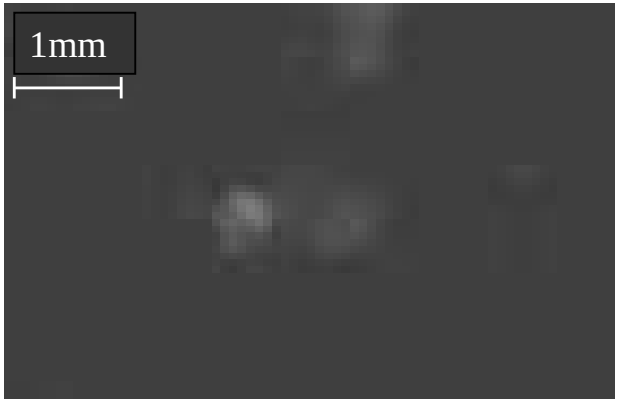

v. 620µs

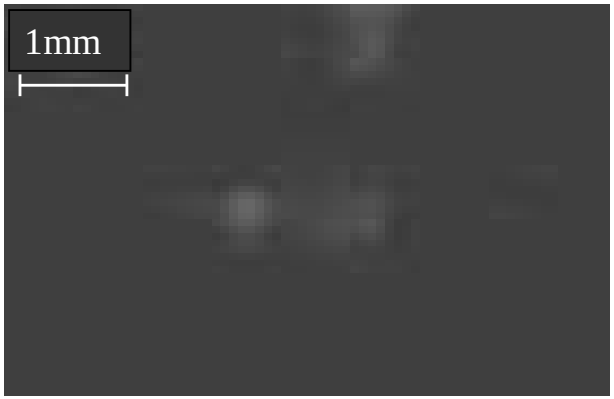

w. 640µs

x. 660µs

Figure 6: Contrast Enhanced Images of Primary Cavitation Bubble – 600µs to 660µs after Plasma Formation

Appendix IX Bubble Volume Estimates Based on Measurements from Still Images

Image H1a – 200μs

cavitation region major axis ~2.75mm
cavitation region minor axis ~0.68mm
eccentricity ~0.25
no. of distinct bubbles = 5
bubble diameters: 0.32, 0.68, 0.82, 0.64, 0.29mm
bubble volumes: 0.02, 0.16, 0.29, 0.14, 0.01mm^3

Image H1b – 220μs

cavitation region major axis ~3.17mm
cavitation region minor axis ~1.21mm
eccentricity ~0.38
no. of distinct bubbles = 4
bubble diameters: 1.00, 1.21, 0.57, 0.39mm
bubble volumes: 0.52, 0.93, 0.10, 0.03mm^3

Image H1c – 240μs

cavitation region major axis ~2.71mm
cavitation region minor axis ~1.71mm
eccentricity ~0.63
no. of distinct bubbles = 2
bubble diameters: 1.71, 1.00mm
bubble volumes: 2.64, 0.52mm^3

Image H1d – 260μs

cavitation region major axis ~3.00mm
cavitation region minor axis ~1.86mm
eccentricity ~0.62
no. of distinct bubbles = 2
bubble diameters: 1.86, 1.14mm
bubble volumes: 3.37, 0.76mm^3

Image H2a – 280μs
cavitation region major axis ~2.86mm
cavitation region minor axis ~2.00mm
eccentricity ~0.70
no. of distinct bubbles = 2
bubble diameters: 2.00, 1.50mm
bubble volumes: 4.19, 1.77mm^3
~40% overlap of minor bubble

Image H2b – 300μs
cavitation region major axis ~2.75mm
cavitation region minor axis ~1.93mm
eccentricity ~0.70
no. of distinct bubbles = 2
bubble diameters: 2.00, 1.64mm
bubble volumes: 4.19, 2.32mm^3
~35% overlap of minor bubble

Image H2c – 320μs
cavitation region major axis ~2.43mm
cavitation region minor axis ~1.79mm
eccentricity ~0.73
no. of distinct bubbles = 2
bubble diameters: 2.07, 0.86mm
bubble volumes: 4.65, 0.33mm^3
~35% overlap of minor bubble

Image H2d – 340μs
cavitation region major axis ~2.36mm
cavitation region minor axis ~2.00mm
eccentricity ~0.85
no. of distinct bubbles = 2
bubble diameters: 2.11, 0.50mm
bubble volumes: 4.90, 0.07mm^3
~75% overlap of minor bubble

Image H3a – 360μs
cavitation region major axis ~2.07mm
cavitation region minor axis ~1.99mm
eccentricity ~0.96
no. of distinct bubbles = 1
bubble diameter: 2.04mm
bubble volume: 4.42mm^3

Image H3b – 380μs
cavitation region major axis ~1.86mm
cavitation region minor axis ~1.79mm
eccentricity ~0.96
no. of distinct bubbles = 1
bubble diameter: 1.86mm
bubble volume: 3.35mm^3

Image H3c – 400μs
cavitation region major axis ~1.36mm
cavitation region minor axis ~1.36mm
eccentricity ~1.00
no. of distinct bubbles = 1
bubble diameter: 1.42mm
bubble volume: 1.53mm^3

Image H3d – 420μs
cavitation region major axis ~0.71mm
cavitation region minor axis ~0.71mm
eccentricity ~1.00
no. of distinct bubbles = 1
bubble diameter: 0.74mm
bubble volume: 0.22mm^3

Appendix X Smoothing of *Bremsstrahlung* via Data Averaging

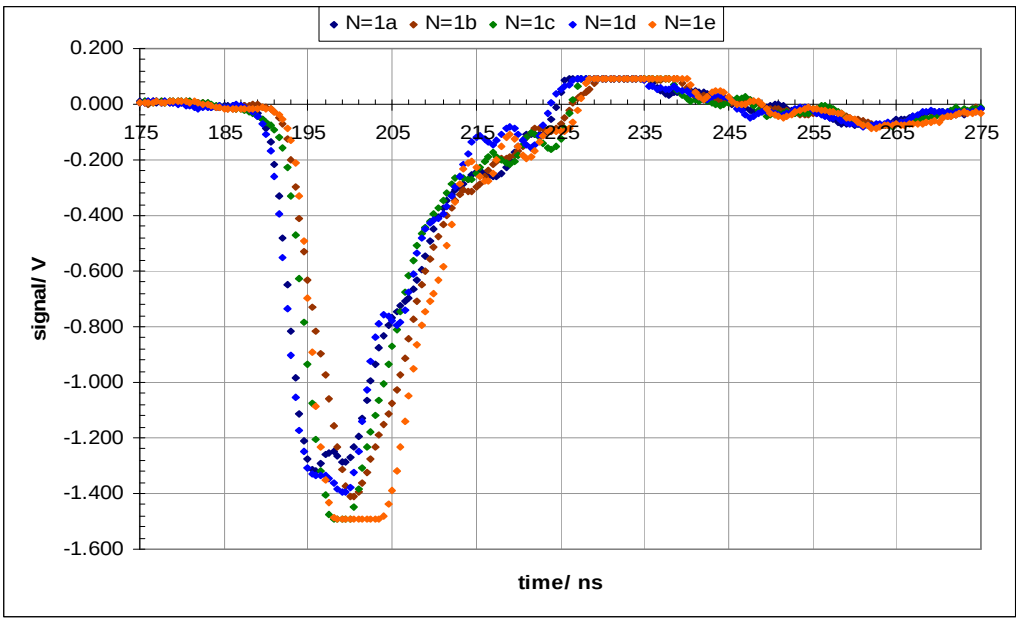

Figure 1: BL Profiles: N = 1

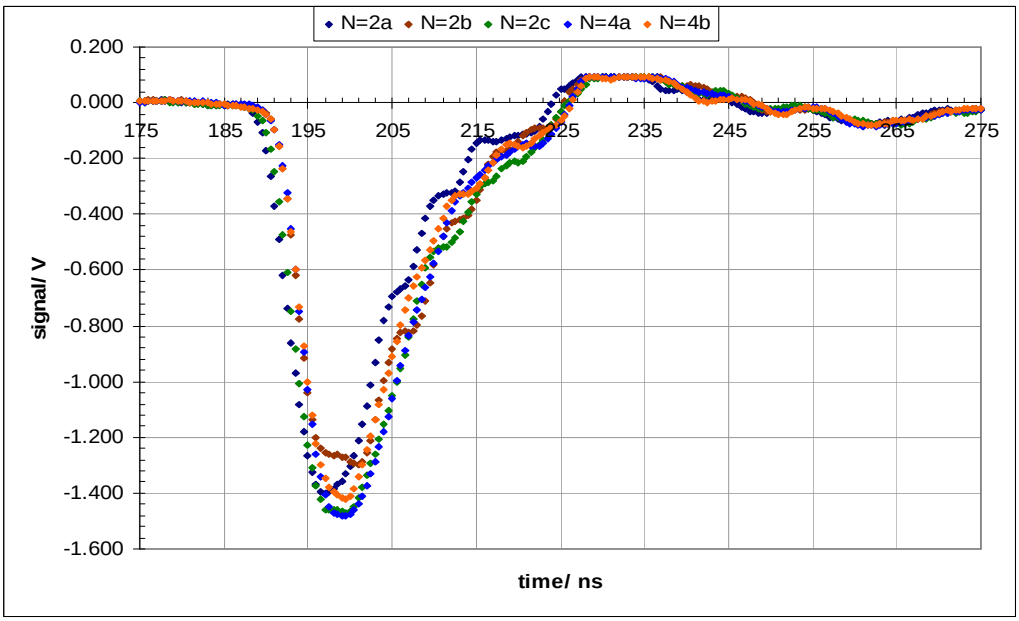

Figure 2: BL Profiles: N = 2 & 4

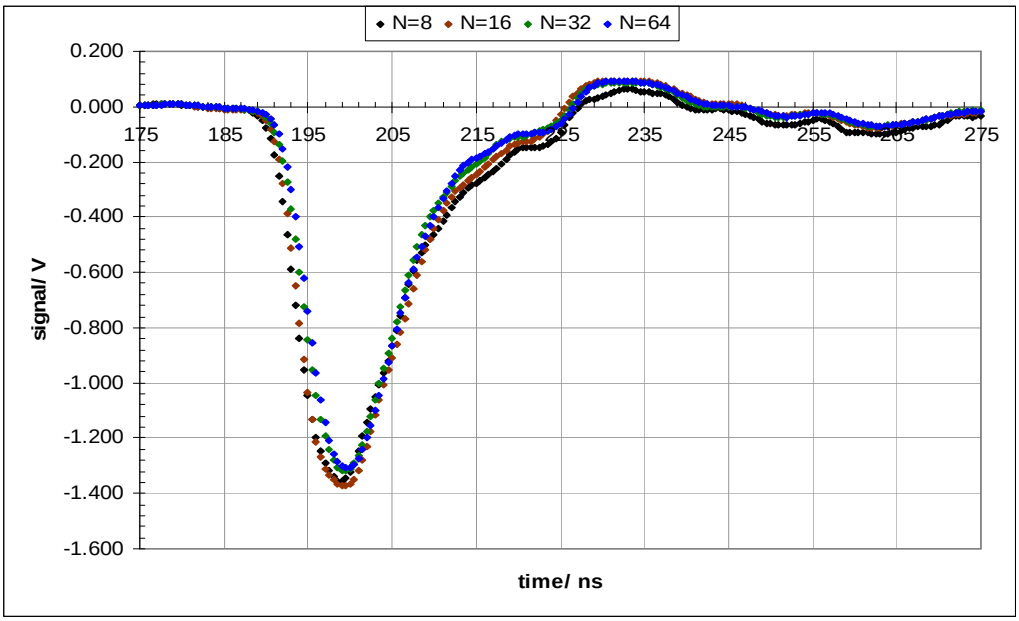

Figure 3: BL Profiles: 8 < N < 64

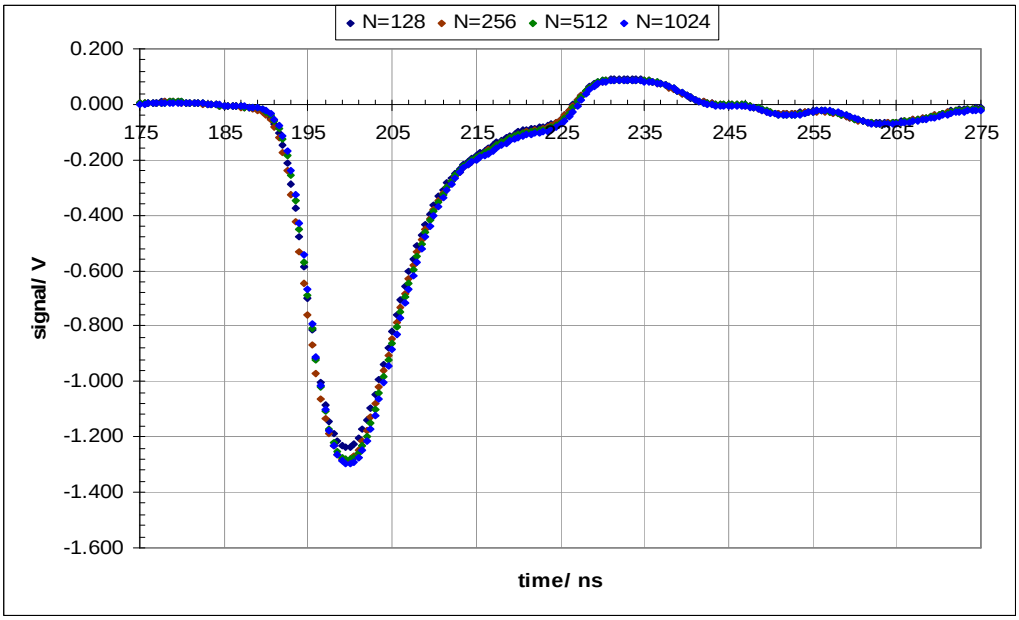

Figure 4: BL Profiles: 128 < N < 1024

Appendix XI Influence of Scattering Centre Concentration on *Bremsstrahlung*

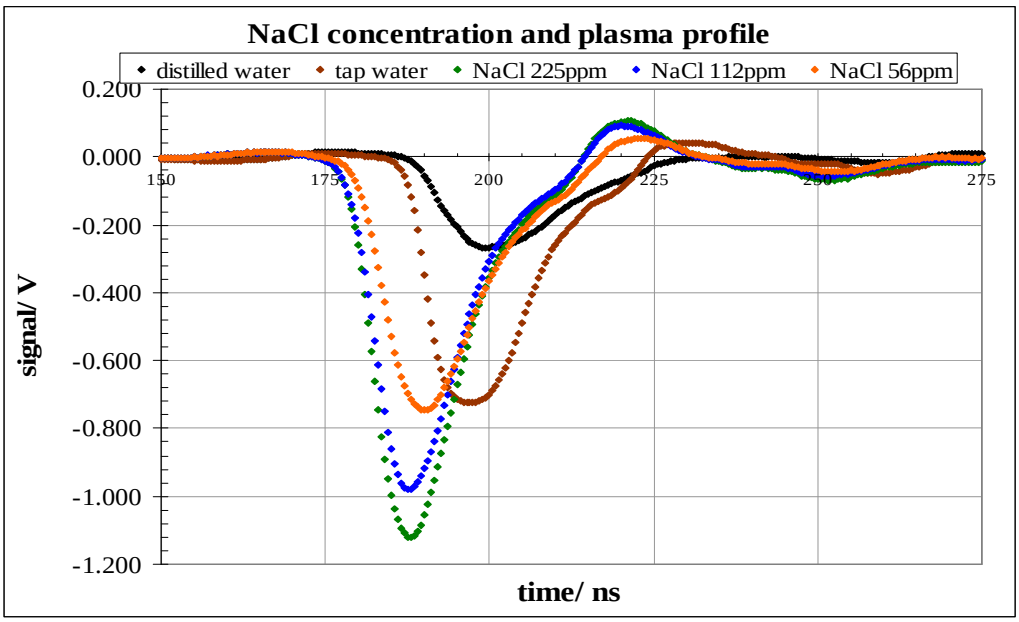

Figure 1: BL Profiles: c_L = 56ppm, 112ppm & 225ppm

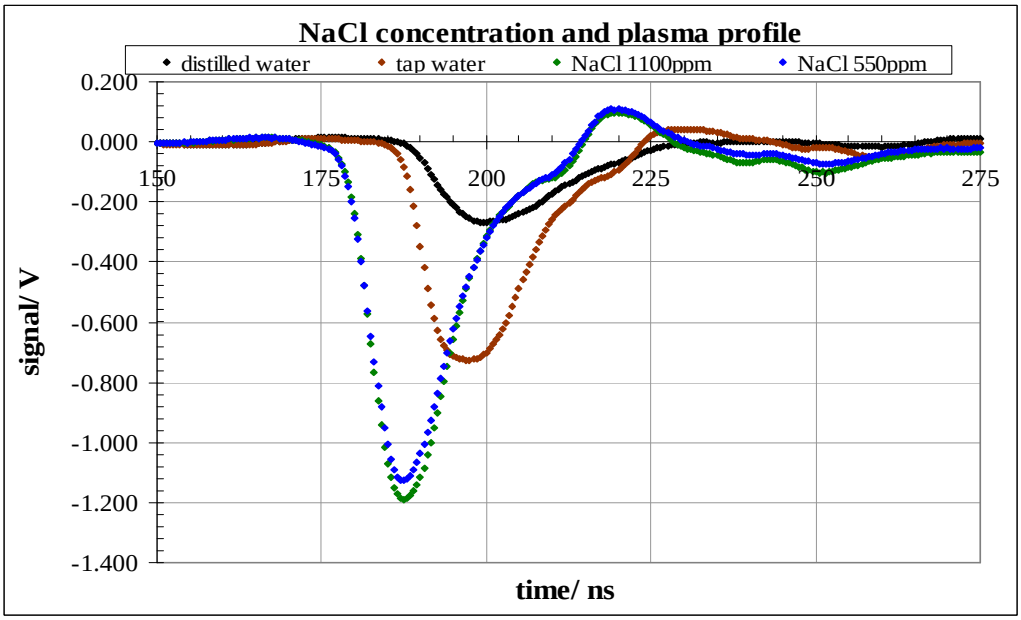

Figure 2: BL Profiles: c_L = 550ppm & 1100ppm

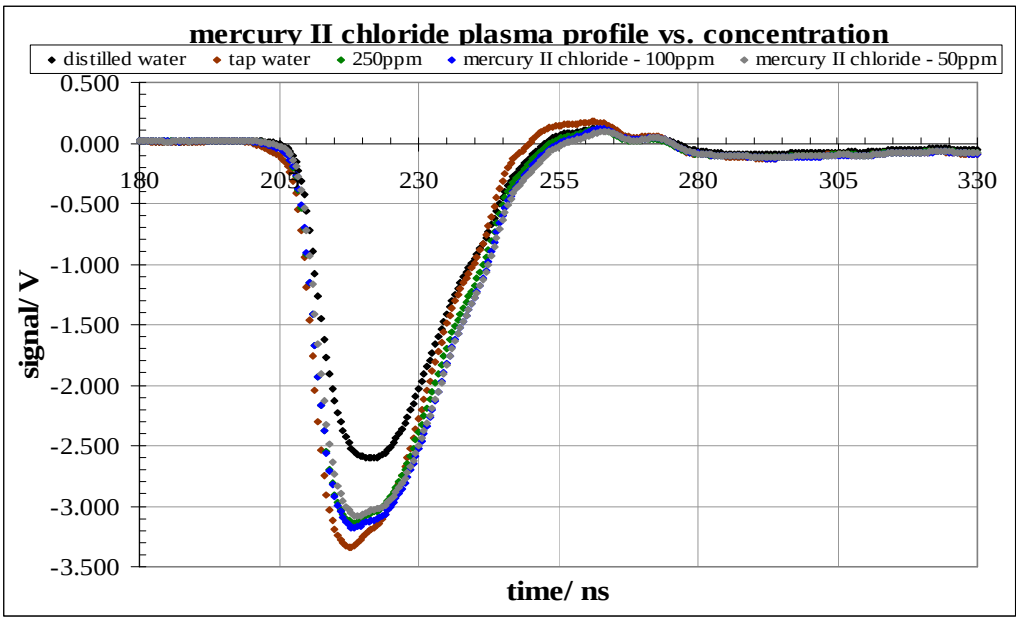

Figure 3: BL Profiles: c_L = 50ppm, 250ppm & 100ppm

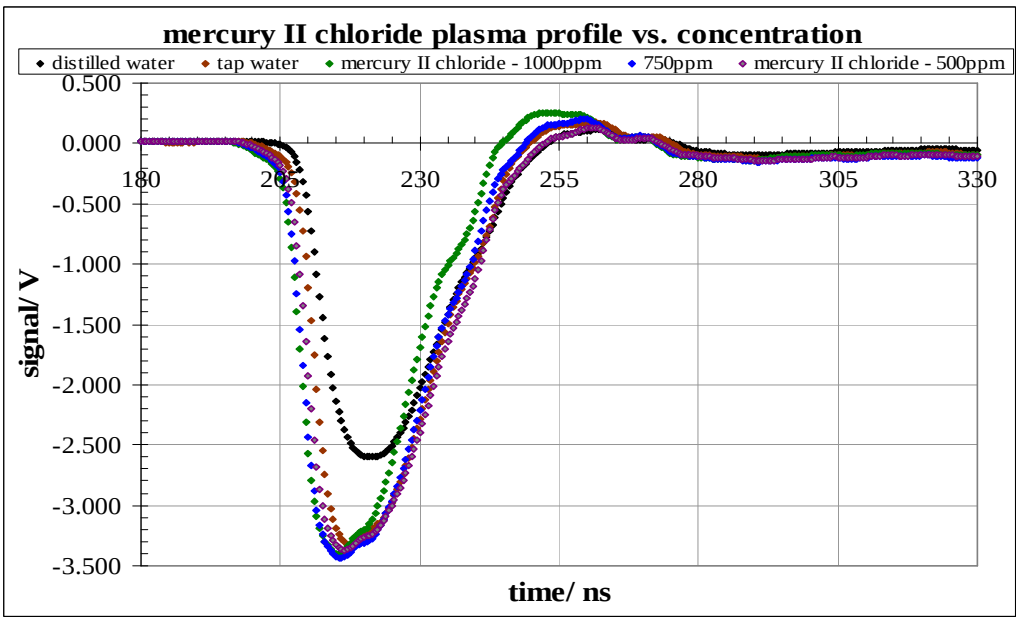

Figure 4: BL Profiles: c_L = 500ppm, 750ppm & 1000ppm

Appendix XII Influence of Pulse Energy on *Bremsstrahlung*

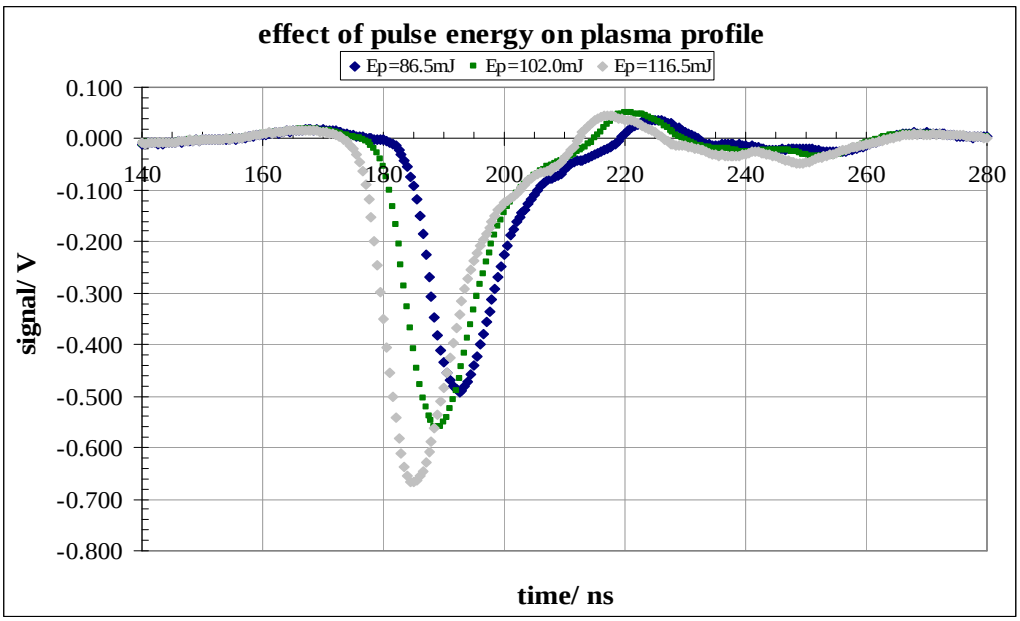

Figure 1: BL Envelopes: E_p = 86.5mJ, 102.0mJ & 116.5mJ

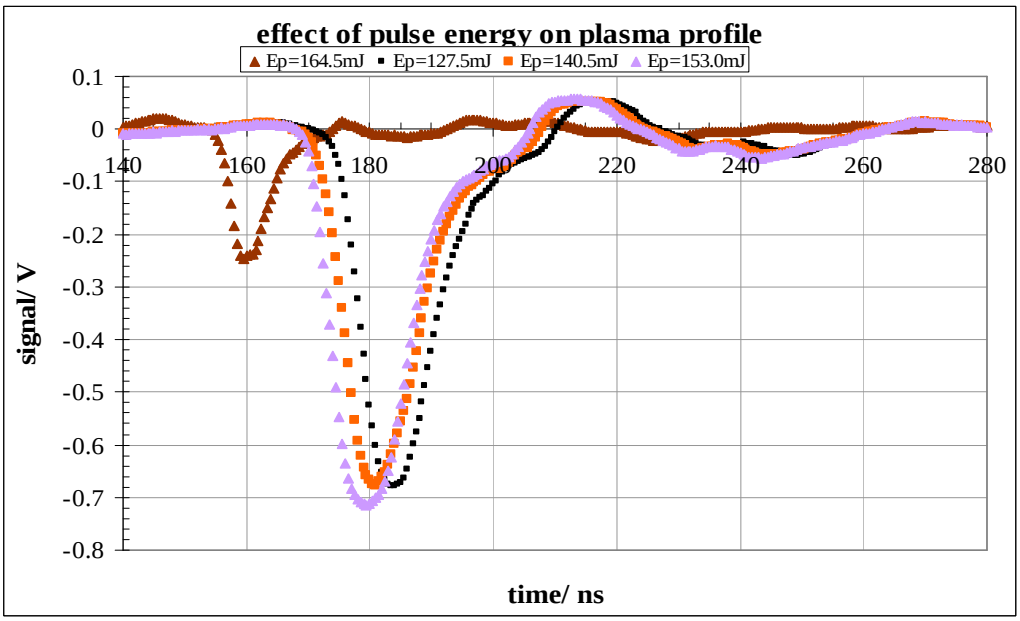

Figure 2: BL Envelopes: E_p = 127.5mJ, 140.5mJ, 153.0mJ & 164.5mJ

Appendix XIII Effect of Delay Time on LIBS Emission Spectrum

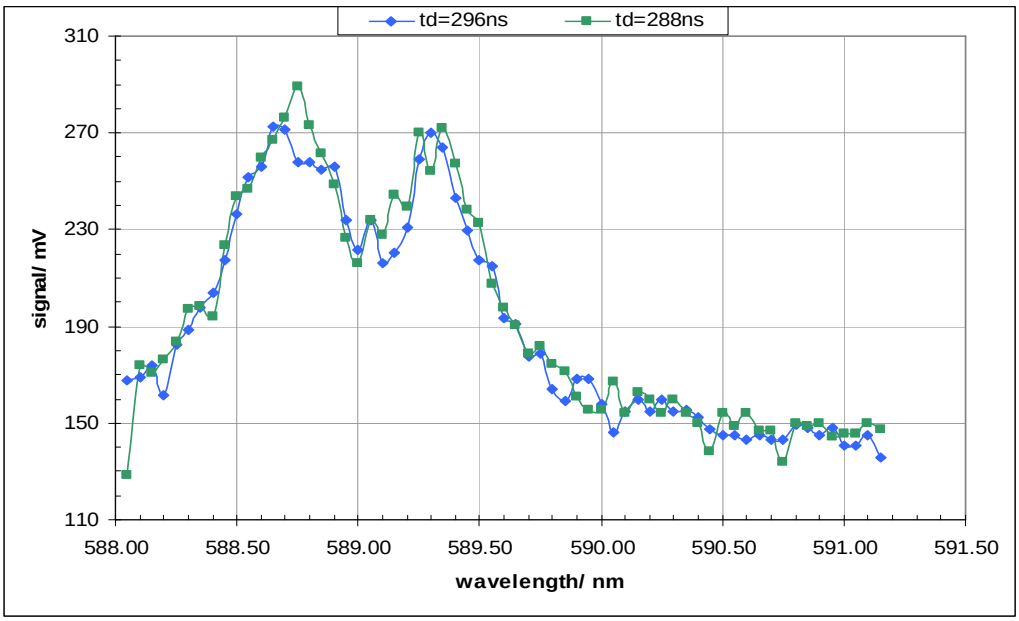

Figure 1: LIBS Spectra: t_d = 288ns & 296ns

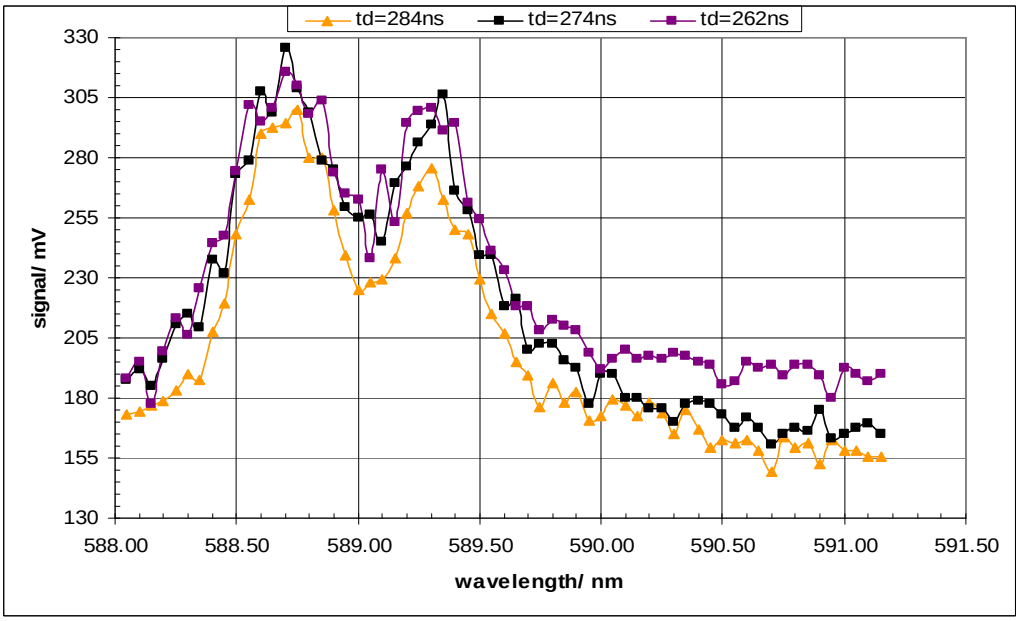

Figure 2: LIBS Spectra: t_d = 262ns, 274ns & 284ns

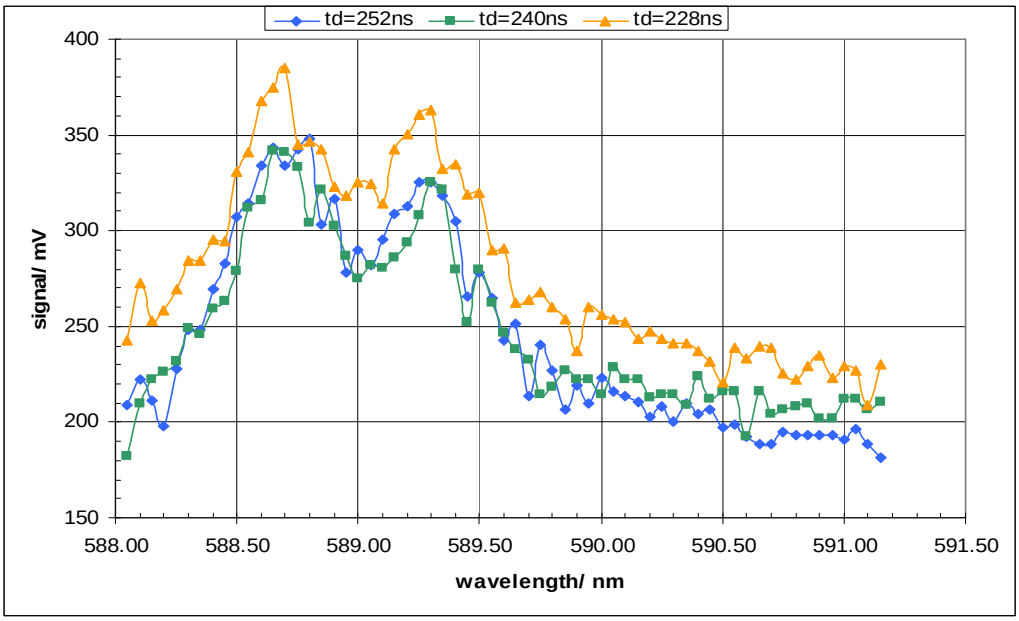

Figure 3: LIBS Spectra: t_d = 228ns, 240ns & 252ns

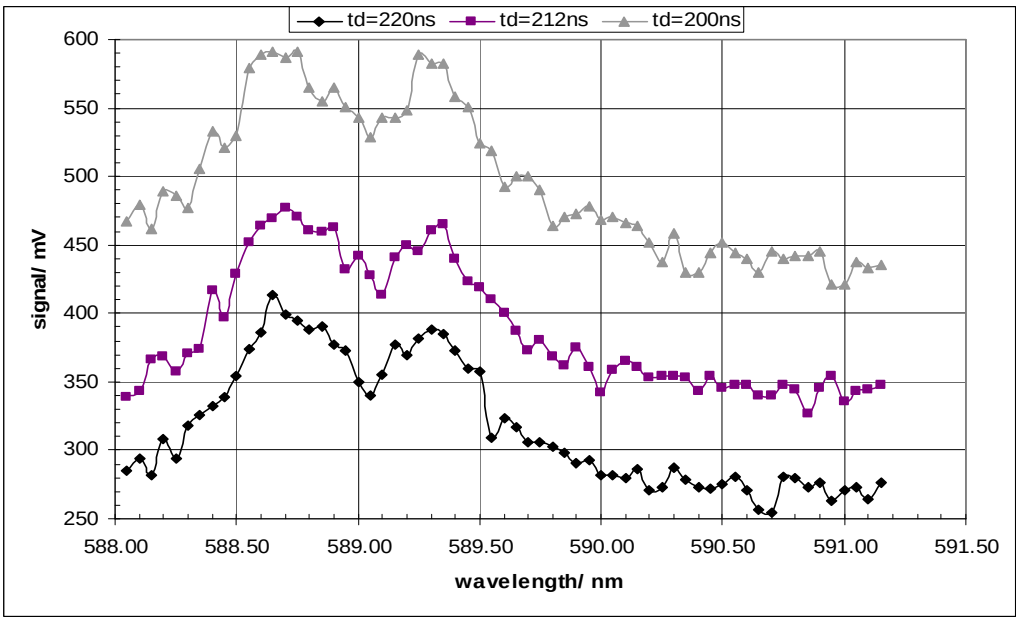

Figure 4: LIBS Spectra: t_d = 200ns, 212ns & 220ns

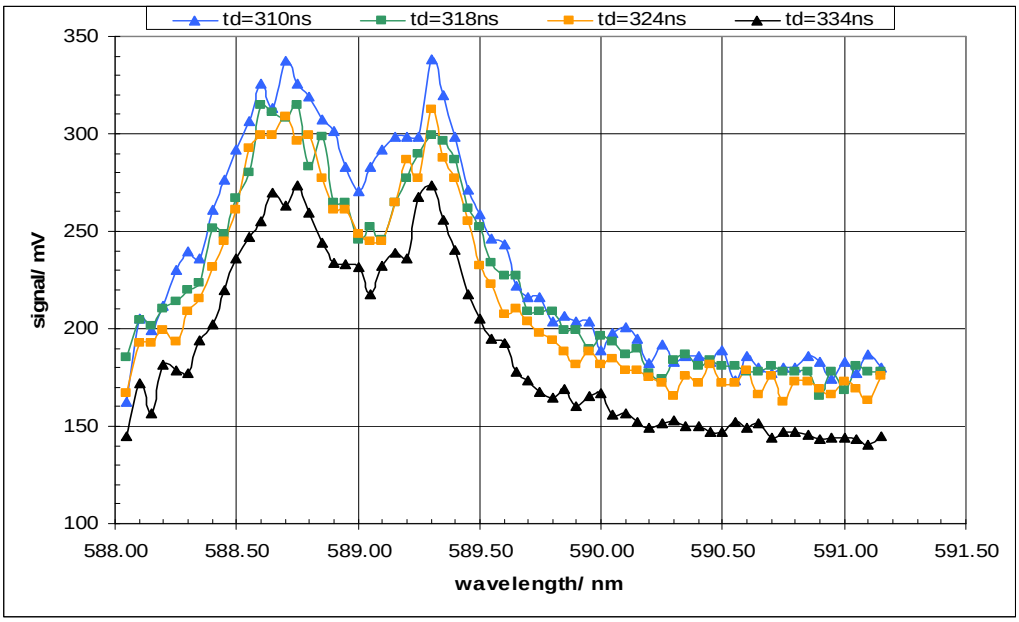

Figure 5: LIBS Spectra: t_d = 310ns, 318ns, 324ns & 334ns

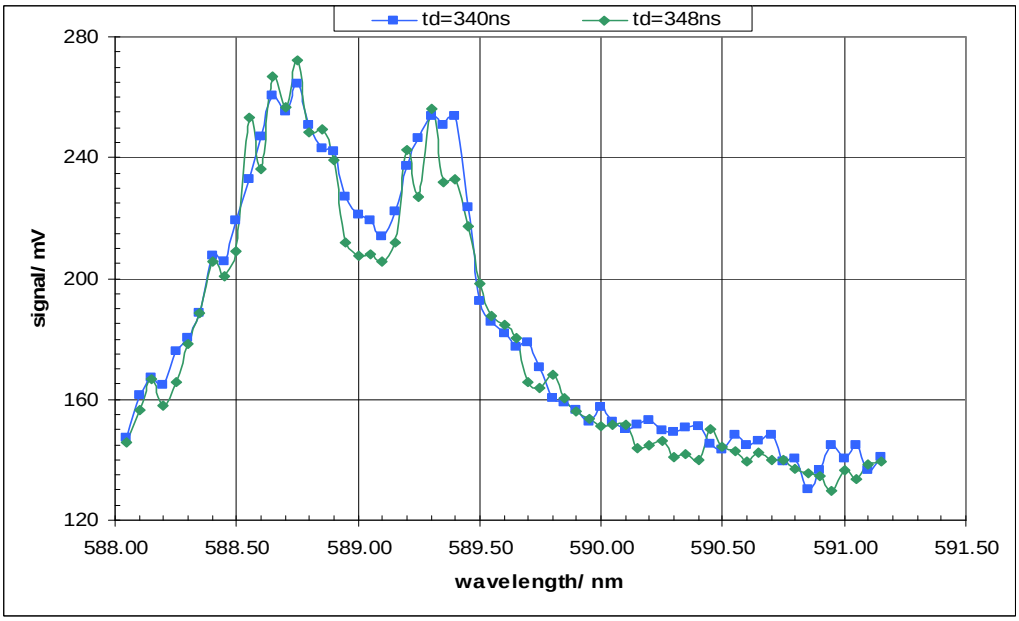

Figure 6: LIBS Spectra: t_d = 340ns & 348ns

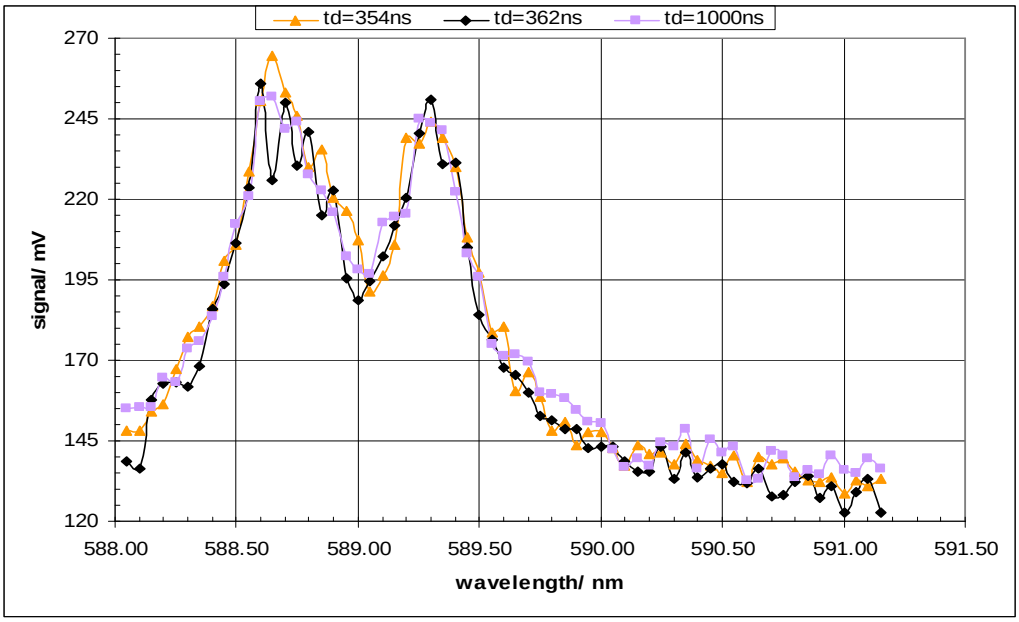

Figure 7: LIBS Spectra: t_d = 354ns, 362ns & 1000ns

Appendix XIV Effect of Gate Width on LIBS Emission Spectrum

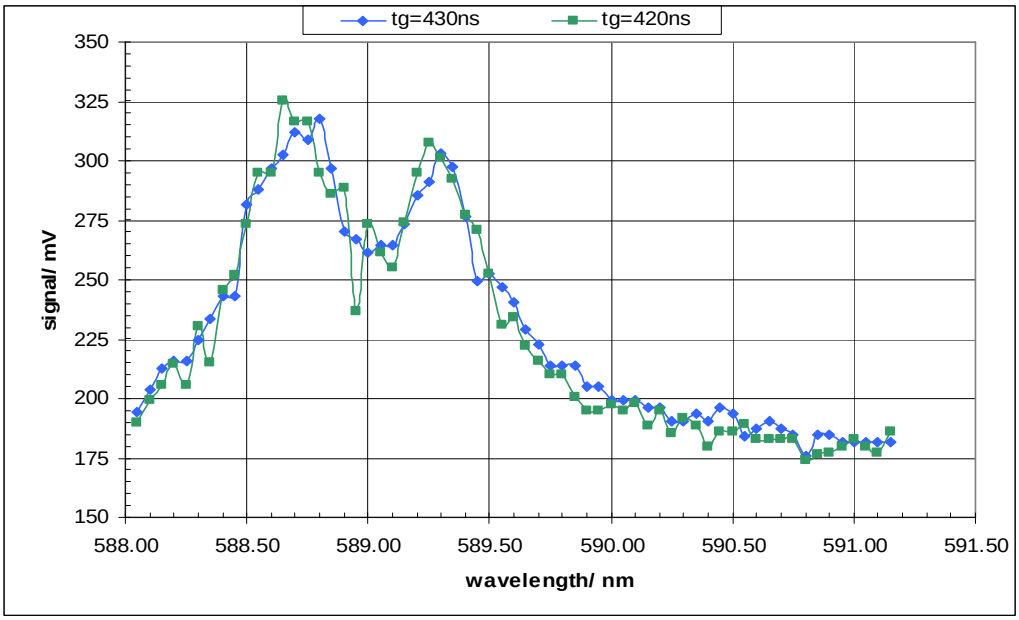

Figure 1: LIBS Spectra: t_g = 430ns & 420ns

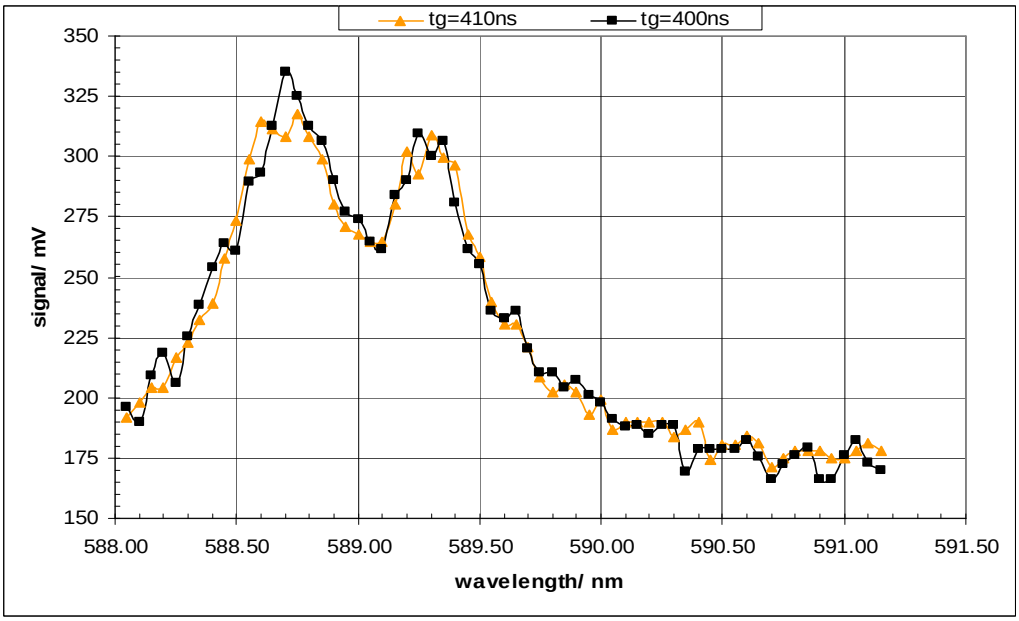

Figure 2: LIBS Spectra: t_g = 410ns & 400ns

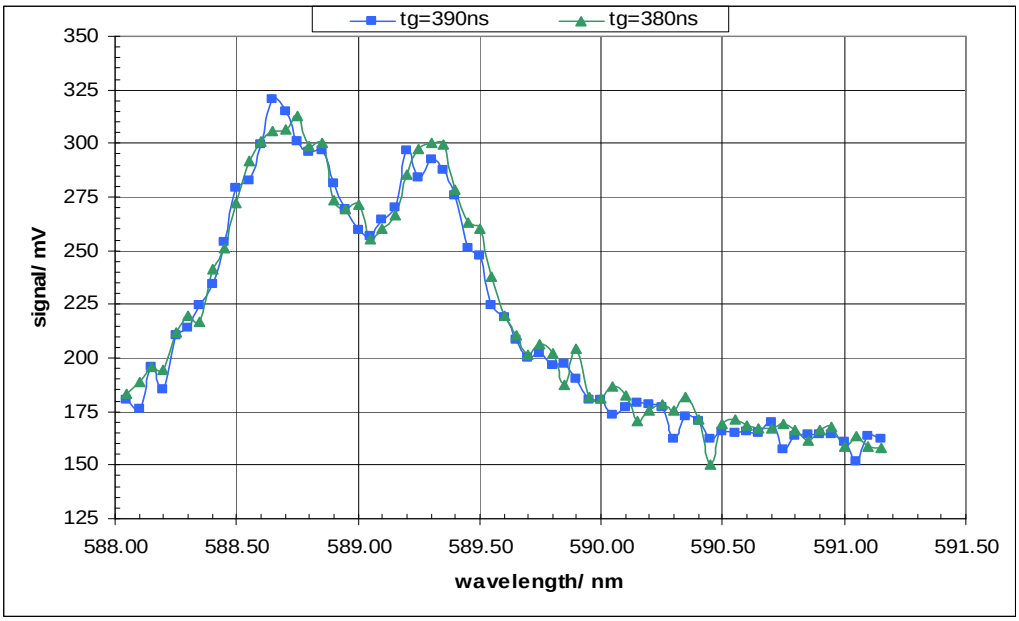

Figure 3: LIBS Spectra: t_g = 390ns & 380ns

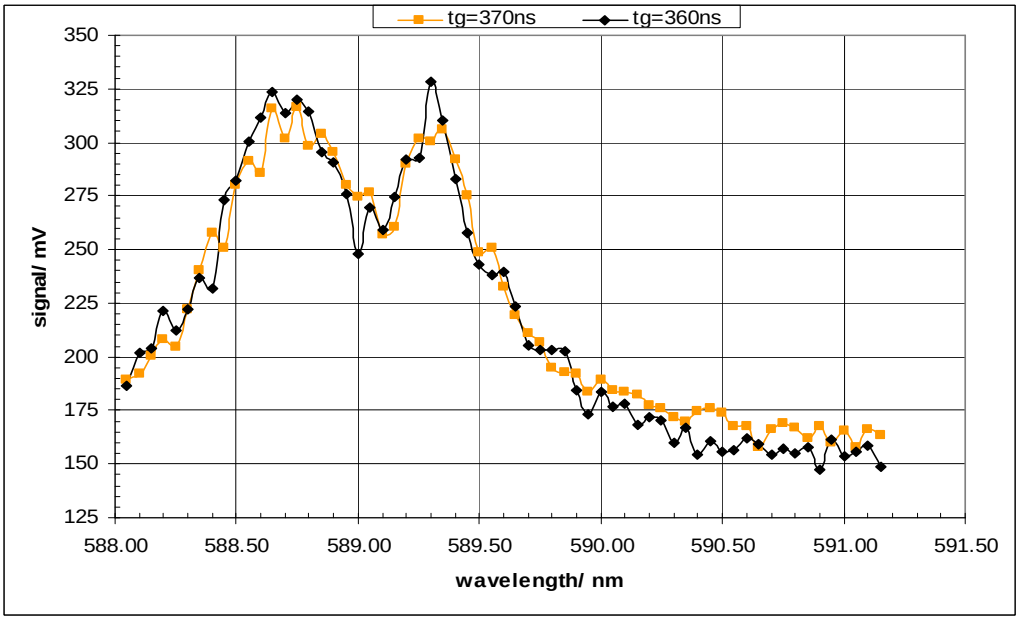

Figure 4: LIBS Spectra: t_g = 370ns & 360ns

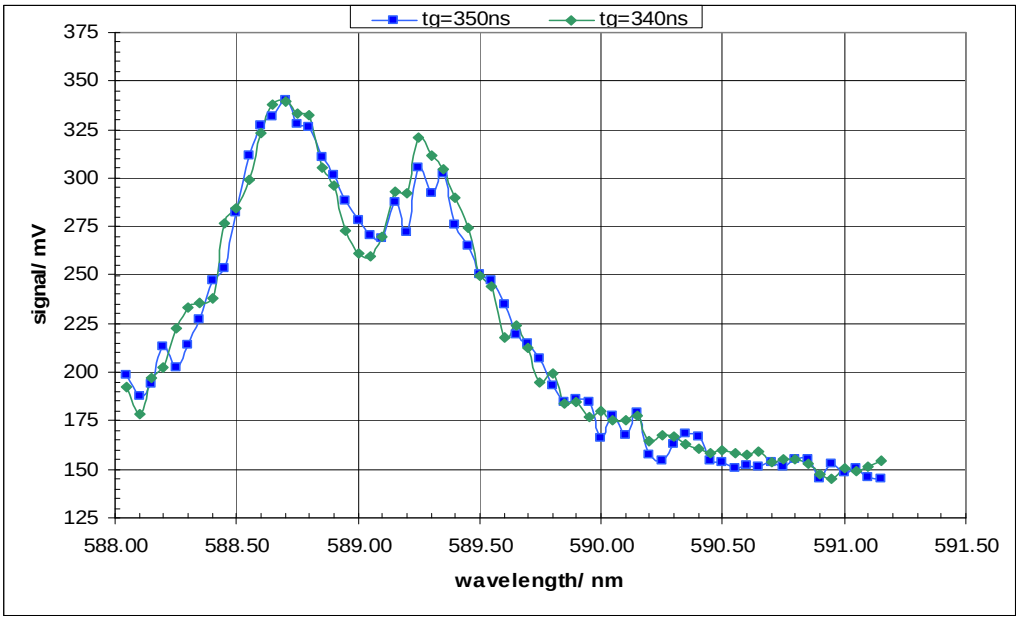

Figure 5: LIBS Spectra: t_g = 350ns & 340ns

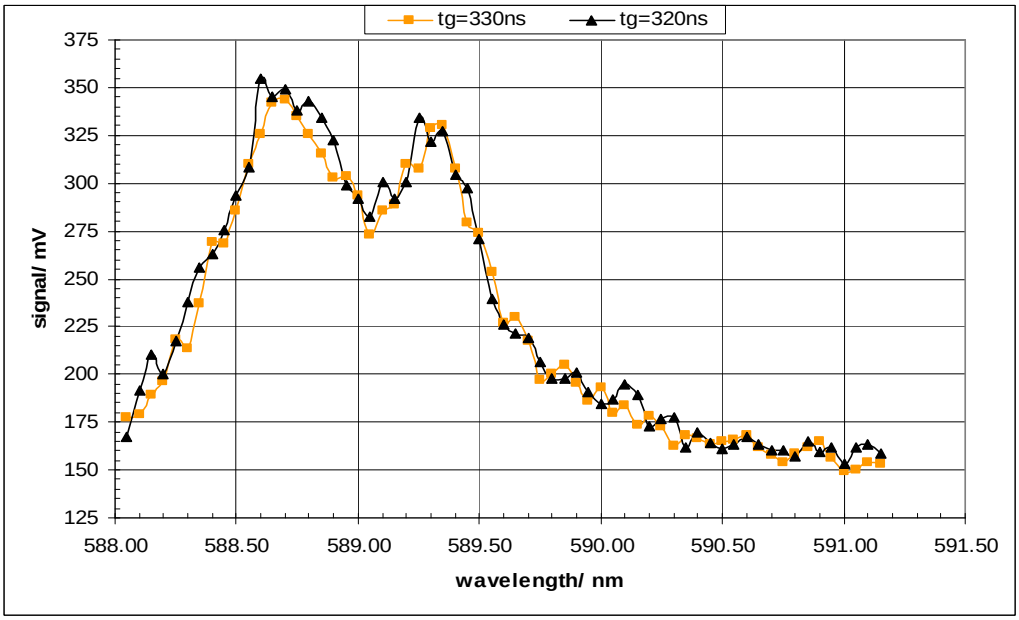

Figure 6: LIBS Spectra: t_g = 330ns & 320ns

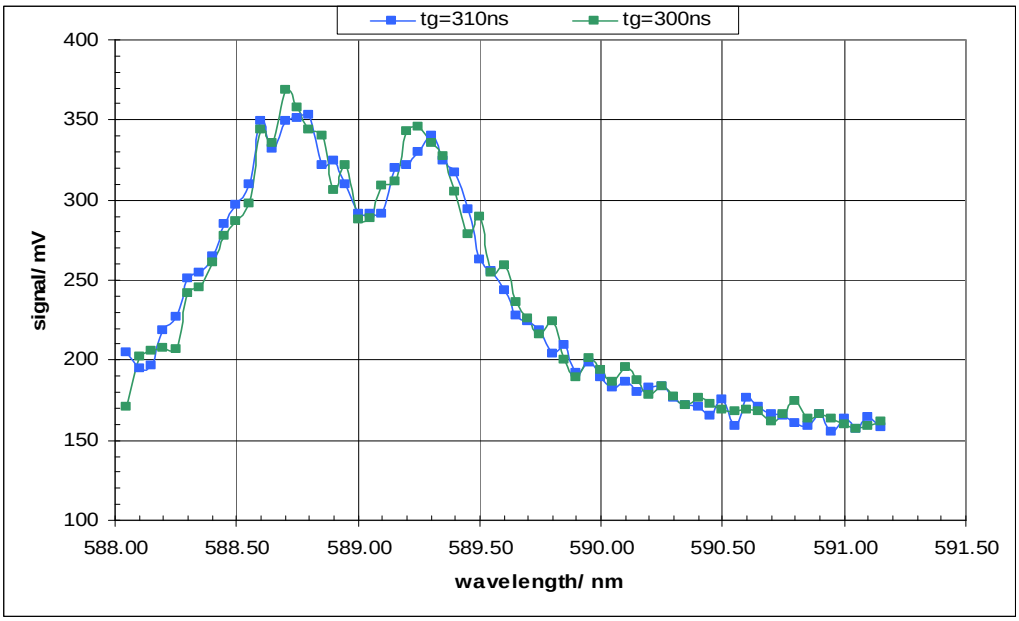

Figure 7: LIBS Spectra: t_g = 310ns & 300ns

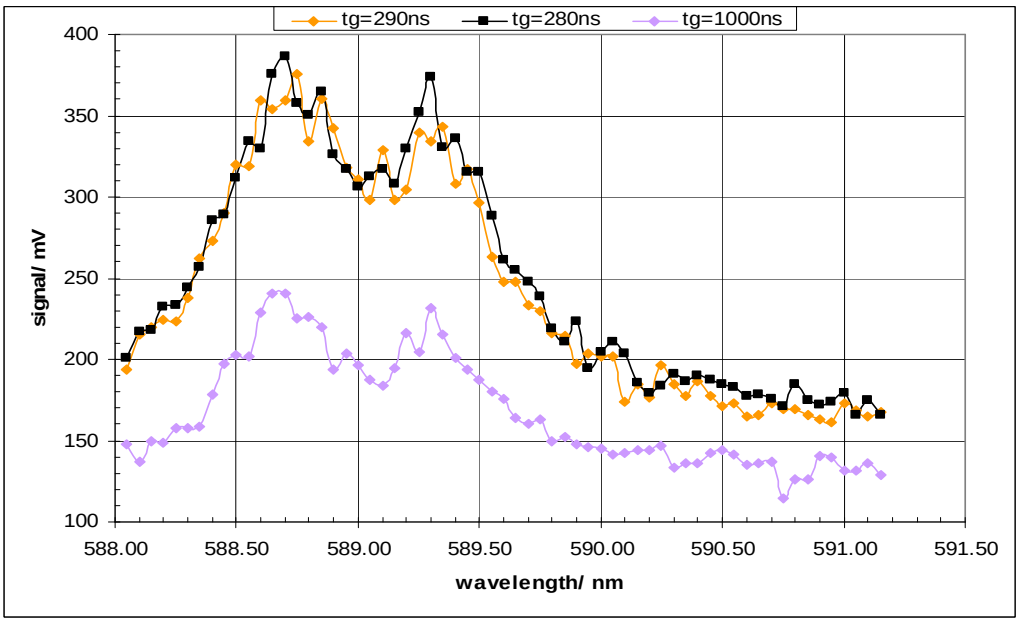

Figure 8: LIBS Spectra: t_g = 290ns, 280ns & 1000ns

Appendix XV Effect of Data Average Number on LIBS Emission Spectrum

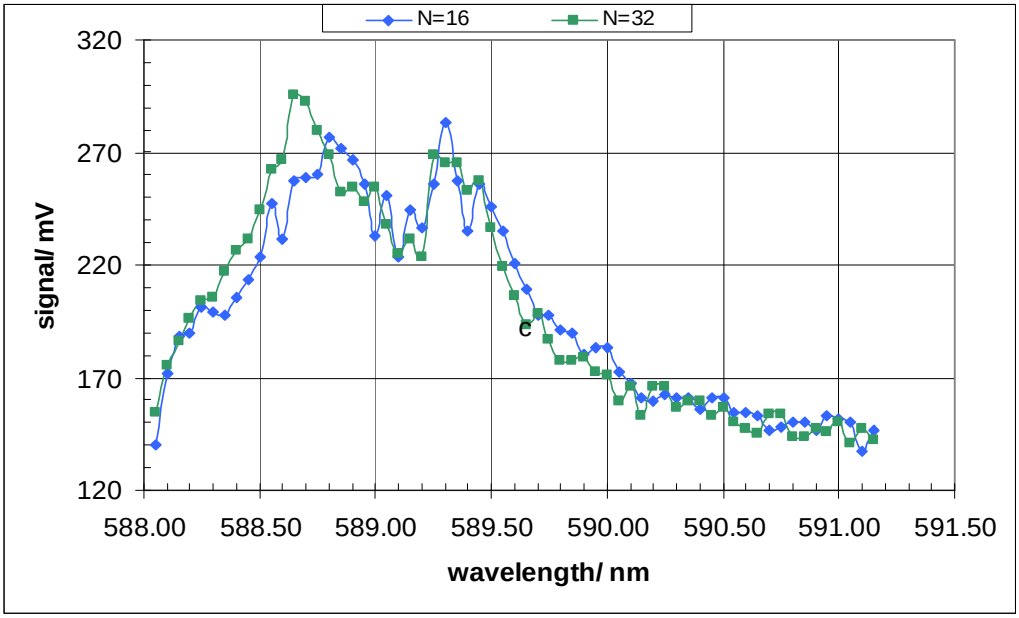

Figure 1: LIBS Spectra: N = 16 & 32

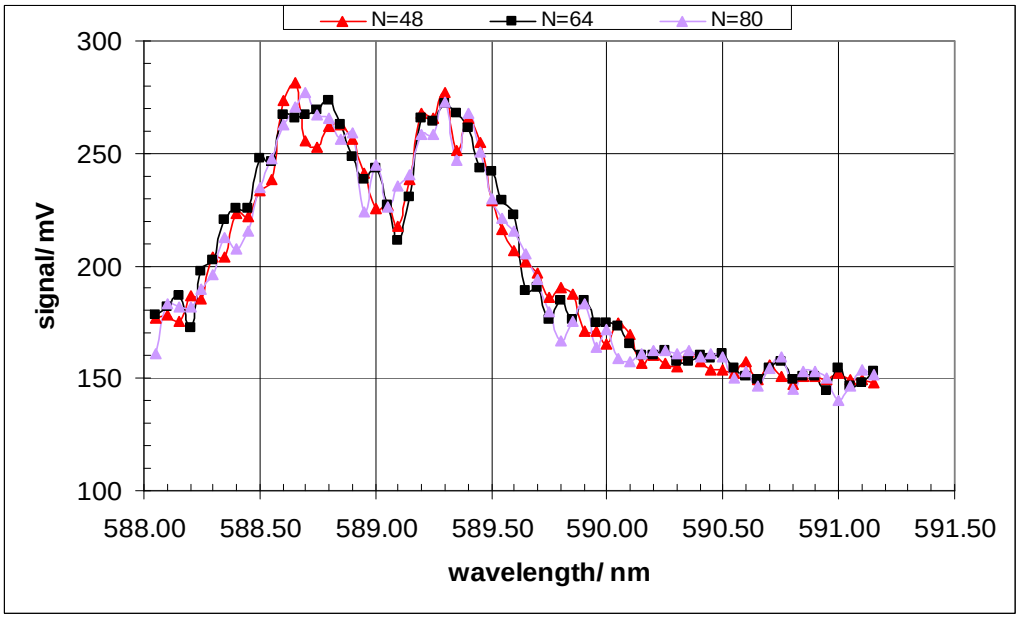

Figure 2: LIBS Spectra: N = 48, 64 & 80

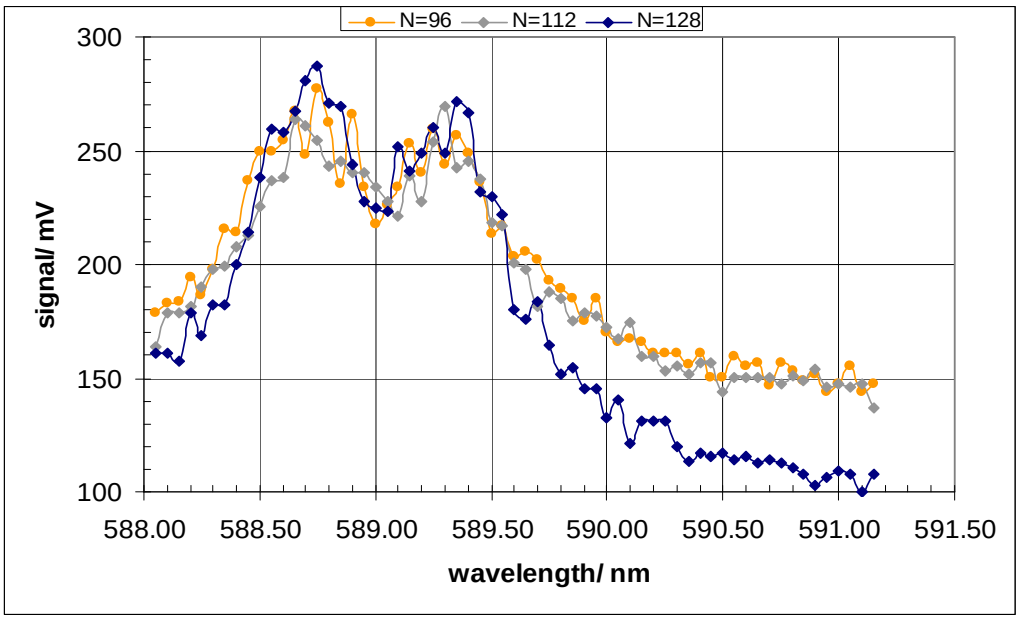

Figure 3: LIBS Spectra: N = 96, 112 & 128

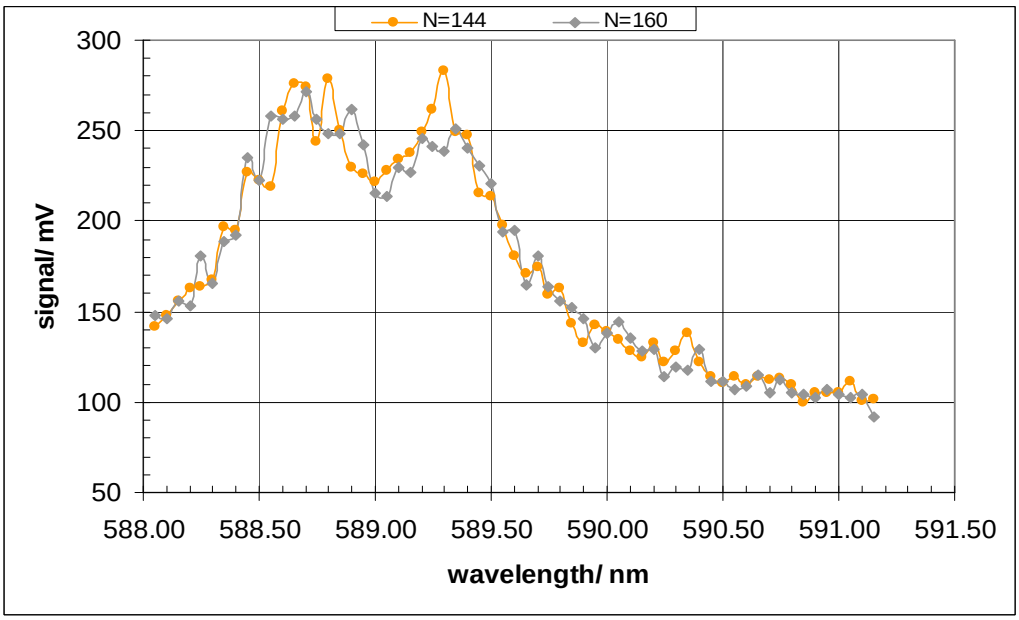

Figure 4: LIBS Spectra: N = 144 & 160

Appendix XVI Effect of Laser Pulse Energy on LIBS Emission Spectrum

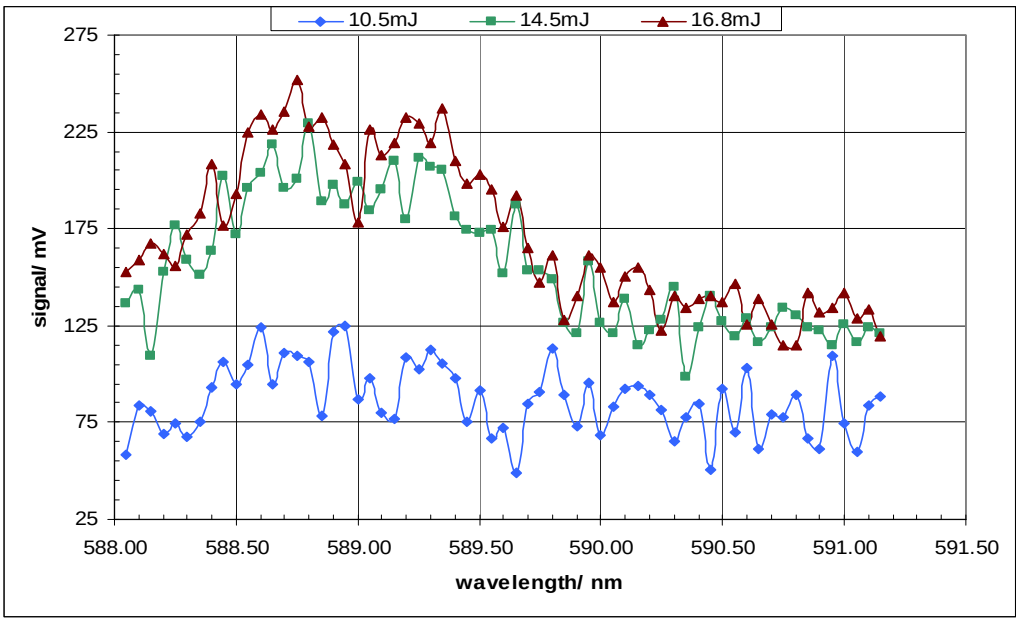

Figure 1: LIBS Spectra: E_p = 10.5mJ, 14.5mJ & 16.8mJ

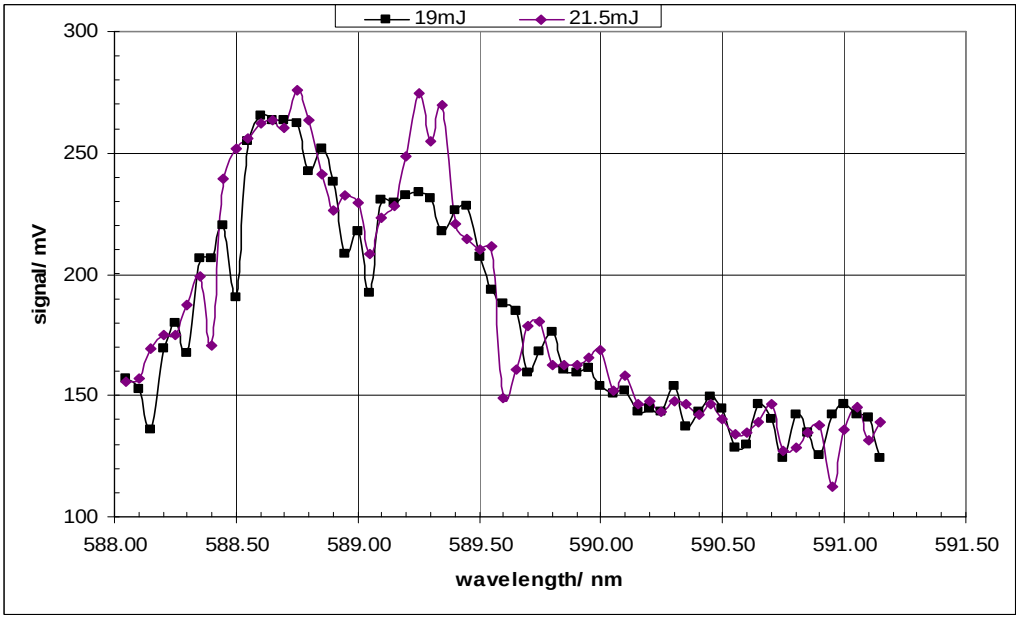

Figure 2: LIBS Spectra: E_p = 19.0mJ & 21.5mJ

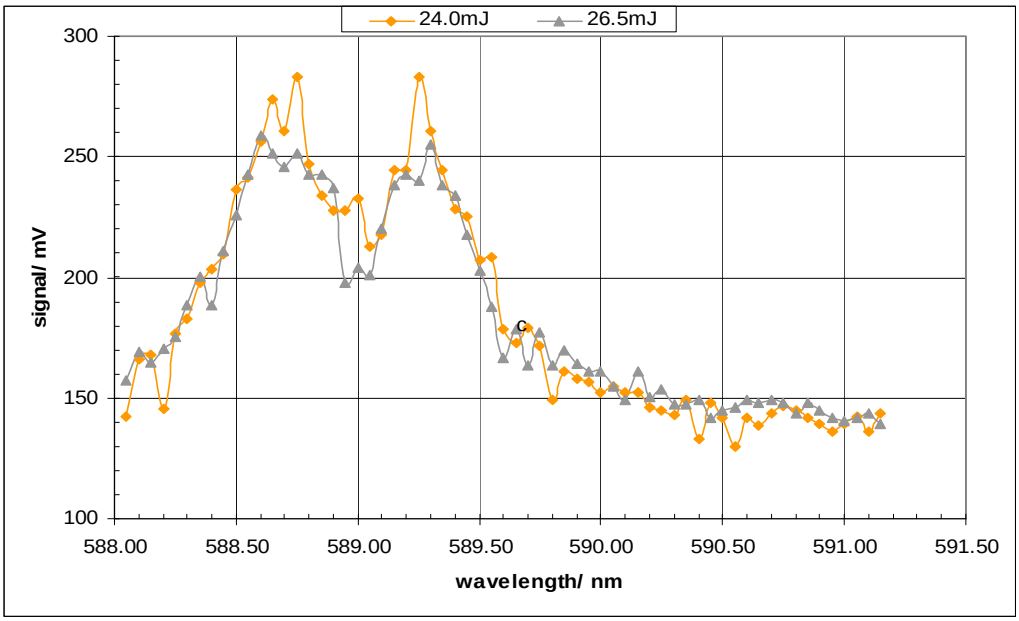

Figure 3: LIBS Spectra: E_p = 24.0mJ & 26.5mJ

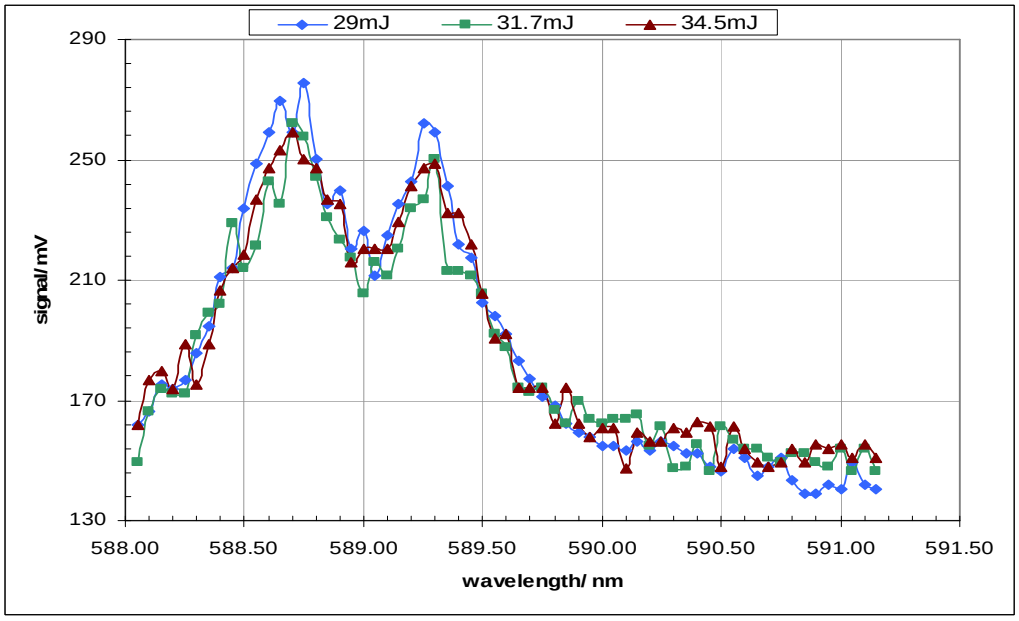

Figure 4: LIBS Spectra: E_p = 29.0mJ, 31.7mJ & 34.5mJ

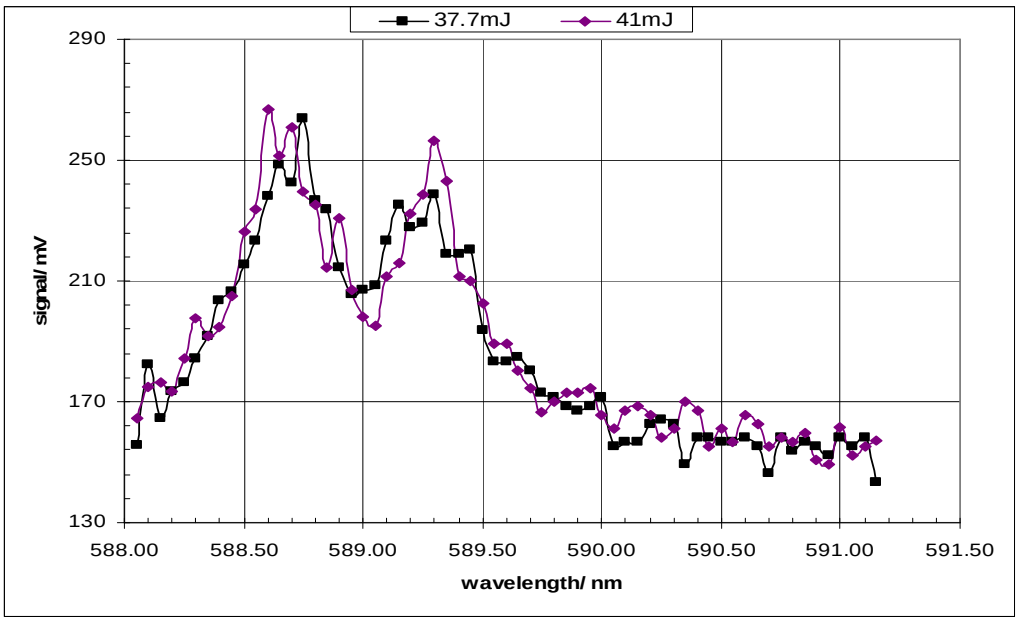

Figure 5: LIBS Spectra: E_p = 37.7mJ & 41.0mJ

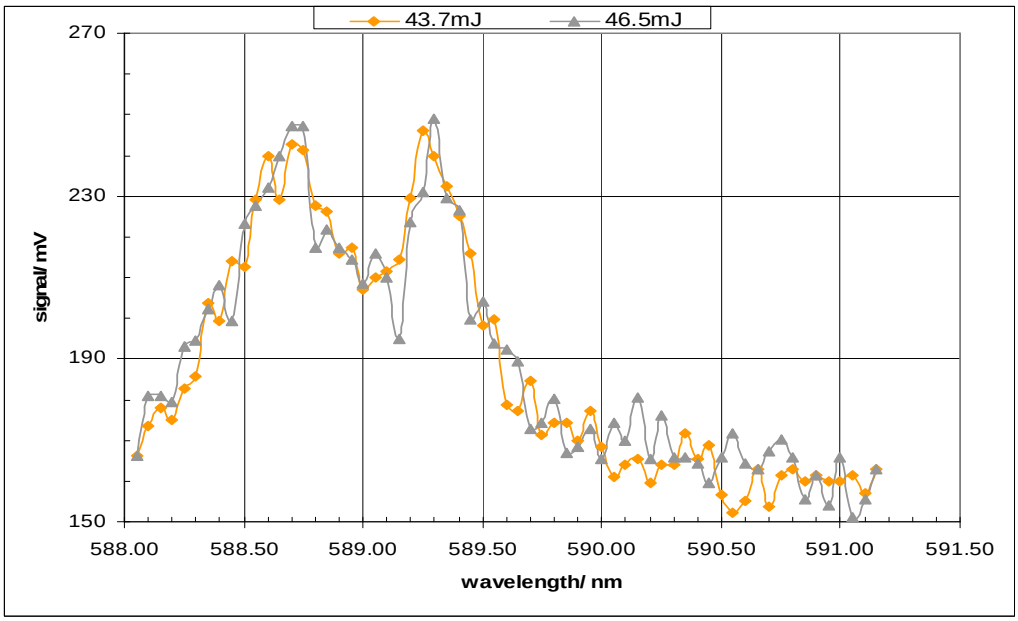

Figure 6: LIBS Spectra: E_p = 43.7mJ & 46.5mJ

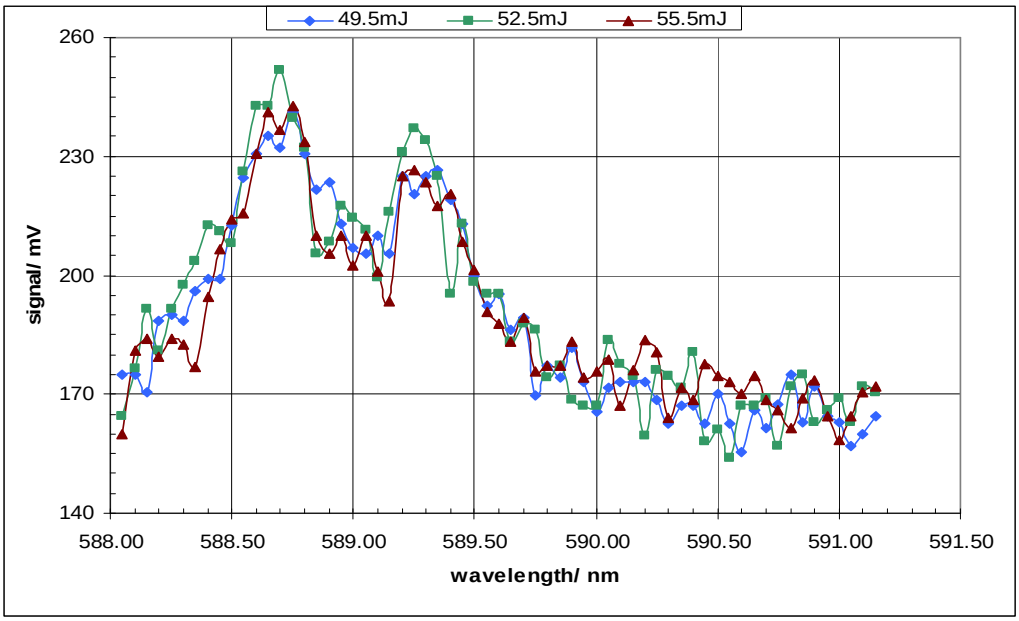

Figure 7: LIBS Spectra: E_p = 49.5mJ, 52.5mJ & 55.5mJ

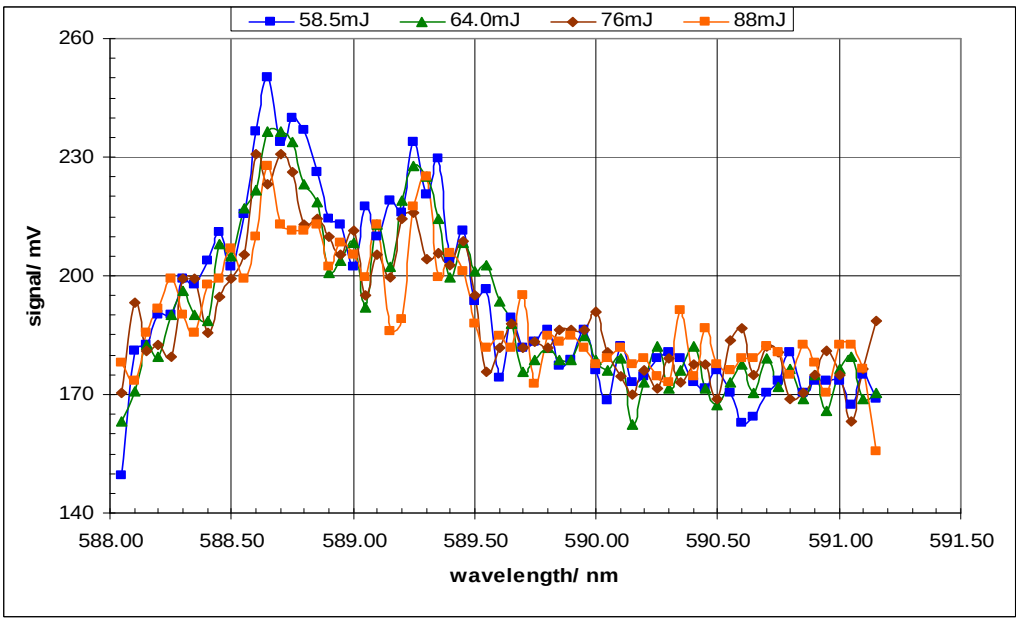

Figure 8: LIBS Spectra: E_p = 58.5mJ, 64.0mJ, 76.0mJ & 88.0mJ

Appendix XVII Optimized LIBS Emission Spectra for Lead Acetate Solution

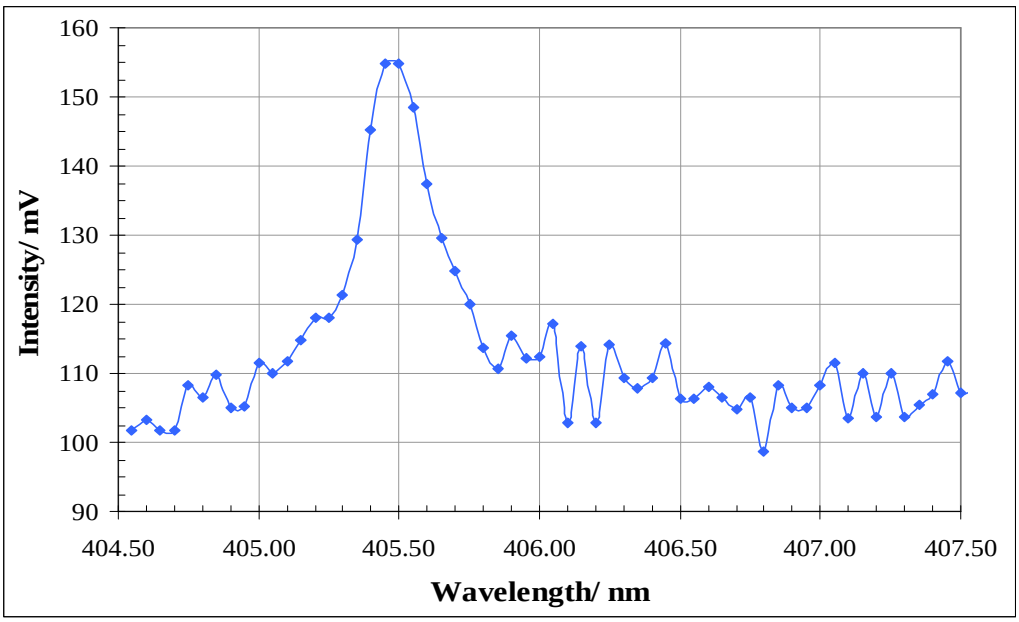

Figure 1: 490ppm lead acetate solution

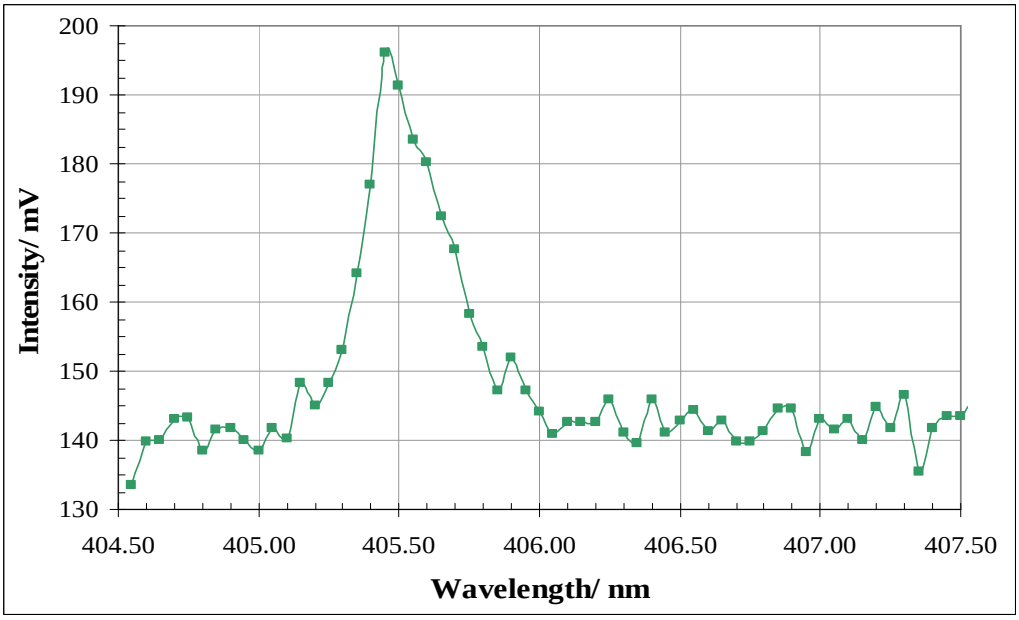

Figure 2: 250ppm lead acetate solution

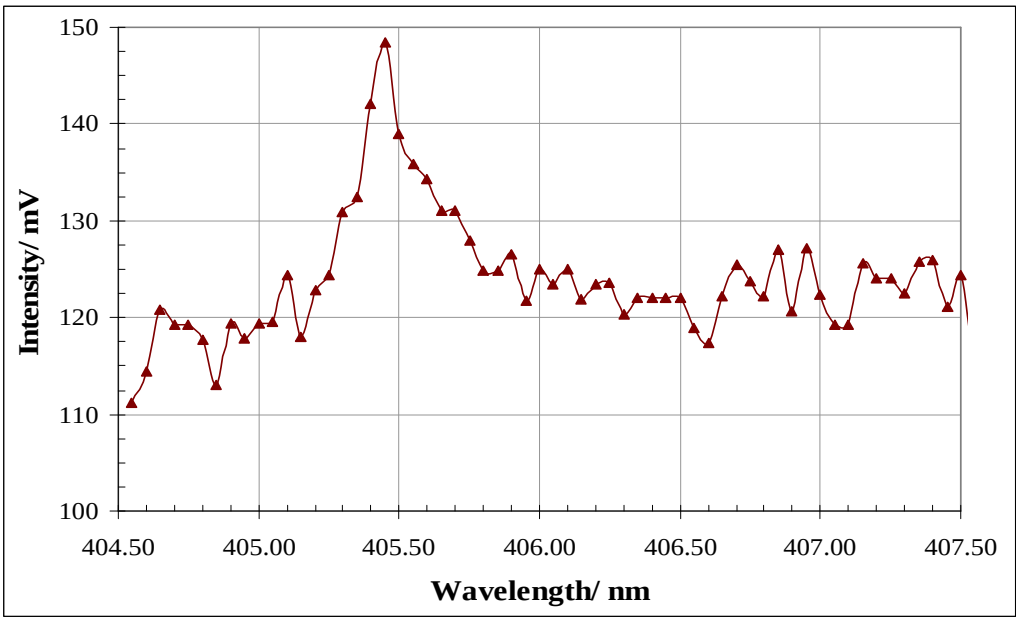

Figure 3: 125ppm lead acetate solution

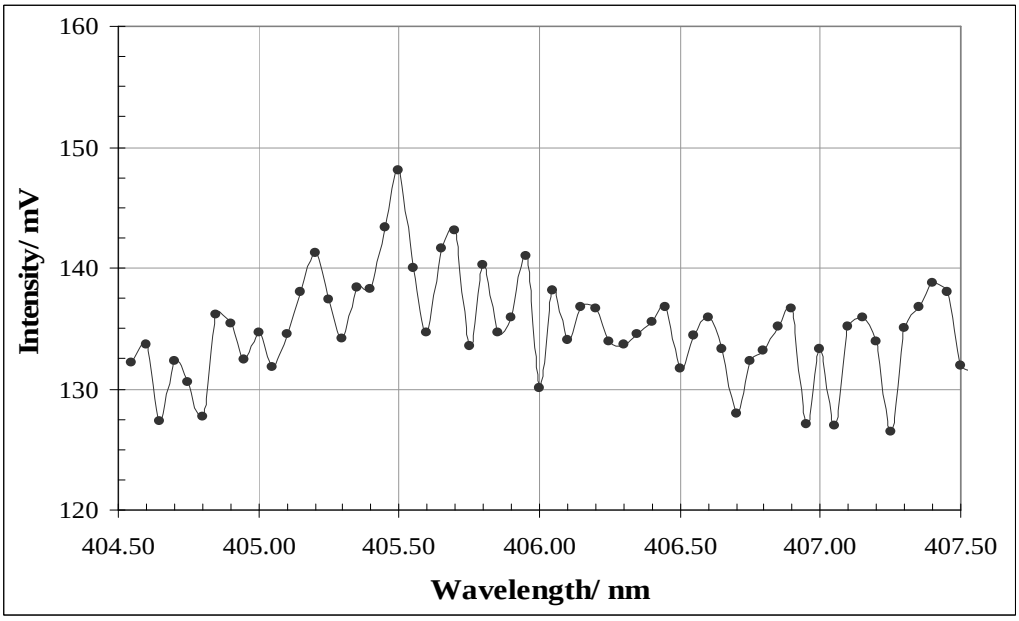

Figure 4: 100ppm lead acetate solution

Appendix XVIII Mechanically Filtered LIBS Spectra – Surface Plasma in Air

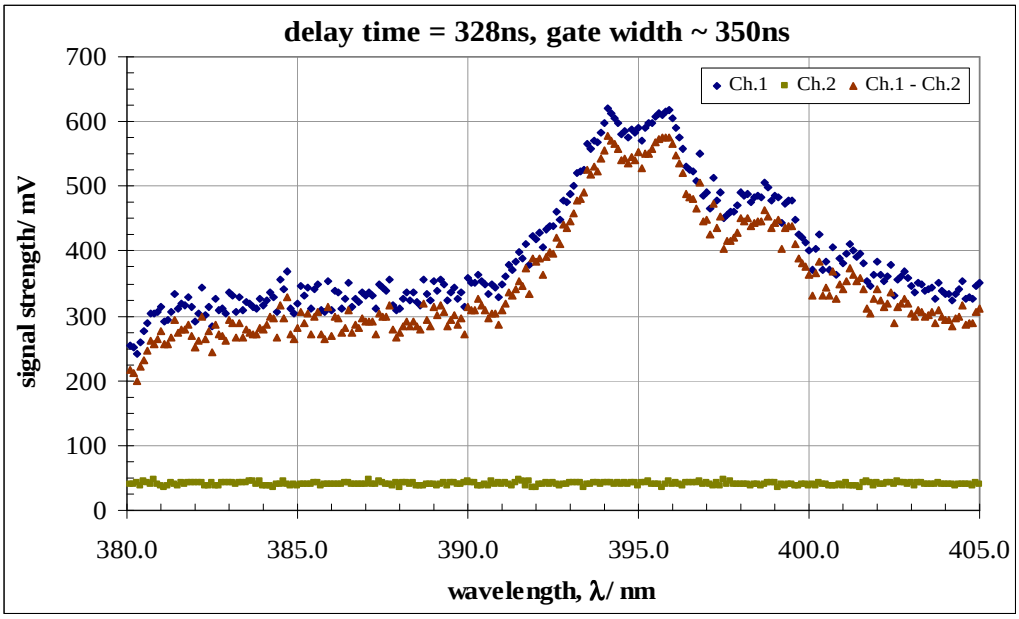

Figure 1: Comparative LIBS Spectra: t_d = 328ns

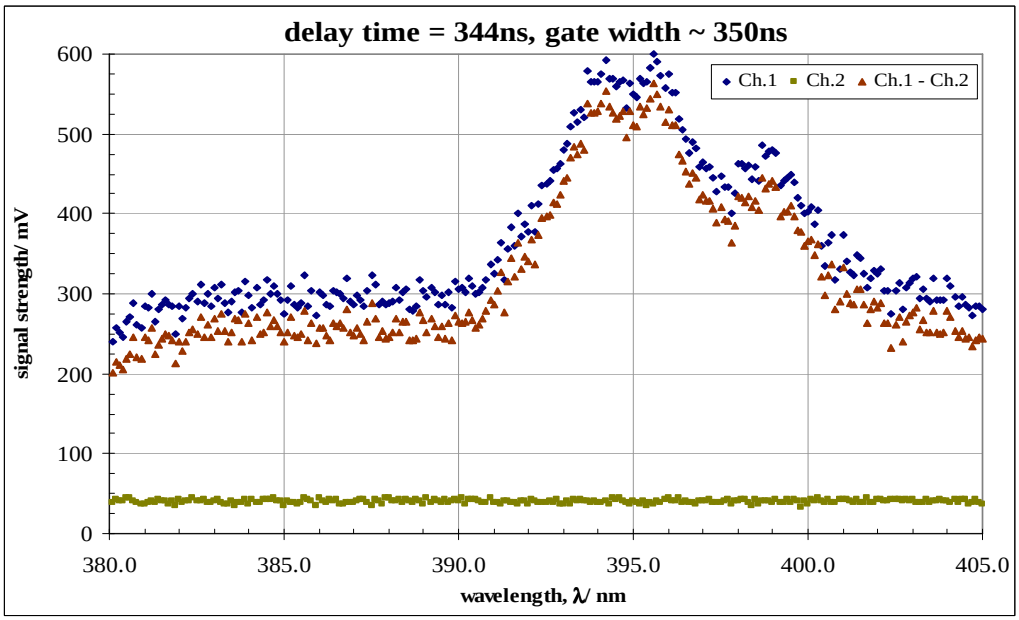

Figure 2: Comparative LIBS Spectra: t_d = 344ns

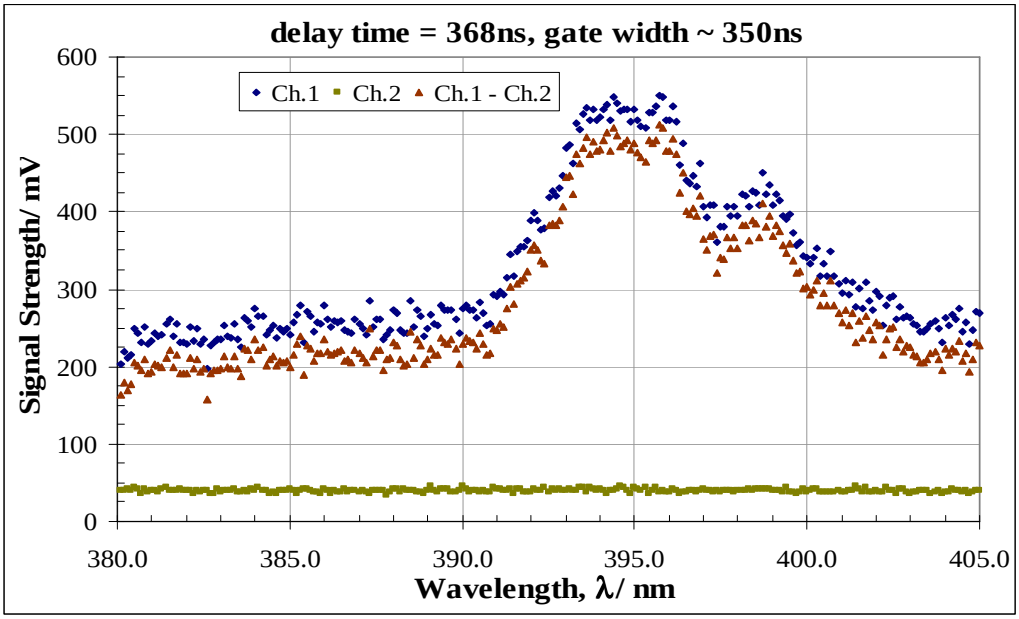

Figure 3: Comparative LIBS Spectra: t_d = 368ns

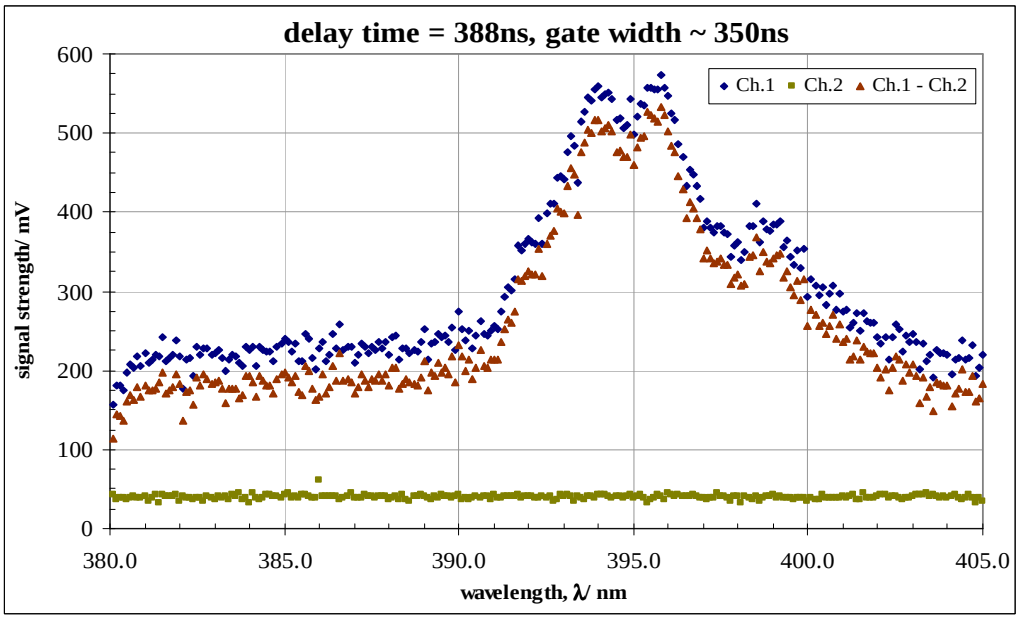

Figure 4: Comparative LIBS Spectra: t_d = 388ns

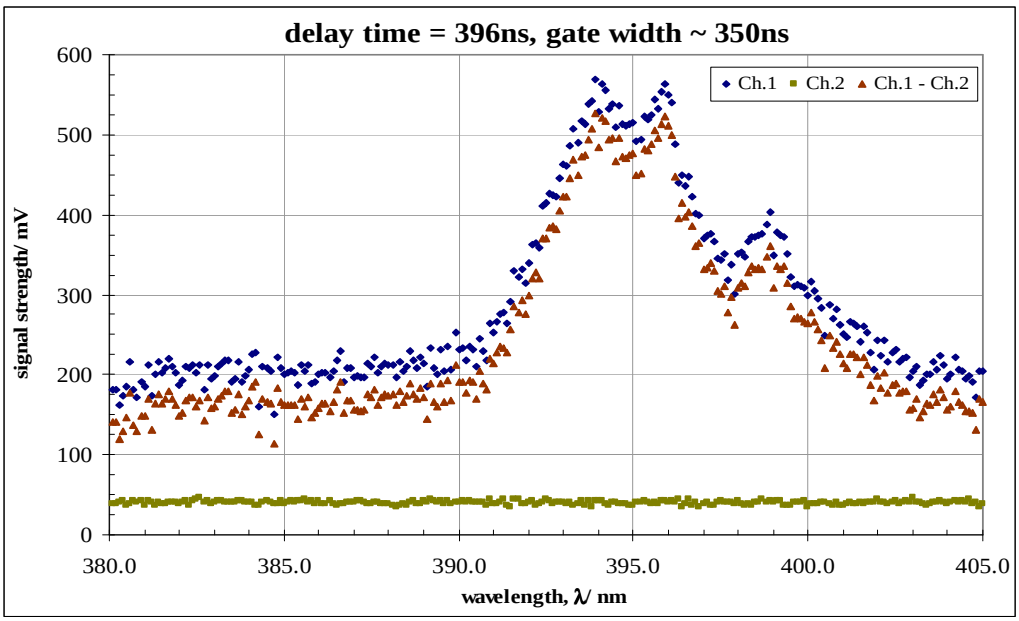

Figure 5: Comparative LIBS Spectra: t_d = 396ns

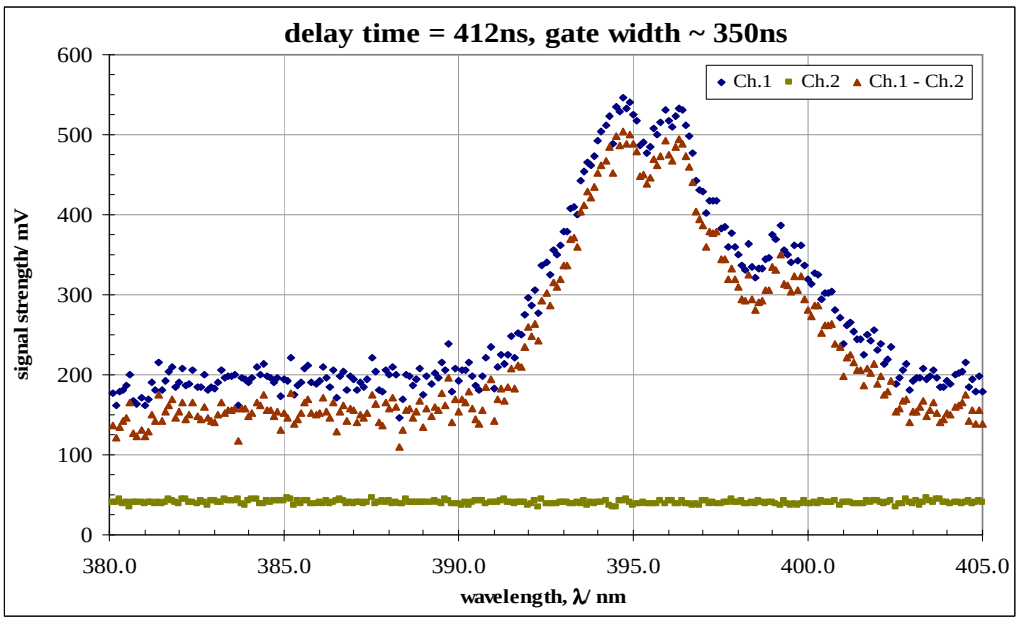

Figure 6: Comparative LIBS Spectra: t_d = 412ns

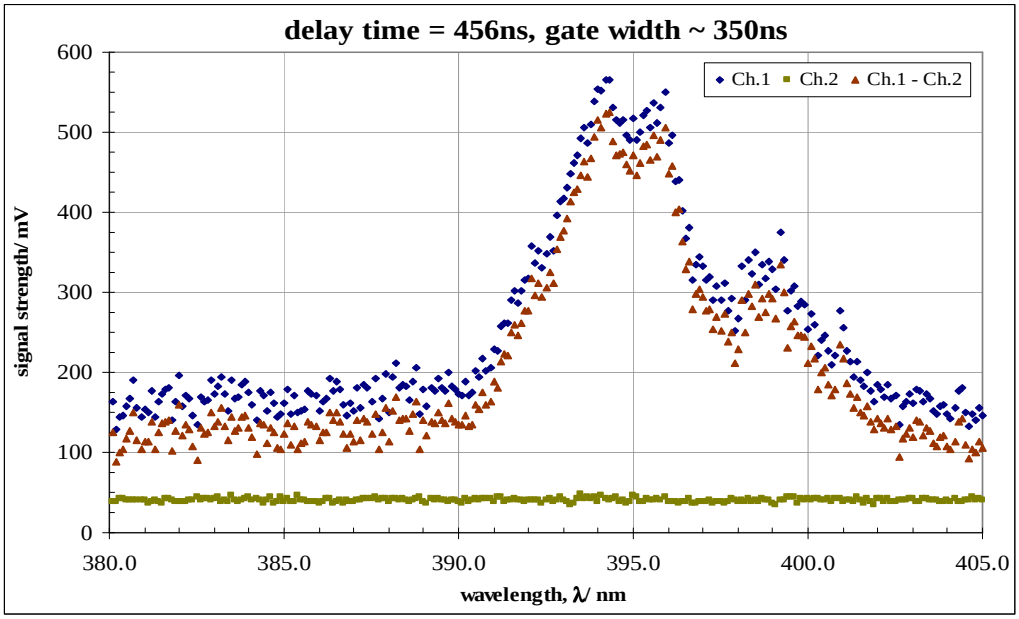

Figure 7: Comparative LIBS Spectra: t_d = 456ns

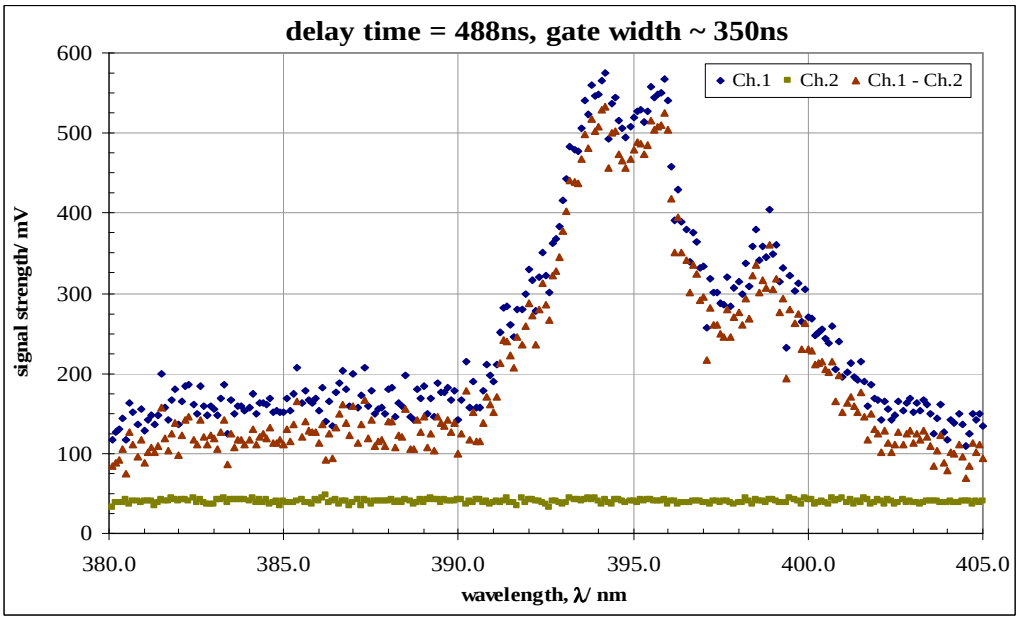

Figure 8: Comparative LIBS Spectra: t_d = 456ns

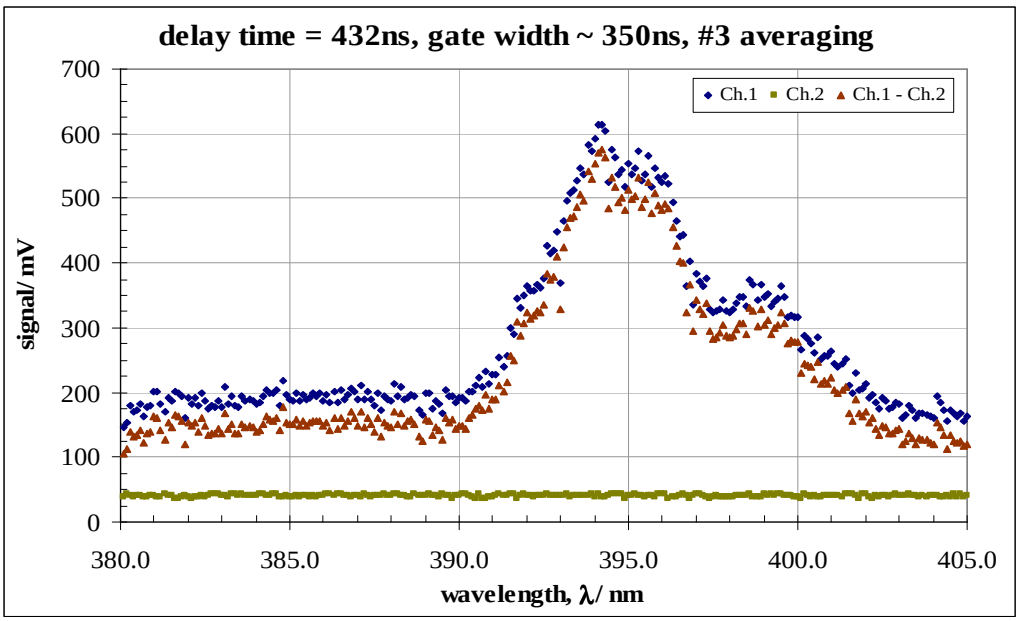

Figure 9: Comparative LIBS Spectra: t_d = 432ns, N = 3

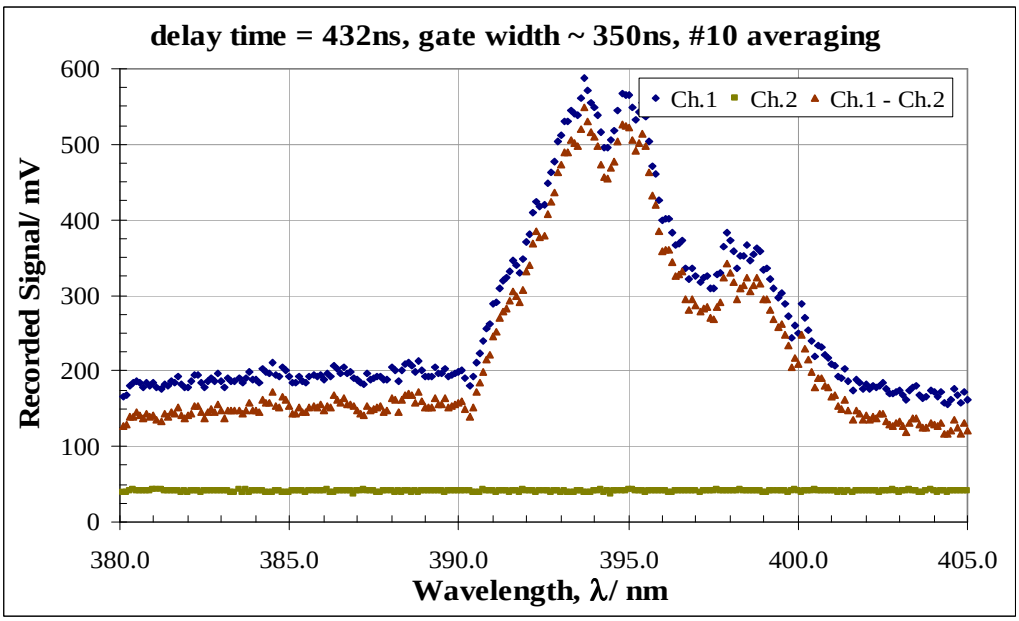

Figure 10: Comparative LIBS Spectra: t_d = 432ns, N = 10

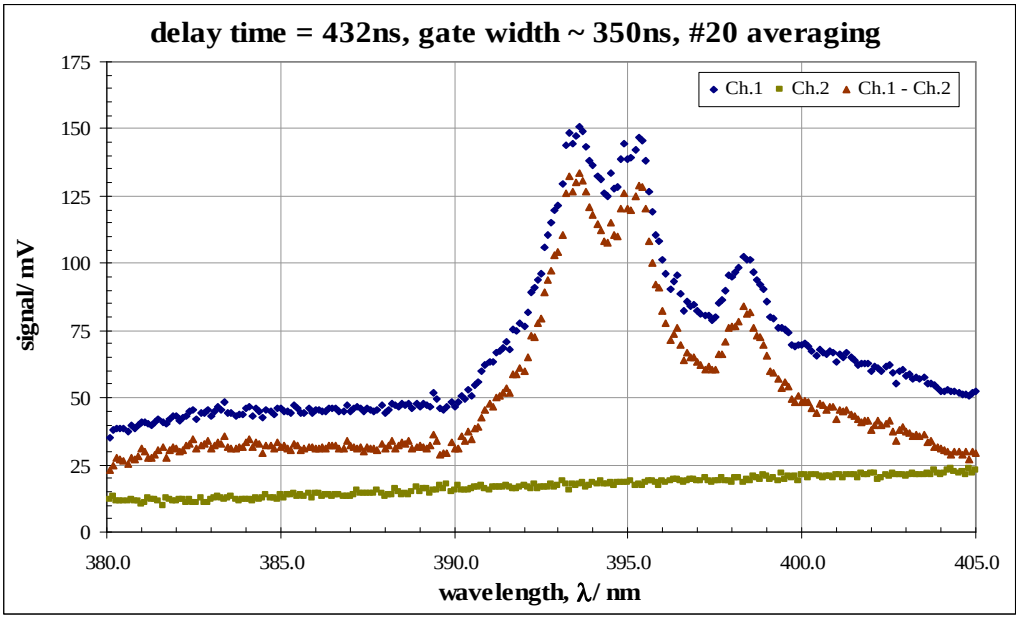

Figure 11: Comparative LIBS Spectra: t_d = 432ns, N = 20

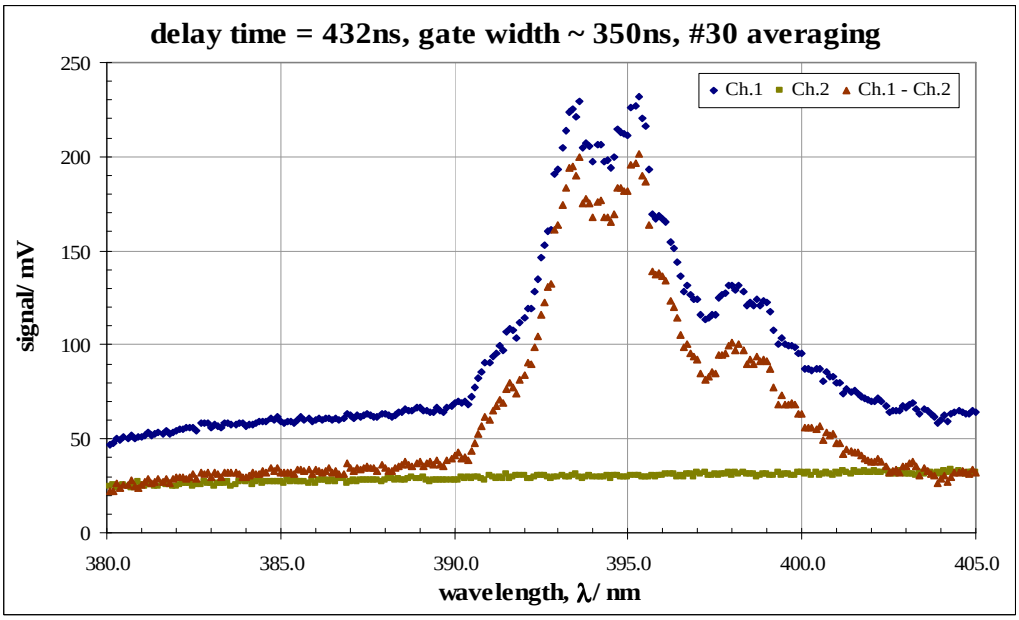

Figure 12: Comparative LIBS Spectra: t_d = 432ns, N = 30

Appendix XIX Mechanically Filtered LIBS Spectra – Liquid Bulk Presentation

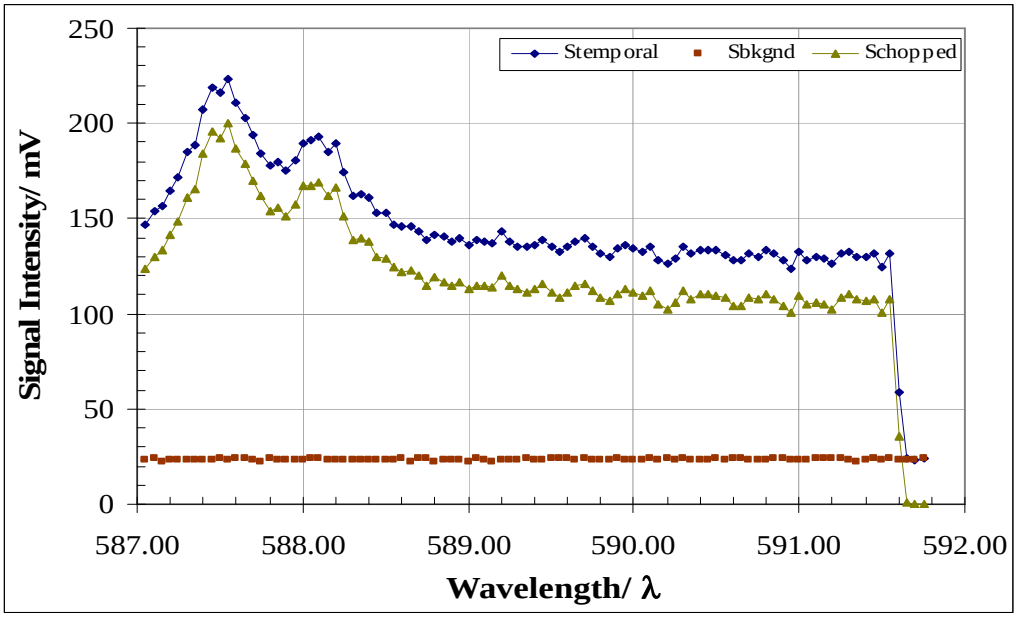

Figure 1: Comparative LIBS Spectra: N = 37

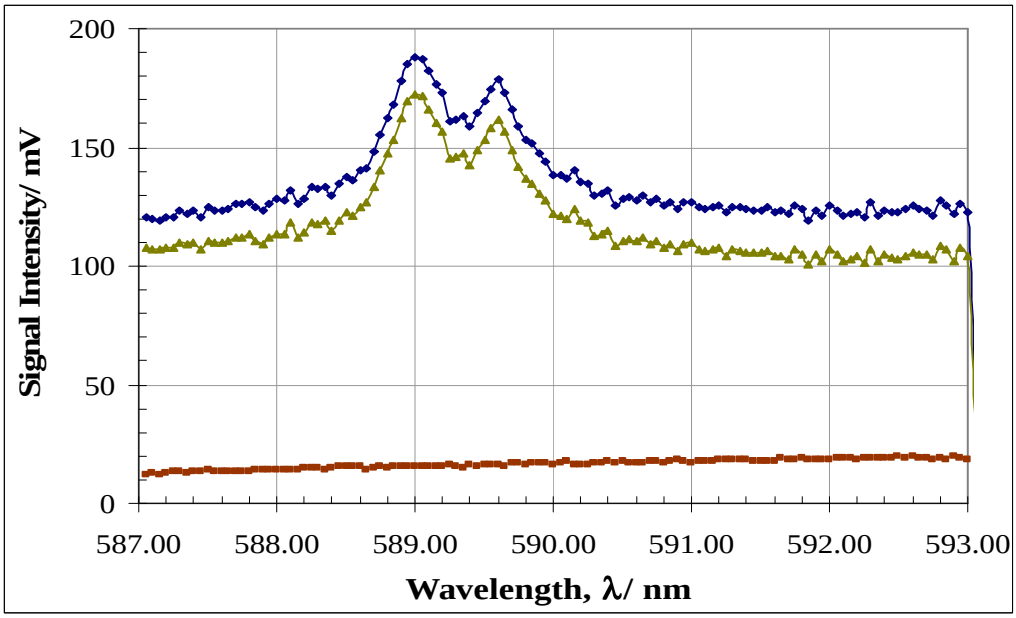

Figure 2: Comparative LIBS Spectra: N = 67

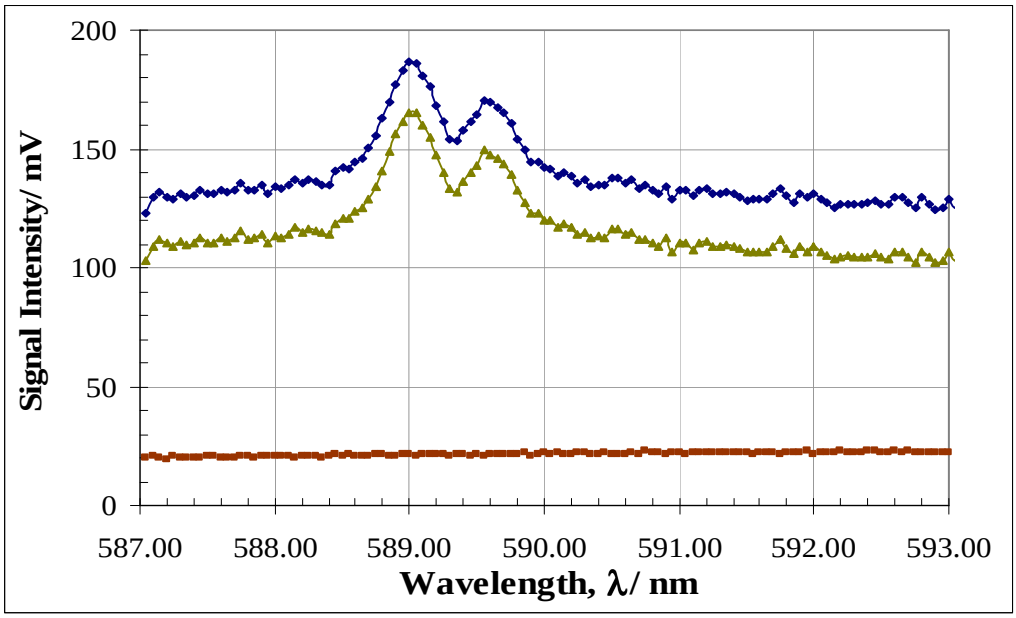

Figure 3: Comparative LIBS Spectra: N = 91

Appendix XX Sensitivity of Line Emission Profile to Grating Setting

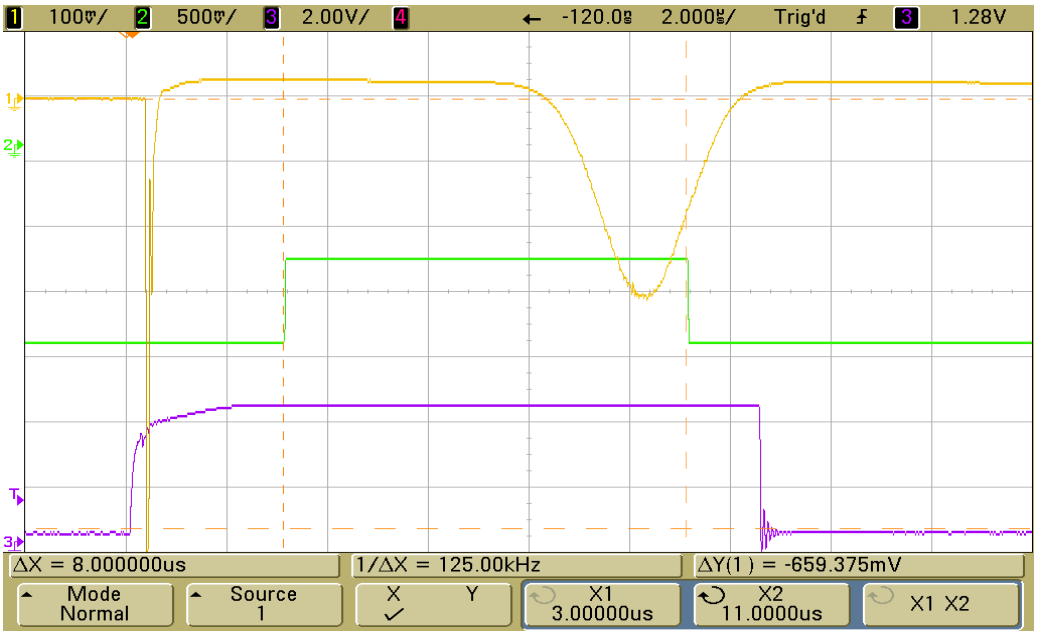

Figure 1: Spectrometer Grating set at 360.00nm

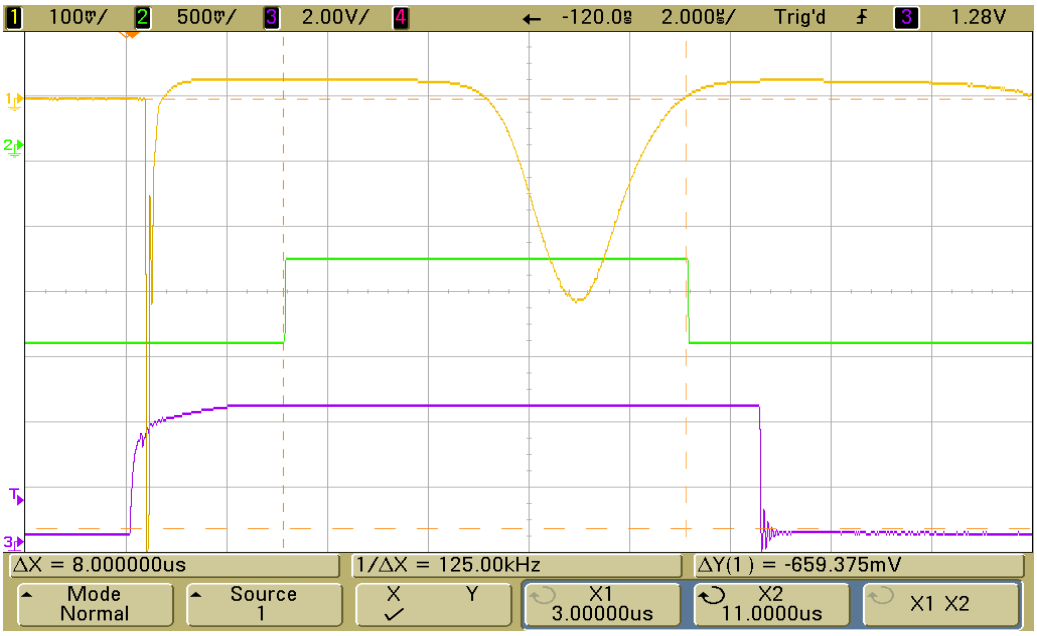

Figure 2: Spectrometer Grating set at 360.15nm

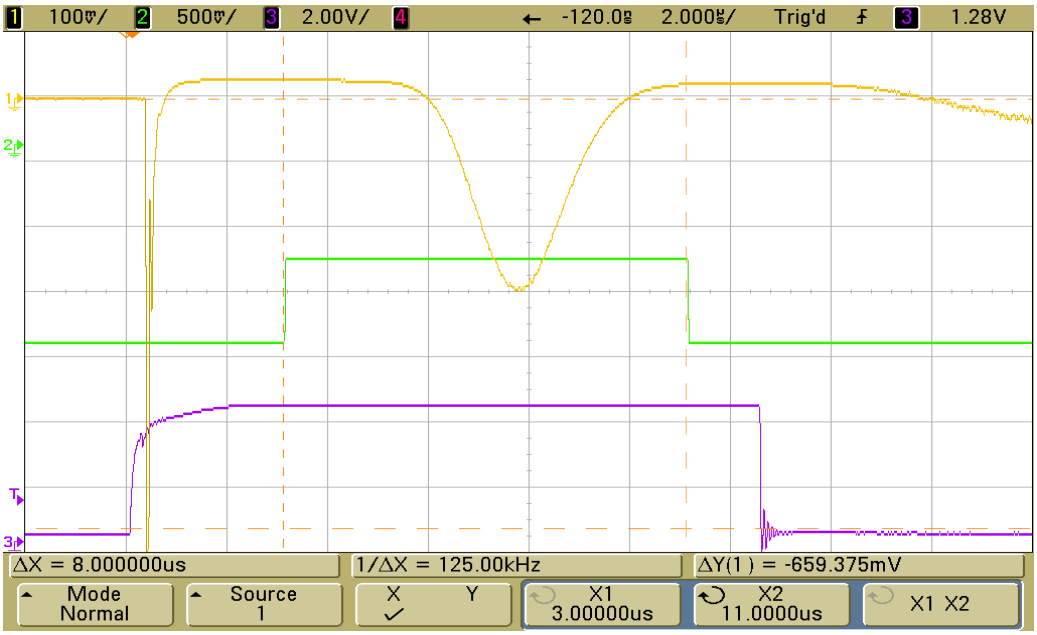

Figure 3: Spectrometer Grating set at 360.20nm

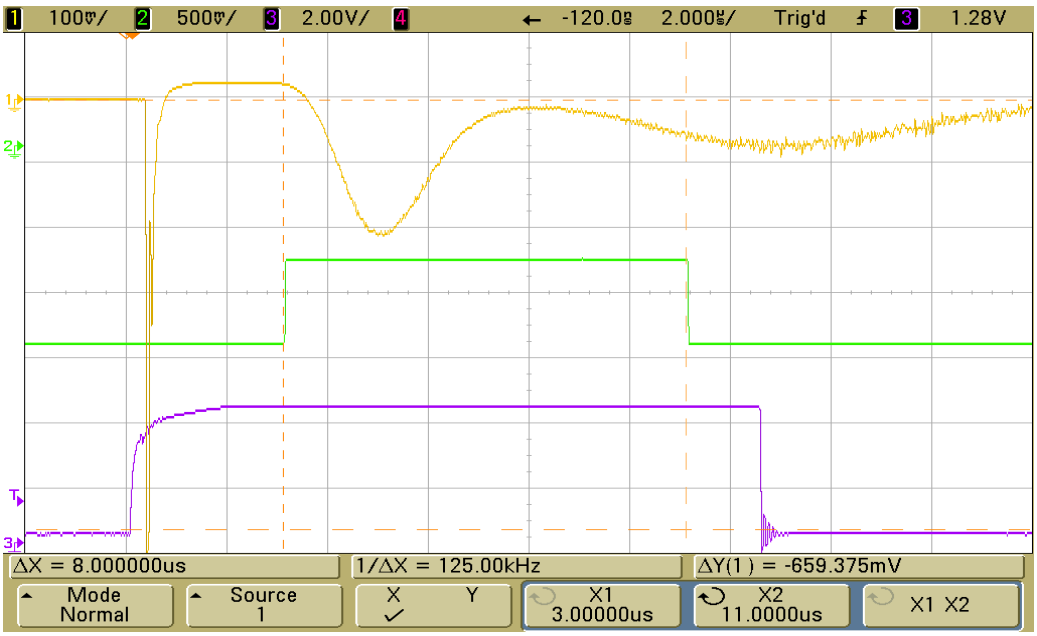

Figure 4: Spectrometer Grating set at 360.45nm

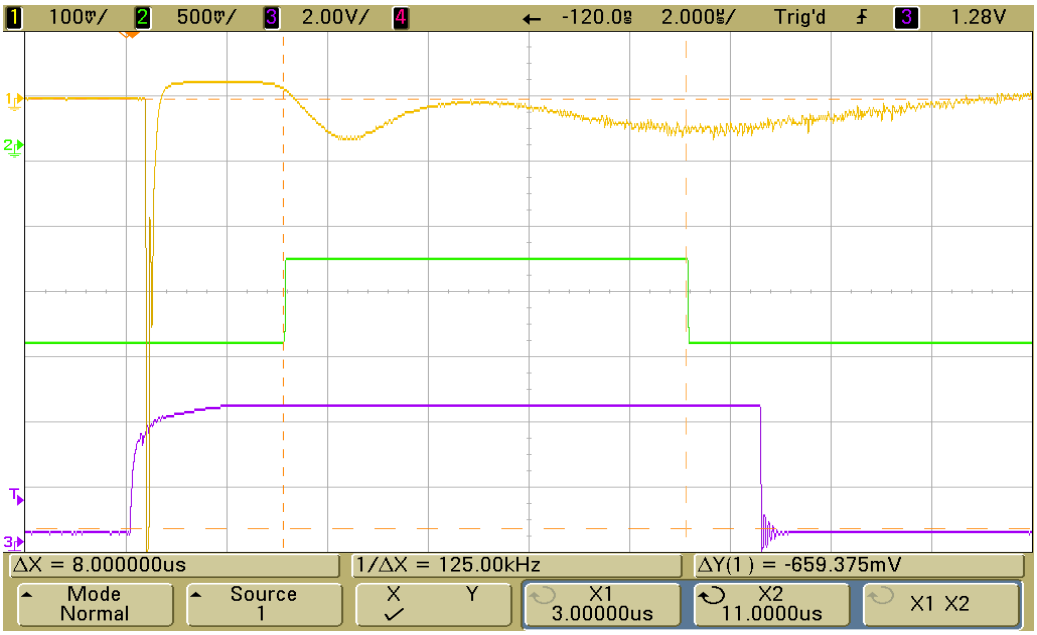

Figure 5: Spectrometer Grating set at 360.70nm

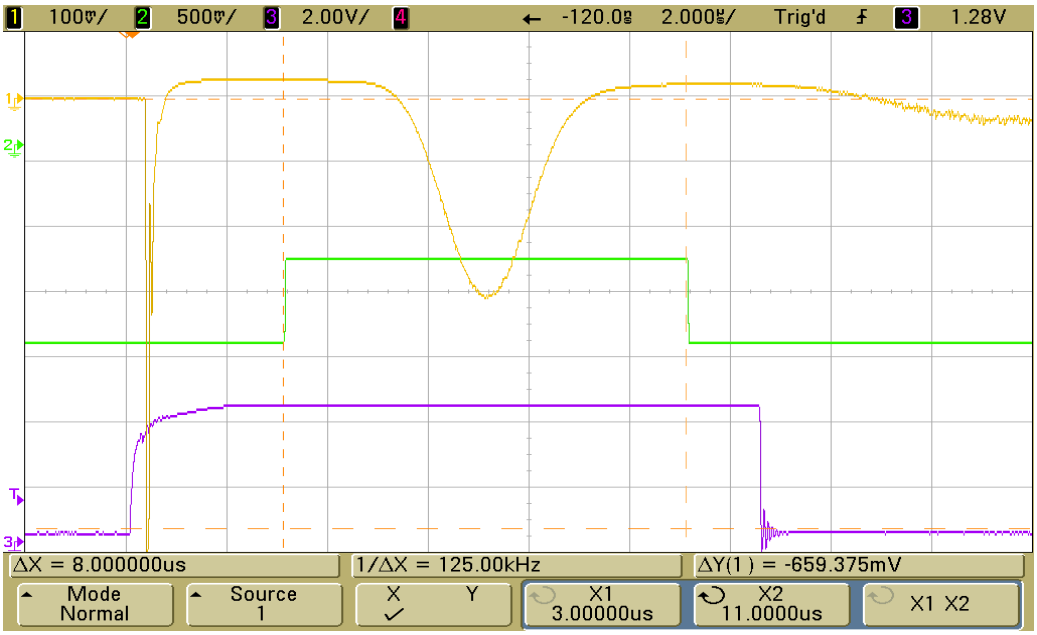

Figure 6: Spectrometer Grating set at 360.225nm

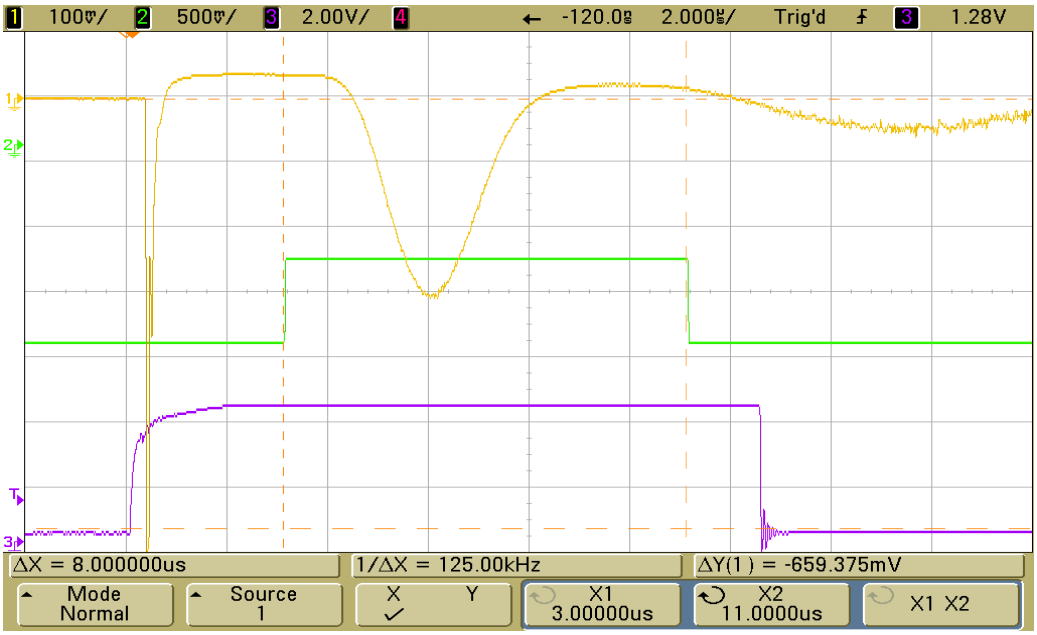

Figure 7: Spectrometer Grating set at 360.275nm

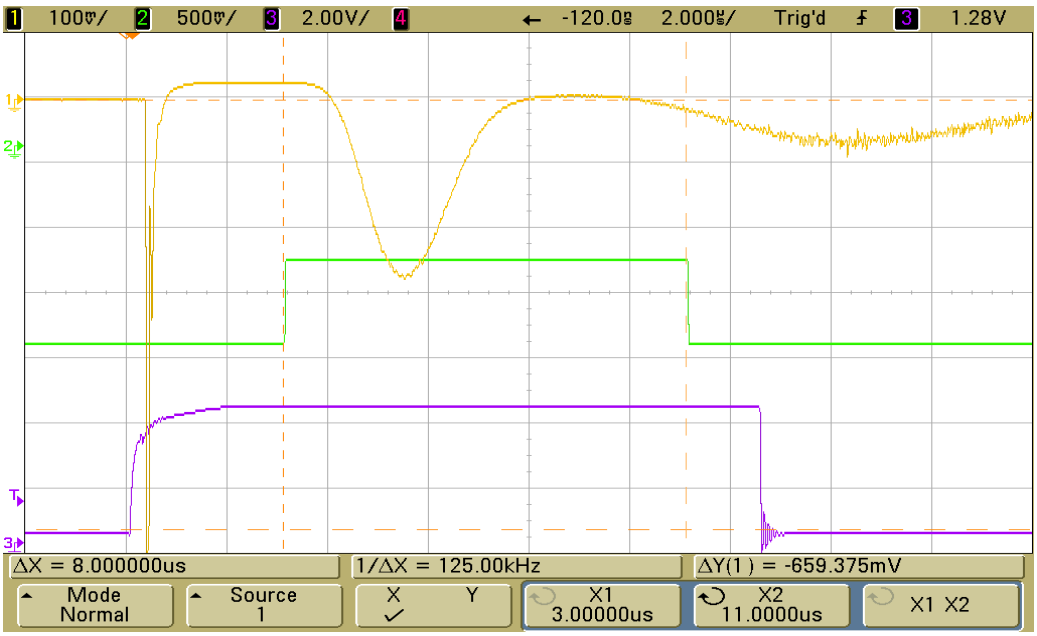

Figure 8: Spectrometer Grating set at 360.325nm

Appendix XXI Effect of Plasma Blocking on *Bremsstrahlung* Profile

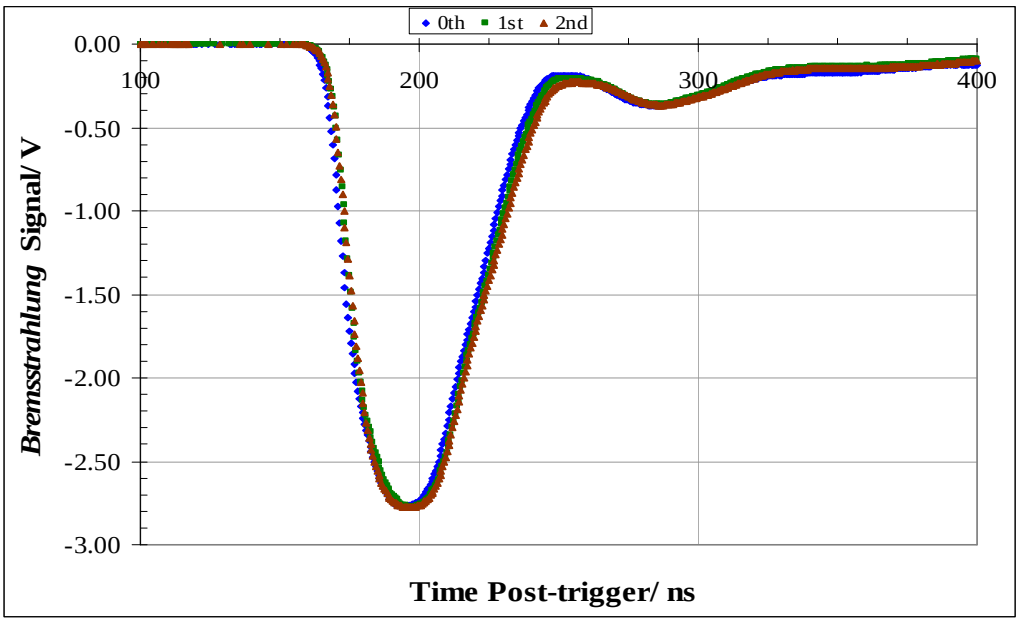

Figure 1: BL Profiles: ΔL = 0, 45 & 90μm

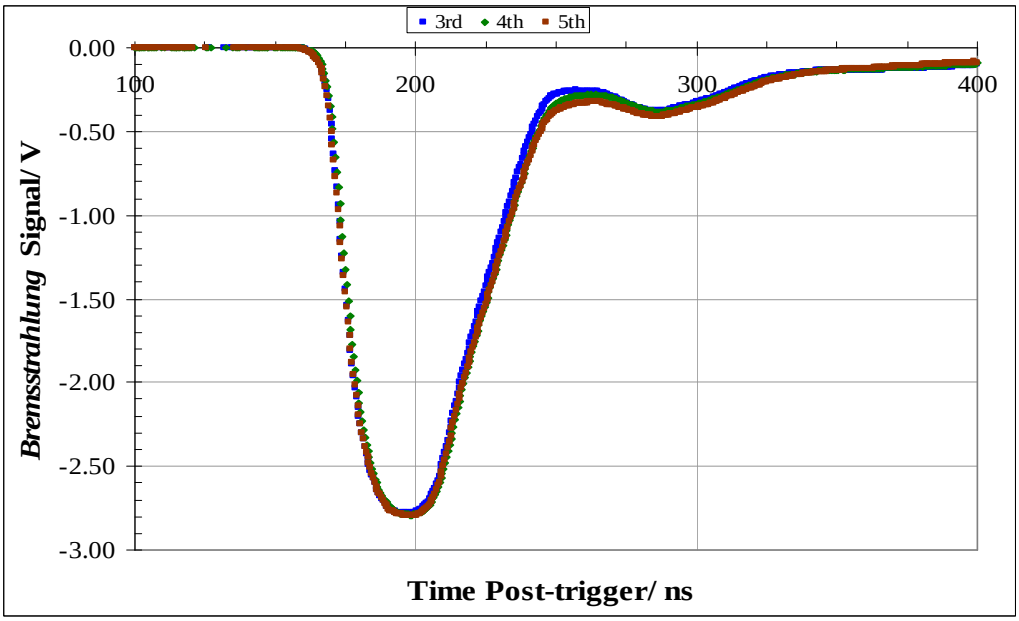

Figure 2: BL Profiles: ΔL = 135, 180 & 225μm

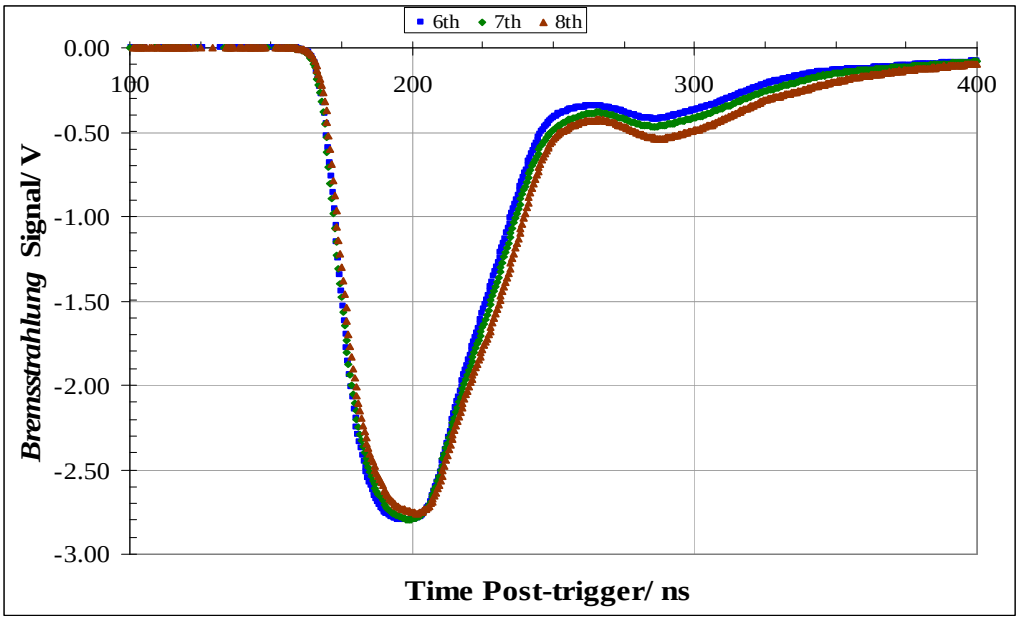

Figure 3: BL Profiles: ΔL = 270, 315 & 360μm

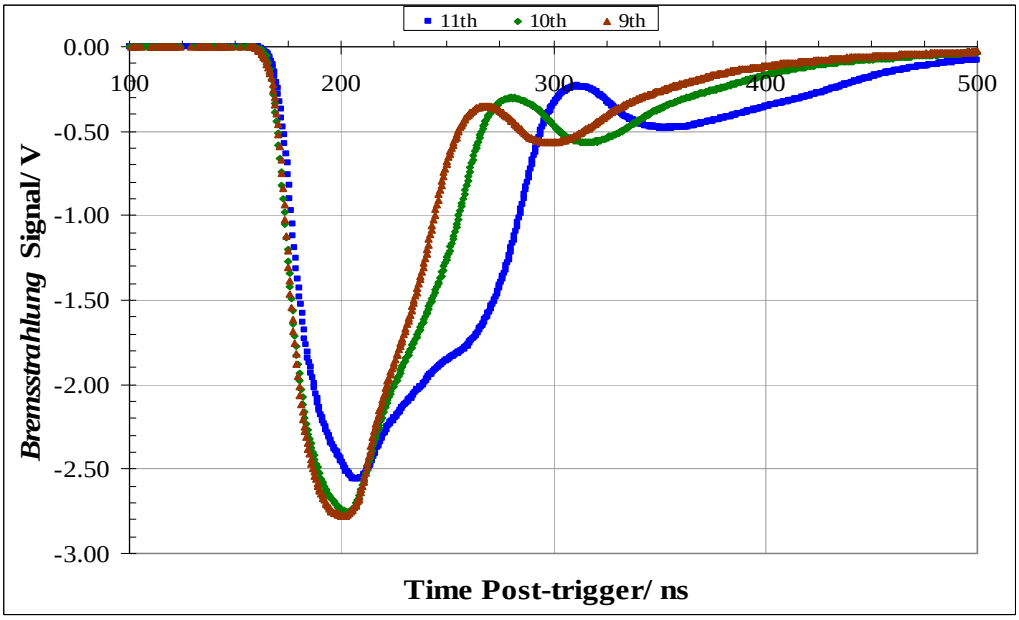

Figure 4: BL Profiles: ΔL = 405, 450 & 495μm

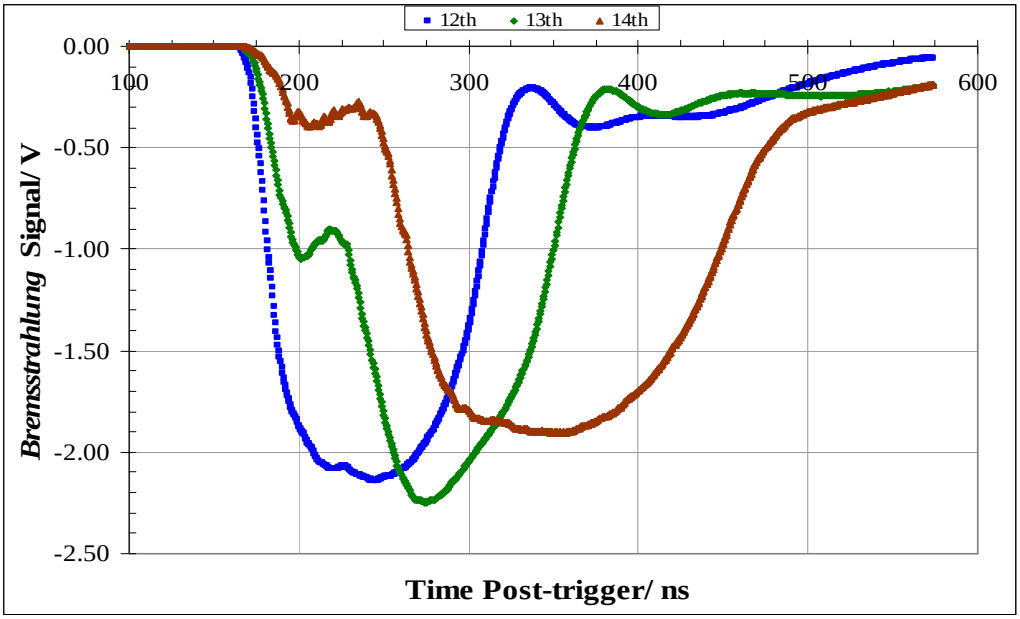

Figure 5: BL Profiles: ΔL = 540, 585 & 630μm

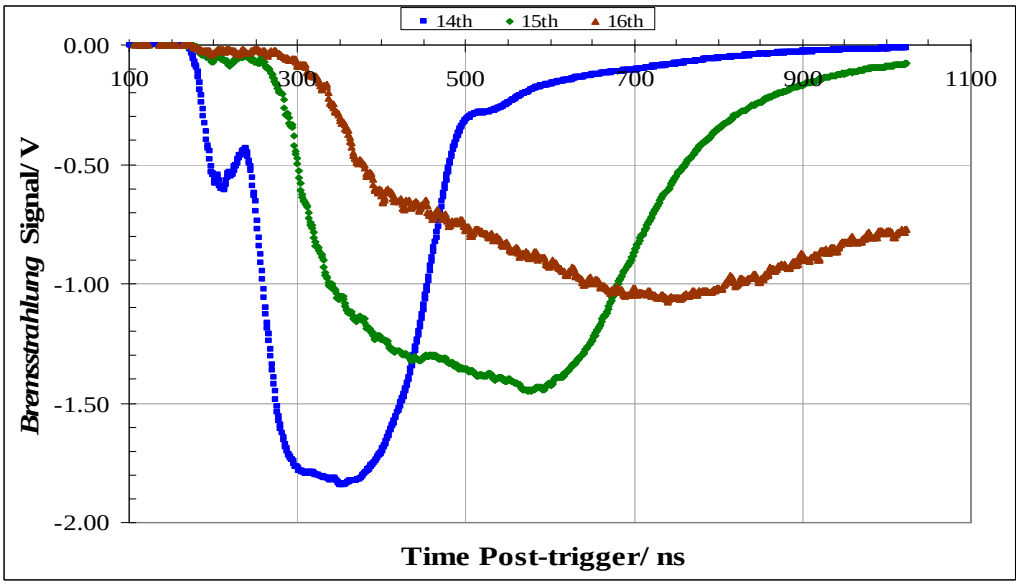

Figure 6: BL Profiles: ΔL = 675, 720 & 765μm

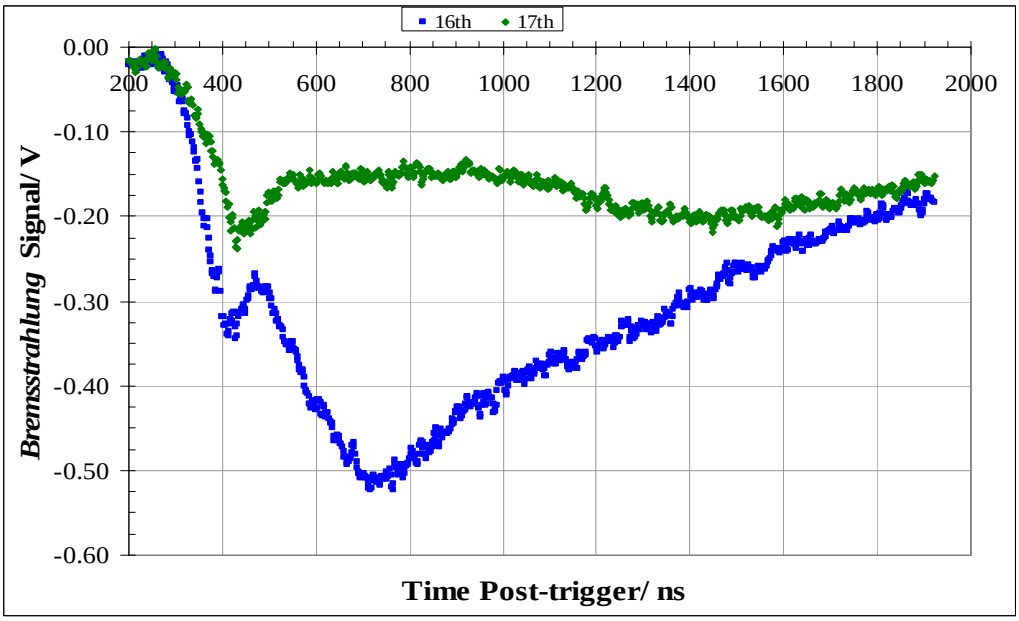

Figure 7: BL Profiles: ΔL = 720 & 765µm

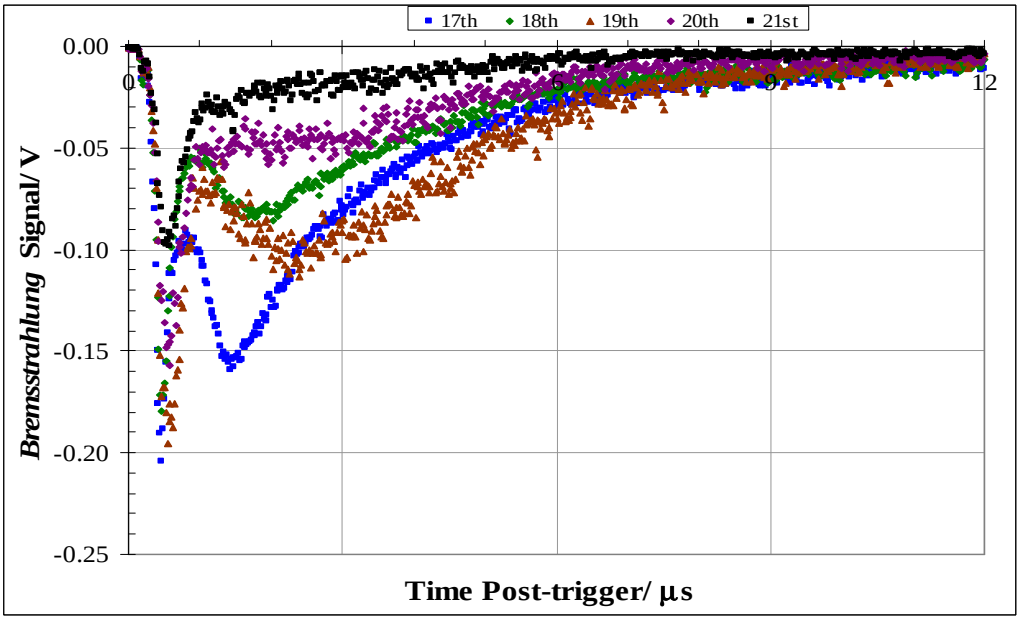

Figure 8: BL Profiles: ΔL = 765, 810, 855, 900 & 945µm

Appendix XXII Effect of Plasma Blocking on Line Emission Profile

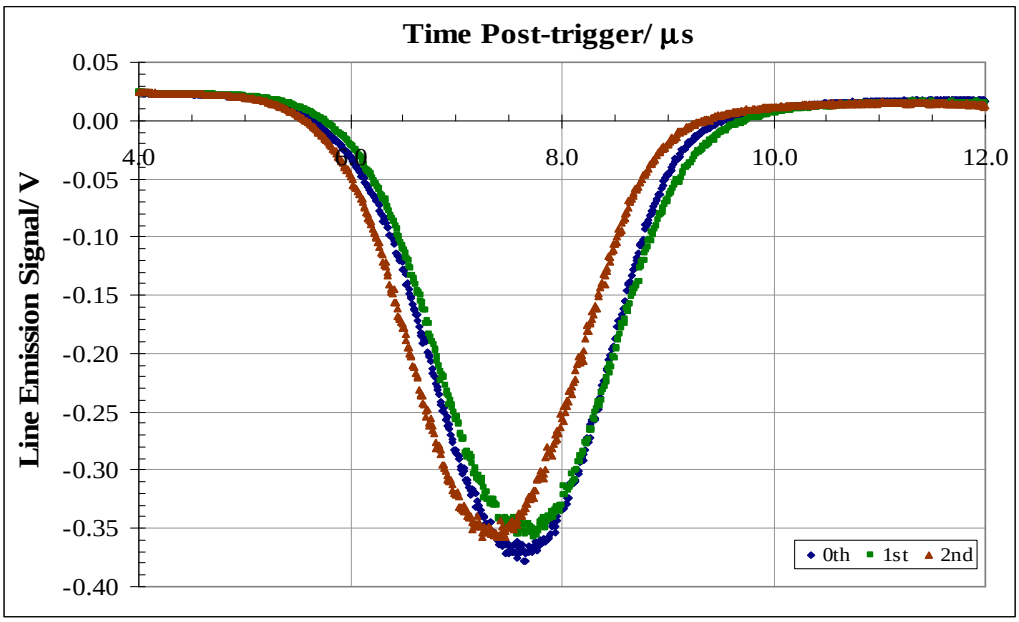

Figure 1: Emission Line Profiles: ΔL = 0, 45 & 90µm

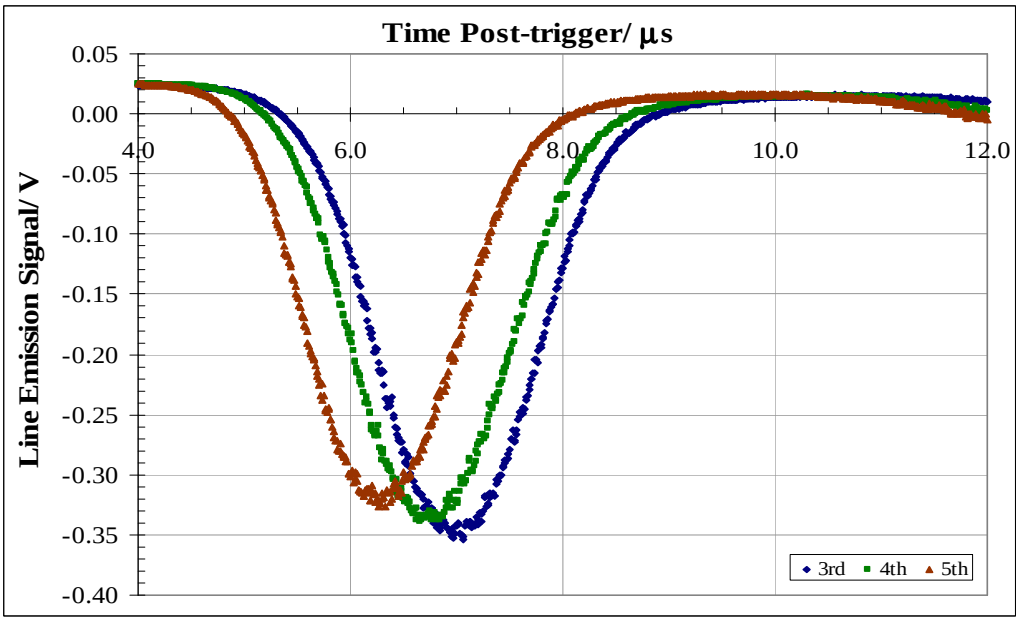

Figure 2: Emission Line Profiles: ΔL = 135, 180 & 225µm

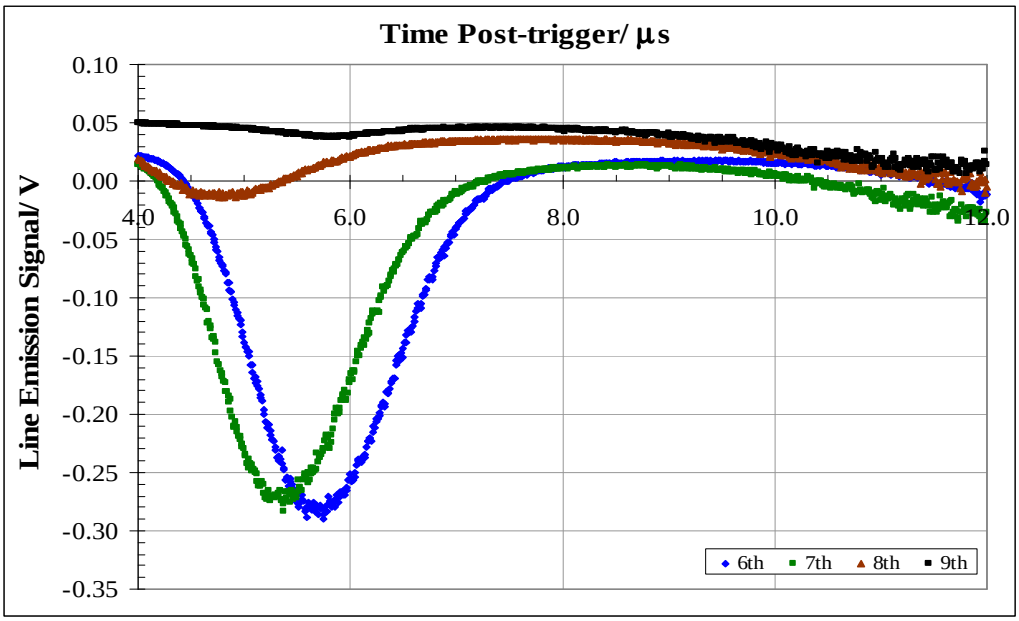

Figure 3: Emission Line Profiles: ΔL = 270, 315, 360 & 405µm

Appendix XXIII LIBS Emission Spectra using Plasma Blocking Technique

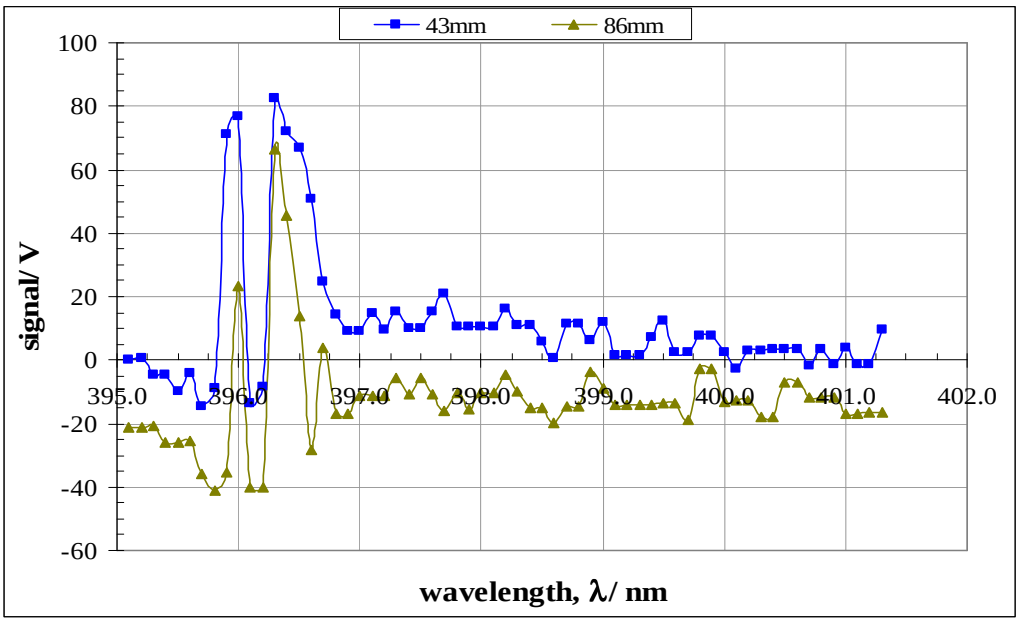

Figure 1: Plasma Blocking, ΔL = 43 & 86µm

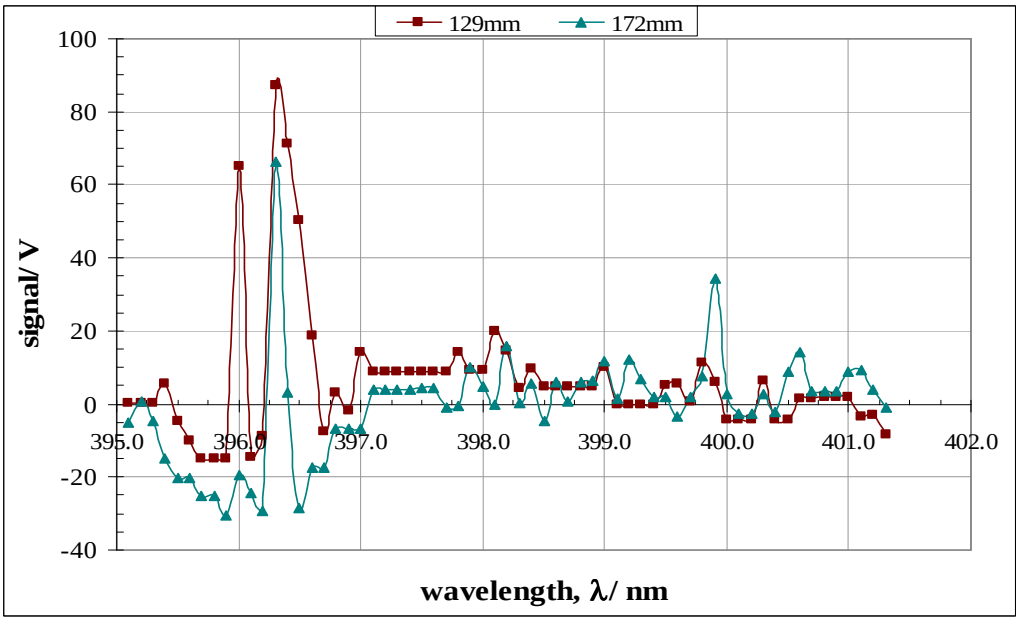

Figure 2: Plasma Blocking, ΔL = 129 & 172µm

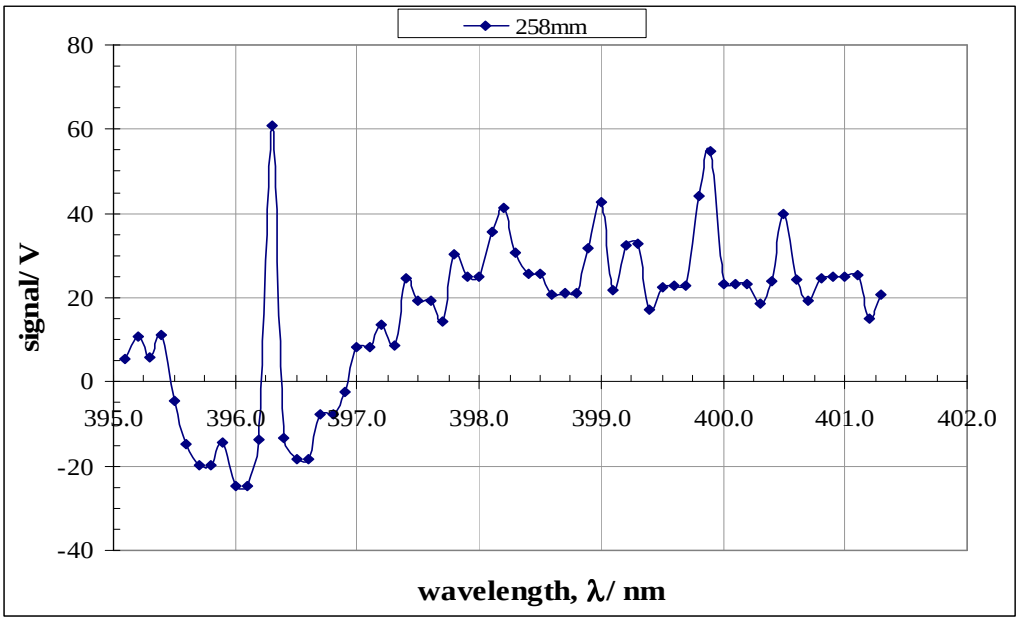

Figure 3: Plasma Blocking, ΔL = 258μm

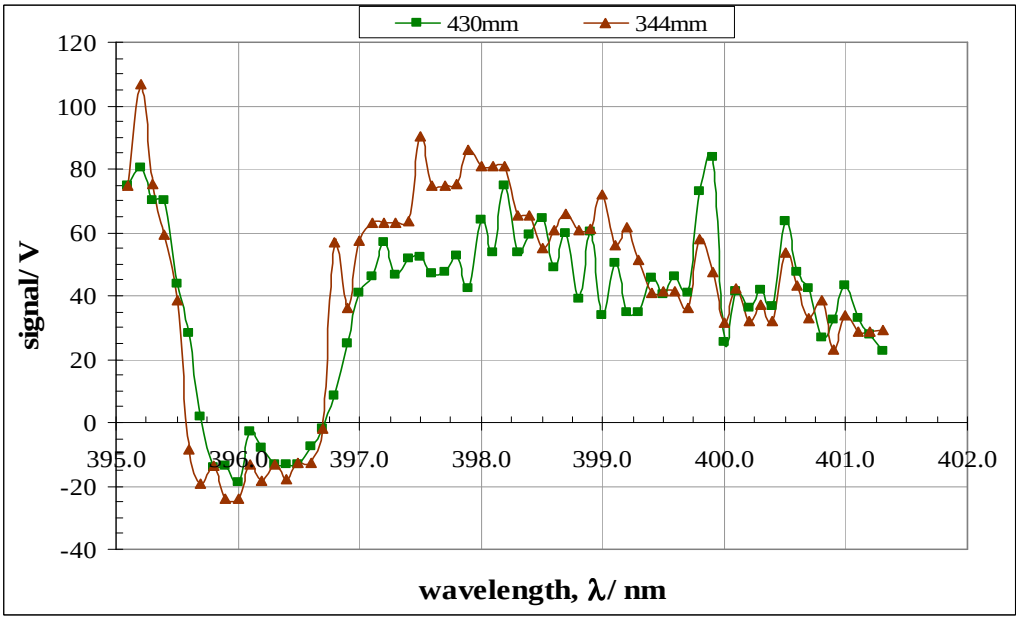

Figure 4: Plasma Blocking, ΔL = 344 & 430μm

Appendix XXIV Author's Research Published in the Peer Reviewed Literature

Appl Phys A
DOI 10.1007/s00339-010-6056-7

Applied Physics A
Materials Science & Processing

Dynamics of laser-induced cavitation in liquid

Christopher S. Peel · Xiao Fang · S. Rafi Ahmad

Received: 10 June 2010 / Accepted: 20 September 2010

Abstract This paper presents an analysis of the rate of bubble expansion and an estimate of maximum bubble diameter and bubble lifetime prior to collapse. Such data are needed for the optimization of system parameters for elemental analysis in water by laser-induced breakdown spectroscopy (LIBS). Two techniques were used for this study: pump-probe beam deflection and high-speed photography. Plasma in the water bulk was generated by a focussed laser pulse with energy of 140 mJ and pulse duration of 10 ns, operating at the fundamental Nd:YAG laser wavelength (1064 nm). Reasonable agreement on the value of maximum bubble diameter was obtained between the photographic and probe beam deflection results. Reasonable agreement for the total duration of the oscillating cavitation bubble was also obtained for the two techniques, with a mean value of ~800 μs. A comparison between empirical results and predictions based on the Rayleigh equation is also presented.

1 Introduction

Formation, expansion and subsequent collapse of bubbles in water bulk, due to the intense heating effect of a focussed laser pulse, are known as the cavitation process. This is a consequence of the generation of plasma following dielectric breakdown of the medium, known as laser-induced breakdown (LIB). This allows implementation of atomic emission spectroscopy for elemental analysis in water bulk [1, 2]. Additionally, the shockwave generated by the collapse of the cavitation bubble may induce fracture in biological calculi immersed in urine, in close proximity to the bubble. This phenomenon has found widespread application in minimally invasive surgical procedures, known as lithotripsy [3, 4]. For effective application in the aforementioned field, a good understanding of the interaction between the focussed laser pulse and water bulk, as well as the dynamics of the subsequent cavitation process, is required. This paper addresses such issues by measurement of principal cavitation bubble parameters. The physicochemistry of water molecules subject to optical energy having irradiance in excess of its dielectric breakdown threshold is a topic of active research, and at present is incompletely understood [5, 6].

Earlier work [7, 8] studied the behaviour of cavitation bubbles in the vicinity of a solid boundary. Ablation damage to the solid boundary from impact by a high pressure liquid jet, emitted on asymmetric collapse of the cavitation bubble, was investigated using laser pulse energies in the range 5.1 to 21.7 mJ. Linearity between bubble energy and laser pulse energy was established, and bubble collapse time was reported to be proportional to the square root of the laser pulse energy. Later work [9–11] reported parametric measurements for cavitation parameters in the liquid bulk using two different monitoring techniques i.e. probe beam deflection (PBD) and high-speed shadow photography. Maximum bubble radii and bubble lifetimes were both found to increase with laser pulse energy. The present paper reports results obtained using a significantly higher laser pulse energy to ascertain whether this trend is valid.

2 Theoretical basis

The contemporary study of laser-induced cavitation dynamics is an extension of the original equation derived by Lord

C.S. Peel · X. Fang (✉) · S.R. Ahmad
Department of Engineering and Applied Science, Defence Academy of the United Kingdom, Cranfield University, Shrivenham SN6 8LA, UK
e-mail: x.fang@cranfield.ac.uk
Fax: +44-01793-785772

Published online: 09 October 2010

Rayleigh [12] for quantifying cavitation in the liquid bulk. This was based on assumptions of infinite extent of the sample volume, and null compressibility and viscosity of the liquid medium. The bubble wall velocity (V_B) as a function of its radius (R_B) is given by [13],

$$V_B = \left[(2/3)p_\infty/\rho_l \cdot \left\{(R_0/R_B)^3 - 1\right\}\right]^{0.5} \quad (1)$$

where p_∞ is the pressure in infinite liquid, ρ_l is the liquid density, and R_0 is the maximum bubble radius.

Integration of the Rayleigh equation (1) allows estimation of bubble collapse time, τ_C, defined as the time taken for the radius to change from maximum to minimum [13]:

$$\tau_C = 0.915 R_0 \cdot (\rho_l/p_\infty)^{0.5}. \quad (2)$$

The parameters V_B and τ_C, which can be deduced from the above equations using measureable parameters, characterize the evolution of the bubble cavitation process. Bubble wall velocity, V_B, is a derived parameter which may be inferred from the time taken for the expanding bubble wall to traverse a specific distance. A combination of probe beam deflection and high-speed photography were utilized in this study to measure these parameters, as described below.

3 Experimental

Experiments were conducted using two different techniques and instrumental setups i.e. pump–probe beam deflection (PBD) and high-speed photography. The apparatus and experimental configurations for these techniques are as follows:

3.1 Pump-probe technique

The setup for the pump–probe beam deflection (PBD) technique was configured as shown in Fig. 1. This allowed measurement of temporal history and diameter of the bubble by varying the separation between the central axis of the unfocussed probe beam and the focus of the pump laser pulse. For these setups the specifications of the apparatus were as follows: Nd:YAG pump laser [Litron Nano-L 200-20] provided pulse energy of 140 mJ at wavelength of 1064 nm, with pulse duration of 10 ns and repetition rate of 1 Hz. A HeNe laser [Uniphase 1125P] delivering power of 6 mW at 632 nm, with nominal diameter of 0.81 mm and beam divergence of 1.0 mrad, was used as the probe laser. The focal lengths of the lenses were 50 mm for focussing the pump laser pulse and 100 mm for collecting the transmitted probe beam.

The variable focal position of the pump laser pulse was controlled by using a vertically mounted slider with vernier scale, and micrometer adjustment of the position of the focussed laser pulse with increments of 100 μm. The transmitted probe beam was detected by a photodiode [Centronic BPX65 series] with peak sensitivity of 0.52 A/W and rise time of 3.5 ns at 820 nm. The probe signal was monitored and recorded using a digitizing oscilloscope [Agilent DSO5054A], having a bandwidth of 500 MHz.

3.2 Photographic technique

Sequences of cavitation events were recorded using a high-speed camera [Vision Research Phantom v12.1]. Bubble

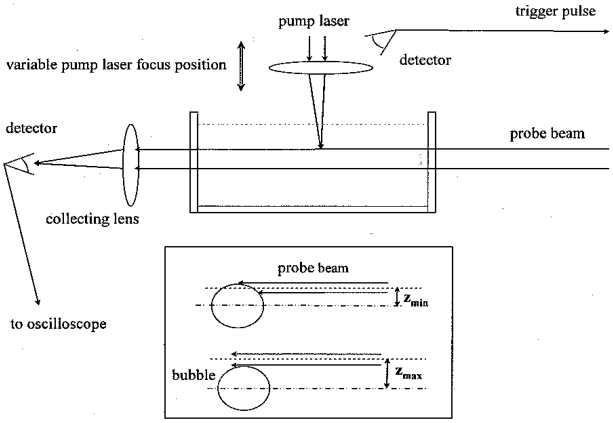

Fig. 1 Schematic of experimental setup for pump-probe beam deflection technique, with *insert* showing relative positions of bubble epicentre and probe beam axis

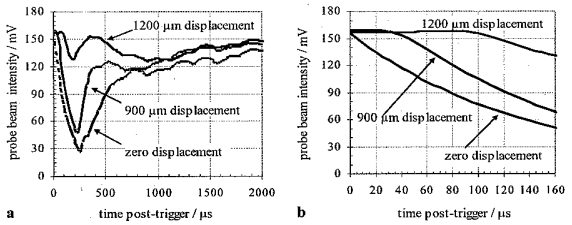

Fig. 2 Temporal change of probe beam signal intensity for (**a**) duration of bubble oscillation, and (**b**) interval prior to signal attenuation

dimensions were measured from selected still images using a travelling microscope. The camera had a maximum frame rate of $\sim 1 \times 10^6$ pictures per second (pps), and a 1280 H × 800 V CMOS sensor giving full resolution at $\sim 6 \times 10^3$ pps. The camera was connected to a laptop with dedicated software, and was externally triggered. A frame rate of 5.45×10^4 pps, i.e. a frame interval of ~20 μs, was used. Bubble volume was estimated from solid geometry equations based upon visual inspection of bubble shape i.e. spherical, spheroid or a series of conjoined spheres.

4 Results and analysis

4.1 Pump-probe beam deflection technique

4.1.1 Critical bubble parameters

The separation, z represents the distance between the epicentre of the cavitation bubble before it has made any significant vertical translation due to its buoyancy, and the central axis of the probe beam. This separation was varied by altering the vertical position of the pump laser focus whilst maintaining the unfocussed probe beam in a fixed position.

Beginning with the bubble epicentre coincident with the probe beam central axis, the separation, z was increased by 100 μm steps above and below the probe beam. For each separation, z an oscilloscope trace of the probe beam signal was recorded. A representative selection of traces is presented in Fig. 2 a for different values of z above the starting position. Note the expanded time base, presented in Fig. 2b, which illustrates the increasing time delay before probe beam signal attenuation, with increasing z.

The traces in Fig. 2a show the immediate decrease in probe beam intensity, following laser-induced cavitation, due to deflection of the beam by the expanding cavitation bubble. Minimal probe beam intensity is indicative of virtually complete deflection of the probe beam away from the detector by the expanding cavitation bubble. Maximum decrease in probe beam intensity occurs after ~180, 230 and

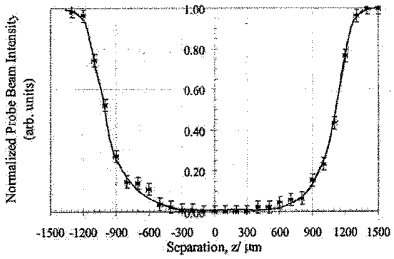

Fig. 3 Normalized probe beam signal intensity as a function of separation

260 μs for separation, z of 1200, 900 and 0 μm, respectively. At higher values of z, the reduction in probe beam intensity steadily reduces, displaying negligible deflection for $z > 1400$ μm. The trailing edges of the oscilloscope traces, for times in excess of ~800 μs, are characterized by chaotically reducing signal intensity. This is likely due to a combination of effects e.g. local temperature rise and fluid density gradients, resulting in unpredictability of the temporal dynamics for secondary and tertiary bubble oscillations. Normalized probe beam intensity is plotted at different separation, z in Fig. 3.

From this graph the critical separation z_{min} (as illustrated in Fig. 1—insert) is estimated to be +405 and −365 μm for bubble epicentre above and below the probe beam, respectively. The critical separation z_{max} (as illustrated in Fig. 1—insert) is estimated to be +1290 and −1190 μm, for bubble epicentre above and below the probe beam, respectively. From the geometrical relationship between z_{min}, z_{max}, maximum cavitation bubble diameter, and probe beam diameter, these critical separations are expressed algebraically as: $z_{min} = \phi/2 - D/2$, and $z_{max} = \phi/2 + D/2$, where ϕ is the maximum bubble diameter and D is the probe beam diameter. Based upon these calculations, an estimate for maximum bubble diameter, ϕ is 1.63×10^3 μm with an error of

Table 1 Time delay between onset of cavitation and initial attenuation of probe beam signal

z/ μm	100	200	300	400	500	600	700	800	900	1000	1100	1200	1300
τ_d/ μs ±1	2	4	9	12	17	22	28	34	47	68	84	111	117

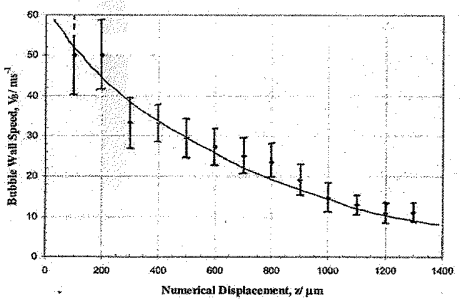

Fig. 4 Plot of bubble wall speed of expansion as a function of separation

20%, averaged over these four critical separations i.e. z_{min} and z_{max} for bubble epicentre below and above the probe beam axis.

By examining the oscilloscope trace for separation, $z = 0$ the bubble lifetime may be estimated. The chaotic pattern of the recovering probe beam signal presents an obstacle for defining an objective criterion for the termination of bubble oscillation. Based upon the recovery of signal intensity to 75% of its initial pre-trigger value, bubble lifetime is estimated to be ~900 μs with an error of 25%.

4.1.2 Bubble wall expansion

The time delay $\tau - d$ between the onset of cavitation and the initial reduction in probe beam signal was measured from the oscilloscope traces, shown in Fig. 2b. At each separation, z, for bubble epicentre below the fixed probe beam axis, these time delays, τ_d are presented in Table 1. The mean rate of bubble expansion, V_B was calculated from $V_B = z/\tau_d$ and is plotted as a function of z in Fig. 4. The decrease in bubble wall expansion speed with increasing bubble diameter is consistent with the Rayleigh equation (1). Bubble wall speed becomes asymptotic for $z > 1300$ μm.

4.2 High-speed photography of the bubble

Still images were selected from high-speed cine camera recording of the dynamic evolution of the laser-induced cavitation bubble. At a frame rate of 5.45×10^4 pps the interval between images was ~20 μs. A representative selection of images of an expanding bubble is shown in Fig. 5. The quoted times represent the interval after delivery of the pump laser pulse i.e. post-trigger.

These images show dynamic profiles of a bubble formed along the trajectory of the incident laser pulse, centred about multiple breakdown sites (the bright spots). The existence of multiple breakdown sites is an indication of dielectric breakdown of the target medium during the early stages of cavitation. The multiple bubbles formed in this way have a tendency to coalesce towards the centre of the cavitation region, forming a single bubble after a specific time (~300 μs post-trigger for the bubble imaged in Fig. 5). Bubble volume estimates for the time interval 200 to 460 μs post-trigger are plotted in Fig. 6. Due to the high intensity of the optical flash at the onset of plasma formation, no details of the cavitation bubble were discernible in the interval up to 200 μs post-trigger.

Bubble diameters were measured using a travelling microscope. They were assumed to have a high degree of symmetry in the plane orthogonal to the incident laser pulse trajectory i.e. each bubble was considered to have circular cross-section in the xy-plane, for z-axis coincident with the trajectory of the incident laser pulse. Account was taken of the overlap of adjacent bubbles in the cavitation region, in the early stages of bubble formation. A high degree of sphericity (low eccentricity) was apparent after ~280 μs. Standard formulae were used to calculate bubble volume, V_β. For bubbles with a high degree of eccentricity, radial and transverse *radii*, R_r and R_t, respectively, were measured. Bubble volume was subsequently estimated from:

$$V_\beta = 4\pi/3 \cdot R_r^2 \cdot R_t. \quad (3)$$

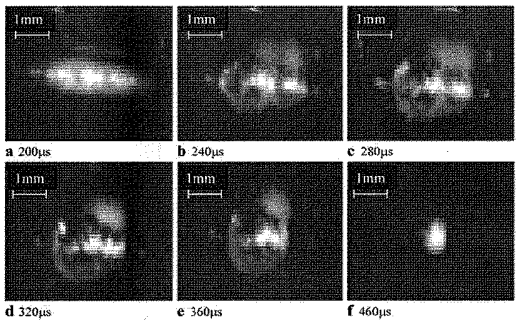

Fig. 5 Dynamics of cavitation bubble dimensions at selected times

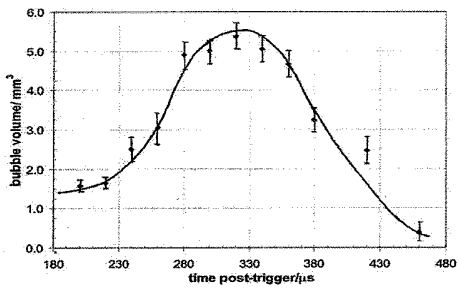

Fig. 6 Plot of bubble volume as a function of time after delivery of laser pulse

From the graph in Fig. 6, maximum bubble volume, V_0, was found to occur at 320 ± 30 μs after the initiation of plasma formation, and is estimated to be $\sim 5.4 \pm 0.5$ mm^3. This implies a maximum bubble diameter of 2.20×10^3 μm, with an error of ~10%. Large errors are likely to occur in the estimation of bubble diameter during the early stages of bubble growth due to the limited contrast between the bubble wall and the background, and the presence of multiple breakdown sites.

The duration of the bubble imaged in Fig. 5 is estimated to be 480 ± 30 μs. This figure is the sum of the time interval prior to the first bubble image (200 μs), and the time taken for the bubble to increase to its maximum volume and then collapse to a minimum volume (280 μs). In order to estimate the total lifetime of the oscillating bubble, images of the secondary and tertiary stages of bubble oscillation were examined. Secondary and tertiary bubble durations were estimated to be 120 ± 20 and 100 ± 20 μs, respectively. Addition of the primary, secondary and tertiary bubble lifetimes gives an estimate for the total bubble lifetime of 700 ± 30 μs.

4.3 Comparison of experimental results and theoretical predictions

The Rayleigh equation (1) expresses the bubble wall velocity, V_B as a function of bubble radius, R_B. Taking natural logarithms allows the relationship between V_B and R_B to be expressed:

$$\ln(V_B) = 0.5 \ln\left\{(R_0/R_B)^3 - 1\right\} + k \qquad (4)$$

where $k = 0.5 \ln\{2p_\infty/(3\rho_l)\}$. This relationship is displayed in Fig. 7 for values of V_B and R_B obtained using the probe beam deflection technique.

From this graph, the slope is estimated to be ~0.18, compared to a theoretical value of 0.50, in the logarithmic form of the Rayleigh equation (4). Further, the y-intercept in Fig. 7 is ~2.54, based upon data acquired under dynamic experimental conditions. In order to compare this value with the value of k from (4), it is necessary to have accurate values for liquid bulk density, ρ_l in the immediate vicinity

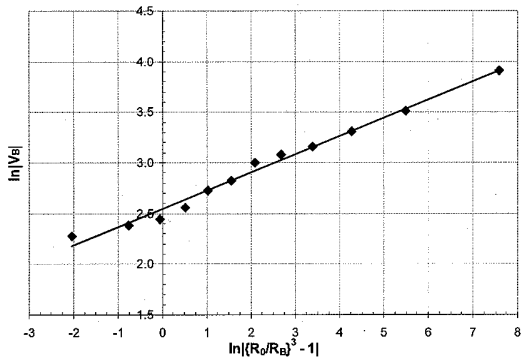

Fig. 7 Natural logarithms of bubble velocity vs. bubble radius

of the cavitation bubble, for the duration of the cavitation process. There are several possible reasons for discrepancies between theoretical estimates and empirically derived data e.g. the a priori assumptions in the derivation of the original Rayleigh equation (1) that the water bulk is both inviscid and incompressible may be invalid for laser-induced cavitation. In addition, the equation was derived specifically for cavitation below the inception pressure for an isothermal fluid. It is self-evident that laser-induced and pressure induced cavitation are not thermodynamically equivalent processes. Also, conditions in the local water volume during laser-induced cavitation are obviously not isothermal.

5 Discussion

Estimates of maximum bubble diameter obtained by the PBD and high-speed cine techniques are within the same order of magnitude, yet are still significantly different. The major advantage of photography compared to the PBD technique was its ability to directly image the parameter under investigation i.e. bubble dimension. By contrast, the PBD technique inferred bubble diameter indirectly, via interpretation of the attenuation profile of the probe beam signal. High-speed imaging was limited, however, by the lack of image contrast between the background and bubble wall at higher frame rates, particularly in the earlier stages of bubble expansion.

A further challenge for high-speed photography is the accurate and consistent estimate of bubble volume in the early stage of bubble expansion, when several bubbles are in close proximity to each other and are coalescing towards the centre. The principal source of multiple breakdown sites ("hot spots") is the non-linear property of self-focussing, which narrows the beam waist independently of the lens optics [6]. It has been reported [5] that self-focussing is negligible for pulse durations longer than 100 ps. A direct result of the presence of multiple breakdown sites is the formation of several cavitation bubbles, in the early expansion stage, which coalesce to form a single bubble of negligible eccentricity. However, the multiple breakdown sites induced using a much longer laser pulse of ~10 ns in this study may be attributed to, instead of self-focussing, the existence of impurities in the sample providing "seeding" centres for dielectric breakdown of the liquid medium. Such "seeding" effect can be overcome by expanding laser beam prior to focusing in the water bulk to only induce the dielectric breakdown at the focal point and therefore a single spherical bubble can be produced [14]. The observed elongated shape of the plasma-forming region, due to the increased absorption coefficient of the non-transparent plasma in the visible and near infrared regions, is consistent with the 'moving breakdown phenomenon' [15].

Primary bubble lifetime of ~480 μs and maximum bubble diameter in the order of 2000 μm, at laser pulse energy 140 mJ, were in reasonable agreement with comparable published data [9, 10] which reported primary bubble lifetimes of 210, 240 and 270 μs, and maximum bubble diameters of ~2300, ~2700 and ~3100 μm, for pulse energies of 4.7, 6.0 and 8.6 mJ respectively. Estimates of total bubble lifetime for the current research are consistent between the two techniques employed i.e. ~900 and ~700 μs for probe beam deflection and high-speed photography, respectively. Primary bubble lifetime is an important parameter for optimization of laser-induced breakdown spectroscopy (LIBS) sensitivity of elemental detection in aqueous media. By fixing the tem-

poral separation between laser pulses to approximately half the primary bubble lifetime i.e. ~250 μs in the current research, a secondary laser pulse may be used to increase the temperature of the plasma encapsulated within the primary cavitation bubble and therefore increase the detection sensitivity.

The consistency between the presently reported data for maximum bubble diameter, and that reported earlier [9, 10] implies a weak functional relationship between maximum bubble volume and pump laser pulse energy. The current research utilized pulse energy of 140 mJ, an order of magnitude larger than that used by Petkovšek and Gregorčič [9, 10]. This appears to confirm the hypothesis of rapid ionization of target medium by the leading edge of the Gaussian pulse profile, followed by rapid heating of the plasma. The plasma thus formed strongly absorbs in the visible and near infrared regions. It is therefore only a proportion of available pump laser energy which is utilized for plasma generation, the remaining energy acting as a high flux source for thermal heating.

Meaningful comparison of experimentally measured bubble wall expansion velocity with Rayleigh equation estimates is not possible without accurate knowledge of the liquid density in the vicinity of the cavitation bubble wall, and particularly the temporal change in this parameter over the bubble lifetime. The material within the cavitation bubble is in a metastable superheated state, and as such has bulk physical properties significantly different from water in the liquid state. The influence of the metastable material within the cavitation bubble on the vapour/liquid boundary makes meaningful comparison between empirical data and theoretical prediction problematic.

A sophisticated differential model has been reported [16] and it may provide a plausible explanation for the disparity between theoretical (classical Rayleigh) and measured properties of the cavitation bubble. In the model Rayleigh's original assumption of incompressible liquid was assumed valid for a "low-mach" regime whereby the rate of bubble wall expansion was less than 30% of the speed of sound in the encapsulated vapour medium. Of interest to the current research is an alternate "high-mach" regime, described in the model, whereby the bubble rate of expansion exceeds the critical limit defined for the "low-mach" regime. In this "high-mach" regime the encapsulated vapour is assumed to obey van der Waals laws, and the liquid is assumed to be compressible. It is suggested that allowing for compressibility of liquid in the vicinity of the vapour/liquid boundary will allow theoretical estimates for bubble wall expansion rate, for any specific bubble radius, to match more closely empirically derived data.

The precision of the probe beam deflection technique may be improved by two refinements. First, a reduction of increment for vertical translation of the pump beam focus will allow more precise measurement of critical separations, z_{min} and z_{max}. Second, by employing a pin-hole aperture at the probe laser head, a significant reduction in probe beam diameter may be achieved. This would also enable more precise discrimination of critical separations, z_{min} and z_{max}.

Imaging the interval between laser-induced plasma generation and 200 μs post-trigger is a principal objective for further application of the high-speed photographic technique. This may be achieved by increasing the frame rate of the camera. This, however, results in a significant reduction in image resolution. A more sophisticated understanding of the imaging software for contrast enhancement, particularly in the post processing phase, may enable images of the earliest stage of bubble formation to be captured with sufficient resolution to allow accurate measurements of bubble parameters.

6 Conclusions

In this paper, two techniques for the determination of principal parameters for laser-induced cavitation bubbles in the water bulk have been demonstrated and discussed. The first method employed the probe beam deflection technique to infer bubble diameter over a complete period of bubble oscillation. The second method employed high-speed photography to directly image the dynamic evolution of the cavitation bubble. Estimates of maximum bubble diameter and bubble lifetime are in reasonable agreement between the two techniques. Comparison between the data presented in this paper and previously published research, for maximum bubble diameter and bubble lifetime, is in reasonable agreement. Estimation of bubble wall speed in the bubble expansion phase has been demonstrated from data acquired with the probe beam deflection technique. The qualitative relationship between bubble radius and wall speed rate of expansion is consistent with the Rayleigh equation. Inconsistencies between the empirical data presented in this paper and theoretical predictions from the Rayleigh equation have been demonstrated. Speculation has been offered for potential reasons for these inconsistencies, based upon deviations in liquid properties under experimental conditions from the a priori assumptions inherent in the derivation of the Rayleigh equation.

Acknowledgements The authors would like to recognize the invaluable support provided by Mr Edwin Billiet in the Centre for Applied Laser Spectroscopy, DEAS, Cranfield University at Shrivenham. A debt of gratitude is owed also to Professor Ian Horsfall, Cranfield University at Shrivenham for the kind loan of the high-speed camera.

References

1. A. De Giacomo, M. Dell'Aglio, O. De Pascale, M. Capitelli, Spectrochim. Acta B **62**, 721 (2007)

2. R. Fantoni, L. Caneve, F. Colao, L. Fornarini, V. Lazic, V. Spizzichino, Spectrochim. Acta B **63**, 1097 (2008)
3. J. Helfmann, G. Müller, Med. Laser Appl. **16**, 30 (2001)
4. J. Anzano, R.-J. Lasheras, Talanta **79**, 352 (2009)
5. P.K. Kennedy, D.X. Hammer, B.A. Rockwell, Prog. Quantum Electron. **21**, 155 (1997)
6. D.X. Hammer, R.J. Thomas, G.D. Noojin, B.A. Rockwell, P.K. Kennedy, W.P. Roach, IEEE J. Quantum Electron. **32**, 4 (1996)
7. X. Chen, R.Q. Xu, Z.H. Shen, J. Lu, X.W. Ni, Opt. Laser Technol. **36**, 197 (2004)
8. J. Lu, R.Q. Xu, X. Chen, Z.H. Shen, X.W. Ni, S.Y. Zhang, C.M. Gao, J. Appl. Phys. **95**, 8 (2004)
9. R. Petkovšek, P. Gregorčič, J. Appl. Phys. **102**, 044909 (2007)
10. R. Petkovšek, P. Gregorčič, J. Možina, Meas. Sci. Technol. **18**, 2972 (2007)
11. P. Gregorčič, J. Možina, Acta Phys. Pol. A **112**, 1137 (2007)
12. Lord Rayleigh, Philos. Mag. **34**, 94 (1917)
13. A. Shima, Shock Waves **7**, 33 (1997)
14. E.A. Brujan, K. Nahen, P. Schmidt, A. Vogel, J. Fluid Mech. **433**, 251 (2001)
15. D.X. Hammer, E.D. Jansen, M. Frenz, G.D. Noojin, R.J. Thomas, J. Noack, A. Vogel, B.A. Rockwell, A.J. Welch, Appl. Opt. **36**, 5630 (1997)
16. I. Akhatov, O. Lindau, A. Topolnikov, R. Mettin, N. Vakhnitova, W. Lauterborn, Phys. Fluids **13**, 2805 (2001)